Metamaterials Analysis, Modeling, and Design in the Point Dipole Approximation

by

Patrick T. Bowen

Department of Electrical and Computer Engineering
Duke University

Date: _____

Approved:

_____
David R. Smith, Supervisor

_____
Daniel Gauthier

_____
Willie Padilla

_____
Maiken Mikkelsen

_____
Nathan Kundtz

Dissertation submitted in partial fulfillment of the requirements for the degree of Doctor of Philosophy in the Department of Electrical and Computer Engineering in the Graduate School of Duke University
2017

Abstract

Metamaterials Analysis, Modeling, and Design in the Point Dipole Approximation

by

Patrick T. Bowen

Department of Electrical and Computer Engineering
Duke University

Date: _____

Approved:

_____
David R. Smith, Supervisor

_____
Daniel Gauthier

_____
Willie Padilla

_____
Maiken Mikkelsen

_____
Nathan Kundtz

An abstract of a dissertation submitted in partial fulfillment of the requirements for the degree of Doctor of Philosophy in the Department of Electrical and Computer Engineering
in the Graduate School of Duke University
2017

Abstract

This dissertation is focused on applying the discrete dipole approximation to modeling metamaterial structures and devices. In particular, it is focused on modeling the linear and nonlinear behavior of one particular kind of metasurface, called a film-coupled metasurface. Film-coupled metasurfaces are periodic structures of metamaterial elements where the elements are placed a deeply subwavelength distance away from a metal film. The optical nanopatch antenna is an example of a particularly interesting film-coupled metasurface, and it is explored in depth in this dissertation. Starting with fundamental coupled mode theory approaches, fully predictive, analytic formula are developed that solve for the polarizabilities of the elements, which in turn are used to compute the reflective properties of the metasurface, including the effects of spatial dispersion using the language of effective medium theory. The theory is able to explain Wood's anomalies of the structure from an effective medium standpoint, again using purely analytic results that show excellent agreement with experiments and full-wave simulations. fThe linear optical theory is extended in later chapters to applications in nonlinear optics including bistability and lasing in four-level systems. The final chapter is devoted to solving for surface modes of the structure with complex eigenfrequencies, which may be useful in future work for explaining recent experiments that show lasing in modes that are spatially coherent across the surface.

Modeling other metamaterial devices using the discrete dipole approximation,

including radio frequency metamaterial antennas, is discussed in the appendices.

To my grandfather, Donald Lanier Bowen, who was the greatest example of husband, father and grandfather that I've witnessed.

Contents

List of Tables

List of Figures

Acknowledgements

I would like to acknowledge Kymeta Corporation, and Dr. Nathan Kundtz in particular for helpful conversations. I would also thank my advisor Dr. David R. Smith for his guidance and Dr. Robert Bryant for helpful conversations.

1

Introduction

This dissertation focuses on the treatment of metamaterial structures under a certain approximation called the *Discrete Dipole Approximation*. In many areas of physics, finding exact analytical solutions to problems can be nearly impossible, and computational methods can only buy as much success as there is computational power available. The success of analytically treating problems in many areas of physics and engineering therefore hinges upon choosing the right approximation for the situation. Metamaterials is one area of physics and engineering where phenomena are particularly difficult to simulate exactly using full-wave techniques because of the vastly different length scales between the features of the metamaterial elements and the overall length scale of the device. An alternative to full-wave models is to approximate the metamaterial as a homogenous medium using effective medium techniques, and then simulate the domains of effective material using a full-wave solver. However, because it is difficult to design metamaterial elements that resonate at wavelengths much larger than ten times the size of the element, simple effective medium techniques of modeling the structure can become quickly suspect. This motivates finding an approximation that is appropriate for metamaterial-type structures that can be

useful in finding an analytic or semi-analytic solution to modeling metamaterial devices.

The field of metamaterials itself has been commonly called a design tool to engineer devices. The archetypical example of metamaterials is the invisibility cloak, where the design for the cloak started with a specific homogeneous material distribution in space that came from transformation optics, and then achieving that material distribution relied on creating an artificial material made of artificial "meta-atoms"[1]. Meta-atoms are inspired by natural materials in the sense that they are typically made of a lattice of elements that resonate at a wavelength that is much larger than the size of the element. The resonance frequency of a scatterer that has the longest wavelength for the element's size is by definition the fundamental resonance of the element, which typically is referred to as an "electric-like" or "magnetic-like" resonance, because it scatters like either an electric or magnetic dipole. Natural materials also dominantly scatter into electric dipole transitions, so the field of modeling natural materials in optics as a collection of dipoles has a long history reaching back to Lorenz[2]. Modeling either a natural or artificial material as a collection of dipoles is known as *effective medium theory*, and a brief review of this field is presented in chapter 2. The hypothesis that metamaterials may be modeled as a collection of scattering point dipoles is, at this point, merely a hypothesis, and needs to be tested for each kind of metamaterial elements that one would like to model. At the end of chapter 2 a scheme is presented to test the validity of applying the point dipole approximation to simple metamaterial elements, and it is seen to hold with good accuracy.

Metamaterial devices themselves have a broad range of application in electromagnetics, from radio frequency (RF) to optics. Applying the discrete dipole approximation to RF metamaterial antennas has been a significant part of this dissertation, but for the sake of coherence that part of the work has been placed in appendix F.

The largest portion of this dissertation is focused on modeling a particular metamaterial structure called a *film-coupled metasurface*, as illustrated in fig. 1.1, which has been recently shown to be an incredibly useful structure for its simple fabrication and plasmonic enhancement in the optical region of the spectrum. It's composed of a flat, metal film that serves as a ground plane, covered by a thin dielectric that is typically a few nanometers in thickness. On top of the dielectric is placed a multitude of *nanopatch antennas* which are metallic, cubic nanoparticles. These can either be colloidally-made and deposited in a random pattern on the surface, or else lithographically fabricated in a top-down approach giving a periodic lattice. This structure was initially particularly interesting for examining the potential applications of plasmonic enhancement of light, since the size of the dielectric gap can be easily and precisely controlled in fabrication, giving exact spacings between the nanopatch and the ground plane.

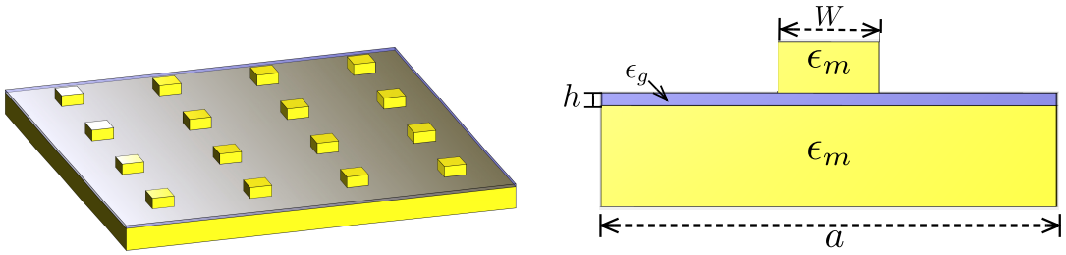

(a) (b)

FIGURE 1.1: Schematic and dimensions of a film-coupled patch antenna metasurface, separated from the metal film by a thin layer of dielectric of thickness h, with lattice constant a. Metals have dielectric constant ϵ_m, and the dielectric spacer has the dielectric constant ϵ_g.

One of the first applications of this particular metamterial structure was in the form of a narrow-band perfect absorber, where all of the light at a particular wavelength will be perfectly absorbed for all angles of incidence for transverse-magnetic (TM) polarization[3]. Again this effect was attributed to the resonance formed in the gap region between the nanopatch and the ground plane, which is precisely controlled

by the thickness of the dielectric. Since the initial application in perfect absorbers, optical patch antennas have been explored as platforms for enhanced fluorescence, single photon emission, optical bistability, and even lasing. This dissertation presents a systematic, fully analytic treatment of the optical patch antenna system starting from a single nanoptach antenna and building the theory to consider periodic arrays of nanopatches, and exploring applications in both linear and nonlinear optics.

After the review of effective medium theory in chapter 2, chapter 3 provides an analytical treatment of a single optical patch antenna based on a perturbative temporal coupled mode theory. Analytical expressions for the resonance frequency, Ohmic losses, radiation losses, and mode amplitudes as a function of frequency, and these are compared with results from full-wave simulations. Chapter 4 shows that optical patch antennas scatter as magnetic dipoles, and calculates the reflectance properties of periodic arrays of film-coupled optical patch antennas. At this point, the perfect absorber phenomenon is explained as the destructive interference between the field radiated by the effective magnetic dipoles of the film-coupled nanopatches and the field reflected by the oscillating electric currents in the metal film. Perfect absorption is maintained at high angles of incidence because of a complex interplay between the increasing radiation loss rate of the lattice at high angles and the decreasing coupling of the nanopatches to free space modes.

In chapter 4, the nanopatch antennas that comprise the film-coupled metasurface were treated as if they do not interact with each other. However, just as in any metasurface, the metamaterial elements in the surface couple to each other strongly, and their coupling is described by the Green's function. In the case of elements that are placed very close to a metal film like optical patch antennas, the Green's function is very strongly perturbed from a free space Green's function due to the surface plasmon modes that exist on the metal film. In chapter 5 this coupling between the elements is taken into account by developing an effective medium theory

of film-coupled metasurfaces. This is done by approximating the Green's function as dominated by the surface plasmon interaction and analytically computing the doubly infinite sum of scattered fields due to all the dipoles in the lattice to form an interaction constant. The theory in this section forms a foundation that is able to explain spatial dispersion, surface modes, and Wood's anomalies that are discussed later in the dissertation.

Wood's anomalies are a phenomenon that have been of intense interest in optics since their discovery by Wood in 1902[4] and their initial treatment by Lord Rayleigh in 1907[5, 6]. Wood's anomalies are sharp changes in the reflected or diffracted field from a metallic grating. In chapter 6, for the first time, a fully analytic explanation of the phenomenon of Wood's anomalies is developed for the first time using an effective medium theory approach. By treating the nanopatch antennas as point dipoles, both the sharp and diffuse anomaly can be explained in terms of the interacting field between the dipoles that comprise the metasurface. The sharp anomaly is shown to be due to the directly radiated field, while the diffuse anomaly is shown to be caused by the surface plasmon interaction between the nanopatches. The theory here is built upon all of the theory developed in chapters 3 to 5, and an experiment is presented that compares the analytically predicted Wood's anomalies and patch antenna resonances with experimentally measured results.

Chapters 7 and 8 explore applications of film-coupled metasurfaces to nonlinear optics. Chapter 7 examines the application of bistability to film-coupled metasurfaces by introducing a nonlinear optical material in the gap region between the nanopatch and the metal film. The pertrubative temporal coupled mode theory introduced in chapter 3 is adapted to take into account the nonlinear currents in the gap, and a bistable reflectance spectrum is predicted and compared with full-wave simulations. Alternatively, chapter 8 introduces a four-level semiclassical gain material in the gap region and uses coupled mode theory to predict lasing thresholds and the

requirements for minimum carrier densities to achieve lasing in single nanocubes.

One final application of interest for film-coupled metasurfaces is lasing in surface modes rather than in individual nanopatch antennas, where all the nanopatch antennas in the surface oscillate coherently. Lasing in surface modes is particularly interesting because, as opposed to radiating in a magnetic dipole pattern like a single nanopatch antenna, surface modes radiate in collimated beams that can be focused or coupled into a fiber. Surface modes can also have a much higher quality factor than the plasmonic nanocavity modes of individual nanopatches.

Surface modes are very closely related to the diffuse Wood's anomalies discussed in chapter 6, but are formally developed in chapter 9 starting with a Lagrangian that includes both the electromagnetic field and the effective magnetic dipoles of the metasurface. A Lagrangian formulation is chosen because the goal is to solve for complex resonance frequencies, which are fundamentally an expansion of the Green's function in the time-domain. The modes derived here are therefore closely related to quasi-normal modes that are commonly discussed in optics literature.

A series of appendices are attached that support the content of the main chapters. Of these, appendix B is worthy of note, where unconjugated coupled mode theory is developed in a cylindrical Hankel basis using Lorentz reciprocity. Cylindrical Hankel functions are not source-free solutions of Maxwell's equations, so the traditional development of coupled mode theory does not apply in this situation. This treatment corrects some problems in published literature and some example analytical problems are treated that reproduce known exact analytical results from other methods.

2

Review of Effective Medium Theory and the Dipolar Description of Materials

This chapter provides a review of effective medium theory, which is a field that has had a long history dating back to Clausius, Mossotti, Lorentz, and Lorenz in the late nineteenth century. The only original work to myself in this chapter is the procedure to validate the dipole approximation of metamaterial elements in section 2.3, and the explicit derivation of the one-dimensional interaction constants that are presented in their final form in eqs. (2.19a) and (2.19b).

Within effective medium theory, materials and metamaterials are both defined as an ensemble of deeply sub-wavelength objects or elements, which under certain conditions will behave collectively as a homogeneous material. This ensemble of elements may be either periodic or a random distributions, and the elements that compose the material or metamaterial are assumed to be small enough to be well-described as point dipoles. Lorentz was the first to propose in his doctoral thesis[7] in 1878 that a body of continuous material, as described by the macroscopic Maxwell's equations, should be described by point sources in vacuum which satisfy the microscopic

Maxwell's equations, or Lorentz equations. According to Einstein, Lorentz thus famously "separated matter and ether,"[8, 9] providing a basic framework by which the effective material parameters used in the macroscopic Maxwell's equations might be derived from a given microscopic structure of point dipoles. Lorentz's early work was improved upon by Planck[9], Ewald[10], Madelung[11], Hoek[12], De Groot[13], and others who have collectively contributed to a long and rich history of relating the effective material parameters of a body to it's microscopic structure. Ewald and Madelung in particular were the first to treat periodic crystals, while Lorentz, Planck, and Hoek were primarily concerned with gasses and amorphous solids. A good review of the early history and results of effective medium theory is available in [9].

One of the primary results of effective medium theory is the relationship between the polarizability of the microscopic point dipoles that compose the medium, and the permittivity or permeability. For cubic lattices of dipoles in the static limit, this is given by

$$\epsilon = 1 + \frac{\alpha/a^3}{1 - C\alpha} \tag{2.1}$$

where α is the polarizability of the dipoles, a is the lattice constant, and $C = 1/3a^3$ is the interaction constant for a cubic lattice in the static limit[14]. This relation is credited to Clausius[15] and Mossotti[16] in the context of electric permittivity and is therefore commonly referred to as the Clausius-Mossoti relation, but was later independently discovered by both Lorentz[2] and Lorenz[17] in the context of optical refractivity, and hence is also called the Lorentz-Lorenz relation.

Unfortunately, the Lorentz-Lorenz relation has a limited range of validity, and naively applying eq. (2.1) to the non-static realm leads to conceptual difficulties because it provides no mechanism for accounting for the radiative loss of the dipoles[18, 19, 20, 21]. When a dipole radiates in any geometry, it exerts a force on itself through

the radiation reaction that causes the amplitude of the dipole to decay exponentially in time. In the frequency domain, this phenomenon is captured through the imaginary part of the polarizability of the dipole, and hence it can be shown that the radiation reaction requires that the imaginary part of the polarizability take a specific value, even when the dipole exhibits no Ohmic losses. However, simply applying the Clausius-Mossotti relation to a complex polarizability would yield a complex permittivity, which would predict that all materials must be lossy, and forbid the existence of transparent materials. Planck himself interpreted the inclusion of radiation damping to the result in eq. (2.1) as a prediction of the "absorption of the suns rays through the atmosphere"[9]. As is pointed out in [9], for a perfectly homogenous medium with no scattering and no Ohmic losses, conservation of energy dictates that should be no absorption. Since the polarizability of a dipole must be complex due to radiation damping, how is it possible that some natural and artificial materials are transparent, and what is the physical mechanism that allows it?

It has been well established in previous work that the answer to this question is lies in the interaction constant C, which arises from the force that the dipoles in the lattice exert on one another. Abraham and Lorentz initially showed that charged particles exert a force on themselves[22], which is referred to as the radiation reaction or Abraham-Lorentz force[23]. Lorentz treated the force by changing the effective mass of the electron, but later authors[24, 19, 18] showed that the radiation reaction force of an oscillating dipole can be taken into account by simply modifying the polarizability of the dipole such that $\alpha_{eff} = \alpha/(1 + i\alpha k^3/6\pi)$. Ref. [9, 20] have proposed that there must be corrections to the Clausius-Mossotti relationship by requiring that the lattice conserve energy, and therefore modified the interaction constant C such that the permittivity would be real for dipoles with no Ohmic losses. The claim was that, in the limit of zero Ohmic loss, the overall permittivity must be real and therefore the dipoles in the lattice must exert a force on one another

that exactly cancels the radiation reaction force that each dipole exerts on itself. References [9, 25, 26, 27] computed the exact interaction constant for two and three dimensional lattices in free space and it can be shown that this is remarkably the case. When a dipole is placed in a one-dimensional array of dipoles with a lattice spacing that is smaller than one wavelength, the dipoles in the lattice exert a force on one another that cancels the radiation reaction force and replaces it with another loss term that represents the losses of a line source. Likewise, when a line source is placed in an array of other line sources, their fields exert a force on each other that exactly counteracts the losses of the line sources, and replaces them with loss terms that represent the plane wave loss of the metasurface. When planes of a metasurface are combined to form a metamaterial the situation is somewhat more complicated, since spatial dispersion necessarily becomes involved. However, the main result is that all of the radiative losses cancel, which results in a material that will have a purely real permittivity or permeability if the dipoles have no Ohmic losses[9].

More recently, interest in effective theory has revived with the popularization of metamaterals, which has brought new challenges to the classical homogenization approaches that were developed in the late 19th and early 20th centuries to model natural materials. Classical homogenization techniques were very commonly based on the assumption, which is originally attributed to Lorentz, that there exists a length scale Δ over which one might average the electric field, which is both much smaller than the wavelength λ and much larger than the lattice spacing a between the atoms[18, 9], i.e

$$a \ll \Delta \ll \lambda. \tag{2.2}$$

However, metamaterials are designed to be resonant, and many metamaterial elements are resonant at wavelengths where $\lambda/10 < a < \lambda/2$[28, 29] since it can be difficult to design resonators that operate at a wavelength that is more than an order

of magnitude larger than the physical dimension of the metamaterial element. In this regime spatial dispersion becomes an important effect, and the classical Lorentz-Lorenz relation will not apply, which has led authors to develop exact formulas for the interaction constant and homogenization of metamaterials and metasurfaces that have a larger lattice spacing relative to the wavelength [25, 26, 27]. These formulas are not only useful for the modeling of metamaterials[30, 27, 31], but also for the extraction of the exact polarizability of metamaterial elements from full-wave simulations[32].

We begin with a brief overview in section 2.1 of how an individual dipole interacts with its environment, both in free space and any other geometry. A brief review of the effective medium theory of metasurfaces is presented in section 2.2, with an emphasis on conservation of energy in the lattice. In section 5.1 we explore a particular geometry of current interest in optics, which is a kind of metasurface with a magnetic response coupled to a metal film, made by the optical analogue of patch antennas. An exact expression for the surface plasmon contribution to the interaction constant of a film-coupled metasurface is derived in sections 5.2 and 5.3, and it is shown that the interaction constant perfectly the cancels the radiation reaction damping force due to the surface plasmon coupling. Although the damping force is perfectly canceled in the limit of no Ohmic losses, the interaction between the metamaterial elements produces a resonance frequency shift, which is given by the real part of the interaction constant. The resonance frequency shift is compared against full-wave simulations in section 5.4 by examining a perfect absorber made of a metasurface of patches that are coupled closely to a metal film, and it is thereby shown that the surface plasmon interaction dominates the coupling between the metamaterial elements.

2.1 The Point Dipole in Free Space

There is a sense in which the polarizability of a dipole itself is not an inherent property of the dipole, but depends on the environment, and therefore may be considered a nonlocal property. Even vacuum is no exception, since the vacuum itself places certain requirements on what values the polarizability of a dipole may take. From the perspective of quantum electrodynamics, any geometry interacts with a dipole through vacuum states, which cause the dipole to spontaneously emit and therefore decay.

This phenomenon is not, however, unique to quantum electrodynamics, and can also be seen in the classical realm. Here we derive the complex polarizability of a point dipole, following a treatment similar to what is presented in Refs. [24, 18]. Consider a single dipole with some polarizability α_m that is placed at position $\mathbf{r}_0$ in an environment that is described by a Green's function $\mathbf{G}(\mathbf{r}, \mathbf{r}')$, and imagine that the environment is illuminated by some incident electric field $\mathbf{E}_0$. The total field in the environment $\mathbf{E}$ will be

$$\mathbf{E}(\mathbf{r}) = \mathbf{E}_0(\mathbf{r}) + \mathbf{G}(\mathbf{r}, \mathbf{r}_0)\mathbf{p}. \tag{2.3}$$

The polarizability of a dipole is the tensor that defines the proportionality between the dipole moment and the field. However, there are two possible ways in which this polarizability might be defined. The polarizability might be expressed as the proportionality with the total field experienced by the dipole, $\mathbf{p} = \bar{\alpha}_e^0 \mathbf{E}$. We define $\bar{\alpha}_e^0$ as the inherent polarizability of the dipole, since all interactions with the environment are contained in $\mathbf{E}$ rather than in the polarizability, and therefore $\bar{\alpha}_e^0$ does not change when the environment changes. The alternative definition of the polarizability is $\mathbf{p} = \bar{\alpha}_e \mathbf{E}_{inc}$, which is the effective polarizability of the dipole, since it is a quantity that is dependent on the environment in which the dipole is placed. The effective

polarizability can be found directly from eq. (2.3),

$$\bar{\alpha}_e = \bar{\alpha}_e^0(1 - \epsilon_0^{-1}\mathbf{G}(\mathbf{r}_0, \mathbf{r}_0)\bar{\alpha}_e^0)^{-1}. \tag{2.4}$$

The real part of Green's tensor at the origin is generally singular or undefined. We note that the average value of the real part of the Green's function at an infinitesimal radius is however finite[33]. In this work, we disregard the real part of Green's tensor at the origin for a dipole in free space, since it does not lead to any restrictions on the range of values that the effective polarizability may take, and hence makes it impossible to observe a difference between the inherent and effective polarizability due to the real part of the Green's function. In Ref. [18] it was pointed out that the real part may be ignored by renormalization, and that only the imaginary part is of physical significance.

The imaginary part of Green's tensor at the origin, however, is always finite, and according to Poynting's theorem corresponds to the power loss of fields radiated by the dipole. A careful calculation of the limiting form of Green's tensor at the origin for a dipole in free space shows that[34]

$$\mathbf{G}(\mathbf{r}_0, \mathbf{r}_0) = -i\frac{k^3}{6\pi}\mathbf{I} \tag{2.5}$$

and so the effective polarizability of a dipole in free space is

$$\bar{\alpha}_e = \bar{\alpha}_e^0(1 + ik^3\bar{\alpha}_e^0/6\pi\epsilon_0)^{-1}. \tag{2.6}$$

This is the well known radiation reaction correction, which corrects the polarizability in order to account for the force that a radiating dipole exerts on itself so that its amplitude decays in time according to the energy that is radiated from the dipole.

If the inherent polarizability of the dipole, $\bar{\alpha}_e$, happens to follow a Lorentzian line shape, i.e.

$$\bar{\alpha}_e^0 = \frac{\epsilon_0 A\omega_0^2}{\omega_0^2 - \omega^2 - i\omega_0^2/Q_\Omega} \tag{2.7}$$

where A is an amplitude coefficient that has units of volume, ω_0 is the resonance frequency, and Q_Ω is the Ohmic Q-factor, then the effective polarizability will also be a Lorentzian, but with a resonance frequency shift in proportion to the real part of the Green's function, and an added loss term through the imaginary part of the Green's function. This is explicitly given by

$$\bar{\alpha}_e = \frac{\epsilon_0 A \omega_0^2}{\tilde{\omega}_0^2 - \omega^2 - i\omega_0^2/Q} \tag{2.8}$$

where

$$\begin{aligned} \tilde{\omega}_0 &= \omega_0 \sqrt{1 - \epsilon_0 \mathrm{Re}\{\mathbf{G}(\mathbf{r}_0, \mathbf{r}_0) A\}} \\ &\approx \omega_0 (1 - \epsilon_0 \mathrm{Re}\{\mathbf{G}(\mathbf{r}_0, \mathbf{r}_0) A/2\}) \end{aligned} \tag{2.9}$$

$$1/Q = 1/Q_\Omega - \mathrm{Im}\{\mathbf{G}(\mathbf{r}_0, \mathbf{r}_0)\} A. \tag{2.10}$$

When the geometry within which a dipole is placed is modified, the resonance frequency and quality factor of the dipole's resonance are both modified as the Green's function is changed.

2.2 Metamaterial Lattices in Free Space

In a similar way in which an effective polarizability might be formed for a single dipole, an effective polarizability might be formed by any arrangement of dipoles where there is sufficient symmetry in the system and incident field $\mathbf{E}_0$ to require that the dipole moments of these dipoles must be equal. Under this assumption, the total field incident on the i^{th} dipole can be written as the sum of the incident field plus the sum of the fields radiated by all the dipoles in the space,

$$\mathbf{E}(\mathbf{r}_i) = \bar{\alpha}^{-1} \mathbf{p}_i = \mathbf{E}_0(\mathbf{r}_i) + \epsilon_0^{-1} \sum_j \mathbf{G}(\mathbf{r}_j - \mathbf{r}_i) \mathbf{p}_j \tag{2.11}$$

where the $j = i$ term in the sum represents the self-interaction of the dipole. The Green's function here has been reduced to a function of a single argument of the

distance between dipoles, which can be done when the dipoles are placed in free space. All of the $\mathbf{p}_i$ terms may be collected to give

$$\left(\bar{\alpha}_e^{-1} - \epsilon_0^{-1}\mathbf{G}(\mathbf{0})\right)\mathbf{p}_i = \mathbf{E}_0(\mathbf{r}_i) + \epsilon_0^{-1}\sum_{j\neq i}\mathbf{G}(\mathbf{r}_j - \mathbf{r}_i)\mathbf{p}_j. \tag{2.12}$$

Moreover, if it is known by the symmetry of the problem that $\mathbf{p}_j = \mathbf{p}_i$ for all j, then the equation may be rewritten in the form

$$\mathbf{p}_i = \left(\bar{\alpha}^{-1} - \epsilon_0^{-1}\sum_j \mathbf{G}(\mathbf{r}_j - \mathbf{r}_i)\right)^{-1}\mathbf{E}_0(\mathbf{r}_i). \tag{2.13}$$

The quantity in the parentheses becomes the new effective polarizability, and the infinite sum over the Green's function is typically defined as the interaction constant[14, 25, 27]

$$\mathbf{C} = \sum_j \mathbf{G}(\mathbf{r}_j - \mathbf{r}_i). \tag{2.14}$$

. Thus we have that

$$\bar{\alpha}_{eff} = \bar{\alpha}(1 - \mathbf{C}\bar{\alpha}/\epsilon_0)^{-1} \tag{2.15}$$

is the effective polarizability of any arrangement or lattice of dipoles that exhibits sufficient symmetry for the dipole moments to be equal.

Once the effective polarizability is known, the effective medium properties of the lattice are immediately available. The trivial example is the single point dipole in free space, where the interaction constant is $C = C^{0D} \equiv -i\frac{k^3}{6\pi}$, and therefore the effective polarizability of the point dipole is given by eq. (2.6). If the set of dipoles are arranged in a column in one dimension with a lattice constant $a < \lambda/2$ then they form a line source with a polarizability per unit length of $\chi = \alpha_{eff}/a$, since $(\alpha_{eff}/a)\mathbf{E}$ will be equal to the average dipole moment per unit length. Similarly, if the dipoles are arranged in a two-dimensional plane with a lattice constant a, then

the surface susceptibility will be $\chi = \alpha_{eff}/a^2$, and the volumetric susceptibility of a three-dimensional lattice will be $\chi = \alpha_{eff}/a^3$.

We will consider here two more examples of geometries that have sufficient symmetry for the dipole moments to be equal: the infinite one-dimensional array and the infinite two-dimensional array. A particularly beautiful work on the one-dimensional array of dipoles through an eigenmode analysis can be found in [35], although here we focus on the effective medium properties under plane wave illumination. Consider a set of dipoles that are arranged in an infinite stack along the z-axis with a lattice spacing of a, and the incident field is constant in the z-direction. We will label the effective polarizabilities in this geometry as α_e^{1D}, and they are related to the inherent polarizabilities by

$$\alpha_{ex}^{1D} = \frac{\alpha_{ex}}{1 - \alpha_{ex}\epsilon_0^{-1}(G_{xx}(\mathbf{0}) + \sum_{m\neq 0} G_{xx}(ma\hat{\mathbf{z}}))} \tag{2.16a}$$

$$\alpha_{ey}^{1D} = \frac{\alpha_{ey}}{1 - \alpha_{ex}\epsilon_0^{-1}(G_{yy}(\mathbf{0}) + \sum_{m\neq 0} G_{yy}(ma\hat{\mathbf{z}}))} \tag{2.16b}$$

$$\alpha_{ez}^{1D} = \frac{\alpha_{ez}}{1 - \alpha_{ex}\epsilon_0^{-1}(G_{zz}(\mathbf{0}) + \sum_{m\neq 0} G_{zz}(ma\hat{\mathbf{z}}))}. \tag{2.16c}$$

We write the interaction constant as $C_{ii} = C^{0D} + C_{ii}^{1D}$, where the sum over the Green's functions at the dipole positions $ma\hat{\mathbf{z}}$, $m \neq 0$ now defines the C^{1D} interaction constant.

$$C_{yy}^{1D} = C_{xx}^{1D} = \sum_{m\neq 0} G_{yy}(ma\hat{\mathbf{z}}) = \frac{1}{2\pi a^3}\sum_{m=1}^{\infty} e^{-imka}\left(\frac{(ka)^2}{m} - \frac{1}{m^3} - \frac{ika}{m^2}\right) \tag{2.17a}$$

$$C_{zz}^{1D} = \sum_{m\neq 0} G_{zz}(ma\hat{\mathbf{z}}) = \frac{1}{\pi a^3}\sum_{m=1}^{\infty} e^{-imka}\left(\frac{1}{m^3} + \frac{ika}{m^2}\right) \tag{2.17b}$$

Using the identities,

$$x^2 \sum_{m=1}^{\infty} \frac{e^{-imx}}{m} \approx -x^2 \ln(2\sin(x/2)) + i\left(-\frac{\pi x^2}{2} + \frac{x^3}{2}\right) \tag{2.18a}$$

$$ix \sum_{m=1}^{\infty} \frac{e^{-imx}}{m^2} \approx -x^2 \ln(x) + x^2 - i\left(-\frac{\pi^2 x}{6} + \frac{\pi x^2}{2} - \frac{x^3}{4}\right) \tag{2.18b}$$

$$\sum_{m=1}^{\infty} \frac{e^{-imx}}{m^3} \approx (x^2/2)\ln(x) - 3x^2/4 + \sum_{1}^{\infty} \frac{1}{m^3} - i\left(\frac{\pi^2 x}{6} - \frac{\pi x^2}{4} + \frac{x^3}{12}\right) \tag{2.18c}$$

the final expression for the interaction constants are,

$$C_{yy}^{1D} = \frac{-1.202}{2\pi a^3} + \frac{k^2}{4\pi a}\left(\ln\left(\frac{ka}{4\sin(ka/2)^2}\right) - \frac{1}{2}\right) - i\frac{k^2}{8a} + i\frac{k^3}{6\pi} \tag{2.19a}$$

$$C_{zz}^{1D} = \frac{1.202}{\pi a^3} - \frac{k^2}{2\pi a}\left(\ln(ka) - \frac{1}{2}\right) - i\frac{k^2}{4a} + i\frac{k^3}{6\pi} \tag{2.19b}$$

Note that the approximations in eqs. (2.18a) to (2.18c) are only in the real part of the sum: the imaginary part is exact for each expression.

The real part of the coupling coefficients given here is accurate up to terms on the order of $(ka)^4$, while the imaginary part is exact. When the coupling coefficient is added to the value of the Green's function at the origin in eqs. (2.16a) to (2.16c), the radiation reaction force is canceled by the $i\frac{k^3}{6\pi}$ term in the interaction constant, and the total imaginary part of the field at the position of the dipoles becomes simply $i\frac{k^2}{4a}$ for dipoles oriented in the z-direction, and $i\frac{k^2}{8a}$ for dipoles in the x- and y directions. In this sense, the force that the dipoles in the one-dimensional array exactly cancels the loss that would normally be present due to the radiation reaction, and replaces it with the loss of a line source. The effective polarizabilities for the stacks of dipoles

are then,

$$\alpha_{ex}^{1D} = \frac{\alpha_{ex}}{1 + \alpha_{ex}\epsilon_0^{-1}\left(\frac{1.202}{2\pi a^3} + \frac{k^2}{4\pi a}\left(\frac{1}{2} - \ln\left(\frac{ka}{4\sin(ka/2)^2}\right)\right) + i\frac{k^2}{8a}\right)} \tag{2.20a}$$

$$\alpha_{ey}^{1D} = \frac{\alpha_{ey}}{1 + \alpha_{ey}\epsilon_0^{-1}\left(\frac{1.202}{2\pi a^3} + \frac{k^2}{4\pi a}\left(\frac{1}{2} - \ln\left(\frac{ka}{4\sin(ka/2)^2}\right)\right) + i\frac{k^2}{8a}\right)} \tag{2.20b}$$

$$\alpha_{ez}^{1D} = \frac{\alpha_{ez}}{1 + \alpha_{ez}\epsilon_0^{-1}\left(-\frac{1.202}{\pi a^3} + \frac{k^2}{2\pi a}\left(\ln(ka) - \frac{1}{2}\right) + i\frac{k^2}{4a}\right)}. \tag{2.20c}$$

It is interesting to note that the dipole stack with the dipoles oriented in the z-direction has twice the radiative loss as the stack with the dipoles oriented in the y-direction. This is because the column with z-oriented dipoles will radiate into a cylindrical wave that radiates evenly in all directions, while the stack with dipoles oriented in the y-direction will radiate into a cylindrical wave that goes as $\cos(\theta)$, and therefore this stack will radiate half as much energy.

Next, consider a two-dimensional lattice of dipoles in free space lying in the xz-plane, with lattice constant a in both directions. The interaction constant for the two-dimensional lattice has been worked out in the static case by Ref.[14], and in the fully dynamic case by Refs. [25, 36, 31, 27]. A convenient approximation to the fully dynamic case is given in Ref. [20], and the quasistatic case, ignoring radiation losses, was worked out in Ref. [37]. In this case, instead of assuming that the dipole moments $\mathbf{p}_j = \mathbf{p}_i$ are all equal, we assume that they are related by some rotating phase such that $\mathbf{p}_j = \mathbf{p}_i e^{-i\mathbf{k}\cdot(\mathbf{r}_j - \mathbf{r}_i)}$. In this case, the interaction constant will be given by

$$\mathbf{C}(\mathbf{k}) = \sum_j \mathbf{G}(\mathbf{r}_j - \mathbf{r}_i) e^{-i\mathbf{k}\cdot(\mathbf{r}_j - \mathbf{r}_i)} \tag{2.21}$$

and thus the effective polarizability will be dependent on the wavenumber $\mathbf{k}$.

In order to more simply evaluate the interaction constant of the two-dimensional lattice, it is typically split up into three terms, $C = C^{0D} + C_{zz}^{1D} + C^{2D}$, where the

C^{2D} term is the contribution due to all of the columns of dipoles in the plane, except for the column on the z-axis. When $\mathbf{k} = 0$ and $a < \lambda$, the contribution from the other columns is,

$$C^{2D} = \frac{-ik}{2a^2} + \frac{ik^2}{4a} + \frac{k^2}{2\pi a}\left(\gamma + \ln(ka/4\pi)\right) + \sum_{\nu=0}^{\infty}\left[\frac{k^2}{a}\left(\frac{1}{\sqrt{(2\pi\nu)^2 - (ka)^2}} - \frac{1}{2\pi\nu}\right) - \sum_{\mu=0}^{\infty}\frac{\Gamma_\mu^2}{\pi a}K_0(\beta_\mu an)\right] \tag{2.22}$$

where $\Gamma_\mu = \sqrt{(2\pi\mu/a)^2 - k^2}$ and γ is Euler's constant[25]. Once again, the $\frac{ik^2}{4a}$ term in the C^{2D} interaction constant cancels the line-source loss term in the C_{zz}^{1D} interaction constant, and replaces is with $\frac{-ik}{2a^2}$, which corresponds to the losses of a plane wave radiated by the plane of dipoles. In fact, as is pointed out in [28], the Q-factor of resonant meta-atoms in a metasurface with a Lorentzian response can be shown to go as $-ikA/2a^2$, simply by integrating the Poynting vector of the plane wave radiated by the lattice. Conservation of energy and Poynting's theorem is thereby maintained by the lattice in a very round-about way: dipoles exert a force on themselves according to their own energy loss via the radiation reaction, but when placed in a lattice, the dipoles exert forces on each other that exactly cancel the radiation reaction force and replace it with a new force that corresponds to the radiation losses of the lattice as a whole.

Similarly, the interaction constant for a three-dimensional lattice can also be worked out, and is available in Ref[25]. In this case, if $a < \lambda$, the imaginary term nets to zero, and hence the interaction constant is purely real. In this way physical, three-dimensional materials made up of polarizable dipoles are able to maintain purely real and lossless effective medium properties: the radiation reaction force that the dipoles exert on themselves is compensated for by the forces that the dipoles exert on one another. In a three-dimensional lattice, every photon that is released by any particular dipole in the lattice is compensated for by absorption of photons released

by the other dipoles in the lattice, such that energy is conserved.

Even though the imaginary part of the interaction constant is zero for three-dimensional lattices with a subwavelength lattice constant, the real part of C will depend on $\mathbf{k}$, i.e. the lattice will be spatially dispersive. For cubic lattices in the limit that $\mathbf{k} \to \mathbf{0}$, $C = 1/3$, which is the classic quasistatic solution originally developed by Lorentz, Lorenz, and Mossotti. A good derivation of the quasistatic interaction constant using Poissson's summation technique is given in [14].

2.3 Applying the Dipole Approximation to Metamaterial Elements

Accurately modeling metamaterials has been a major topic of study since their inception. Traditionally, metamaterials have been thought of as a design approach to creating a material that has a certain permeability and permittivity. Obtaining the required permeability or permittivity is done by simulating an infinite lattice of metamaterial elements with a full-wave numerical solver with periodic boundary conditions. The full-wave solver is set up to simulate a reflection and transmission experiment through a slab of the lattice of a certain thickness, and the effective material properties are "retrieved" using the scattering parameters. Once the effective medium properties are achieved, it is assumed that the material will exhibit these properties when placed in a device, and so the overall device is simulated using a full-wave solver that models only the effective medium properties. Simulating the actual details of all the elements within the device is generally not possible for most metamaterial devices, because the difference in the length scales between the features of the elements and the scale of the device make the mesh far too large to simulate.

The traditional approach to designing a metamaterial device by retrieval of effective medium parameters is subject to several approximations. Although metamaterial elements are designed to be subwavelength so that their resonance lies in part of the spectrum where $a < \lambda$, it is difficult to design the elements to be sufficiently

subwavelength to where the lattice will not exhibit spatial dispersion, which typically requires a lattice constant that is a factor of ten or more smaller than the wavelength. This presents a problem for any finite sized device, because the elements in a spatially dispersive material will be sensitive to the finite boundaries of the device. Moreover, if the device involves a gradient index metamaterial, like the invisibility cloak, then a unit cell that would create an infinite lattice with certain effective medium properties will not maintain those properties when it is placed amongst unit cells that are not identical to itself. In other words, effective medium properties are nonlocal properties of a lattice, and cannot be associated with any particular unit cell.

There is, however, a property that is local to a unit cell that can be associated with the unit cell regardless of the geometry within which the unit cell is placed: the electric and magnetic polarizability. Because the elements are very small with respect to the wavelength, the dominant term in the multipole expansion of their scattered fields tends to be the electric or magnetic dipole term. Therefore, a useful way to model a metamaterial is to approximate each element as a point dipole, and then model the device as a lattice of interacting dipoles. This approach is called the Discrete Dipole Approximation to model metamaterial devices. Previously, the DDA was exclusively used to model continuous materials, where the geometry must be discretized into a set of polarizable dipoles[38]. Instead of using the DDA to model continuous materials, metamaterials offer an interesting new application of the DDA because of their unique structure. This was first done in [30], where metamaterial invisibility cloaks were modeled using the DDA.

The primary question is, what are the limits of applicability of the dipole approximation to metamaterial elements? Here I present an easy way to check whether or not the interaction between the elements is dominated by the dipole interaction. This is done by first simulating a metasurface of elements using periodic boundary conditions in a full-wave solver, with a certain lattice constant a. The effective polar-

izability of the lattice can be easily shown to be related to the scattering parameters of the metasurface by

$$\alpha_e^{2D} = \frac{ia^2}{k}(t + r - 1) \tag{2.23a}$$

$$\alpha_m^{2D} = \frac{ia^2}{k}(t - r - 1) \tag{2.23b}$$

where r and t are the reflection and transmission coefficients of the metasurface, respectively, at normal incidence.

If the lattice acts as a set of dipoles, the intrinsic polarizability is related to the effective polarizability by the interaction constant $C(a, \mathbf{k}) = C_{zz}^{1D}(a, \mathbf{k}) + C^{2D}(a, \mathbf{k})$, where we exclude the C^{0D} term to allow the dipoles to maintain their radiative losses. The intrinsic polarizability is then found by inverting eq. (2.15), .

$$\alpha_e(\omega) = \frac{\alpha_e^{2D}(a, \mathbf{k})}{1 + C(a, \mathbf{k})\alpha_e^{2D}} \tag{2.24a}$$

$$\alpha_m(\omega) = \frac{\alpha_m^{2D}(a, \mathbf{k})}{1 + C(a, \mathbf{k})\alpha_m^{2D}}. \tag{2.24b}$$

It is shown explicitly that the effective polarizability and the interaction constant both depend on the lattice constant, a, but the intrinsic polarizability does not. Therefore, if the lattice does indeed act as a set of interacting dipoles, then many simulations could be run of the metasurface with different values of a, and all of the intrinsic polarizabilities of the elements from these simulations should match. In the limit of large a they should match perfectly, but as the elements get closer together higher order interactions will become important, and the dipole approximation will be broken.

To test this theory, a metasurface of spheres made of titanium dioxide with a diameter of 150nm is simulated and the scattering parameters are used to calculate the effective polarizability, which is in turn used to calculate the intrinsic polarizability.

The results of extracting the intrinsic polarizability for different values of the lattice constant a are plotted in section 2.3. The plot is put in terms of the gap g between the particles rather than the lattice constant, which is related to the gap and the radius R by $a = 2R + g$. As can be seen in the plot, the intrinsic polarizability is nearly invariant to a change in the lattice constant until the gap size is less than a tenth of the radius of the spheres.

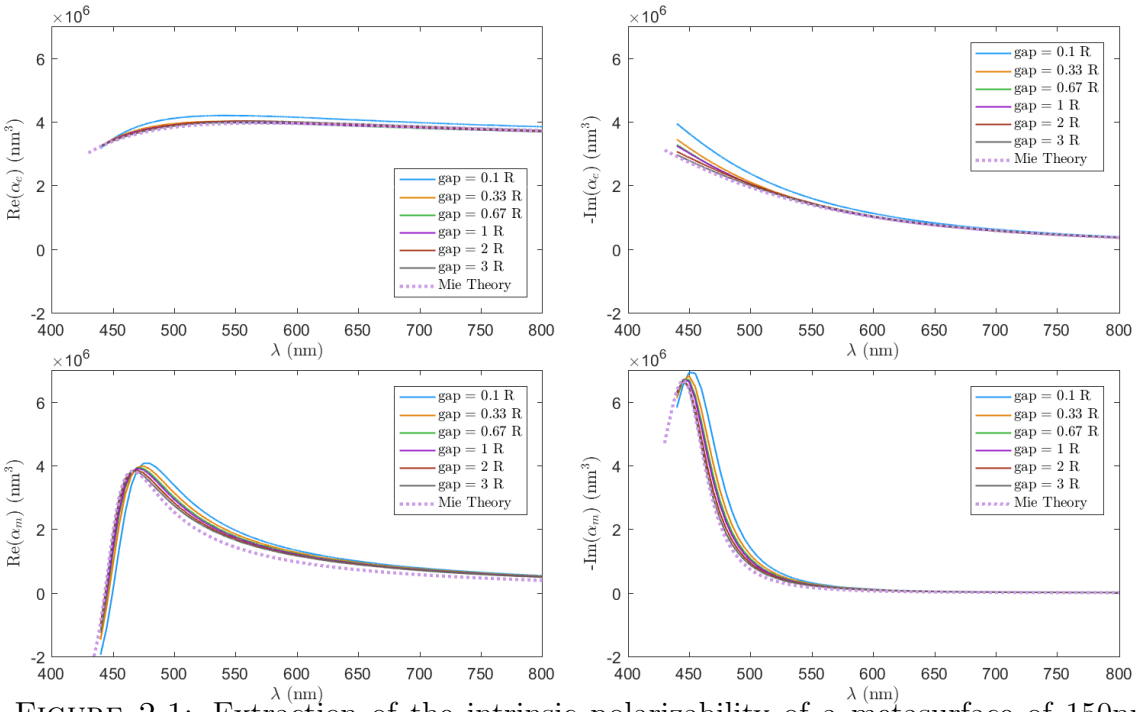

FIGURE 2.1: Extraction of the intrinsic polarizability of a metasurface of 150nm titanium dioxide spheres for different values of the lattice constant, $a = 2R + g$, where R is the radius of the sphere and g is the gap size..

3

Coupled Mode Theory Analysis of Plasmonic Patch Antennas

In this chapter, we return to the discussion of metasurfaces, but focus on film-coupled optical patch antennas. Metasurfaces in this geometry are of significant interest in optics as absorbers[29], fluorescence enhancing surfaces[39], and single photon sources[40]. These plasmonic patch antennas are usually made out of metallic nanocubes, which can be fabricated by colloidal methods and readily deposited on an insulating spacer layer over a metal film. Film-coupled plasmonic nanocubes and other planar film-coupled systems represent advantageous plasmonic platforms for several reasons. The field distribution of a nanoparticle spaced closely above a metal film strongly resembles that of a nanoparticle dimer [41]–two nanoparticles separated by a nanoscale gap–which is known to exhibit some of the largest and most strongly localized field enhancements[42]. A wide variety of optical phenomena can be impacted within such enhancement volumes, including fluorescence[43], photocatalysis[44], optical bistability[45], surface plasmon amplification (spasing)[46], two-photon absorption[47], four-wave mixing[48], and many others.

The film-coupled nanoparticle system retains the desirable field enhancement

properties of the dimer; however, film-coupled nanoparticle systems are much more controllable and amenable to experimental realization, particularly for the most extreme (sub-nanometer) gap dimensions[49]. The film-coupled geometry as an experimental platform has allowed nearly unprecedented control over the gap thickness, leveraging planar deposition methods such as layer-by-layer approaches for organic spacer layers, or atomic layer deposition (ALD) for inorganic spacer layers. Film-coupled nanocubes were therefore suggested as a convenient and inexpensive means of forming large-area, controlled reflectance surfaces[50], and have more recently been applied in the context of fluorescence enhancement[43].

The analysis in this chapter is largely a reproduction of the work published in Ref. [28], which was developed solely by myself under the guidance of my advisor, David R. Smith. The goal of this section is to find an analytic solution to the fields in the gap region of the patch antenna using an expansion into cavity modes. The scattering properties of a film-coupled nanocube at optical wavelengths bear considerable resemblance to those of the patch antenna, ubiquitous in microwave engineering. Methods of analysis to predict the radiation characteristics of driven patch antennas are well-known in microwave engineering[51], and are becoming increasingly common to describe the scattering characteristics of optical patch antennas. Although the film-coupled nanocube can be considered as an example of an optical patch antenna, we note the theoretical approach outlined here is not restricted to nanocubes.

Ciraci et al.[52] recently presented an analytical treatment of the scattering characteristics of a film-coupled nanocube, applying the transmission line circuit model to solve for the gap-plasmon propagating in the gap between the cube and film. The nanocube was assumed to be excited to a normally incident plane wave, coupled to the nanocube resonance via the magnetic flux passing through the gap. The transmission line model for the nanopatch antenna was modified by introducing the gap-plasmon dispersion relation, allowing the more complex optical response of

the metal to be modeled. In this work, only the fundamental cavity mode of the nanopatch was considered. A comparison of the resulting analytical formulas with full-wave numerical simulations revealed reasonable agreement between the spectral properties of the nanopatch as well as the field enhancement within the gap region as a function of excitation wavelength; however, additional mode structure found in the numerical simulations, as well as in later experiments[53], was not captured by the analytical treatment, and was presumed to be related to higher-order mode excitation.

Our goal in the present section is to use Coupled Mode Theory (CMT)[54, 55, 56, 57, 58, 59] to provide a more detailed analytical analysis of the film-coupled nanocube system that incorporates potentially all of the higher order modes that can be excited within the gap region. The complete mode set assumes greater importance, for example, when the excitation is a point source located within the gap region. By including all higher order modes, we effectively construct the Green's function for the nanopatch, which can ultimately be used to determine the optical properties of emitters embedded within the gap region.

The model presented in this section is not unlike the cavity model used for patch antennas[51], where the gap between the patch and the metal film is modeled as a resonator cavity with perfectly electric conducting (PEC) boundaries on the patch and ground plane surfaces and perfectly magnetic conducting (PMC) boundaries on the gaps. In this paper, we develop a similar model for the film-coupled nanocube system, but modify it by analytically including the coupling to the incident field, gap plasmon effects, and the Ohmic and radiative losses.

We begin by introducing the standard cavity eigenmode expansion of Maxwells equations[14], derived using a variation of Lorenz Reciprocity. We then define an eigenvalue problem that is similar to the real problem but excluding all lossless by replacing the gap volume with a lossless, rectangular cavity, where the open slots

replaced by PMCs and the dielectric constant of the metal is purely real. The field solutions within the lossless cavity can be expressed as a set of orthogonal eigenmodes, which we define as the lossless eigenmodes. We take this approximation initially as an *ansatz*, later confirming its validity by full-wave simulation. The coupling of the incident field to the eigenmodes and the radiative losses can then be found analytically using the lossless eigenmode fields. Ohmic losses are found by allowing the imaginary part of the dielectric constant to resume it's physical value, and integrating the resulting Poynting vector over the metal surfaces.

When losses are included in any system, the eigenvalues are no longer real and the eigenmodes are no longer necessarily orthogonal. This has been recently demonstrated specifically for plasmonic resonances by Lalanne et al[57], where it was shown that mode non-orthogonality must be taken into account in order to compute the correct eignenmode amplitude spectrum. In this paper the eigenmode non-orthogonality is handled in three different approaches. In the first approach, mode non-orthogonality is ignored and all of the modes are assumed to be decoupled. Assuming that the modes are orthogonal allows very intuitive and simple equations to be derived that describe the resonances of the gap plasmon eigenmodes.

In the second approach, the losses and the resulting eigenmode cross-coupling is calculated based on the assumption of a surface impedance of the slots. The surface-impedance approach is able to explain the presence of resonances in the amplitude spectrum that are observed in simulation, but should be zero if the modes are orthogonal. Some of these resonances can be considered "dark" in the sense that they cannot directly couple to the far-field, but are excited by cross-coupling with a bright mode.

The third and final approach presented utilizes a Fourier method[51] to calculate the radiation damping and cross-coupling between modes. This approach results in the best match between the analytically computed eigenmode amplitude spectrum

and the amplitude spectrum extracted from simulation.

3.1 Derivation of Eigenmode Coupled Equations

Our goal in this section is to solve for the fields within the gap region of a film-coupled nanocube, assuming excitation by an incident driving wave. We assume the actual electric and magnetic fields within the gap can be expanded in a sum over cavity eigenmodes, defined by the volume underneath the nanocube as well as the bounding metal and free-space surfaces, or

$$\mathbf{E} = \sum_{\mu} e_{\mu}(\omega)\mathbf{E}_{\mu}(\mathbf{r}) \tag{3.1a}$$

$$\mathbf{H} = \sum_{\mu} h_{\mu}(\omega)\mathbf{H}_{\mu}(\mathbf{r}). \tag{3.1b}$$

We seek to determine the electric and magnetic field coefficients and their dependence on the driving field, radiation damping and Ohmic losses. In the following, we derive a set of two coupled infinite-rank matrix equations: one in which radiative damping appears as a perturbative term, and another in which Ohmic loss appears as a perturbative term. The perturbative terms additionally serve to couple the eigenmodes together.

Each of the eigenmodes satisfies the homogeneous Maxwell's equations, or

$$\nabla \times \mathbf{H}_{\mu} = j\omega_{\mu}\epsilon_0\mathbf{E}_{\mu} \tag{3.2a}$$

$$\nabla \times \mathbf{E}_{\mu} = -j\omega_{\mu}\mu_0\mathbf{H}_{\mu}. \tag{3.2b}$$

As a starting point, we first assume the fields can be expanded in the set of lossless eigenmodes. To obtain lossless eigenmodes, we replace the slots by PMCs and requiring the dielectric constant of the metal film to be real, as shown in fig. 3.1(b). Simulation results and previous work show that modes in which the electric field

is zero on the boundaries are overly damped and do not play a role in the system response. Thus, for the modes of relevance, the electric field is maximum and the magnetic field is minimum at the slots (or gap edges) of the cube.

The eigenvalue problem given by eqs. (3.6a) and (3.6b), together with the PMC and metal boundary conditions, is satisfied if[51]

$$E^x_{mn} = E_0 \cos(k_{xmn}x)\cos(m\pi y/W)\cos(n\pi z/W) \tag{3.3a}$$

$$E^y_{mn} = E_0 \frac{k_{xmn}W}{\pi}\frac{m}{m^2+n^2}\sin(k_{xmn}x)\sin(m\pi y/W)\cos(n\pi z/W) \tag{3.3b}$$

$$E^z_{mn} = E_0 \frac{k_{xmn}W}{\pi}\frac{n}{m^2+n^2}\sin(k_{xmn}x)\cos(m\pi y/W)\sin(n\pi z/W) \tag{3.3c}$$

$$H^x_{mn} = 0 \tag{3.3d}$$

$$H^y_{mn} = -i\frac{E_0}{Z_0}\frac{\omega_{mn}W}{c\pi}\frac{n}{m^2+n^2}\cos(k_{xmn}x)\cos(m\pi y/W)\sin(n\pi z/W) \tag{3.3e}$$

$$H^z_{mn} = i\frac{E_0}{Z_0}\frac{\omega_{mn}W}{c\pi}\frac{m}{m^2+n^2}\cos(k_{xmn}x)\sin(m\pi y/W)\cos(n\pi z/W) \tag{3.3f}$$

for $(x, y, z) \in V$ where V is the volume of the gap: $V = \{[-h/2, h/2]\times[0, W]\times[0, W]\}$. In these equations, ω_{mn} is the resonance frequency, $Z_0 = \sqrt{\frac{\mu_0}{\epsilon_0}}$ is the impedance of free space, c is the speed of light, and E_0 is an arbitrary constant with units of electric field that is used to normalize the modes. The double index mn was used in these equations rather than the single index μ to classify the modes in terms of the number of nodes in the y and z directions.

Unlike patch antennas, where the metal is considered to be PEC, k_{xmn} must be allowed to be non-zero and the plasmon dispersion relation must be used to find k_{xmn} and ω_{mn}. In the metal, the fields follow the same y, z dependence as eq. (3.3), but with an exponentially decay of $e^{-\kappa_{mn}|x|}$ into the metal. The plasmon dispersion relation for an infinite parallel plate metal-insulator-metal waveguide, together with the Helmholtz equation evaluated in the gap and in the metal, provide three equations

that can be simultaneously solved for three unknowns $\{k_{xmn}, \kappa_{mn}, \omega_{mn}\}$.

$$\tan\left(\frac{k_{xmn}h}{2}\right) + \frac{j\kappa_{mn}}{k_{xmn}\mathrm{Re}\{\epsilon(\omega_{mn})\}} = 0 \tag{3.4a}$$

$$\left(\frac{m\pi}{W}\right)^2 + \left(\frac{n\pi}{W}\right)^2 + k_{xmn}^2 = \frac{\omega_{mn}^2}{c^2} \tag{3.4b}$$

$$\left(\frac{m\pi}{W}\right)^2 + \left(\frac{n\pi}{W}\right)^2 - \kappa_{mn}^2 = \mathrm{Re}\{\epsilon(\omega_{mn})\}\frac{\omega_{mn}^2}{c^2} \tag{3.4c}$$

where the real part of the permittivity was used to keep the modes lossless. If the permittivity is real then k_{xmn} must be purely imaginary, as has been shown in previous work developing a transmission line model for nano cube resonances[52].

The modes introduced in eq. (3.3) are lossless and orthogonal, and their orthogonality makes them a convenient basis to use when expanding the field in the gap. However, the expansion in terms of eq. (3.3) would not allow the losses of the real nanocube system to be taken into account. Therefore we will also need an expansion in terms of lossy eigenmodes,

$$\mathbf{E} = \sum_{\mu} \tilde{e}_{\mu}(\omega)\tilde{\mathbf{E}}_{\mu}(\mathbf{r}) \tag{3.5a}$$

$$\mathbf{H} = \sum_{\mu} \tilde{h}_{\mu}(\omega)\tilde{\mathbf{H}}_{\mu}(\mathbf{r}).. \tag{3.5b}$$

which are defined by the source-free solution to Maxwell's equations in the exact nanocube geometry,

$$\nabla \times \tilde{\mathbf{H}}_{\mu} = j\tilde{\omega}_{\mu}\epsilon(\mathbf{r}, \tilde{\omega}_{\mu})\tilde{\mathbf{E}}_{\mu} \tag{3.6a}$$

$$\nabla \times \tilde{\mathbf{E}}_{\mu} = -j\tilde{\omega}_{\mu}\mu_0\tilde{\mathbf{H}}_{\mu}. \tag{3.6b}$$

including the full complex permittivity and radiative boundary conditions on the slots. Although the exact solution to this eigenvalue problem is unknown, the solution inside the gap and sufficiently far from the slots must converge to eqs. (3.3) and (7.3), with the exception that the complex permittivity must be used in eq. (7.3).

Using the lossless eigenmode expansion of the fields, we seek to solve the inhomogeneous Maxwell's equations, or

$$\nabla \times \mathbf{H} = j\omega\epsilon_0\mathbf{E} + \mathbf{J}_e \tag{3.7a}$$

$$\nabla \times \mathbf{E} = -j\omega\mu_0\mathbf{H} - \mathbf{J}_m. \tag{3.7b}$$

The arbitrary field distribution can be expanded into a sum of lossless eigenmodes as in eqs. (3.5a) and (3.5b), where the mode amplitudes and fields are indexed with the single variable μ rather than the pair mn for convenience, but without loss of generality. Note that the mode amplitudes are functions of frequency. We take the inner product of the electric curl equation with $\mathbf{E}_\mu^*$:

$$\int \mathbf{E}_\mu^* \cdot (\nabla \times \mathbf{H})\mathrm{d}V = j\omega\epsilon_0 \int \mathbf{E}_\mu^* \cdot \mathbf{E}\mathrm{d}V + \int \mathbf{E}_\mu^* \cdot \mathbf{J}_e\mathrm{d}V. \tag{3.8}$$

Using standard vector identities and substitution of the homogeneous Maxwells equations given in eqs. (3.6a) and (3.6b), we obtain

$$\mathbf{E}_\mu^* \cdot (\nabla \times \mathbf{H}) = \mathbf{H} \cdot (\nabla \times \mathbf{E}_\mu^*) - \nabla \cdot (\mathbf{E}_\mu^* \times \mathbf{H}) \tag{3.9}$$

$$= j\omega_\mu\mu_0\mathbf{H} \cdot \mathbf{H}_\mu^* - \nabla \cdot (\mathbf{E}_\mu^* \times \mathbf{H}) \tag{3.10}$$

Substituting these equations, we obtain

$$j\omega_\mu\mu_0 \int \mathbf{H} \cdot \mathbf{H}_\mu^*\mathrm{d}V - \int (\mathbf{E}_\mu^* \times \mathbf{H}) \cdot \mathbf{n}\mathrm{d}S$$

$$= j\omega\epsilon_0 \int \mathbf{E}_\mu^* \cdot \mathbf{E}\mathrm{d}V + \int \mathbf{E}_\mu^* \cdot \mathbf{J}_e\mathrm{d}V \tag{3.11}$$

where the surface integral is evaluated over the boundary of the gap region V, and $\mathbf{n}$ is the normal vector to the surface. Using the orthogonality of the lossless eigenmodes and substituting eqs. (3.5a) and (3.5b), the equation simplifies to

$$j\omega e_\mu - j\omega_\mu h_\mu + \frac{1}{2U_\mu} \int (\mathbf{E}_\mu^* \times \mathbf{H}) \cdot \mathbf{n}\mathrm{d}S = -\frac{1}{2U_\mu} \int \mathbf{E}_\mu^* \cdot \mathbf{J}_e\mathrm{d}V \tag{3.12}$$

where

$$U_\mu = \frac{\epsilon_0}{2}\int |\mathbf{E}_\mu|^2 \mathrm{d}V = \frac{\mu_0}{2}\int |\mathbf{H}_\mu|^2 \mathrm{d}V \tag{3.13}$$

are the normalization constants for the electric and magnetic energy in the cavity, respectively. The uniqueness theorem ensures that the electric and magnetic field energies are equal for the lossless eigenmodes[14].

Although we have used the lossless magnetic eigenmodes to reduce the first volume integral in eq. (3.11), we have not reduced the surface integral term in the same manner, as it requires more care. Because the boundary conditions on the fields at the slots are open rather than PMC, the tangential component of the magnetic field at the slots is not precisely zero, as is the case for the lossless eigenmodes in eq. (3.3). Therefore, a field expansion on the slot surface in terms of the lossless magnetic modes $\mathbf{H}_\mu$ cannot be performed since this expansion could never reproduce the appropriate radiation boundary condition. Instead, we expand the field on the surface in terms of lossy modes, $\mathbf{H} = \sum_\nu \tilde{h}_\nu \tilde{\mathbf{H}}_\nu$. Then the surface integral in eq. (3.12) can be expressed as

$$\begin{aligned}\frac{1}{2U_\mu}\int (\mathbf{E}_\mu^* \times \mathbf{H})\cdot \mathbf{n}\mathrm{d}S &= \sum_\nu \frac{\tilde{h}_\nu(\omega)}{2U_\mu}\int (\mathbf{E}_\mu^* \times \tilde{\mathbf{H}}_\nu)\cdot \mathbf{n}\mathrm{d}S \\ &= \sum_\nu \tilde{h}_\nu(\omega) P_{\mu\nu}^{rad}\end{aligned} \tag{3.14}$$

The matrix $P_{\mu\nu}^{rad} = \int (\mathbf{E}_\mu^* \times \tilde{\mathbf{H}}_\nu)\cdot \mathbf{n}\mathrm{d}S/2U_\mu$ is representative of losses, but is normalized by the mode energy to have units of frequency. It includes a contribution from both Ohmic losses and radiative losses, with Ohmic losses resulting when the integral is evaluated on the metal surfaces and radiative losses when it is evaluated on the slots. However, the Ohmic loss contribution in this integral is vanishing when $k_{x\mu}h/2$ is small, and can be neglected when the gap size is small. Therefore we use

this matrix to include only the radiative losses by evaluating the surface integral only over the slots. The main contribution to Ohmic losses will be included later by considering the analogous equation derived from the electric curl equation.

Even though the magnetic fields of the lossy eigenmodes are unknown in the slots, if the total tangential electric field on the edge of the cube is well approximated by a sum of the electric fields of the lossless eigenmode fields, then a Fourier transform method can be used to solve for the magnetic field in the slot due to the electric field from each eigenmode. In this method, the lossy eigenmode magnetic field is approximated in the slots by the magnetic field that must exist in each slot given the radiative boundary condition and the existence of an electric field $\mathbf{E}_\nu$ in the gap, where $\mathbf{E}_\nu$ is the electric field from the lossless eigenmode. The method is outlined in **??**, where coefficients of the form $\frac{1}{2}\int(\mathbf{E}_\mu^* \times \tilde{\mathbf{H}}_\nu) \cdot \mathbf{n}\mathrm{d}S$ are evaluated based on the expression for $\mathbf{E}_\mu$ given by the lossless eigenmode problem. The fundamental resonance of the film-coupled nano-cube radiates particularly strongly, and so the radiative losses must be taken into account[60] despite the deeply sub-wavelength scale of the structure[61].

We note that the surface integral in eq. (3.14) is also representative of the extent to which mode orthogonality has been broken by the existence of losses. The diagonal elements of $P_{\mu\nu}^{rad}$ represent the losses of the individual eigenmodes, and the off-diagonal elements will be shown later to function as a cross-coupling between the modes.

This expansion, left as it is, remains un-useful because the introduction of the coefficients $\tilde{h}_\mu$ will yield more variables than equations. However, if the losses included in the lossy eigenvalue problem are sufficiently small, then $\mathbf{H}_\mu \approx \tilde{\mathbf{H}}_\mu$ in the volume of the gap. In this case, the expansion of the field into lossless and lossy eigenmodes will yield approximately the same coefficients, so that $h_\mu \approx \tilde{h}_\mu$. Applying that approximation yields the first of two coupled equations needed to solve the

system:

$$j\omega e_\mu - j\omega_\mu h_\mu + \sum_\nu h_\nu(\omega) P^{rad}_{\mu\nu} = -\frac{1}{2U_\mu}\int \mathbf{E}^*_\mu \cdot \mathbf{J}_e \mathrm{d}V. \tag{3.15}$$

The second equation for the electric and magnetic coefficients can be derived using the curl equation for the electric field and following a similar procedure:

$$j\omega h_\mu - j\omega_\mu e_\mu + \frac{1}{2U_\mu}\int (\mathbf{E}\times\mathbf{H}^*_\mu)\cdot\mathbf{n}\mathrm{d}S = -\frac{1}{2U_\mu}\int \mathbf{H}^*_\mu \cdot \mathbf{J}_m \mathrm{d}V. \tag{3.16}$$

To derive this equation, both sides of the curl equation were multiplied by the mode magnetic field $\mathbf{H}_\mu$, and then mode orthogonality was applied. The electric field in the surface integral can be expanded into a sum of lossy eigenmodes, $\mathbf{E} = \sum_\nu \tilde{e}_\nu \tilde{\mathbf{E}}_\nu \approx \sum_\nu e_\nu \tilde{\mathbf{E}}_\nu$, that satisfy the boundary conditions of the lossy metal film

$$\begin{aligned} j\omega h_\mu - j\omega_\mu e_\mu + \sum_\nu e_\nu \frac{1}{2U_\mu}\int (\tilde{\mathbf{E}}_\nu \times \mathbf{H}^*_\mu)\cdot\mathbf{n}\mathrm{d}S \\ = -\frac{1}{2U_\mu}\int \mathbf{H}^*_\mu \cdot \mathbf{J}_m \mathrm{d}V. \end{aligned} \tag{3.17}$$

The lossless eigenmode field $\mathbf{H}^*_\mu$ has zero tangential component on the surfaces of the slot, and therefore the surface integral vanishes on the edges of the cube and doesn't contribute to radiative loss. It does not, however, vanish on the metal surface, so Ohmic losses may be included in this surface integral.

$$j\omega h_\mu - j\omega_\mu e_\mu + \sum_\nu e_\nu(\omega) P^{\Omega}_{\mu\nu} = -\frac{1}{2U_\mu}\int \mathbf{H}^*_\mu \cdot \mathbf{J}_m \mathrm{d}V \tag{3.18}$$

$$P^{\Omega}_{\mu\nu} = \frac{1}{2U_\mu}\int (\tilde{\mathbf{E}}_\nu \times \mathbf{H}^*_\mu)\cdot\mathbf{n}\mathrm{d}S \tag{3.19}$$

A detailed evaluation of the Ohmic losses is given in Appendix 3.3. It is also shown that the Ohmic loss matrix is zero for the film-coupled nanocube system if $\mu \neq \nu$, so eq. (3.18) can be further simplified

$$j\omega h_\mu - (j\omega_\mu - P^{\Omega}_{\mu})e_\mu = -\frac{1}{2U_\mu}\int \mathbf{H}^*_\mu \cdot \mathbf{J}_m \mathrm{d}V. \tag{3.20}$$

Equations 3.15 and 3.20 form a set of linear equations that can be solved for the coefficients $\{e_\mu(\omega), h_\mu(\omega)\}$.

Note that a simpler, alternative formulation to evaluating the far-field coupling in eq. (3.12) may be found by assuming a gap admittance so that, at every point along the edge of the cube, we have that

$$\mathbf{H}_t = Y_g \mathbf{E} \times \mathbf{n}. \tag{3.21}$$

If eq. (3.21) is used in eq. (3.15), then the boundary term becomes a sum over electric field coefficients instead of magnetic field coefficients. The equivalent matrix equation becomes

$$j\omega e_\mu - j\omega_\mu h_\mu + \sum_\nu e_\nu P_{\mu\nu}^{rad} = -\frac{1}{2U_\mu} \int \mathbf{E}_\mu^* \cdot \mathbf{J}_e \mathrm{d}V \tag{3.22}$$

where the surface integral becomes a surface overlap integral of the tangential electric fields:

$$P_{\mu\nu}^{rad} = \frac{Y_g}{2U_\mu} \int (\mathbf{E}_\mu^* \times \mathbf{n}) \cdot (\mathbf{E}_\nu \times \mathbf{n}) \mathrm{d}S. \tag{3.23}$$

Depending on the frequency dependence of the gap admittance, this system will behave slightly differently as a function of frequency than eq. (3.15), since the radiative losses are now coupled through the electric eigenmode amplitudes rather than the magnetic eigenmode amplitudes.

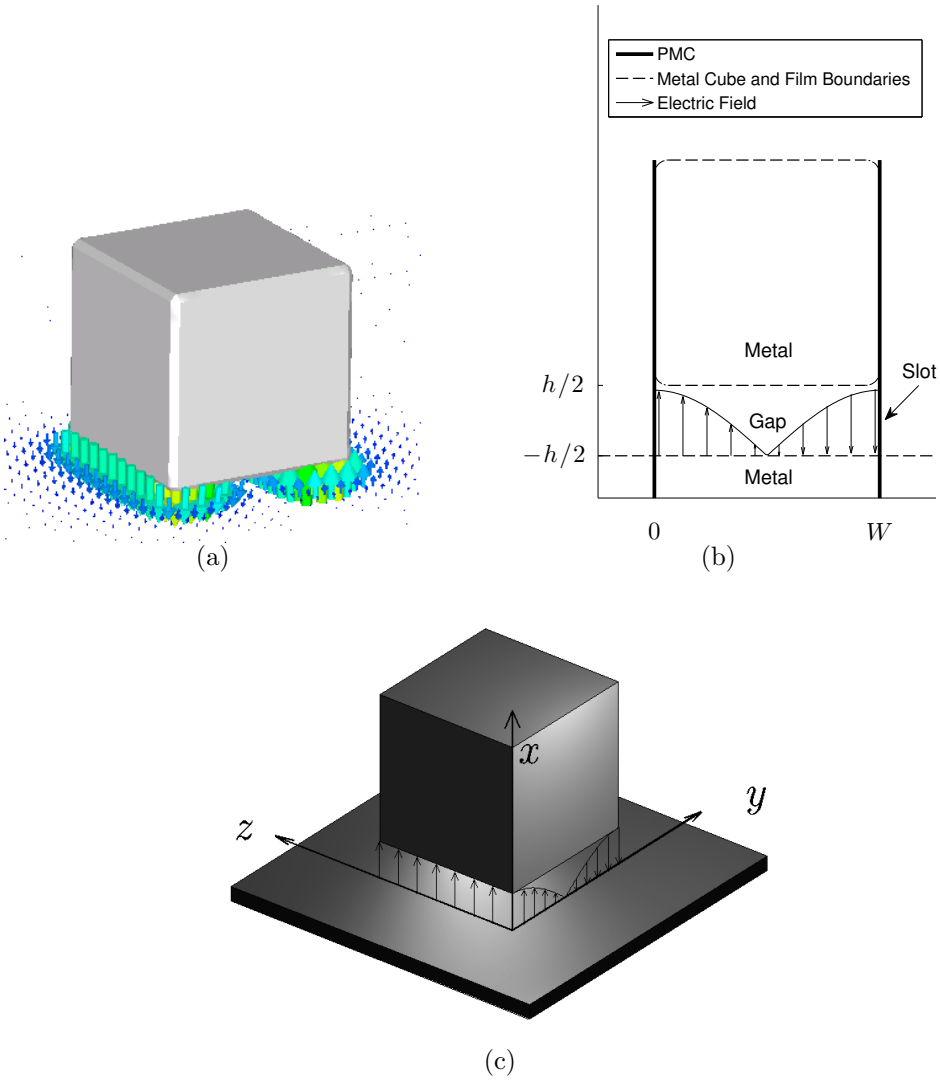

FIGURE 3.1: (a) Fields from a simulated film-coupled nano-cube at the resonance frequency of the $\mathbf{E}_{01}$ mode. (b) The lossless cavity eigenmode problem, with boundary conditions. (c) Illustration of coordinate system convention for a film-coupled nanocube.

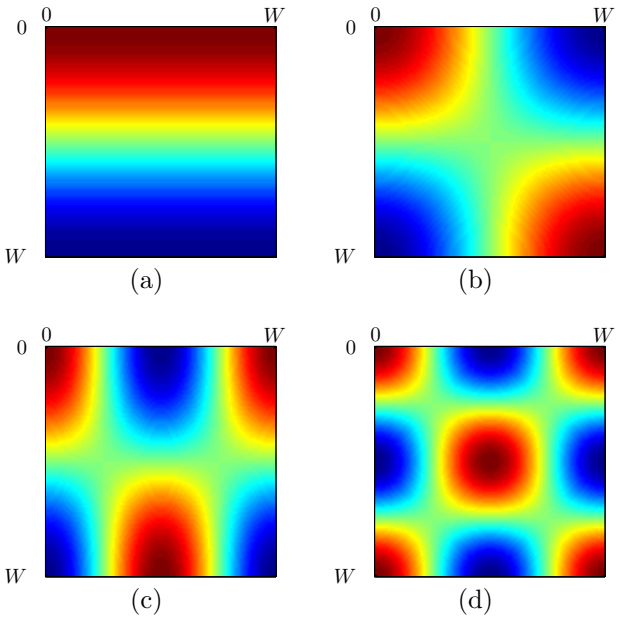

FIGURE 3.2: The lossless eigenmodes (a) $\mathbf{E}_{0,1}(\mathbf{r})$, (b) $\mathbf{E}_{1,1}(\mathbf{r})$, (c) $\mathbf{E}_{2,1}(\mathbf{r})$, and (d) $\mathbf{E}_{2,2}(\mathbf{r})$.

3.2 Coupling to the Far-Field

Equations 3.15 and 3.16 include source terms that relate to electric currents (Eq. 14) and effective magnetic currents (Eq. 18). To investigate the scattering from the film-coupled nanocube illuminated by an external driving field, $(\mathbf{E}_0, \mathbf{H}_0)$, our strategy is to compute the effective source terms based on the application of one of Schelkunoff's equivalence principles[62, 14, 51]. Consider the surface defined by the eigenmode problem, but excluding the PMC at the slots. The total electric and magnetic fields inside this surface can be found through the scattering of an equivalent electric and an equivalent magnetic surface current, which are given by the tangential magnetic and electric fields at the slot, respectively. The electric and magnetic surface currents are given by

$$\mathbf{K}_e = \mathbf{n} \times \mathbf{H} \quad \mathbf{r} \in \partial V \tag{3.24a}$$

$$\mathbf{K}_m = \mathbf{E} \times \mathbf{n} \quad \mathbf{r} \in \partial V \tag{3.24b}$$

where $\mathbf{H}$ and $\mathbf{E}$ are the total tangential electric and magnetic fields, including both the incident and scattered fields. The coupling of the incident electric and magnetic fields into a particular eigenmode is given by

$$\int \mathbf{E}_\mu^* \cdot \mathbf{J}_e \mathrm{d}V = \int \mathbf{E}_\mu^* \cdot \mathbf{K}_e \mathrm{d}S = -\int (\mathbf{E}_\mu^* \times \mathbf{H}) \cdot \mathbf{n} \mathrm{d}S \tag{3.25a}$$

$$\int \mathbf{H}_\mu^* \cdot \mathbf{J}_m \mathrm{d}V = \int \mathbf{H}_\mu^* \cdot \mathbf{K}_m \mathrm{d}S = -\int (\mathbf{E} \times \mathbf{H}_\mu^*) \cdot \mathbf{n} \mathrm{d}S. \tag{3.25b}$$

We seek to evaluate these expressions for the special case where the system is excited by a plane wave at normal incidence, and in the long-wavelength limit where the incident field $\{\mathbf{E}_0, \mathbf{H}_0\}$ can be considered a constant vector field over the film-coupled nanocube system.

The electric current coupling in eq. (3.25a) must be zero on the metal surfaces, since the overlap integral of the tangential part of the lossless modes with a normally

incident plane wave is zero on those surfaces. On the slots, the mode's lossless magnetic field is zero, and so the total magnetic field on the slot is approximated by the incident magnetic field. The incident magnetic field is symmetric, while the normal vector to any two opposing slots is asymmetric. Therefore the incident magnetic field can only couple to modes that are asymmetric in the electric field.

The magnetic current coupling must likewise be zero in the slots, where the lossless mode's tangential magnetic field is zero. On the bottom of the cube and the top of the film, the electric field of the lossless eigenmode is symmetric, and the incident electric field is also very nearly symmetric on the bottom of the cube and top of the metal film when applied at normal incidence. Therefore the total incident and scattered field will be very nearly symmetric on the two metal surfaces. Since the electric field is symmetric, the mode's magnetic field is symmetric, and the normal vector is asymmetric, the equivalent magnetic current (and hence the incident electric field) does not couple to the cube system at normal incidence. Then the coupling into the modes reduces to

$$\int \mathbf{E}_\mu^* \cdot \mathbf{J}_e \mathrm{d}V = -2 \int_{slots} (\mathbf{E}_\mu^* \times \mathbf{H}_0) \cdot \mathbf{n} \mathrm{d}S \tag{3.26}$$

$$\int \mathbf{H}_\mu^* \cdot \mathbf{J}_m \mathrm{d}V = 0 \tag{3.27}$$

where $\mathbf{H}_0$ is the incident magnetic field, and the additional factor of two is due to the reflection of the incident field off of the metal film[51].

3.3 Ohmic Losses of Plasmonic Nanopatch Antennas

Unlike the radiative loss matrix, where a closed-form expression for the exact, lossy magnetic field is unknown in the slots, the electric field of the lossy eigenmodes can be found analytically on the bottom of the cube and top of the film using eq. (3.3) and allowing k_x to be the value found by solving the dispersion relation in eq. (7.3)

using a complex permittivity. Then it can be seen by inspection of eq. (3.3) that this overlap surface integral is only non-zero for $\mu = \nu$, and therefore the modes do not couple to each other due to Ohmic losses. This result can be used to simplify eq. (3.18) by requiring that the ohmic loss matrix in eq. (3.19) is purely diagonal,

$$j\omega h_\mu U_\mu - j\omega_\mu e_\mu U_\mu + e_\mu P_\mu^\Omega = \frac{1}{2}\int \mathbf{H}_\mu^* \cdot \mathbf{J}_m \mathrm{d}V \tag{3.28}$$

where $P_\mu^\Omega = \frac{1}{2U_\mu}\int(\tilde{\mathbf{E}}_\mu \times \mathbf{H}_\mu^*) \cdot \mathbf{n}\mathrm{d}S$ and is given by

$$P_{\mu(m,n)}^\Omega = \frac{2cW^2}{\pi^2 h(m^2+n^2)}\mathrm{Re}\{-ik_{xmn}\sin(k_{xmn}h/2)\omega_{mn}/c\} \tag{3.29}$$

In this equation, the single index μ has been given an arbitrary mapping to a double index mn using the notation $\mu(m,n)$.

3.4 No Modal Cross-Coupling Approximation

If the radiative loss rate matrix $P_{\mu\nu}^{rad}$ is diagonal, then the two equations for the electric and magnetic field present a coupled system of oscillators.

$$j\omega e_\mu - (j\omega_\mu - P_\mu^{rad})h_\mu = -\frac{1}{2U_\mu}\int \mathbf{E}_\mu \cdot \mathbf{J}_e \mathrm{d}V \tag{3.30}$$

$$j\omega h_\mu - (j\omega_\mu - P_\mu^\Omega)e_\mu = -\frac{1}{2U_\mu}\int \mathbf{H}_\mu \cdot \mathbf{J}_m \mathrm{d}V \tag{3.31}$$

We can immediately gain insight into the mechanism of the interaction between elements in the system from the equations of motion above. The magnetic field and electric field are coupled to one another through the constant coupling coefficients of $j\omega_\mu$. The electric current drives the electric mode, while the magnetic current drives the magnetic mode. Because of the way in which the lossy eigenmodes were introduced, energy in the form of radiative losses exits the system through the magnetic

field, and ohmic losses exit the system through the electric field. The solution to the coupled system is

$$e_\mu = \frac{-j\omega\frac{1}{2U_\mu}\int \mathbf{E}_\mu^* \cdot \mathbf{J}_e \mathrm{d}V - (j\omega_\mu - P_\mu^{rad})\frac{1}{2U_\mu}\int \mathbf{H}_\mu^* \cdot \mathbf{J}_m \mathrm{d}V}{(j\omega_\mu - P_\mu^{rad})(j\omega_\mu - P_\mu^{\Omega}) + \omega^2} \tag{3.32}$$

$$h_\mu = \frac{-(j\omega_\mu - P_\mu^{\Omega})\frac{1}{2U_\mu}\int \mathbf{E}_\mu^* \cdot \mathbf{J}_e \mathrm{d}V - j\omega\frac{1}{2U_\mu}\int \mathbf{H}_\mu^* \cdot \mathbf{J}_m \mathrm{d}V}{(j\omega_\mu - P_\mu^{rad})(j\omega_\mu - P_\mu^{\Omega}) + \omega^2} \tag{3.33}$$

The system can be simplified by applying the coupling coefficients for the incident field.

$$e_\mu = \frac{j\omega\int(\mathbf{E}_\mu^* \times \mathbf{H}_0) \cdot \mathbf{n}\mathrm{d}S/U_\mu}{(j\omega_\mu - P_\mu^{rad})(j\omega_\mu - P_\mu^{\Omega}) + \omega^2} \tag{3.34a}$$

$$h_\mu = (\omega_\mu/\omega - jP_\mu^{\Omega}/\omega)e_\mu \tag{3.34b}$$

If the fundamental mode, $(m, n) = (1, 0)$, is the assumed to be the only important mode within the frequency range of interest and $k_{x\mu}h/2$ is sufficiently small, then eq. (3.34a) leads to a very simple expression for the enhancement factor near the fundamental resonance.

$$\mathbf{E}(\mathbf{r}, \omega)/E_0 = e_{1,0}(\omega)\mathbf{E}_{1,0}(\mathbf{r}) \tag{3.35}$$

$$\approx \frac{(j8\omega c/W)\cos(\pi y/W)}{\omega^2 - \omega_{1,0}^2 - j\omega_{1,0}(P_{1,0}^{rad} + P_{1,0}^{\Omega}) + P_{1,0}^{\Omega}P_{1,0}^{rad}} \tag{3.36}$$

$$\approx \frac{(j8\omega c/W)\cos(\pi y/W)}{\omega^2 - \omega_{1,0}^2 - j\omega_{1,0}(P_{1,0}^{rad} + P_{1,0}^{\Omega})} \tag{3.37}$$

Hence, the imaginary part of the slot impedance functions as a frequency shift of the mode, and the real part contributes to losses. Similar equations to eq. (3.37) can be easily derived for all of the higher order modes.

The primary difficulty from here is in determining the imaginary part of the radiative loss. The electric field is very uniform across the slots, and for the lowest order mode it is also constant along one of the dimensions of the cube. This suggests

that the impedance for an infinitely wide slot with a constant field could be used[51]

$$Y_g = \frac{hk}{2}\left(1 - (kh)^2/24 + j(1 - 0.636\ln(kh))\right) \tag{3.38}$$

where $k = \omega/c$. The real part of the radiative loss can accurately fixed using the radiation resistance from patch antenna theory. The radiation resistance $R_r(\omega)$ for the fundamental mode is well-known and is given in many textbooks [51, 52]. The radiated power can then be written as,

$$P_{1,0}^{rad} = \frac{h^2 E_0^2}{2R_r(\omega)} + j\frac{\mathrm{Im}\{Y_g\}}{2}\int |\mathbf{n} \times \mathbf{E}_{1,0}|^2 \mathrm{d}S \tag{3.39}$$

The above analytical equations were tested against full-wave FEM simulations in CST Microwave Studio of a nano-cube of dimension 80nm and separated 5nm air gap from the metal substrate. The nanocube and metal film were composed of silver using data from Johnson and Christy[63]. The edges of the nanocube were given a radius of curvature of 3nm to accommodate the tetrahedral mesh. A mode amplitude spectrum was extracted from the electric fields obtained from the simulation by taking the overlap integral of the simulated fields in the gap with the lossless eigenmode fields:

$$e_\mu^{sim}(\omega) = \frac{\int \mathbf{E}^{sim}(\mathbf{r},\omega)\cdot\mathbf{E}_\mu^* \mathrm{d}V}{\int \mathbf{E}_\mu \cdot \mathbf{E}_\mu^* \mathrm{d}V}. \tag{3.40}$$

where $\mathbf{E}^{sim}(\mathbf{r},\omega)$ is the field sampled from the simulation in the gap between the cube and the substrate, and V is the volume of the gap where the lossless eigenmodes are defined.

Based on the simulation results shown in fig. 3.3, it is apparent that there are only two lossless eigenmodes that play a significant role when the cube is illuminated under normal incidence. The fundamental mode, $e_{1,0}$, appears as expected. This mode is a bright mode, and is commonly used in fluorescence enhancement and other applications where a high quantum yield is desired. [43]

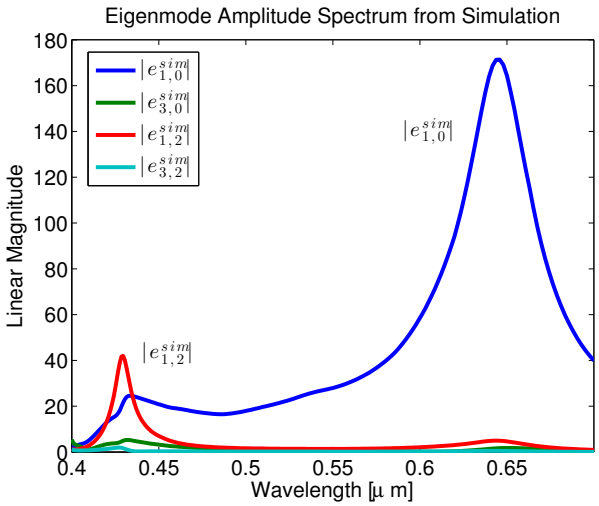

FIGURE 3.3: The eigenmode amplitude spectrum extracted from full-wave simulation of an 80nm cube using eq. (3.40). The fundamental, bright mode is $|e^{sim}_{1,0}(\omega)|$, while $|e_{1,2}(\omega)|$ is a higher order dark mode.

An additional higher order mode $e_{1,2}$ also has a small peak near $430nm$. This mode may be called a "dark mode," since it exhibits nearly zero radiative loss. The appearance of this mode is surprising, since the integral in eq. (3.34a) would require that the mode $e_{1,2}$ has zero coupling to the incident field when excited at normal incidence. It will be shown in sections 4.2 and 4.3 that the excitation of this mode can be explained by allowing for the eigenmodes of the system to be non-orthogonal due to the radiative losses. A modal cross-coupling between the bright and dark modes is also consistent with the strong amplitude transition of the bright mode at the dark mode resonance frequency, and the small peak in the dark mode at the bright mode resonance frequency. This modal cross-coupling can be captured using the formalism developed in section 4.1 by allowing the radiative loss matrix to have non-zero off-diagonal matrix elements, which will be demonstrated in sections 3.5 and 3.6 of this paper.

The quality factor and maximum excitation of the bright mode amplitude can be very accurately predicted using eq. (3.34a). Unfortunately, the imaginary part

of the surface impedance in eq. (3.38) does not give the correct frequency shift for the fundamental mode. Some disagreement is to be expected since it doesn't take into account the finite size of the cube, the non-constant distribution of the field on two of the sides, or the interactions between the various sides of the cube. However, good agreement with simulation is obtained if the imaginary part of the impedance given in eq. (3.38) is multiplied by a constant factor of 0.3, as shown in fig. 3.5. We note that this correction factor is dependent on the radius of curvature of the edges of the cube and the height of gap, not unlike the corrections used when computing the effective resonance wavelength of optical nano-rod antennas[64].

In fig. 3.4 we study the impact of the radius of curvature on the resonance frequency of the modes and the correction factor for the imaginary part of the surface impedance. Based on the simulation results in fig. 3.4, as the radius of curvature increases, the resonance frequency of both the bright and dark modes increases while the excitation of the dark mode also increases. The effects of increasing the correction factor in the coupled mode theory model are that the resonance frequency of each of the modes decreases, and the cross-coupling between modes with non-zero surface integrals increases. For this reason, the finite radius of curvature cannot be modeled by only modifying the effective imaginary surface impedance, but the effective width of the cube should also be decreased as the radius of curvature is increased so that the resonance frequency is increased in a way that is consistent with fig. 3.4. This idea of an effective cube width has also been used in both optical[52] and RF patch antenna theory[51] to account for the shift in resonance frequency of the modes from the ideal value computed by the dispersion relation. In this paper we choose to analyze cubes with a radius of curvature of 2nm, where the effective width is identical with the width of the cube and the correction factor on the surface impedance is 0.3. A larger radius of curvature could be modeled by changing both the effective width of the cube and the imaginary surface impedance accordingly.

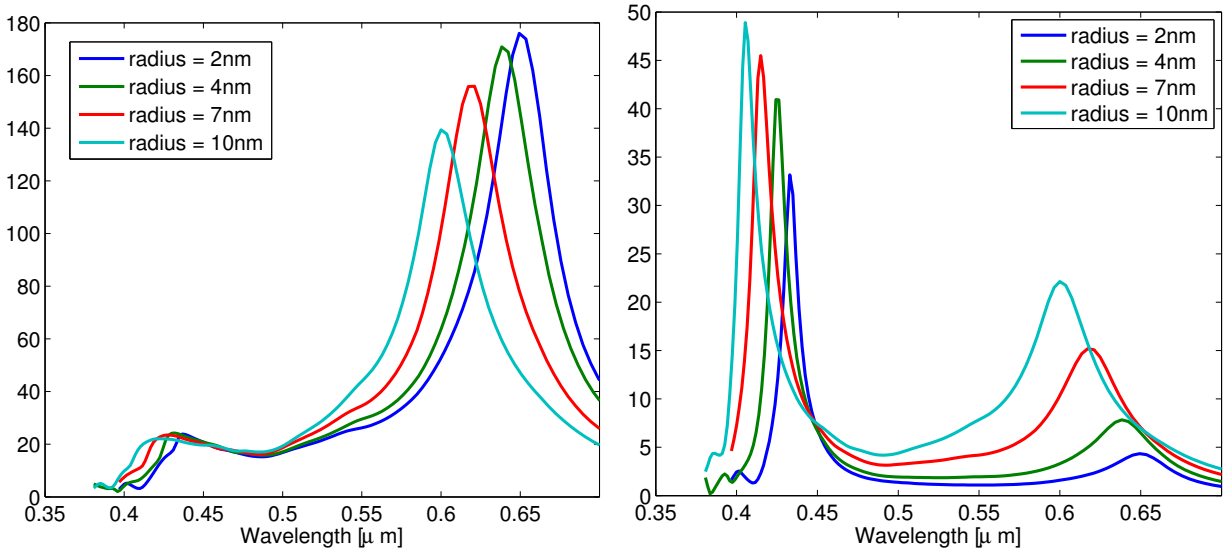

FIGURE 3.4: (a) The amplitude of the bright mode is plotted as the radius of curvature of the corners of the cube is varied. (b) The amplitude of the dark mode is plotted as the radius of curvature is varied. The resonance frequency of both modes shifts roughly linearly in wavelength as the radius of curvature is varied, and the coupling to the dark mode increases with increasing radius of curvature.

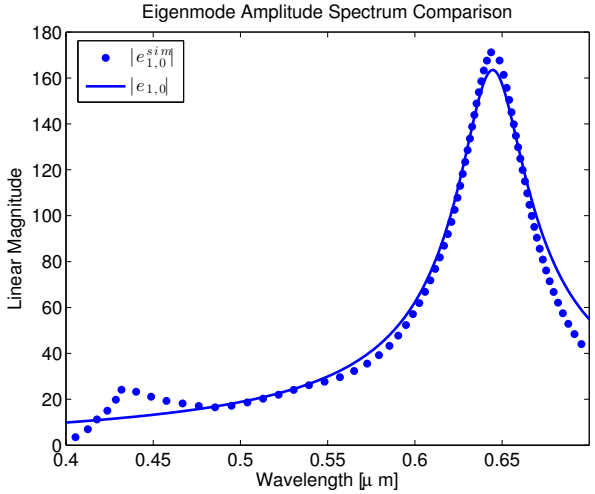

FIGURE 3.5: Comparison of the magnitude of the fundamental mode extracted from full-wave simulation, $|e_{1,0}^{sim}(\omega)|$, with the magnitude of the fundamental mode analytically computed from eq. (3.34a), $|e_{1,0}(\omega)|$. A correction factor of 0.3 is included in the imaginary part of the impedance to accommodate the frequency shift.

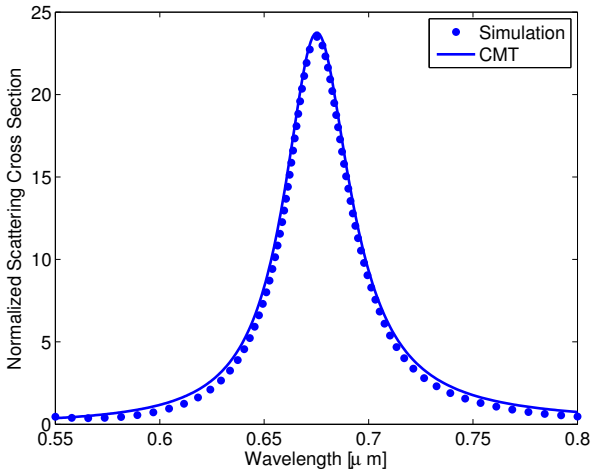

FIGURE 3.6: Normalized scattering cross section, defined by SCS = $P_{scatt}/W^2 I_{inc}$, where I_{inc} is the intensity of the normally incident beam.

The eigenmode expansion formalism has also given an easy, intuitive approach to calculating various experimentally measurable parameters. As an example, we consider the total scattered power of the cube, which can be intuitively calculated from the radiative loss matrix. In the orthogonal case, the scattered power is given by

$$P_{scatt} = \frac{1}{2}\int_{slots} \mathrm{Re}\{\mathbf{E}\times\mathbf{H}^*\}\cdot\mathbf{n}\mathrm{d}S = \sum_{\mu}\mathrm{Re}\{e_\mu h_\mu^* U_\mu P_\mu^{rad*}\}. \tag{3.41}$$

which gives excellent agreement with the scattered power found from the simulation results in fig. 3.6.

x

3.5 Modal Cross Coupling Due to Radiation Damping: Surface Impedance Approach

In the nano cube system, and in lossy systems in general, the loss matrices are not diagonal, even though in this case the ohmic losses are well approximated by a diagonal matrix. The cross-coupling in the radiation matrix can be seen by looking

at the impedance-boundary form of $P_{\mu\nu}^{rad}$ and comparing with the eigenmode fields defined in eq. (3.3). The overlap integral of the tangential components,

$$P_{\mu\nu}^{rad}(\omega) = -\frac{Y_g(\omega)}{2}\int(\mathbf{E}_\mu^* \times \mathbf{n}) \cdot (\mathbf{E}_\nu \times \mathbf{n})\mathrm{d}S, \tag{3.42}$$

will not always be zero for different modes. Using this form for the radiative loss matrix, together with eqs. (3.18) and (3.22), the mode amplitude equations become

$$h_\mu = (\omega_\mu/\omega - jP_\mu^\Omega/\omega)e_\mu \tag{3.43}$$

$$\sum_\nu \left[j\left(\omega - \frac{\omega_\mu}{\omega}(\omega_\mu - jP_\mu^\Omega)\right)\delta_{\mu\nu} + P_{\mu\nu}^{rad}\right]e_\nu$$

$$= -\int(\mathbf{E}_\mu^* \times \mathbf{H}_0) \cdot \mathbf{n}\mathrm{d}S/U_\mu \tag{3.44}$$

The left-hand side of the electric mode amplitude equation forms a matrix that may be inverted to solve the system. The array factor is included as outlined in section 3.4. With these assumptions, and using the correction factor on the surface impedance of 0.3 that was determined in 3.4, the model gives the results shown in fig. 3.7.

Although this is a crude approach to deterring the exact elements of the radiative loss matrix, it does give an explanation for why the E_{21} eigenmode is excited. For many eigenmodes of the structure, the surface integral of the tangential component of the fields is zero across the gap for the lossless eigenmode fields. However, for the modes E_{10} and E_{12}, the surface overlap integral is large and non-zero on two opposite sides of the cube. Therefore these modes become coupled through the surface admittance of the gap.

Since the surface impedance given in eq. (3.38) comes from an expression that assumes an infinitely wide slot with constant electric field, using this approximation

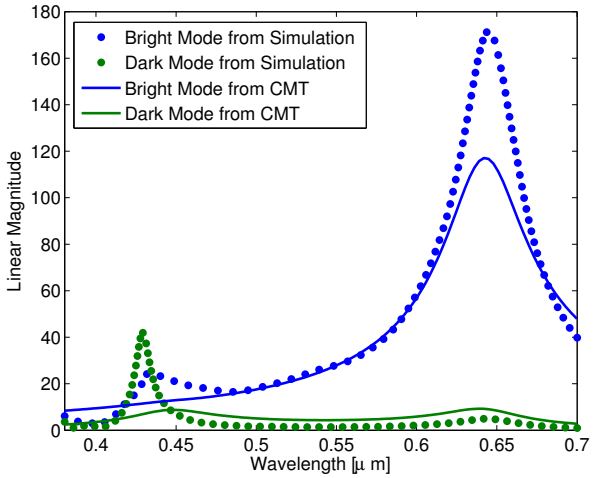

FIGURE 3.7: Magnitude of the main bright mode, $e_{1,0}$, and the dark mode, $e_{1,2}$, found analytically using eqs. (3.43) and (3.44). The magnitudes of the corresponding modes were extracted from simulation and are shown in the dotted lines.

in eq. (3.42) greatly overestimates the radiative losses due to slots that do not have a constant electric field. The result is that both the bright mode and the dark mode appear to be much more damped than is seen in simulation.

3.6 Modal Cross-Coupling Due to Radiation Damping: Fourier Method

If the impedance assumption is not made, then the radiative loss matrix is given by

$$P_{\mu\nu}^{rad}(\omega) = \frac{1}{2}\int (\mathbf{E}_\mu^* \times \mathbf{H}_\nu) \cdot \mathbf{n} \mathrm{d}S \tag{3.45}$$

where $\mathbf{E}_\mu$ is the exact eigenmode field, and the tangential component of $\mathbf{H}_\nu$ on the surface is given by the Fourier method presented in the appendix. These matrix elements will again be a function of frequency. The real part of the radiative loss matrix may be determined by this method, but the imaginary part is shown in the appendix to not converge. Therefore the imaginary part will remain approximated by a surface impedance as it was in section 3.6.

In this formulation of the problem, the system solution is given by the linear

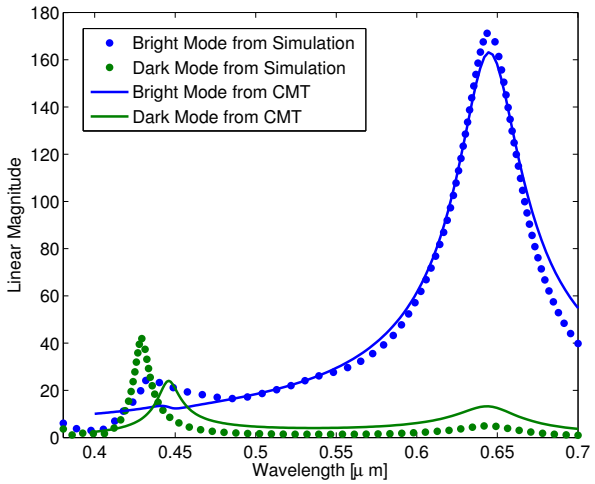

FIGURE 3.8: Magnitude of the main bright mode and the dark mode using an analytically evaluated radiative loss matrix, and compared to full-wave simulation results. A correction factor of 0.29 was included in the imaginary part of the radiation impedance to accommodate the resonance frequency shift.

system

$$h_\mu = (\omega_\mu/\omega - jP_\mu^\Omega/\omega)e_\mu \tag{3.46}$$

$$\sum_\nu \left[j\left(\omega - \frac{\omega_\mu}{\omega}(\omega_\mu - jP_\mu^\Omega)\right)\delta_{\mu\nu} + ((\omega_\mu - jP_\mu^\Omega)/\omega)P_{\mu\nu}^{rad} \right] e_\nu$$

$$= -\int (\mathbf{E}_\mu^* \times \mathbf{H}_0)\cdot \mathbf{n}\mathrm{d}S/U_\mu. \tag{3.47}$$

where the matrix on the left hand side must be inverted to solve the system. Solving this system using eigenmodes with (m, n) ranging from $(0, 0)$ to $(2, 2)$ gives excellent agreement with simulation results shown in fig. 3.8.

The solution to this equation works very well compared to the simulation results for the fundamental mode, and it reproduces the main features of the dark mode. The resonance frequency does appear to be shifted for the dark mode, and this disagreement is likely because the imaginary part of the radiation matrix is still used to compute the radiation loss matrix, which determines the resonance frequency shift

of the modes. The imaginary part assumes that the mode profile is constant across the gap, and this approximation is worse for higher order modes. Therefore we do not expect as good agreement for the higher order modes, but it qualitatively reproduces their behavior and cross coupling to the fundamental mode.

4

Metamaterial Perfect Absorbers

Absorption is the fundamental mechanism behind both light detection and light generation. Far from being an unwanted annoyance for these applications, absorption is crucial and must be maximized to achieve best performance. Examples include solar cells, in which light must be absorbed and converted to electricity [65]; thermal sources, in which a desired emissivity spectrum directly correlates to the absorption spectrum [66]; and bolometric detectors, which are used to form imaging systems across the infrared bands [67].

For nearly a decade, the community of researchers investigating artificially structured materials have enthusiastically contemplated the use of metamaterials to design devices that offer detailed control over the absorption of light[68, 69, 70, 71, 72, 73, 74, 75, 76, 77, 78, 50]. Many designs and experimental realizations of ideal absorbers have been proposed and fabricated by both top-down [68, 69, 70, 71, 72, 73, 74, 75, 76, 77, 78] as well as bottom-up approaches [50], for operation in both the visible [68, 50] and the infrared [69, 71, 72, 73].

Metamaterial absorbers can be divided into two broad categories based on their principle of operation. The first category consists of devices impedance-matched

to free space, while simultaneously exhibiting large imaginary parts in the effective permittivity and permeability[79, 80, 81]. If the material is impedance matched with large and lossy values of permittivity and permeability, then the surface will be reflectionless at normal incidence and the incident field will decay rapidly once inside.

The second category of absorbers is based on electrically responsive metamaterial elements closely coupled to a ground plane, in such a way that they resemble patch antennas. Such absorbers have been experimentally demonstrated throughout the electromagnetic spectrum from the RF to the visible[78, 82, 83, 76, 71, 69, 50]. These absorbers typically involve a resonant structure, and therefore have a narrow frequency response. However, the remarkable property of these absorbers is their ability to absorb TM-polarization nearly perfectly over all angles of incidence. For many applications, like thermophotovoltaics and microbalometer arrays, the narrow frequency response is a benefit rather than a nuisance, since a deeply sub wavelength structure that provides a narrowband emission can be used in combination with other narrowband structures to engineer an arbitrary absorption spectrum[84]. In these cases, the broad angular response becomes the limiting factor in the performance of the device[80].

To date, patch antenna absorbers are predominantly designed using extensive full-wave numerical simulations. There are a few works that present a theory of the underlying mechanism of perfect absorption, either explaining absorption in terms of an interference theory[85, 86], or in terms of the balance of Ohmic and radiation losses[77, 74]. However, none of these previous theoretical works describe the off-axis absorption that is so striking for patch antenna absorbers, or offer a first principles derivation of the absorption mechanism. Here we introduce a first principles theory that clarifies the underlying physics of the patch-antenna perfect absorbers, including their off axis performance, and reconciles the two previous theories of absorption that

have been presented.

This chapter is organized as follows. In section 4.1, the fundamental limits on the absorption of a homogeneous, anisotropic material are derived, and it is shown that it is impossible to engineer a single layer of anisotropic material such that it will absorb perfectly at all angles of incidence. However, it is demonstrated in section 4.2 that a surface with an equal distribution of effective electric and magnetic surface currents can provide the boundary condition needed to produce a perfect absorber. Since patch antennas are known to scatter as effective magnetic dipoles, film-coupled nano patches are considered in section 4.3 as a candidate for a system that can be designed as a perfect absorber, and their magnetic polarizabilities are calculated using coupled mode theory. The reflection coefficient of a periodic array of film-coupled nano patch antennas is derived using these polarizabilities in section 4.5. Some corrections to the radiation Q of the lattice of nano patches are considered in section 4.6, and in section 4.7 it is shown that the radiation Q, the Ohmic losses, and the balance of effective electric and magnetic currents are intricately connected to one another, and thereby the previous theories of absorption by patch antenna absorbers are reconciled.

The derivation of the limits on the absorption of homogenous materials was done by my advisor, Dr. David R. Smith, and the rest of the theory in demonstrating the mechanism of perfect absorption by film-coupled metasurfaces was done by myself. The full-wave simulations that are used to compare with the theory were performed by Dr. Alexandre Baron.

4.1 Limits on the Absorption of a Homogenous, Anisotropic Material

To enhance the absorption of light within a medium, both the reflectance as well as the transmittance of the medium must be minimized. While any opaque material, such as a metal, can essentially eliminate transmittance, eliminating the reflectance

is generally more difficult. Assume a general anisotropic material defined by its electric permittivity tensor $\bar{\epsilon} = \mathrm{diag}(\epsilon_x, \epsilon_y, \epsilon_z)$ and magnetic permeability tensor $\bar{\mu} = \mathrm{diag}(\mu_x, \mu_y, \mu_z)$, with its interface to free space parallel to the xy plane. A wave with wave vector $\mathbf{k} = k_x\hat{\mathbf{x}} + k_z\hat{\mathbf{z}}$ is incident on the plane from the $-\hat{\mathbf{z}}$ direction. The reflection coefficient for a transverse electric (TE) wave has the form

$$r_{TE} = \frac{\cos(\theta) - \sqrt{\epsilon_y/\mu_z - \sin^2(\theta)/(\mu_z\mu_x)}}{\cos(\theta) + \sqrt{\epsilon_y/\mu_z - \sin^2(\theta)/(\mu_z\mu_x)}} \tag{4.1a}$$

and the form

$$r_{TM} = \frac{\cos(\theta) - \sqrt{\mu_y/\epsilon_z - \sin^2(\theta)/(\epsilon_z\epsilon_x)}}{\cos(\theta) + \sqrt{\mu_y/\epsilon_z - \sin^2(\theta)/(\epsilon_z\epsilon_x)}} \tag{4.1b}$$

for a transverse magnetic wave. We define the generalized impedances $Z_0/Z_{TE}(\theta) = \sqrt{\epsilon_y/\mu_z - \sin^2(\theta)/(\mu_z\mu_x)}$ and $Z_{TM}(\theta)/Z_0 = \sqrt{\mu_y/\epsilon_z - \sin^2(\theta)/(\epsilon_z\epsilon_x)}$. It should be apparent from the above equations that an impedance matched medium ($\epsilon = \mu$) can only exhibit zero reflectance for waves incident normally on the interface. For waves at oblique incidence, there are generally no zeros for eqs. (4.1a) and (4.1b), and thus it is not possible with an isotropic medium to make an absorber over all angles of incidence unless the permittivity and permeability of the material also have the same magnitudes as those of vacuum (i.e., $|\epsilon| = |\mu| = 1$). Requiring that the material be uniaxially anisotropic and impedance-matched, i.e. $\bar{\epsilon} = \bar{\mu} = \mathrm{diag}(\epsilon_t, \epsilon_t, \epsilon_z)$, makes the reflection coefficient both zero at normal incidence and polarization independent. The best that can be done to take the value of the impedance as close to unity as possible for all angles of incidence is to let $|\epsilon| \to \infty$, and then $\mu_y/\epsilon_z = \epsilon_y/\mu_z = Z_{TE}/Z_0 = Z_{TM}/Z_0 = 1$. This is the concept behind the Dällenbach layer and some of the other metamaterial absorbers[79, 80, 81]. However, even in the limit as the permittivity and permeability go to infinity, the reflection coefficient

becomes

$$r_{TE} = r_{TM} = \frac{\cos(\theta) - 1}{\cos(\theta) + 1} \tag{4.2}$$

Equation (4.2) shows that the reflectance of any perfect absorber formed from a medium with matched permittivity and permeability will follow a universal curve, with poorer absorption for large angles of incidence. It makes no difference whether the constitutive parameters are real or complex, so that we can assume a lossy medium whose thickness is larger than the effective skin depth.

4.2 Surface Impedance Requirements of Perfect Absorbers

Our goal is then to adjust the surface impedance of the layer such that reflectance is minimized over all angles of incidence. This cancellation can be accomplished conceptually by imagining a checkerboard surface divided into regions of perfect electric conductors (PECs) and perfect magnetic conductors (PMCs). We imagine a surface comprising alternating patches of perfect electric and magnetic conductors, for which the surface impedance of the electric conductors is zero and that for the magnetic conductors is infinite. For either type of surface, both TE and TM polarized waves are entirely reflected, and we can imagine the surface to have infinitesimal thickness. For a TE wave reflecting from a magnetic patch, the transverse field components are

$$E_x = 2E_0 \tag{4.3a}$$

$$H_y = 0 \tag{4.3b}$$

while the field components of a TE wave at the surface of an electric patch are

$$E_x = 0 \tag{4.4a}$$

$$H_y = 2E_0 \frac{k_z}{\epsilon_0 \omega} \tag{4.4b}$$

If we now average the fields over the surface to find the effective surface impedance, we obtain

$$Z_{TE} = \frac{\bar{E}_x}{\bar{H}_y} = Z_0 \frac{k_0}{k_z} = \frac{Z_0}{\cos(\theta)}. \tag{4.5}$$

The same argument applied to a TM wave shows that $Z_{TM} = Z_0 \cos(\theta)$. Using these expressions for the impedances in eqs. (4.1a) and (4.1b) yields a zero reflection coefficient for all angles of incidence. Though such a hypothetical surface is unphysical, the result of creating a surface comprising equal areas of electric and magnetic conductors is that the effective surface impedance achieves the exact angular distribution needed to produce complete absorption over all angles of incidence.

4.3 Magnetic Polarizability of Patch Antennas

The hypothetical checkerboard pattern of PEC and PMC regions can be mimicked by a conducting film decorated with an array of film-coupled nanoparticles. The film-coupled nanopatch, being the optical analog of a patch antenna, can be shown to radiate as a pair of effective magnetic dipoles. The patch antenna supports a series of resonant cavity modes formed by two actual electric boundaries (where the transverse electric field vanishes) on the top and bottom of the patch and four approximate magnetic boundaries (where the transverse magnetic field nearly vanishes) on the sides of the patch[28]. Fields radiating from the effective magnetic boundaries can be handled perturbatively using Schelkunoff's equivalence principles[28, 14]. If $\mathbf{E}$ represents the electric field at the sides of the patch, then the scattered fields from the patch can be attributed to fictitious magnetic surface densities of the form $\mathbf{K}_M = (1 - r_{TM})\mathbf{E} \times \hat{\mathbf{n}}$ [51], where $\hat{\mathbf{n}}$ is the normal vector to the sides of the patch, and r_{TM} is the reflection coefficient of TM waves off the metal film, which takes into account the image dipoles of the surface currents. Because of the small size of the gap, the multipole expansion of the surface currents on each of the slots will

be dominated by the magnetic dipole term. Moreover, because of the asymmetric nature of the fundamental resonance and small size of the structure, the magnetic dipoles generated in each slot will generate a scattered field pattern from the patch antenna that is approximately the sum of the fields of two magnetic dipoles that are separated by the width of the patch. Here we will treat the plasmonic patch antenna as a pair of magnetic dipoles, and therefore a periodic or random array of these particles produces an effective magnetic current.

The plasmonic patch antenna is, moreover, a convenient structure to consider because arrays of patch antennas can be easily fabricated. Nanoparticles of various sizes and shapes can be made colloidally and deposited on a planar metal film covered in a thin layer of dielectric. Both the thickness of the dielectric layer and the size of the nanoparticles can be controlled precisely and over a large area, so these kinds of structures are relatively easy to realize experimentally[50].

The scattering properties of plasmonic patch antennas have recently been analyzed using both a transmission line model[52] and a cavity eigenmode approach[28]. Here we summarize the main results from the eigenmode approach, and carry the calculations forward to compute the effective polarizability of a single plasmonic patch antenna for the case of TM incident fields. The cavity eigenmode approach is based on an expansion of the fields in the gap of the form $\mathbf{E} = \sum_\mu e_\mu(\omega)\mathbf{E}_\mu(\mathbf{r})$, where $\mathbf{E}_\mu(\mathbf{r})$ are lossless modes that are defined by covering the sides of the gap with perfect magnetic conductors and solving for the cavity modes in the limit that the permittivity is purely real. The losses can then be found using pertubative techniques by integrating the Poynting vector over the surface that encloses the volume of the gap region of height h and width and depth W. Once the loss rates are calculated, the expansion coefficients of the modes, $e_\mu(\omega)$, can be shown to follow a Lorentzian,

$$e_\mu(\omega) = \frac{-i\omega C_\mu H_0}{\omega_\mu^2 - \omega^2 + i\omega_\mu^2/Q_\mu} \tag{4.6}$$

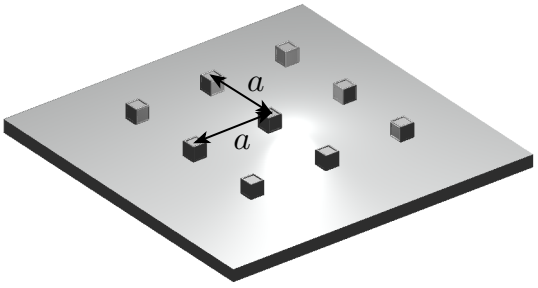

(a)

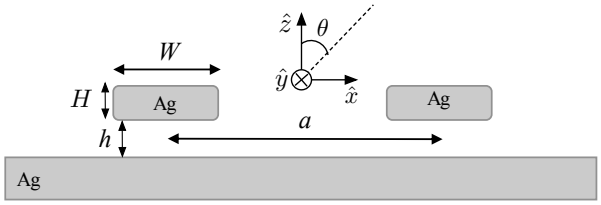

(b)

FIGURE 4.1: (a) Illustration of nanopatch antenna array. (b) Schematic of array of nanopatch antennas, with dimensions. The angle θ designates the angle of the TM polarized incident plane wave with respect to the optic (z) axis, so that the magnetic field is oriented in the $\hat{y}$-direction.

where H_0 is the amplitude of the incident magnetic field and $1/Q_\mu = 1/Q_\mu^{rad} + 1/Q_\mu^{\Omega}$ is the Q factor of the mode due to both radiative and Ohmic losses, and an $e^{i\omega t}$ harmonic time dependence is used. Analytic expressions for the Ohmic losses, resonance frequencies, and mode fields can be found in [28]. However, the radiation losses of a single cube will not be valid, since these need to be computed in the context of the array of dipoles. Although the mechanism for the radiative Q is due to a complex interaction between the dipole fields in the plane, the radiative Q itself can be found through simple conservation of energy arguments, which are presented in section 4.6.

The coupling C_μ to the μ^{th} mode is computed using an overlap surface integral of the total field incident upon the gap region of the cube, including the field reflected

off of the metal film, with the electric field of the mode:

$$C_\mu = \frac{\int \mathbf{E}_\mu^* \times \mathbf{H}_{inc} \cdot \mathbf{n} \mathrm{d}S}{\epsilon_0 H_0 \int \|\mathbf{E}_\mu\|^2 \mathrm{d}V}. \tag{4.7}$$

The surface integral in this expression is evaluated on the slots of the cube, and the volume integral is evaluated over the volume of the gap between the cube and the metal film.

Consider the case of a TM-polarized wave with the magnetic field oriented in the $\hat{\mathbf{y}}$ direction and wavenumber k, which reflects off of a metal film with a reflection coefficient r_{TM} at an incident angle θ relative to the z-axis. Then the total magnetic field on the surface of the metal film in the absence of the nanopatch antennas is

$$\mathbf{H}_{inc} = H_0 \hat{\mathbf{y}} e^{-ik\sin(\theta)x} \left(e^{ik\cos(\theta)z} - r_{TM} e^{-ik\cos(\theta)z} \right) \tag{4.8}$$

which we define as the incident field when the nanopatch antennas are introduced on the surface of the film. Consider now an array of nanopatch antennas of width W, gap size h and pitch a. If the gap size h between the nanopatches and the film is much smaller than the wavelength, then the incident magnetic field near the gap is approximately

$$\mathbf{H}_{inc} = H_0 (1 - r_{TM}) \hat{\mathbf{y}} e^{-ik\sin(\theta)x}. \tag{4.9}$$

Using this approximation for the coupling coefficients leads to

$$C_\mu = \begin{cases} \frac{4(1-r_{TM})}{\tilde{E}_0 W \epsilon_0} \cos(\sin(\theta) kW/2) & \mu \text{ odd} \\ \\ \frac{4(1-r_{TM})}{\tilde{E}_0 W \epsilon_0} \sin(\sin(\theta) kW/2) & \mu \text{ even.} \end{cases} \tag{4.10}$$

where $\tilde{E}_0$ is a normalization constant of the mode electric field, defined such that $|\mathbf{E}_\mu(\mathbf{0}))| = \tilde{E}$.

Schelkunoff's equivalence principle can be used to relate the electromagnetic field in the slots to an effective magnetic current, which yields a magnetic dipole moment

for each slot. The scattering of these fields need to be computed using the exact Green's function of the geometry, including the finite height of the cube and the reflection of the substrate. The reflection of the substrate is easily taken into account by simply adding the image dipoles of the metal film, but including the effect of the finite height of the nano patches in the Green's function is not straightforward. Here we neglect the impact of the thickness of the nanopatch antenna on the Green's function, but assume that it can be modeled by separating the dipoles of each slot by an effective width, W_{eff}, which is the *effective width* of the cube.

We emphasize that the effective width is not a fit parameter in the model, but is needed to describe the far-field radiation pattern of a single nanocube. Since the nanopatch antennas have a finite thickness, their radiation pattern can deviate significantly from what is predicted by patch antenna theory. The radiation is further perturbed by scattering off of neighboring patches, and so this parameter must be extracted from full-wave simulations of a small array of patches. The effect is that the radiation from the patch is as if the patch were significantly wider than its actual size, and so the pattern may be fit by using an effective width. This parameter may be extracted from full-wave simulations of small arrays of nano patches, as is described in section 4.8. Once this parameter is known, it deterministically predicts the behavior of infinite, periodic arrays of nano patches.

Let the magnetic dipole corresponding to the slot at $x = 0$ be $\mathbf{m}_1$, and the magnetic dipole corresponding to the slot at $x = W$ be $\mathbf{m}_2$. For the first slot, the dipole moment of the slot is

$$i\omega\mu_0\mathbf{m}_1 = \int_{\text{slot1}} \mathbf{K}_M \mathrm{d}S$$

$$\mathbf{m}_1 = \frac{-\hat{\mathbf{y}}(1 - r_{TM})hW\tilde{E}_0}{i\omega\mu_0} \sum_{\mu} e_\mu(\omega), \tag{4.11a}$$

and the symmetry of the modes requires that the dipole moment of the second slot

must be

$$i\omega\mu_0\mathbf{m}_2 = \int_{\text{slot2}} \mathbf{K}_M \mathrm{d}S$$

$$\mathbf{m}_2 = \frac{-\hat{\mathbf{y}}(1-r_{TM})hW\tilde{E}_0}{i\omega\mu_0}\sum_{\mu}(-1)^{\mu+1}e_\mu(\omega). \tag{4.11b}$$

Using this result, we can write the radiation pattern of a single plasmonic nanopatch antenna as the sum of two magnetic dipoles with polarizabilities $\alpha_1 = \sum_\mu \alpha_1^\mu$ and $\alpha_2 = \sum_\mu \alpha_2^\mu$, where

$$\alpha_1^\mu = \frac{4hc^2(1-r_{TM})^2\cos(\sin(\theta)kW_{eff}/2)}{\omega_\mu^2 - \omega^2 + i\omega_\mu^2/Q_\mu} \tag{4.12a}$$

$$\alpha_2^\mu = \frac{(-1)^{\mu+1}4hc^2(1-r_{TM})^2\cos(\sin(\theta)kW_{eff}/2)}{\omega_\mu^2 - \omega^2 + i\omega_\mu^2/Q_\mu}. \tag{4.12b}$$

4.4 Calculation of the Magnetic Field Radiated by an Array of Magnetic Dipoles using Poisson's Summation Technique

This section serves to compute the scattered fields from a two-dimensional periodic array of magnetic dipoles that are excited at oblique incidence, using Poisson's summation technique. Consider a two-dimensional lattice of magnetic dipoles with moments $\mathbf{m}_1 = \alpha_1 H_0 \hat{\mathbf{y}}$. If an incident field strikes a lattice of dipoles at oblique incidence, then the dipoles will successively be excited with a phase difference relative to one another of $e^{ik_x x}$, and hence the n^{th} dipole will have a relative phase of $e^{ik_x an}$. The Hertzian potential produced by such a lattice of dipoles would be given by the doubly infinite sum

$$\Pi_y = \sum_{m=-\infty}^{\infty}\sum_{n=-\infty}^{\infty}\frac{m_1}{4\pi}e^{-ik_x an}\frac{e^{-ikr_{mn}}}{r_{mn}} \tag{4.13}$$

where

$$r_{mn} = \sqrt{z^2 + (x-an)^2 + (y-am)^2} \tag{4.14}$$

is the distance between each dipole and some observation point x, y, z. This sum can be much more conveniently computed by using Poisson's summation formula, which replaces an infinite sum of functions by the infinite sum of their Fourier transforms. The formula is

$$\sum_{n=-\infty}^{\infty} f(\alpha n) = \frac{1}{\alpha} \sum_{n=-\infty}^{\infty} F\left(\frac{2\pi n}{\alpha}\right) \tag{4.15}$$

when the convention for the normalization of the Fourier transform is defined by $F(k) = \int_{-\infty}^{\infty} f(x) e^{ikx} \mathrm{d}x$. Applying Poisson's summation first in the y-direction yields

$$\Pi_y = \frac{m_1}{2\pi a} \sum_n e^{-ik_x an} \sum_m K_0(\Gamma_m \sqrt{z^2 + (x - an)^2}) e^{i2\pi m y/a} \tag{4.16}$$

where $\Gamma_m = \sqrt{(2m\pi/a)^2 - k^2}$, and K_0 is the modified Bessel function of the second kind. Note that the Bessel function decays exponentially for large real arguments. Therefore, if we require that $a < \lambda$, then only the $m = 0$ term is propagating and all of the other terms may be dropped. Then the expression for the Hertzian potential in the far-field limit reduces to

$$\Pi_y = \frac{m_1}{2\pi a} \sum_n e^{-ik_x an} K_0(ik\sqrt{z^2 + (x - an)^2}). \tag{4.17}$$

Poisson's formula may be applied once more in the x direction, which yields the much simpler expression

$$\Pi_y = \frac{m_1}{2a^2} \sum_n \frac{e^{-C_n z}}{C_n} e^{i(2\pi n x/a - k_x x)} \tag{4.18}$$

where

$$C_n = \sqrt{(2n\pi/a - k_x)^2 - k^2}. \tag{4.19}$$

If $\sin(\theta) < \lambda/a - 1$, then only the $n = 0$ term propagates,

$$\Pi_y = \frac{-im_1}{2a^2 k \cos(\theta)} e^{-ik(\cos(\theta)z + \sin(\theta)x)} \tag{4.20}$$

and a propagating plane wave solution is recovered from the lattice sum. The condition that $\sin(\theta) < \lambda/a - 1$ is a manifestation of the grating equation, since this is the pitch that would be required to obtain higher diffractive orders at angles of $\theta_n = \text{asin}(2\pi n/a)$, as can be seen in eq. (4.18).

Assuming the pitch is sufficiently sub-wavelength to prevent all diffractive orders, the magnetic field of the plane wave emitted by the array of dipoles is

$$H_y = (k^2 + \partial_y^2)\Pi_y = \frac{-im_1 k}{2a^2 \cos(\theta)} e^{-ik(\cos(\theta)z + \sin(\theta)x)} \tag{4.21}$$

4.5 Reflection of Film-Coupled Patch Antenna Arrays

In order to find the field radiated by an array of patch antennas, we will use Poisson's summation technique to directly sum the radiated far-fields of all the dipoles. This is worked out in detail in appendix section 4.4, where it is shown that the field radiated by a single periodic array of dipoles that is illuminated at incident angle θ and with moments $\mathbf{m}_1 = m_1\hat{\mathbf{y}}$ is

$$H_y = \frac{-im_1 k}{2a^2 \cos(\theta)} e^{-ik(\cos(\theta)z + \sin(\theta)x)} \tag{4.22}$$

under the assumption that $\sin(\theta) < \lambda/a - 1$. When $\sin(\theta) > \lambda/a - 1$, additional far-field terms must be kept that will yield additional resonances in the spectrum (see fig. 4.2 and the corresponding discussion in section 4.7).

The magnetic field from the periodic array of nanopatch antennas can by found by adding the magnetic field radiated from the lattice with dipole moments $\mathbf{m}_2$, but offset with an array factor of $e^{-ik_x W}$, where $k_x = k\sin(\theta)$. If we define $m_1^\mu = \alpha_1^\mu H_0$ and $m_2^\mu = \alpha_2^\mu H_0$, then the symmetry of the modes requires that $m_2^\mu = (-1)^{\mu+1} e^{-ik_x W_{eff}} m_1^\mu$, and the total magnetic field radiated by the nanopatch antenna

lattice can be written

$$H_y = \frac{-ike^{-i\mathbf{k}\cdot\mathbf{r}}}{2a^2\cos(\theta)} \sum_{\mu} m_1^{\mu} \left(e^{ik_x W_{eff}/2} + (-1)^{\mu+1} e^{-ik_x W_{eff}/2} \right). \tag{4.23}$$

If the width of the patches is sufficiently subwavelength, then the dipoles m_1^{μ} and m_2^{μ} will strongly destructively interfere for even μ, and so we can restrict the summation to only odd values of μ. The total reflected field will be the field from the array of nanoptach antennas, plus the incident field reflected off of the metal film:

$$\mathbf{H}_r = -\mathbf{H}_0 \left(r_{TM} + \frac{ik\cos(\sin(\theta)kW_{eff}/2)}{a^2\cos(\theta)} \sum_{\mu \text{ odd}} \alpha_1^{\mu} \right). \tag{4.24}$$

This yields a reflection coefficient of the form

$$r = r_{TM} + \frac{A_f(\theta)}{\cos(\theta)} \sum_{\mu \text{ odd}} \frac{i4kh(c^2/a^2)(1 - r_{TM})^2}{\omega^2 - \omega_{\mu}^2 + i\omega_{\mu}^2/Q_{\mu}} \tag{4.25}$$

where

$$A_f(\theta) = \cos^2(\sin(\theta)kW_{eff}/2). \tag{4.26}$$

This equation predicts that the reflection spectrum is given by a baseline reflection coefficient of r_{TM}, plus a sum of resonances of odd modes of the nano patches, where all parameters used thus far are completely analytic.

4.6 Radiation Q-Factor of a Periodic Lattice of Patch Antennas

The Q-factor in used in eq. (4.30) is not equivalent to the Q-factor of a single patch antenna, because the interference of neighboring antennas in the infinite lattice restricts the amount of power that any individual resonator may radiate, which increases the radiation Q. The radiation Q of a single dipole is affected by the rest of the lattice through the complex, mutual interactions of the dipoles in the lattice[20, 21].

However, this interaction must be such that the radiation of the lattice satisfies conservation of energy, and so the power radiated by an individual dipole can be found by first calculating the total intensity radiated by the lattice and then dividing by the number density of the dipoles. Here we exploit this fact in order to make a conservation of energy argument for the radiation Q of the dipoles.

The radiation Q corresponding to resonance μ is defined by

$$Q_\mu^r = \frac{\omega_\mu U_\mu |e_\mu|^2}{p_r} \tag{4.27}$$

where $U_\mu = \epsilon_0/2 \int |\mathbf{E}_\mu|^2 \mathrm{d}V$ is the mode volume, and p_r is the power radiated by a single dipole in the lattice [28, 87]. When the gap size is sufficiently small, the field is in the gap dominated by the z-component and is uniform across the gap. In this limit, the mode volume is $U_\mu \approx \epsilon_0 h W^2 \tilde{E}_0^2/4$.

The total intensity radiated by the lattice is the time-averaged Poynting vector of the radiated field by the lattice in the direction normal to the lattice:

$$p_r = a^2 \langle \mathbf{S} \cdot \hat{\mathbf{n}} \rangle = \frac{Z_0 |\mathbf{m}_1|^2 k^2 A_f(\theta)}{2a^2 \cos(\theta)}. \tag{4.28}$$

Using eqs. (4.11a) and (4.28) in eq. (4.27) gives

$$Q_\mu^r = \begin{cases} \frac{ka^2 \cos(\theta)}{2h|1-r_{TM}|^2 A_f(\theta)} & \mu \text{ odd} \\ \infty & \mu \text{ even.} \end{cases} \tag{4.29}$$

This expression can finally be used in eq. (4.12) to determine the polarizability of the plasmonic patch antennas, which can in turn be used to compute the reflection coefficient of the film-coupled plasmonic patch antenna system.

4.7 Perfect Absorption by Film-Coupled Nanopatches

Since all aspects of the nanopatch response can be computed analytically (aside from the effective width), it is possible to arrive at a closed-form expression for the reflection coefficient of a periodic array of film-coupled nanopatches with period a (see fig. 5.2), which is independent of the effective width at normal incidence. The final expression is

$$r = r_{TM} + \frac{A_f(\theta)}{\cos(\theta)} \sum_{\mu \text{ odd}} \frac{i4kh(c^2/a^2)(1-r_{TM})^2}{\omega^2 - \omega_\mu^2 + i\omega_\mu^2/Q_\mu}. \tag{4.30}$$

with

$$Q_\mu^{rad} = \frac{ka^2\cos(\theta)}{2h|1-r_{TM}|^2 A_f(\theta)}. \tag{4.31}$$

where $A_f(\theta) = \cos^2(\sin(\theta)kW_{eff}/2)$. Since the performance of the absorber near a single resonance are of primary concern, we need only include the mode corresponding to the $\omega = \omega_\mu$ resonance. When the system is driven on resonance, eq. (4.30) reduces to

$$r = r_{TM} + \frac{(1-r_{TM})^2}{|1-r_{TM}|^2} \frac{2Q_\Omega}{Q_r + Q_\Omega}. \tag{4.32}$$

We first consider the on-axis properties of eq. (4.32) before examining the off-axis absorption. For the sake of gaining a qualitative understanding of eq. (4.32), consider a few limiting cases. If the substrate is a perfect conductor then $r_{TM} = -1$, and there are three interesting cases to consider based on the ratio of Ohmic to radiative losses. If the Ohmic losses go to zero, $Q_\Omega \to \infty$, and therefore $r = 1$, which means that the nanopatch antennas are so responsive that they cause the surface to behave like a PMC. In the limit where Ohmic losses dominate, $Q_\Omega \to 0$, and hence $r = -1$. In this case the nanopatch antennas have become virtually without response, and the surface reduces to a simple PEC.

If there is to be a balance between electric and magnetic currents to produce a perfect absorber such that the surface acts like a combination of PEC and PMC, then the Ohmic losses of the nanopatch antennas need to lie between these two extremes. For a PEC substrate, eq. (4.32) predicts perfect absorption of light at normal incidence if the radiative losses balance the Ohmic losses, i.e. $Q_r = Q_\Omega$. In this case we achieve the required balance of electric and magnetic surface currents to absorb all the incident radiation.

Returning now to eq. (4.30), we note that the effective width is not relevant when the array is illuminated at normal incidence, and in this case it is possible to predict the amplitude, position and spectral width of the resonance of the ideal absorbing metasurface given only the material and four geometrical parameters: the width of the patch W, the pitch of the array a, the spacing layer h between the nanocube and the metallic substrate, and the height of the patch H. We can compare the semi-analytical model against full wave simulations using a simple nanopatch antenna system at normal incidence, as illustrated in fig. 4.2. We initially choose patches that are representative of the nanocube perfect absorbers[50] with the choice of material parameters ($W = 80nm, h = 5nm, H = 80nm$), while sweeping the pitch a of the array. The nanocube and metallic substrate were both chosen to be silver, with data taken from [63], and we assume that the substrate has sufficient thickness to prevent any transmission. The reflection coefficient in eq. (4.30) is plotted alongside the results of 3D full-wave simulations in fig. 4.2 for normal incidence, which shows excellent agreement between the dipole model and the simulations.

Additional sharp features appear in the two lower panels of fig. 4.2, which are on the left-hand side of the fundamental resonance. These resonances are Wood's anomalies [4], which satisfy the Rayleigh cutoff conditions $\lambda/a = (n_\mathrm{S} \pm \sin(\theta))/m$, where θ is the angle of incidence, m is an integer [5] and n_S refers to the effective index of substrate or superstrate modes. These arise in the wavelength range

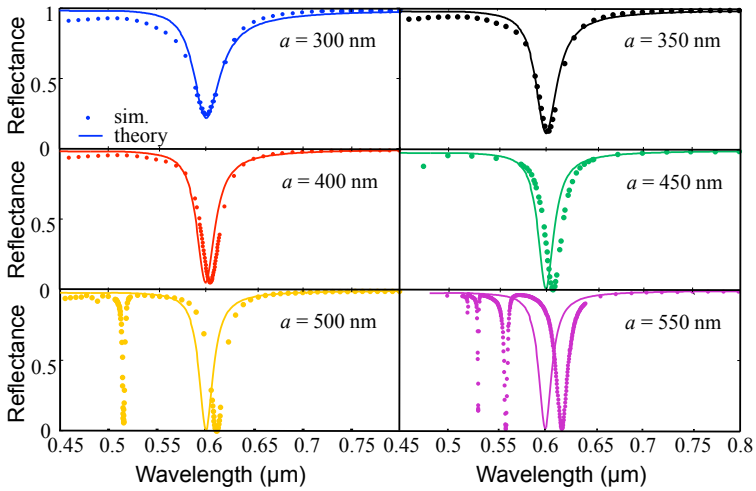

FIGURE 4.2: Reflectance of a metasurface composed of an array of film-coupled optical patch antennas under illumination by a normally incident plane wave. The graphs compare the theoretical model (solid line) with numerical calculations (dots) for varying pitches a.

where additional terms from the Poisson's summation method (see appendix 4.4) become propagating, and would need to be considered when calculating the reflection coefficient. As the pitch increases, the resonance frequency appears to shift in simulation, which we attribute to the interaction between the approaching resonance of the Wood's anomaly and the mode due to the gap resonance.

Returning to the off-axis properties of eq. (4.32), it's clear that, since Q_r depends on the incident angle, merely balancing the Ohmic and radiative losses will not be sufficient to produce a perfect absorber at all angles of incidence. However, upon inspection of eq. (7.5), it is apparent that choosing an appropriate value for the width of the cube will make the dependence on angle of the numerator and denominator approximately cancel. To make this dependence on angle more explicit, we define the parameter $C_r \equiv ka^2/8hQ_\Omega$, which is equivalent to the ratio of the radiation and Ohmic losses at normal incidence in the case of a PEC substrate. Using this notation,

the reflection coefficient is

$$r = \frac{A_f(\theta) - C_r \cos(\theta)}{A_f(\theta) + C_r \cos(\theta)} \tag{4.33}$$

where we see that $Z_{TM}(\theta)/Z_0 = A_f(\theta)/C_r$. Note that, if the width of the patch antenna is deeply sub-wavelength then $A_f(\theta) = 1$. In this case, and if $C_r = 1$, i.e. the losses are balanced between radiative and Ohmic, then we obtain the same as the limit on the reflectance of a homogenous, impedance matched material. However, if the electrical size of the patch antennas is significant, then $A_f(\theta)$ can be made to approximately cancel the $\cos(\theta)$ term in the numerator of eq. (4.33). To see this, we expand the numerator and denominator to third order in θ,

$$r = \frac{(1 - C_r)}{1 + C_r} + \theta^2 \left(\frac{C_r \left(1 - k^2 W_{eff}^2/2\right)}{(1 + C_r)^2} \right) + \mathcal{O}(\theta^4). \tag{4.34}$$

This expression shows that, if the losses are matched so that $C_r = 1$ and the effective width is fixed such that $W_{eff} = \sqrt{2}/k$, then the reflection coefficient vanishes to third order in θ.

If perfect absorption is desired to higher than third order in θ, the off-axis performance can be further improved if the substrate is not required to be a PEC and is instead defined by a complex dielectric with dielectric constant ϵ_s. In this case, r_{TM} will also depend on the incident angle, and if an appropriate value for ϵ_s is chosen, then the variation of the reflection coefficient of the substrate with angle can be made to nearly completely compensate the variation of the radiative losses with angle. To illustrate this effect, fig. 4.3 plots the reflection coefficient of nanopatch arrays with $C_r = 1$ and $W = 0$, but using the dielectric constant of a silver film at varying wavelengths as the reflective substrate. For silver films there is a certain wavelength where perfect absorption may be observed up to very high angles, on the order of 80°.

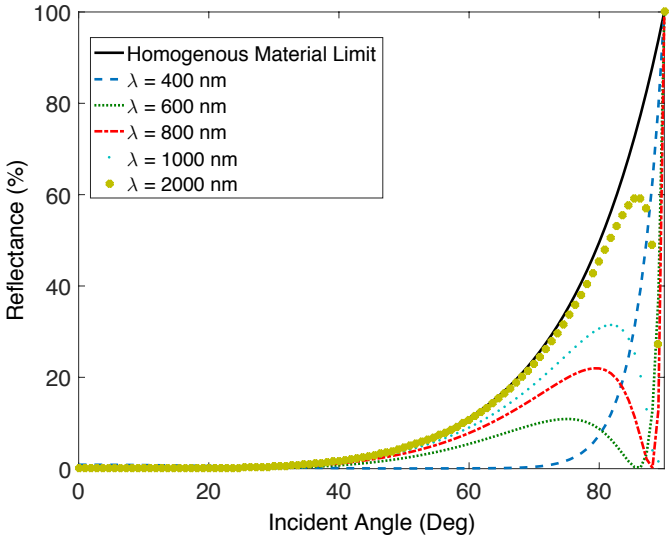

FIGURE 4.3: Reflection coefficient of a silver metal film covered in an array of nanopatch antennas, designed so that $C_r = Q_\Omega$. The permittivity of silver yields a perfect absorber design at 400nm. The solid black line shows the function $|(1-\cos(\theta))/(1+\cos(\theta))|^2$, which is the limit for the reflectance of a homogenous impedance matched material or a PEC backed metasurface.

Unfortunately, this design approach restricts the permittivity of the substrate to take on very specific values. However, the range of values might be broadened if the Ohmic and radiative losses are allowed to become slightly unbalanced at normal incidence. In this case the absorber will not absorb perfectly at normal incidence, but a very even absorption profile versus incident angle may be obtained. To design an absorber at an arbitrary wavelength, we first choose a particular metal film and an operating wavelength. Then the ratio of radiative to Ohmic losses C_r is varied while keeping $W_{eff} = \sqrt{2}/k$ until the desired reflectance profile is found. This is done in fig. 4.4, where we have chosen to design an absorber for a wavelength of $\lambda = 1000nm$, using patches with $W = 100nm$ on a silver substrate. For a value of $C_r = 1.4$, a very flat reflectance profile is obtained, where the reflectance is less than 4.9% over the entire range from 0° to 88°.

To test this theory of absorption, the design process outlined above was followed

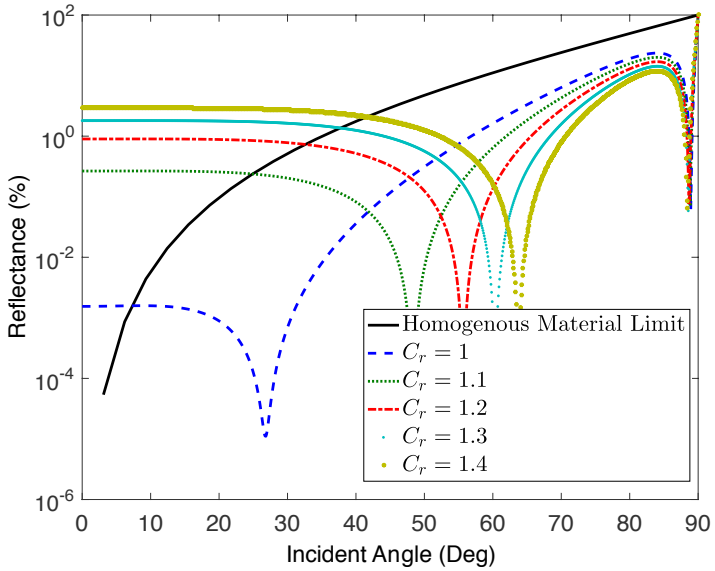

FIGURE 4.4: Illustration of how the balance between radiation and Ohmic losses C_r alter the off-axis reflectance of the system. At a certain value of C_r, a very even reflectance is obtained as a function of incident angle.

to design an absorber using silver nanopatches over a silver substrate at a wavelength of $1.35\mu m$. Tuning the gap size h to $2nm$ and the width W to $140nm$, causes the patches to resonate at the desired wavelength, which can be found by solving the dispersion relations given in [28]. We then choose a value of $C_r = 1.4$, which corresponds to a pitch a of $600nm$, and provides a good compromise between the absorption at normal incidence and the off-axis performance. The height H of the patches is finally determined by simulations that extract the effective width, since it must be chosen to keep the appropriate effective width. For this particular design, $H = 46nm$ yields an effective width of the patch of $308nm$, which yields the off-axis absorption profile presented in fig. 4.5. The off-axis absorption is able to far surpass what is possible with a homogenous, anisotropic, impedance matched absorber.

Here we have presented a new theory of the perfect absorption properties of patch antenna absorbers, which is based on a first principles derivation of the scattering of an infinite periodic array of nanopatch antennas that are coupled to a metal film

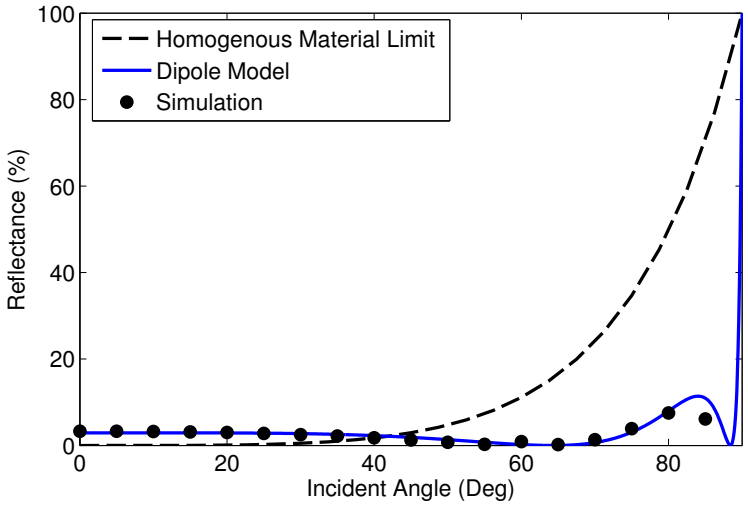

FIGURE 4.5: Off-axis performance of a perfect absorber designed using the method outlined in the text. The reflectance is evaluated both in simulation and theoretically using the dipole model.

and excited by a TM polarized wave. It can be shown by a simple extension of the theory presented here that the nanopatch antenna system cannot produce a perfect absorber for TE polarization. However, the rigorous calculations presented here allow the theory to explain the complete off-axis behavior of perfect absorption under TM polarization, and reconcile the previous theories that have been published.

4.8 Extraction of the Effective Width

The effective width of a nanopatch antenna is defined as the separation distance between two magnetic dipoles that is required to describe the far-field pattern of the fundamental resonance of the nanopatch antenna. Unfortunately, because of both the finite height of the nanopatch and the proximity of neighboring patches, the far-field pattern is perturbed from the analytical description of two dipoles separated by a width W equal to the nanopatch width, and must instead be described using two dipoles that are separated by an effective width, W_{eff}, which must be extracted from numerical simulations.

In order to find the effective width of a nanopatch, we simulate a 3×3 array of nanopatches on a metal film using a frequency-domain finite element method solver. The array is illuminated by a plane wave at normal incidence, and the solver is configured to solve for the scattered fields. In order to find the scattered fields from the resonance of only a single cube, all of the cubes are grounded by replacing the vacuum of the gap region for each of the 8 cubes on the perimeter with metal, and only leaving the gap of the patch at the center as vacuum. In this configuration, the far-field is dominated by the scattering of the center patch, since its resonance has an enhancement factor on the order of several hundred. The far-field of the entire domain is computed, and then fitted with $A_f(\theta) = (1 - r_{TM}(\theta)) \cos(\sin(\theta) k W_{eff}/2)$ in order to extract the effective width.

5

Effective Medium Theory of Film-Coupled Metasurfaces

In chapter 4, the reflectance properties of a periodic film-coupled patch antenna array were calculated and compared against full-wave simulations. There was, however, an important approximation that was made in calculating the reflection coefficient that resulted in fig. 4.2, which is that the dipoles in the lattice were assumed to not interact with each other. More explicitly, the driving field that was assumed to drive each polarizable magnetic dipole was the magnetic field of the incident plane wave, while in reality it should be the sum of the magnetic field of the incident plane wave plus the magnetic field scattered by the dipoles. This section removes that approximation using the methods of effective medium theory, and in the process homogenizes the lattice into an effective medium that exhibits spatial dispersion and surface modes. The theory presented in this chapter was developed solely by myself, while the full-wave simulations were performed by Dr. Alexandre Baron. The work was published in [92].

As was discussed in chapter 2, when a dipole radiates in any geometry, it exerts a force on itself through the radiation reaction that causes the amplitude of the dipole

to decay exponentially in time[24]. In the frequency domain, this phenomenon is captured through the imaginary part of the polarizability of the dipole, and hence it can be shown that the radiation reaction requires that the imaginary part of the polarizability take a specific value, even when the dipole exhibits no Ohmic losses. When dipoles are placed in a lattice to form a material, the imaginary part of the polarizability of the dipoles would normally lead to absorption in the material, if the dipoles did not interact with each other. However, conservation of energy is maintained by the lattice in a very round-about way: dipoles exert a force on themselves according to their own energy loss via the radiation reaction, but when placed in a lattice, the dipoles exert forces on each other that exactly cancel the radiation reaction force and replace it with a new force that corresponds to the radiation losses of the lattice as a whole. Proving this conservation of energy relationship is one of the primary tasks of effective medium theory[24, **?**].

Here we return to the effective medium theory of metasurfaces, but when the metasurface is placed close enough to a metal film that the interactions between the metamaterial elements is dominated by the surface plasmon interaction, and the radiation reaction force is modified by the emission of each dipole into surface plasmon modes. Here we demonstrate for the first time that the contribution to the radiation reaction force from the emission into surface plasmons is exactly canceled by the force that the dipoles exert on one another through surface plasmons, and derive an exact expression for the effective susceptibility of the metasurface in terms of the microscopic polarizability.

The total field incident on the i^{th} dipole can be written as the sum of the incident field plus the sum over all the other dipoles,

$$\alpha^{-1}\mathbf{m}_i = \mathbf{H}_0(\mathbf{r}_i) + \sum_j \mathbf{G}(\mathbf{r}_j - \mathbf{r}_i)\mathbf{m}_j. \tag{5.1}$$

where we include the $j = i$ term in the sum, because this term represents the

radiation reaction force, or self force of the dipole which is responsible for radiative damping. For a metasurface that is illuminated under normal incidence, symmetry requires that $\mathbf{m}_j = \mathbf{m}_i$ for all j, and the equation may be rewritten in the form $\mathbf{m}_i = \left(\bar{\alpha}^{-1} - \sum_j \mathbf{G}(\mathbf{r}_j - \mathbf{r}_i)\right)^{-1} \mathbf{H}_0(\mathbf{r}_i)$. The quantity in parentheses becomes the new effective polarizability, and the infinite sum over the Green's function is typically defined as the interaction constant $\mathbf{C} = \sum_j \mathbf{G}(\mathbf{r}_j - \mathbf{r}_i)$. Hence we have that $\alpha_{eff} = \alpha(1 - \mathbf{C}\alpha)^{-1}$, and the surface susceptibility is given by $\chi = \alpha_{eff}/a^2$ where a is the distance between unit cells in the lattice. In terms of effective polarzabilities, the question that this chapter seeks to address is, how are the interaction constants between dipoles in a metasurface modified when a metasurface is tightly coupled to a metal film that supports surface plasmons?

To examine how a metasurface conserves energy, the interaction constant may be split up into two terms, $\mathbf{C} = \mathbf{C}^{0D} + \mathbf{C}^{1D} + \mathbf{C}^{2D}$, where $\mathbf{C}^{0D} = \mathbf{G}(0)$ and $\mathbf{C}^{1D} + \mathbf{C}^{2D} = \sum_{j \neq i} \mathbf{G}(\mathbf{r}_j - \mathbf{r}_i)$. The first term, $\mathbf{C}^{0D}$, represents the self-force of the dipole due to its emission into surface plasmon modes, while $\mathbf{C}^{1D} + \mathbf{C}^{2D}$ represents the force that all of the dipoles exert on each other, as illustrated in figs. 5.1(a) to 5.1(c). As was discussed in chapter 2, the imaginary part of $\mathbf{C}$ represents work done on the dipoles, and hence represents the transfer of energy, while the real part of $\mathbf{C}$ may be considered reactive power that causes a resonance frequency shift in dipoles with a natural Lorentzian response.

5.1 The Film-Coupled Magnetic Dipole

In this section, the contribution to the radiation reaction force experienced by a single dipole due to the coupling to a surface plasmon mode in a metal film is calculated, as shown in fig. 5.1(a). In particular, we are interested in magnetic dipoles that are oriented parallel to the surface of a metal film, and separated by some distance d from

the film along the z-axis. The radiation reaction force for any dipole is given by the imaginary part of the Green's function evaluated at the location of the dipole. One of the standard approaches for computing the Green's function in any waveguide-like geometry is to expand the field into a set of bound modes and radiation modes[88]. For a dipole in free space, there are no bound modes, and so the Green's function for a dipole in free space can be computed using only radiation modes. However, for a dipole placed near a metal film, there is a set of bound surface modes, which are surface plasmons. Here we show that the coupling of the dipole to surface plasmon modes yields an imaginary part of the Green's function at the location of the dipole that corresponds to the power loss of the dipole into surface plasmon modes.

The coupling to the surface plasmon is found using a modified formulation of coupled mode theory, adapted particularly for expansions of the field into a basis of cylindrical Hankel functions, i.e. by expanding the field in a sum of modes

$$\mathbf{E} = \sum_{\mu\nu} A^+_{\mu\nu} \mathbf{E}^+_{\mu\nu} \tag{5.2a}$$

$$\mathbf{H} = \sum_{\mu\nu} A^+_{\mu\nu} \mathbf{H}^+_{\mu\nu} \tag{5.2b}$$

where $\mathbf{H}^+_{\mu\nu}$ and $\mathbf{E}^+_{\mu\nu}$ are the outgoing cylindrical Hankel basis defined in appendix A. The Hankel basis is a convenient choice for this problem, because there is only one bound cylindrical wave that a magnetic dipole can excite when it is oriented parallel to the surface of the metal film. However, unlike most of the bases used in coupled mode theory, which assume that the basis is a set of source free solutions to Maxwell's equations, it is shown in appendix B that the Hankel functions are not source-free solutions to Maxwell's equations, since they imply the existence of a delta-function source at the origin. The modification of the coupled mode theory equations due to this source is taken into account in appendix B, and the final expression for the

amplitude $A^+_{\mu\nu}$ of an outgoing cylindrical Hankel wave $\{\mathbf{E}^+_{\mu\nu}, \mathbf{H}^+_{\mu\nu}\}$ is

$$A^+_{\mu\nu} = \frac{ik^2}{4L\epsilon_0(1+\delta_{\nu 0})} \int \mathbf{P}\cdot(\mathbf{E}^+_{\mu\nu} + \mathbf{E}^-_{\mu\nu}) - \mu_0 \mathbf{M}\cdot(\mathbf{H}^+_{\mu\nu} + \mathbf{H}^-_{\mu\nu})\mathrm{d}V. \tag{5.3}$$

where $\{\mathbf{E}^-_{\mu\nu}, \mathbf{H}^-_{\mu\nu}\}$ is the incoming Hankel basis, and L is a normalization constant that is described in appendix A. This equation is in disagreement with the expressions given in [89], and in agreement with the expressions in the supplementary material presented in [90], although no rigorous proof was provided in [90] for eq. (5.3), and Refs [89, 90] both treated the Hankel basis as source-free.

Consider a magnetic dipole sitting at some distance d along the z-axis from a metal film with relative dielectric constant ϵ, the surface of which is on the xy-plane. Then in eq. (5.3), we have that $\mathbf{M} = m_y \hat{\mathbf{y}}\delta(z-d)\delta(r)/2\pi r$. A careful calculation shows that

$$H^{TM+}_{\mu\nu y}(d\hat{\mathbf{z}}) + H^{TM-}_{\mu\nu y}(d\hat{\mathbf{z}}) = \frac{-i}{Z_0} Z^{TM}_\mu(d)\delta_{\nu 1} \tag{5.4a}$$

$$H^{TE+}_{\mu\nu y}(d\hat{\mathbf{z}}) + H^{TE-}_{\mu\nu y}(d\hat{\mathbf{z}}) = \frac{i}{Z_0 k}\frac{d}{dz} Z^{TE}_\mu(d)\delta_{\nu 1}. \tag{5.4b}$$

where $Z^{TM}_\mu(z)$ and $Z^{TE}_\mu(z)$ are the profiles of the TE and TM modes in the z-direction, with mode numbers μ, as defined in appendix A. The mode amplitudes excited by this source are therefore

$$A^{TMc}_{\mu\nu} = \frac{-m_y k^2 Z_0}{4L} Z^{TM}_\mu(d)\delta_{\nu 1} \tag{5.5a}$$

$$A^{TMs}_{\mu\nu} = 0 \tag{5.5b}$$

$$A^{TEc}_{\mu\nu} = 0 \tag{5.5c}$$

$$A^{TEs}_{\mu\nu} = \frac{m_y k Z_0}{4L}\frac{d}{dz} Z^{TE}_\mu(d)\delta_{\nu 1}. \tag{5.5d}$$

In the particular case of the geometry where there is only a single interface between a metal and a dielectric, there is only one bounded TM mode, and there are no

bounded TE modes, and so the TE mode amplitudes become irrelevant. For the single bounded TM mode, an expression for $Z_\mu^{TM}(z)$ is given in eq. (A.8).

Using the excited mode amplitudes in eqs. (5.5a) to (5.5d), together with the mode definitions provided in eqs. (A.13e) and (A.13f), the y-component of the magnetic field excited by the dipole is shown to be

$$H_y(r,\theta,z) = \frac{-im_y\beta^3\sqrt{-\epsilon}}{4(1-\epsilon)}e^{-k_z^+(d+z)}\left[H_0^{(2)}(\beta r) - \cos(2\theta))H_2^{(2)}(\beta r)\right], \tag{5.6}$$

where $k_z^+ = ik/\sqrt{\epsilon+1}$ and $\beta = k\sqrt{\epsilon/(\epsilon+1)}$ is the surface propagation constant. Taking the limit as $r \to 0$, the real part of eq. (5.6) becomes singular, as it is for a dipole in free space. The imaginary part, however, is simply $\mathrm{Im}\{H_y(0)\} = \frac{-m_y\beta^3\sqrt{-\epsilon}}{4(1-\epsilon)}e^{-2k_z^+ d}$. According to Poynting's theorem, the power dissipated by the horizontal magnetic dipole into the surface plasmon is given by $P_{sp} = (-\omega/2)\mathrm{Im}\{\mathbf{m}^*\cdot\mathbf{H}\}$, and therefore the power dissipated into the surface plasmon is,

$$P_{sp} = \omega|m_y|^2\mathrm{Re}\left\{\frac{\beta^3\sqrt{-\epsilon}}{4(1-\epsilon)}e^{-2k_z^+ d}\right\}. \tag{5.7}$$

Moreover, the coupling factor due to the radiation reaction from the SPP mode is then,

$$C^{0D} = H_y(0)/m_y = \frac{-i\beta^3\sqrt{-\epsilon}}{4(1-\epsilon)}e^{-2k_z^+ d}. \tag{5.8}$$

5.2 One Dimensional Array of Film-Coupled Magnetic Dipoles

Consider a one-dimensional array of magnetic dipoles placed along the y-axis, oriented in the y-direction, separated by some distance a_y from each other, and placed at a distance d over a metal film that lies in the xy-plane. Moreover, assume that the one-dimensional array is illuminated by a TM plane-wave with a free-space wave vector of $\mathbf{k} = (k_x, k_y, k_z)$, with $k_z = \sqrt{k^2 - k_x^2 - k_y^2}$ and polarized with the magnetic field oriented in the y-direction. The phase of the moments of the dipoles that

comprise the one-dimensional array will therefore be related by the phase of the illuminating plane wave, such that dipole $\mathbf{m}_i = m_i\hat{\mathbf{y}}$ at location $\mathbf{r}_i$ will have dipole moment $m_i = m_y e^{-i\mathbf{k}\cdot\mathbf{r}_i}$.

The dipole at the origin is excluded when computing the C^{1D} interaction constant, as illustrated in fig. 5.1(b). The effective polarizability of the magnetic dipoles in the array is determined by the fields that the dipoles exert on each other. The field experienced by the magnetic dipole at the origin due to all the other dipoles is given by

$$H_y^{1D}(0) = \frac{-im_y\beta^3\sqrt{-\epsilon}}{2(1-\epsilon)}e^{-2k_z^+(z+d)}\sum_{\mu=-\infty}^{\infty}{}' \frac{H_1^{(2)}(\beta|\mu a_y|)}{\beta|\mu a_y|}e^{-ik_y\mu a_y}. \tag{5.9}$$

This sum converges quickly, but a simpler expression for the real part of the sum, which corresponds to the power loss due to radiation into surface plasmons, can be found by applying Poisson's summation formula[14]. The Poisson summation formula states that,

$$\sum_{\mu=-\infty}^{\infty} f(\mu a) = \frac{1}{a}\sum_{\mu=-\infty}^{\infty} F\left(\frac{2\pi\mu}{a}\right) \tag{5.10}$$

where $F(\omega)$ is the Fourier transform of $f(t)$. We are interested in applying this formula to aid in evaluating the infinite sum

$$\begin{aligned}\sum_{\mu=-\infty}^{\infty}{}' \frac{H_1^{(2)}(\beta|\mu a_y|)}{\beta|\mu a_y|}e^{-ik_y\mu a_y} &= -\lim_{z\to 0}\frac{J_1(z)}{z} + \sum_{\mu=-\infty}^{\infty}\frac{J_1(\beta|\mu a_y|)}{\beta|\mu a_y|}e^{-ik_y\mu a_y} - i\sum_{\mu=-\infty}^{\infty}{}'\frac{Y_1(\beta|\mu a_y|)}{\beta|\mu a_y|}e^{-ik_y\mu a_y} \\ &= \frac{-1}{2} + \sum_{\mu=-\infty}^{\infty}\frac{J_1(\beta|\mu a_y|)}{\beta|\mu a_y|}e^{-ik_y\mu a_y} - i\sum_{\mu=-\infty}^{\infty}{}'\frac{Y_1(\beta|\mu a_y|)}{\beta|\mu a_y|}e^{-ik_y\mu a_y}.\end{aligned} \tag{5.11}$$

Using the Fourier transform

$$\mathscr{F}\left\{\frac{J_1(\beta|t|)}{\beta|t|}\right\} = \begin{cases}\frac{2}{\beta^2}\sqrt{\beta^2-\omega^2} & \omega < |\beta| \\ 0 & \text{otherwise}\end{cases} \tag{5.12}$$

we can transform the infinite sum over the bessel function of the first kind as

$$\sum_{\mu=-\infty}^{\infty} \frac{J_1(\beta|\mu a_y|)}{\beta|\mu a_y|} e^{-ik_y \mu a_y} = \sum_{\mu \in U} \frac{2\Gamma_\mu}{\beta^2 a_y} \tag{5.13}$$

where

$$\Gamma_\mu = \sqrt{\beta^2 - (2\pi\mu/a_y - k_y)^2}. \tag{5.14}$$

The sum is evaluated over all of the Γ_μ modes that are *propagating*, which satisfy the relationship $|2\pi\mu/a - k_y| < |\beta|$. We define the set U as the set of all mode numbers μ such that Γ_μ is propagating:

$$U = \{\mu \mid |2\pi\mu/a - k_y| < |\beta|\}. \tag{5.15}$$

Then the total magnetic field experienced by the dipole at the origin is expressed as,

$$H_y^{1D}(0) = \frac{m_y\sqrt{-\epsilon}}{(1-\epsilon)} e^{-2k_z^+(z+d)} \left[\frac{i\beta^3}{4} - \sum_{\mu \in U} \frac{i\beta\Gamma_\mu}{a_y} - \beta^3 \sum_{\mu=1}^{\infty} \frac{Y_1(\beta\mu a_y)}{\beta\mu a_y} \cos(k_y \mu a) \right]. \tag{5.16}$$

Let $C^{1D} = H^{1D}(0)/m_y$ be defined as the part of the interaction constant due to all of the dipoles along the y-axis, excluding the dipole at the origin. The total interaction constant for the one-dimensional array of dipoles lying along the y-axis and oriented in the y-direction is $C = C^{0D} + C^{1D}$, where C^{1D} is given by

$$C^{1D} = \frac{\sqrt{-\epsilon}}{(1-\epsilon)} e^{-2k_z^+(z+d)} \left[\frac{i\beta^3}{4} - \sum_{\mu \in U} \frac{i\beta\Gamma_\mu}{a_y} - \beta^3 \sum_{\mu=1}^{\infty} \frac{Y_1(\beta\mu a_y)}{\beta\mu a_y} \cos(k_y \mu a) \right]. \tag{5.17}$$

In the limit that β is purely real, the final sum on the right hand side of eq. (5.17) is purely real, and all losses are due to the two purely imaginary terms, and these two terms therefore represent the radiative damping force. As was the case for the one-dimensional array of dipoles in free space, the dipoles in the column exert a

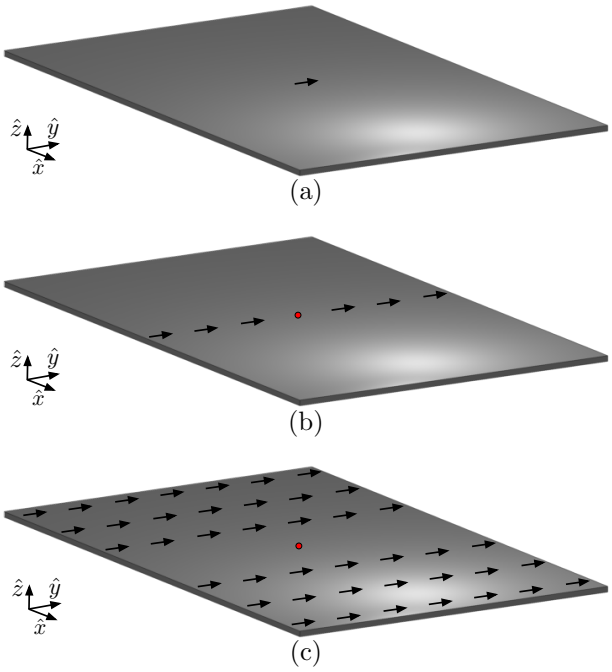

FIGURE 5.1: Illustration of the dipoles summed to produce the (a) C^{0D}, (b) C^{1D}, and (c) C^{2D} components of the interaction constant. The interaction constant is found by computing the fields of the dipoles at the location of the red dot, which designates the origin.

force on each other that cancels the force proportional to $i\beta^3/4$ that they exert on themselves due to the radiation reaction, and replaces it with a force proportional to the sum of the energy carried in all surface plasmon diffraction orders that are radiated by the line of dipoles.

5.3 Two Dimensional Array of Film-Coupled Magnetic Dipoles

Now consider a two-dimensional lattice of dipoles oriented in the y-direction with lattice spacing a_x and a_y in the x and y directions, excluding the line of dipoles along the y-axis, as illustrated in fig. 5.1(c). The two-dimensional lattice may be thought of as a set of lines of dipoles parallel to the y-axis, and at positions na_x along the x-axis. The total field of the lattice is the sum of the fields radiated by the lines of dipoles, and so we first compute the field radiated by a single line of

dipoles lying along the y-axis and oriented in the y-direction. Directly summing the magnetic fields of this lattice would be cumbersome because the field in the Hankel basis is given in cylindrical coordinates, and the redefinition of the cylindrical unit vectors would need to be taken into account for each dipole in the lattice. Instead of summing the magnetic fields, we compute the total z-component of the electric field, and the total electric field from all of the dipoles can be easily summed since $\hat{z}$ is translationally invariant. Then the y-component of the magnetic field can be found using

$$H_y = \frac{ik}{Z_0\beta^2}\frac{\partial}{\partial x}E_z. \tag{5.18}$$

which is valid when the field in the entire surface is assumed to vary as $e^{-k_z^+ z}$, and the field is purely transverse magnetic[88].

The total z-component of the electric field radiated by a single line of dipoles, which is denoted by E_z^{1D}, is given by the infinite sum of the field radiated by each of the individual dipoles. Using the same methods outlined in section 5.1 and appendix B, the z-component electric field in the surface plasmon mode radiated by a single magnetic dipole placed over a metal surface is

$$E_z = \frac{-m_y Z_0 \beta^4 \sqrt{-\epsilon}}{2k(1-\epsilon)} e^{-k_z^+(z+d)} \cos(\theta) H_1^{(2)}(\beta r) \tag{5.19}$$

and therefore the total electric field radiated by a line of dipoles along the y-axis is,

$$E_z^{1D} = \frac{-m_y Z_0 \beta^4 \sqrt{-\epsilon}}{2k(1-\epsilon)} e^{-k_z^+(z+d)} \sum_{\mu=-\infty}^{\infty} \frac{x H_1^{(2)}(\beta\sqrt{x^2+(y-\mu a_y)^2})}{\sqrt{x^2+(y-\mu a_y)^2}} e^{-ik_y \mu a_y}. \tag{5.20}$$

Applying Poisson's summation technique to the sum in eq. (5.20), the total field is

$$E_z^{1D} = \frac{-i m_y Z_0 \beta^3 \sqrt{-\epsilon}}{k a_y (1-\epsilon)} e^{-k_z^+(z+d)} e^{-ik_y y} \sum_{\mu=-\infty}^{\infty} \text{sign}(x) e^{-i|x|\Gamma_\mu} e^{-i(2\pi\mu/a_y)y}. \tag{5.21}$$

where Γ_μ is given in eq. (5.14), and the Fourier transform

$$\mathscr{F}\left\{\frac{H_1^{(2)}(\beta\sqrt{x^2+(y-t)^2})}{\sqrt{x^2+(y-t)^2}}\right\} = \frac{2i}{\beta|x|}e^{-i|x|\sqrt{\beta^2-(\omega-k_y)^2}}e^{-i(\omega-k_y)y}. \tag{5.22}$$

was used[91]. If the distance between the dipoles is less than the surface plasmon wavelength, then only the $\mu = 0$ mode will be propagating.

The total electric field generated all of the lines of dipoles in the lattice together, E_z^{2D}, excluding the line of dipoles at $x = 0$, is the sum of the electric field radiated by each line of dipoles individually:

$$E_z^{2D} = \frac{-im_y Z_0\beta^3\sqrt{-\epsilon}}{ka_y(1-\epsilon)}e^{-k_z^+(z+d)}e^{-ik_y y}\sum_{\mu=-\infty}^{\infty}\sum_{\nu=-\infty}^{\infty}{}' \operatorname{sign}(x-\nu a_x)e^{-i|x-\nu a_x|\Gamma_\mu}e^{-ik_x\nu a_x}e^{-i(2\pi\mu/a_y)y}. \tag{5.23}$$

If we restrict ourselves to considering the region of space where $|x| < a_x$, then

$$E_z^{2D} = \frac{-2m_y Z_0\beta^3\sqrt{-\epsilon}}{ka_y(1-\epsilon)}e^{-k_z^+(z+d)}e^{-ik_y y}\sum_{\mu=-\infty}^{\infty}e^{-i(2\pi\mu/a_y)y}\sum_{\nu=1}^{\infty}e^{-i\Gamma_\mu\nu a_x}\sin(\Gamma_\mu x - k_x\nu a_x). \tag{5.24}$$

The magnetic field in the region $|x| < a_x$ due to dipoles for all $\nu \neq 0$, is found using eqs. (5.18) and (5.24) to be

$$H_y^{2D} = \frac{-i2\beta m_y\sqrt{-\epsilon}}{a_y(1-\epsilon)}e^{-k_z^+(z+d)}e^{-ik_y y}\sum_{\mu=-\infty}^{\infty}\Gamma_\mu e^{-i(2\pi\mu/a_y)y}\sum_{\nu=1}^{\infty}e^{-i\Gamma_\mu\nu a_x}\cos(\Gamma_\mu x - k_x\nu a_x). \tag{5.25}$$

and here we are interested more specifically in the magnetic field at the location of the dipole,

$$H_y^{2D}(0) = \frac{-i2\beta m_y\sqrt{-\epsilon}}{a_y(1-\epsilon)}e^{-2k_z^+ d}\sum_{\mu=-\infty}^{\infty}\Gamma_\mu\sum_{\nu=1}^{\infty}e^{-i\Gamma_\mu\nu a_x}\cos(k_x\nu a_x). \tag{5.26}$$

A straightforward application of Poisson's summation technique can again be used to simplify the sum over ν, yielding

$$\sum_{\nu=1}^{\infty}e^{-i\Gamma_\mu\nu a_x}\cos(k_x\nu a_x) = -1/2 - \sum_{\nu=-\infty}^{\infty}\frac{i\Gamma_\mu}{a_x\Gamma_{\mu\nu}^2} \tag{5.27}$$

where $\Gamma_{\mu\nu} = \sqrt{\beta^2 - (2\pi\mu/a_y - k_y)^2 - (2\pi\nu/a_x - k_x)^2}$.

The contribution to the interaction constant due to all of the lines of dipoles excluding the line at $x = 0$ is defined as $C^{2D} = H^{2D}(0)/m_y$, which is

$$C^{2D} = \frac{\sqrt{-\epsilon}}{(1-\epsilon)} e^{-2k_z^+ d} \left[\sum_{\mu=-\infty}^{\infty} \frac{i\beta\Gamma_\mu}{a_y} - \frac{2\beta}{a_x a_y} \sum_{\mu=-\infty}^{\infty} \sum_{\nu=-\infty}^{\infty} \frac{\Gamma_\mu^2}{\Gamma_{\mu\nu}^2} \right]. \tag{5.28}$$

The total interaction constant is finally

$C = C^{0D} + C^{1D} + C^{2D}$

$$C = \frac{\sqrt{-\epsilon}}{(1-\epsilon)} e^{-2k_z^+ d} \left[\sum_{\mu=-\infty}^{\infty} \frac{i\beta\Gamma_\mu}{a_y} - \sum_{\mu\in U} \frac{i\beta\Gamma_\mu}{a_y} - \frac{2\beta}{a_x a_y} \sum_{\mu=-\infty}^{\infty} \sum_{\nu=-\infty}^{\infty} \frac{\Gamma_\mu^2}{\Gamma_{\mu\nu}^2} - \beta^3 \sum_{\mu=1}^{\infty} \frac{Y_1(\beta\mu a_y)}{\beta\mu a_y} \cos(k_y \mu a) \right]$$

$$C = \frac{\sqrt{-\epsilon}}{(1-\epsilon)} e^{-2k_z^+ d} \left[\sum_{\mu\notin U} \frac{i\beta\Gamma_\mu}{a_y} - \frac{2\beta}{a_x a_y} \sum_{\mu=-\infty}^{\infty} \sum_{\nu=-\infty}^{\infty} \frac{\Gamma_\mu^2}{\Gamma_{\mu\nu}^2} - \beta^3 \sum_{\mu=1}^{\infty} \frac{Y_1(\beta\mu a_y)}{\beta\mu a_y} \cos(k_y \mu a) \right]. \tag{5.29}$$

Notice that, in the limit of purely real permittivity, the contribution to the interaction constant from the $2D$ lattice in eq. (5.28) contains a sum over all modes propagating away from each column of dipoles in constant x. This term serves to cancel out the imaginary term in eq. (5.17) that corresponds to the power loss due to the modes propagating away from each column of dipoles. Provided that the permittivity is purely real, then the interaction constant $C = H_y(0)/my$ is purely *real*, meaning that there is no net loss by the dipoles to the surface plasmon. Conservation of energy and Poynting's theorem is thereby maintained by the lattice in a very round-about way: dipoles exert a force on themselves according to their own energy loss via the radiation reaction, but when placed in a lattice, the dipoles exert forces on each other that exactly cancel the radiation reaction force and replace it with a new force that corresponds to the radiation losses of the lattice as a whole. This is already known to be true for metamaterial lattices in free-space[25], but here we have demonstrated this it is also true when the dipoles are coupled to a metal film such that their Green's function is dominated by the surface plasmon mode.

5.4 Applications to Metamaterial Absorbers

Although the main result in eq. (5.29) is that there is no net alteration to the Q-factor of a metasurface when it is coupled to a metal film that supports surface plasmons, the real part of the interaction constant predicts a resonance frequency shift, and the imaginary part predicts additional Ohmic losses due to absorption by surface plasmons. Furthermore, there is a singularity in the term

$$\frac{2\beta}{a_x a_y} \sum_{\mu=-\infty}^{\infty} \sum_{\nu=-\infty}^{\infty} \frac{\Gamma_\mu^2}{\Gamma_{\mu\nu}^2} \tag{5.30}$$

in eq. (5.29) when $\Gamma_{\mu\nu} = 0$, which for $\mu = 0$ and $\nu = 1$ occurs when $\beta^2 = (2\pi/a_x - k_x)^2 + k_y^2$, and so eq. (5.29) predicts that, under normal incidence, there will be an additional resonance when the period of the lattice is equal to the surface plasmon wavelength. We claim that these resonances are the Wood's anomalies of the film-coupled metasurface.

As an example application of the theory, we consider a metamaterial surface consisting of nanopatches that are placed a small distance h away from a silver film, with a lattice constant of a. The gap region between the nanopatch and the metal film is known to support a set of cavity modes, which couple to the incident magnetic field and scatter as a magnetic dipole[28]. The excitation of the cavity modes due to the incident field can be found using a form of temporal coupled mode theory, and the magnetic polarizability of the nanopatch is found from the amplitude of the magnetic dipole moment of the scattered field from the cavity. The magnetic polarizability of the nanopatch antenna given in [3] is

$$\alpha = \frac{8hc^2 \cos^2(\sin(\theta)kW/2)}{\omega_0^2 - \omega^2 + i\omega_0^2/Q} \tag{5.31}$$

where W is the width of the nanopatch and θ is the angle of the incident magnetic field. Expressions for ω_0 and Q can be found in [28, 3]. The reflection coefficient of

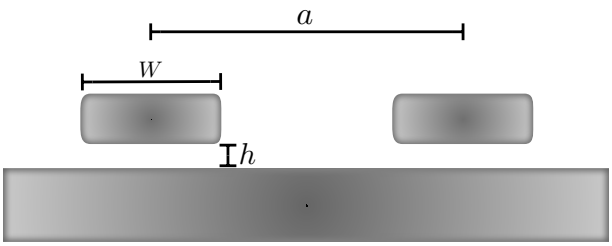

FIGURE 5.2: Illustration of the film-coupled metasurface of optical patch antennas. Each patch is a cuboid of width W and height H that is lifted off the film by a distance h.

the entire flim-coupled nanopatch metasurface system is [3, 92],

$$r = r_{TM} + \frac{-ik(1 - r_{TM})^2}{2a^2 \cos(\theta)}\alpha \tag{5.32}$$

where r_{TM} is the fresnel reflection coefficient of the bare metal film under TM polarization.

In Ref. [3], all interactions between the nanopatches through surface plasmons or evanescent radiation modes were neglected, and only the loss due to propagating radiation modes was taken into account by a choice of Q that included the radiation loss of the metasurface. However, since the nanopatch antennas scatter as magnetic dipoles and are placed very close to the surface of the metal film, they will couple through surface plasmons. Neglecting the evanescent radiation mode interaction and assuming the remaining coupling is primarily mediated through surface plasmon modes, the effective polarizability of the dipoles will become

$$\alpha_{eff} = \frac{\alpha}{1 - C\alpha} \tag{5.33}$$

where C is the interaction constant in eq. (5.29). The interaction constant is calculated using the measured Johnson and Christy data for the dielectric constant of silver[63]. The magnetic dipole that is generated by the film-coupled nanopatch is

created by an effective magnetic surface current that lies on the boundary of the gap region between the nanopatch and the metal film. Since the size of this gap is typically extremely sub-wavelength ($\sim 5nm$), we take $d = 0$ in the calculation of C, which places the magnetic dipole exactly adjacent to the metal film.

The new, corrected reflection coefficient with the surface plasmon interaction taken into account will now be

$$r = r_{TM} + \frac{-ik(1 - r_{TM})^2}{2a^2 \cos(\theta)} \alpha_{eff}, \tag{5.34}$$

which is plotted alongside eq. (6.15) in fig. 5.3 and compared with simulation results. The particular system presented in fig. 5.3 is for a periodic array of cubic patches illuminated under normal incidence with a width W of 80nm, and separated from a metal film by a distance of $h = 5$nm. Since the coupling coefficient is able to perfectly account for the resonance frequency shift and predict nearly all other features of the reflection spectrum, the coupling between nanopatches must be dominated by surface plasmon interactions, and the evanescent and propagating radiation modes play nearly no effect, aside from the propagating radiation modes determining the radiation Q-factor.

We note that there is an additional resonance in fig. 5.3(d) at around 530nm that is not predicted by the theory. This resonance does not appear to be due to the surface plasmon interaction, since there is no value of μ, ν where $\Gamma_{\mu\nu} = 0$ in this region of the spectrum. This resonance may be due to evanescent radiation modes, which have been ignored in our calculation. It is also possible that this resonance arises because the nanopatch antennas are not ideal point dipoles, and so this resonance may be a phenomenon of the details of the geometry. Whatever the cause of the additional resonance may be, it appears from fig. 5.3(a)-fig. 5.3(d) that the approaching additional resonance slightly shifts the resonance frequency of the fundamental Wood's anomaly at around 500nm in fig. 5.3(d).

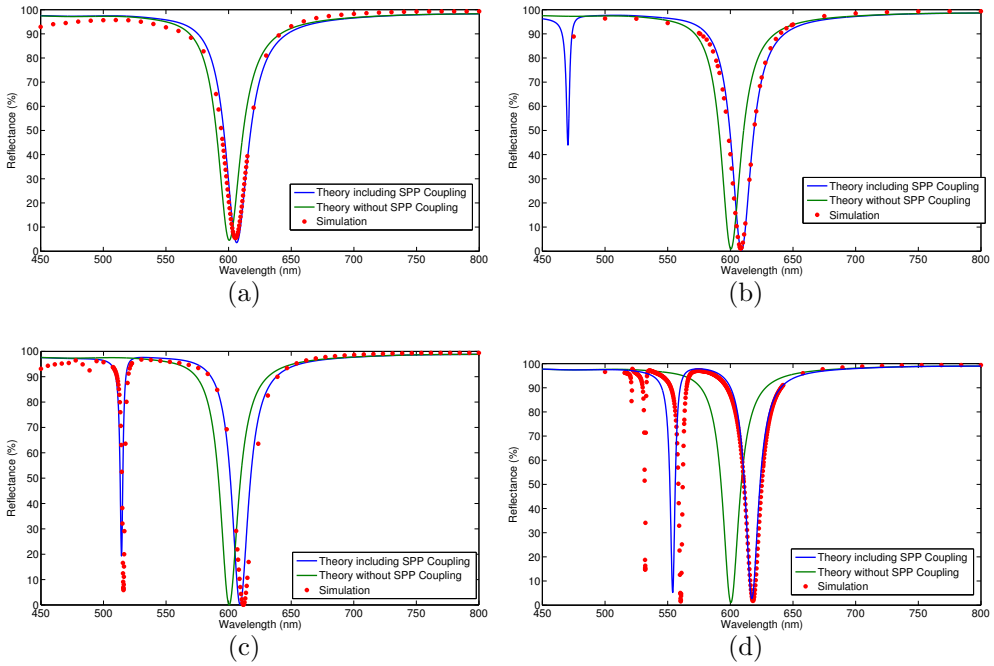

FIGURE 5.3: Comparison of reflection coefficient including surface plasmon coupling (blue line) and excluding surface plasmon coupling (green line) with full-wave simulation results (dots) for nanopatches with a pitch of (a) 400nm, (b) 450nm, (c) 500nm, and (d) 550nm.

Returning to eq. (2.10), we note that the imaginary part of the interaction constant of the lattice is a measure of the loss rate of each magnetic dipole to surface plasmons. Every dipole in the lattice may be thought of as emitting surface plasmons into the metal film at a certain rate, which is proportional to the radiation reaction force due to the surface plasmon coupling, or C^{0D}, in eq. (5.8). The surface plasmons are then either re-absorbed by another dipole, which is proportional to the sum $C^{1D}+C^{2D}$, or dissipate into Ohmic losses. The imaginary part of the interaction constant given in eq. (5.29), which is due to the surface plasmon interaction between the dipoles, is therefore a measure of the loss rate of any particular dipole in the lattice to surface plasmons, minus the reabsorption rate. The imaginary part of C is then the overall rate of loss of the lattice to surface plasmons that are eventually dissipated in Ohmic losses rather than reabsorbed by the dipoles in the lattice, which

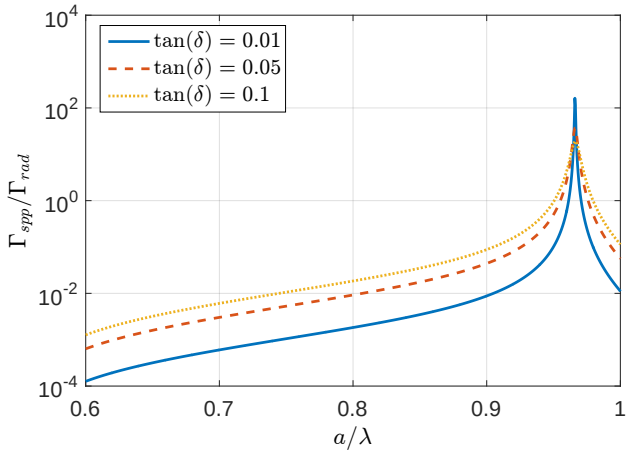

FIGURE 5.4: Ratio of the losses of the metasurface to surface plasmons relative to the radiative loss rate, when coupled to a metal film with $\epsilon = -15(1 + i\delta)$. The metasurface is assumed to be placed infinitely close to the metal film (i.e. $d = 0$).

we refer to as the Ohmic loss rate due to surface plasmons, or

$$\Gamma_{spp} = \omega_0/Q_{spp} = \omega_0 A \mathrm{Im}\{C\}. \tag{5.35}$$

The constant A is the amplitude of the dipole's Lorentzian response, as in eq. (2.8). We compare the Ohmic loss rate to surface plasmons with the radiative loss rate of the dipoles, which was found in [28] to be

$$\Gamma_{rad} = \omega_0/Q_{rad} = \omega_0 A \frac{2k|1 - r_{TM}|^2}{a^2} \tag{5.36}$$

for a periodic metasurface of dipoles coupled to a metal film with lattice constant a. The ratio $\Gamma_{spp}/\Gamma_{rad}$ is plotted in fig. 5.4 as a function of the lattice constant for fixed wavelength, for a metal film with $\epsilon = -15(1 + i\delta)$, where δ is the loss tangent. Surprisingly, the surface plasmon losses are below or on the order of a few percent of the total loss rate, until it approaches the Wood's anomaly at $a/\lambda = k/\beta \approx 0.97$. At that point, the losses are by far dominated by the surface plasmon losses since the field becomes dominated by standing waves between the dipoles.

6

Wood's Anomalies in Film-Coupled Optical Nanopatch Antenna Arrays

6.1 Introduction to Wood's Anomalies

Wood's anomalies are sudden changes in the amplitude of diffracted orders of any periodic optical system, and they have been a subject of experimental, computational, and analytical study for decades. In this chapter I present a novel approach based on effective medium theory to understanding and analytically predicting Wood's anomalies and scattering spectra in optical, metallic gratings, and we compare this theory with experimental and computational results. The theory was developed by myself, while the full-wave simulations were performed by Zhiqin Huang. The experiments were performed by my collaborators Xiaomeng Jia, Chris Bingham, and Xiaojun Liu.

As a test geometry, we choose to base our study on a metasurface consisting of a periodic array of film-coupled plasmonic nanopatch particles, which is a platform that is of interest for many practical applications. It has already been shown that the film-coupled nanopatch can exhibit a "perfectly absorbing" resonance in the

reflectance spectrum at a wavelength determined by the nanopatch geometry, and this resonance is insensitive to the incident angle. However, a second sharp absorption dip is present in the spectra that varies strongly as a function of incidence angle, and there are additional very sharp features in the spectrum at the Rayleigh wavelengths. Using an approach based on effective medium theory, we are able to not only predict the reflection and scattering spectra, but we are also able to compute the surface modes of the structure and show how the resonant anomaly corresponds to a surface mode, and that the sharp anomaly corresponds to a change in radiation Q due to the addition or subtraction of propagating diffraction orders. The reflectance spectra are in excellent agreement with both analytical calculations and full-wave numerical simulations.

Periodic systems are well known to exhibit a wide array of interesting and sometimes useful phenomena, particularly in the realm of wave physics. One, two, and three dimensional periodic structures can all be analyzed in terms of Bloch modes, which could be categorized as bulk modes of an unbounded crystal, or surface modes of a bounded crystal. Bulk modes of unbounded crystals can be used to create photonic or electronic band-gap structures, while surface modes can be used to create topologically protected states.

When it comes to conducting or semiconducting periodic structures in the optical region of the spectrum, the physics of periodicity is now very strongly coupled to light due to the presence of induction currents in the metal that can be excited by the incident electric field. Depending on the geometry, the restoring force imposed by the polarization of the nanoparticle can lead to a plasmon resonance, in which the polarization response is resonantly enhanced, leading to large scattering cross sections as well as large locally enhanced optical fields. The wavelengths where plasmonic resonances occur relate not only to the nanoparticle geometry, but also to the dielectric function of the plasmonic material. Thus, the resonances of the individual

plasmonic structures that compose the periodic system can occur for wavelengths of light that are much larger than the size of the structure. On their own, plasmon resonant nanoparticles have become a potentially important tool for nanophotonic applications because of their ability to enhance light and other optical processes.

Returning to periodic systems, one of the older known phenomena related to the surface modes of two-dimensional, metallic, optical periodic systems is Wood's anomalies. These are sudden changes in the scattering spectrum of reflected or diffracted light from periodic, metallic gratings, which have been a subject of intense study for decades. A brief history and description of Wood's anomalies is presented in section 6.2. In this chapter, we are considering a novel description of the theory of Wood's anomalies from an effective medium perspective, and presenting measurements of the reflection spectra of a grating made of a periodic array of plasmon resonant nanoparticles.

The system under examination in this paper is a periodic arrangement of gold nanopatched antennas placed over a gold film, and separated from it by a small gap. This structure could be thought of as a kind grating with a period equal to the distance between the nanoparticles. We solve the problem of reflection and diffraction from this grating by first performing a multipole expansion of the scattered fields from each period of the structure. Using coupled-mode theory analysis[28, 3], it can be shown that each of the individual nanopatch antennas scatters as a magnetic dipole, and hence all the higher order multipoles may, to a good approximation, be neglected. The magnetic dipole type of scattering from each nanopatch antenna not only scatters in the farfield via radiation modes, but also scatters into propagating surface plasmons, which cause the nanopatch antennas to couple to each other. A careful calculation, based on effective medium theory techniques, has been used to show that the mutual coupling between the nanopatches is the physical mechanism behind additional resonances in the spectrum, or Wood's anomalies[92]. Here we

extend that calculation to provide a more rigorous derivation of the radiation loss rate of the structure, present an experimental demonstration of this system, and compare reflection measurements with explicit analytic expressions based on the effective medium theory approach presented in Ref. [92]. We also present an extension of the coupled-mode theory of the optical nanopatch antenna and the effective medium theory framework to take into account the dielectric constant of the spacer layer, and include the modification of the radiation losses when the spacing of the dipoles is large enough to allow for multiple diffraction orders.

This chapter is moreover concluded with an experiment where a periodic array of gold optical nanopatch antennas was fabricated lithographically on top of a gold film, separated by an aluminum oxide layer that serves as the dielectric gap. The reflectance of the film was measured as a function of incidence angle for TM-polarization, and compared with theoretical and simulation results in **??**.

6.2 Historical Context of Wood's Anomalies

In 1902, Wood published a famous paper[4] where he experimentally observed sudden changes in the amplitude of the diffracted orders from a diffraction grating. The initial explanation for these anomalies was done by Rayleigh[6, 5], where he identified specific wavelengths where the Wood's phenomena are expected to occur. These wavelengths were found by calculating the field scattered by the grating as an expansion of outgoing waves, and noting that there is a singularity in the amplitude of the scattered field precisely at the Rayleigh wavelengths, λ_R, which are given by the grating formula

$$n\lambda_R/d = \sin(\theta) \pm 1 \tag{6.1}$$

Later, Fano pointed out that Wood's anomalies could be distinguished into two distinct anomalies.[93] The first is a "sharp" anomaly that occurs exactly at the

Rayleigh wavelengths, is characterized by a sudden, discontinuous change in intensity of the refracted light from a grating. These he explained as originating from the introduction or removal of a diffracted order from the scattering spectrum. The second is a "diffuse" anomaly which is a smoother change in intensity of the diffracted beam, which Fano described as beginning at the sharp anomaly and extending for a wide interval towards the red. Fano pointed out that only the sharp anomalies occur at the Rayleigh wavelengths, and he explained the diffuse anomalies as a resonance of a surface mode. Following in the footsteps of Lord Rayleigh[5], Fano treated the grating as a perturbation of the problem of light reflecting off of a flat metal surface, by expanding the field as a sum of plane waves with amplitude coefficients that go as orders of the depths of the grooves. However, Fano further recognized that a flat metal surface supports surface plasmon waves (although that term was not in use at the time) and that the surface modes of the grating were a perturbation of surface plasmon modes due to the grooves. Fano therfore explained the location and lineshape of the diffuse anomalies as the complex propagation constant of the surface mode of the geometry.

Although Fano's formalism was phenomenologically correct, the theory was not rigorous enough to be predictably useful. Others have presented equivalent surface impedance models of gratings[94], which likewise explain the diffuse anomaly in terms of surface modes of the periodically varying surface impedance structure. However, these models are only able to phenomenologically produce the same results as the grating but have no predictive power, since there is no way to predict the equivalent surface impedance.

Throughout the 1970s there was a large body of numerical-integral computational codes produced to predict Wood's anomalies, and the most central issue of this literature was on the question of whether or not the metal could be considered as a perfect conductor[95, 96, 97]. It was eventually shown that the finite conductivity

and negative permittivity of the metal was an indispensable part of any predictive numerical model, particularly for metallic gratings in the infrared and visible parts of the spectrum.[98]

More recently, analytical works by Maradudin et al.[99] have focused on Wood's anomalies in perfectly conducting gratings with square grooves, and shown that they can be explained by a surface mode of the grating structure. The results can accurately predict numerical simulation results of the same structure, but it is not clear whether these results can be applied to optical gratings since the grating is assumed to be a perfect conductor.

The approach presented in this chapter is a purely analytical method to solving for both the surface modes and the reflectance and diffraction spectra of gratings where the scattered field from the elements of the grating can be accurately approximated as fields from dipoles. One such structure is the plasmonic patch antenna[28], and other structures might be considered under the same formalism, or else by including higher order multipoles in the same fashion. The approach is novel in that the formalism follows the methods of effective medium theory in deriving the effective polarizability of the elements as a function of both frequency and wavevector by computing the total field exerted on each element of the structure as the sum of the incident wave plus the fields due to all the other elements in the lattice.

6.3 Theory

Our starting point is the polarizability of a single optical nanopatch antenna, which was developed in chapter 4. Assuming that the nanopatch is much smaller than the wavelength, the polarizability has the simple form,

$$\alpha(\omega) = \frac{8hc^2/\epsilon_g}{\tilde{\omega_1}^2 - \omega^2} \tag{6.2}$$

where it is also assumed that the mode amplitude is dominated by the fundamental mode, i.e. $\mu = 1$, with $\tilde{\omega}_1 = \omega_1(1 - i/2Q)$ being its complex resonance frequency. We have also modified eq. (6.2) from the form presented in chapter 4 and **??** in order to take into account the dielectric constant ϵ_g of the material in the gap.

The Q-factor is given by an Ohmic loss contribution Q^Ω and a radiative loss contribution Q^r, such that $1/Q = 1/Q^r + 1/Q^\Omega$. The Ohmic Q-factor is calculated using a perturbation theory in chapter 3 and is given by

$$1/Q^\Omega = \frac{W^2 \mathrm{Re}\{-ik_{x1}\sin(k_{x1}h/2)\}}{\pi^2 h} \tag{6.3}$$

Ultimately, radiation Q is a phenomena of the radiation reaction force, and it can be shown using either the radiation reaction force or conservation of energy that the radiation Q of a single magnetic dipole (with a Lorentzian response as given in eq. (6.2)) placed parallel to a metal film must be $Q^r_{dip} = 3\pi\epsilon_g\omega_1^2/16kh\omega^2$.[92]

However, when a metasurface of magnetic dipoles is created, the radiation Q of the metasurface is modified because the dipoles exert forces on one another through their scattered fields that counteract the radiation reaction force that corresponds to radiation losses of a single dipole, and replaces it with another force that corresponds to the overall radiation losses of the metasurface. For metasurfaces in free space, these scattered fields take the form of a free-space Green's function, which can be used to predict the radiation losses through the overall radiation reaction forces. When a metasurface is placed closed to a metal film, the Green's function is modified, and may be decomposed as the sum of the bound surface plasmon mode and radiation modes. In this case, the modification of the radiation Q will come from the radiation modes contribution to the Green's function. In this paper, instead of directly calculating the contribution of the radiation modes to the radiation reaction force, we take into account the modification of the radiation Q using a conservation of energy argument. The radiative Q was calculated in [28] for a periodic array of

film-coupled magnetic dipoles under a similar argument, but under the assumption that the dipoles were separated less than half a free space wavelength apart. Here we extend that calculation to allow for any lattice constant.

The radiative Q for any particular nanopatch antenna in the array can be written in terms of the final power radiated by any particular nanopatch p_r as[14, 28]

$$Q^r_{array} = \frac{\omega U_\mu |e_1|^2}{p_r}. \tag{6.4}$$

The power radiated by each patch is simply the time-averaged Poynting vector radiated by the surface times the area taken up by a period of the structure, i.e. $p_r = a_x a_y \mathrm{Re}\{\langle \mathbf{S} \cdot \hat{\mathbf{z}} \rangle_t\}$. The total radiated power from the metasurface is calculated in appendix C, and the final result can be written as

$$\begin{aligned}\langle \mathbf{S} \cdot \hat{\mathbf{z}} \rangle_t = \frac{Z_0 k |m|^2}{8 a_x^2 a_y^2} \sum_{\mu,\nu} \left(k^2 - (G^z_{\mu\nu})^2\right)^{-1} \Bigg[& G^z_{\mu\nu} (G^y_{\mu\nu})^4 |1 - r_{TE}(G^z_{\mu\nu})|^2 + \frac{k^2}{G^{z*}_{\mu\nu}} (G^x_{\mu\nu})^4 |1 - r_{TM}(G^z_{\mu\nu})|^2 \\ & + \frac{k^2}{G^{z*}_{\mu\nu}} (G^x_{\mu\nu})^2 (G^y_{\mu\nu})^2 \left(1 - r_{TE}(G^z_{\mu\nu})\right) \left(1 - r_{TM}(G^z_{\mu\nu})\right)^* \\ & + G^z_{\mu\nu} (G^x_{\mu\nu})^2 (G^y_{\mu\nu})^2 \left(1 - r_{TE}(G^z_{\mu\nu})\right)^* \left(1 - r_{TM}(G^z_{\mu\nu})\right) \Bigg].\end{aligned} \tag{6.5}$$

where the wavenumbers of each diffracted beam are given by

$$G^x_{\mu\nu} = 2\pi\nu/a_x - k_x \tag{6.6a}$$

$$G^y_{\mu\nu} = 2\pi\mu/a_y - k_y \tag{6.6b}$$

$$G^z_{\mu\nu} = \sqrt{k^2 - (G^x_{\mu\nu})^2 - (G^y_{\mu\nu})^2}. \tag{6.6c}$$

We simplify this expression by defining

$$L_{\mu\nu} = \left(k^2 - (G^z_{\mu\nu})^2\right)^{-1} \Bigg[G^z_{\mu\nu}(G^y_{\mu\nu})^4 |1 - r_{TE}(G^z_{\mu\nu})|^2 + \frac{k^2}{G^{z*}_{\mu\nu}}(G^x_{\mu\nu})^4 |1 - r_{TM}(G^z_{\mu\nu})|^2 + \frac{k^2}{G^{z*}_{\mu\nu}}(G^x_{\mu\nu})^2 (G^y_{\mu\nu})^2 \left(1 - r_{TE}(G^z_{\mu\nu})\right) \left(1 - r_{TM}(G^z_{\mu\nu})\right)^* + G^z_{\mu\nu}(G^x_{\mu\nu})^2 (G^y_{\mu\nu})^2 \left(1 - r_{TE}(G^z_{\mu\nu})\right)^* \left(1 - r_{TM}(G^z_{\mu\nu})\right) \Bigg]. \tag{6.7}$$

so that the Poynting vector can be written as

$$\langle \mathbf{S} \cdot \hat{\mathbf{z}} \rangle_t = \frac{Z_0 k |m|^2}{8a^4} \sum_{\mu\nu} L_{\mu\nu}. \tag{6.8}$$

The final relationship that is required in order to compute the radiation Q is the relationship between the dipole moment of the nanopatch and the mode amplitude, which was found to be $|e_\mu|^2 = (Z_0 k / hW\tilde{E})^2 |m|^2$. Using this relationship together with eqs. (6.4), (6.7) and (6.8) yields

$$Q^r_{array} = \frac{\epsilon_g a_x a_y k^2}{2h} \left(\mathrm{Re} \left\{ \sum_{\mu,\nu} L_{\mu\nu} \right\} \right)^{-1}. \tag{6.9}$$

The radiation Q in eq. (6.9) immediately explains the origin of the *sharp* Wood's anomaly. This can be seen by noting that every term in $L_{\mu\nu}$ contains a factor of either $G^z_{\mu\nu}$ or $(G^z_{\mu\nu})^{-1}$. Hence, when an additional diffraction mode is introduced or removed, it's propagation constant in the z-direction changes from imaginary to real or else vice-versa, and hence alters the radiation Q of the structure.

The diffuse anomaly, on the other hand, is due to surface modes of the structure. We treat these here by applying effective medium theory techniques to distinguish between the *intrinsic polarizability* and *effective polarizability* of the effective dipole

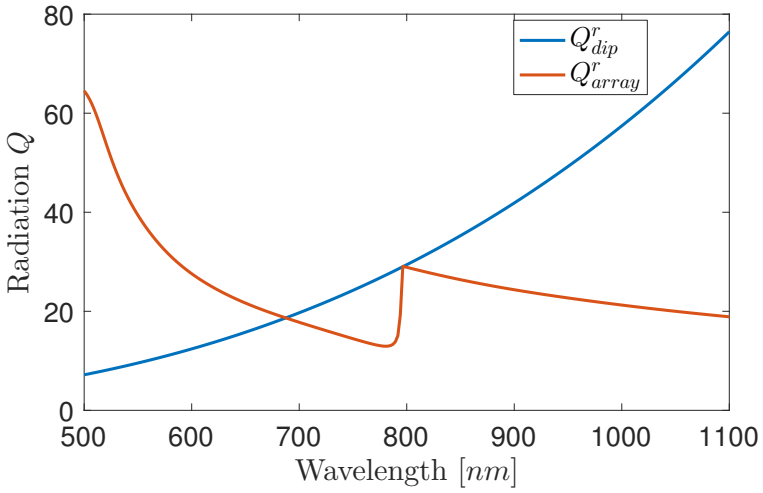

FIGURE 6.1: Analytically computed radiative Q for the fabricated nanopatches, in both isolation (blue) where $Q^r_{dip} = 3\pi\epsilon_g\omega_1^2/16kh\omega^2$, and in the context of an array (red), where Q^r_{array} is given by eq. (6.9).

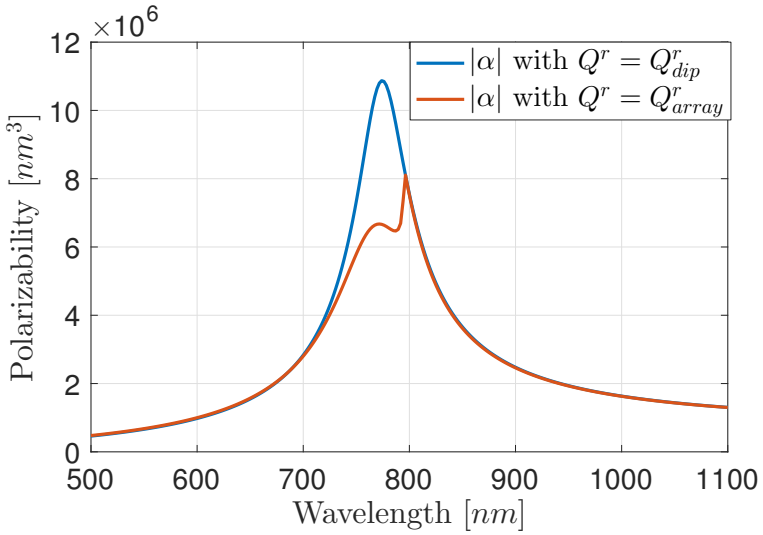

FIGURE 6.2: Analytically computed polarizability of the fabricated nanopatch geometry, according to eq. (6.2). The gap size is $h = 13nm$, the width of the nanopatch is $W = 100nm$, the dielectric constant of the gap material is taken to be $\epsilon_g = 2.37$, and the dielectric properties of silver are taken from Johnson and Christy. The period of the array, for the calculation of the radiation Q, is $a = 450nm$

moments of the elements. The polarizability presented in eq. (6.2) is the intrinsic polarizability of the dipole, which is the polarizability it has when the coupling to all other dipoles in the surface are ignored. The effective polarizability, on the other hand, is the dipole moment induced in each nanopatch antenna of the structure including all the coupling between the elements. In order to take into account this coupling, we formulate the *effective polarizability*, by writing down the total field incident upon the i^{th} dipole, as the sum of fields due to all the other dipoles in the system:

$$\mathbf{H}(\mathbf{r}_i) = \alpha^{-1}\mathbf{m}_i = \mathbf{H}_0(\mathbf{r}_i) + \sum_{j\neq i} \mathbf{G}(\mathbf{r}_j - \mathbf{r}_i)\mathbf{m}_j. \tag{6.10}$$

The Green's function here has been reduced to a function of a single argument of the distance between dipoles, which can be done when the dipoles are placed in free space. If the incident magnetic field varies as a plane wave according to $\mathbf{H}_0(\mathbf{r}_i) = \mathbf{H}_0 e^{-i\mathbf{k}\cdot\mathbf{r}_i}$, then the magnetic dipole moments must also satisfy $m_j = m_i e^{-i\mathbf{k}\cdot(\mathbf{r}_j - \mathbf{r}_i)}$ by conservation of transverse momentum. All of the $\mathbf{m}_j$ terms may then be collected to give

$$\left(\alpha^{-1} - \sum_{j\neq i} \mathbf{G}(\mathbf{r}_j - \mathbf{r}_i)e^{-i\mathbf{k}\cdot\mathbf{r}_j}\right)\mathbf{m}_i = \mathbf{H}_0 \tag{6.11}$$

The quantity in parentheses becomes the new effective polarizability α_{eff}, and the infinite sum over the Green's function is typically defined as the interaction constant[14, 25, 27, 92]

$$\mathbf{C}(\omega, \mathbf{k}) = \sum_j \mathbf{G}(\mathbf{r}_j - \mathbf{r}_i)e^{-i\mathbf{k}\cdot\mathbf{r}_j}. \tag{6.12}$$

. In the case of a square lattice the interaction constant is isotropic, and thus we have that

$$\alpha_{eff}(\omega, \mathbf{k}) = \frac{\alpha(\omega)}{1 - C(\omega, \mathbf{k})\alpha(\omega)} \tag{6.13}$$

is the effective polarizability of any square lattice of dipoles when excited by a plane wave of frequency ω and wavevector $\mathbf{k}$. This interaction constant has been worked out explicity in [92] under the assumption that the dipoles are placed close enough to the metal film that the Green's function is dominated by the surface plasmon mode. The work in [92] also assumed that there was no dielectric material in the gap between the metal film and the nanopatches, which needs to be taken into account in any practical experiment. Following the general coupled mode theory formalism in [92], but generalizing it to include the dielectric material with ϵ_g in the gap, we obtain

$$C(\omega,\mathbf{k}) = \frac{-Z^2(z)k^2\epsilon^2(z)}{2\beta^3}\left[\frac{i\beta^3}{4} + i\beta^3\sum_{\nu=1}^{\infty}\frac{H_1^{(2)}(\beta|\nu|a_y)}{\beta|\nu|a_y}\cos(k_y\nu a_y)\right.$$
$$\left. + \frac{i2\beta}{a_y}\sum_{\mu=-\infty}^{\infty'}\sum_{\nu=1}^{\infty}\Gamma_\mu e^{-i\nu\Gamma_\mu a_x}\cos(k_x\nu a_x)\right]. \qquad (6.14)$$

Returning back to eq. (6.13), it is clear that there will be a singularity in the effective polarizability when $C(\omega,\mathbf{k})\alpha(\omega) = 1$, which implies that a surface mode exists at the set of frequencies and wavenumbers which satisfy this equation. Indeed, looking at eq. (6.11), it is clear that when the incident field $\mathbf{H}_0$ is set to zero there may exist source-free or eigensolutions to eq. (6.11) when $C(\omega_s,\mathbf{k})\alpha(\omega_s) = 1$. The solutions to this equation therefore trace out a curve of complex valued resonance frequencies $\omega_s(\mathbf{k})$ that depend on the wavenumber $\mathbf{k}$ in the plane of the lattice.

The intrinsic polarizability $\alpha(\omega)$ of the nanopatches is plotted in fig. 6.2, while the interaction constant $C(\omega,\mathbf{k})$ is shown in figs. 6.3 and 6.4. The interaction constant shows a single clear resonance for each angle of incidence, and this resonance was shown in [92] to occur at $\beta = \sqrt{(2\pi\nu/a_x - k_x)^2 + (2\pi\mu/a_y - k_y)^2}$, where β is the propagation constant of the surface plasmon. When operating under TM incidence along the main axes of the crystal, we have that $k_y = 0$ and $k_x = k\sin(\theta)$. Hence the fundamental resonance occurs when $\beta = 2\pi/a_x - k\sin(\theta)$, which a condition that

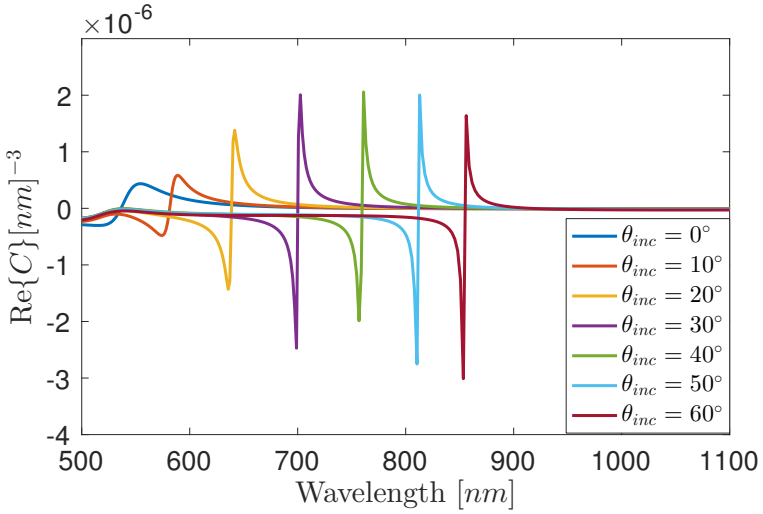

FIGURE 6.3: Real part of the interaction constant $C(\omega, \mathbf{k})$ for different values of θ, for $a = 450nm$.

is similar to the Rayleigh equation but with the surface plasmon wavelength used instead of the free-space wavelength.

It is clear that if the eigenmode equation $C(\omega_s, \mathbf{k})\alpha(\omega_s) = 1$ is to be satisfied, the interaction constant must be on the same order of magnitude as the inverse of the polarizability. When the polarizability is small, as it is for the nanopatches, then

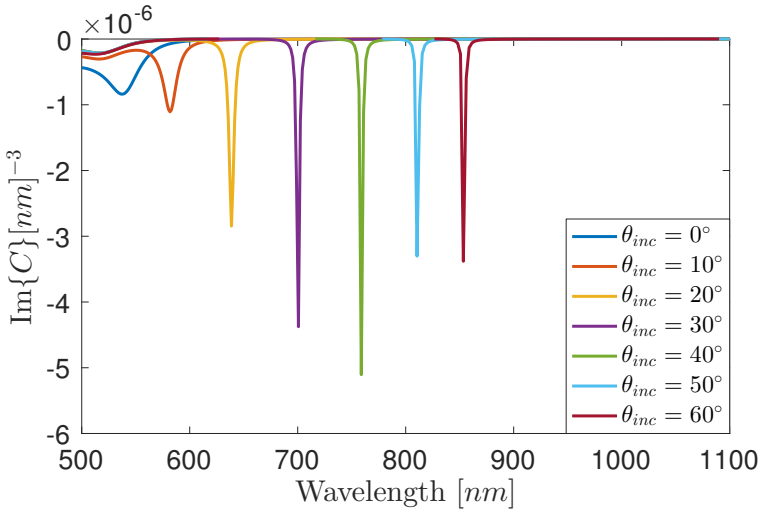

FIGURE 6.4: Real part of the interaction constant $C(\omega, \mathbf{k})$ for different values of θ, for $a = 450nm$.

this will occur approximately at the resonances of the interaction constant, i.e. when $\beta = 2\pi/a_x - k\sin(\theta)$. When the polarizability is large then this may occur at a slightly different wavelength, in accordance with the eigenmode equation. Therefore we can expect that the diffuse anomaly will not follow $\beta = 2\pi/a_x - k\sin(\theta)$ and instead be shifted in frequency when the diffuse anomaly approaches the resonance frequency of the intrinsic polarizability of the dipoles.

Once the effective polarizability is calculated via eq. (6.13), the total reflection coefficient of the film is given by[3, 92]

$$r = r_{TM} + \frac{-ik(1 - r_{TM})^2}{2a^2\cos(\theta)}\alpha_{eff} \tag{6.15}$$

where r_{TM} is the fresnel reflection coefficient of the metal film under TM polarization. We use eq. (6.15) together with the predictions of both the sharp and diffuse anomalies discussed above with experimental measurements of the reflection spectra of the structure. The sharp anomaly can be clearly seen at the Raleigh wavelength λ_r, while the diffuse anomaly occurs at $\lambda_s = 2\pi c/\omega_s$. We note that these results are purely analytic and contain no fit parameters.

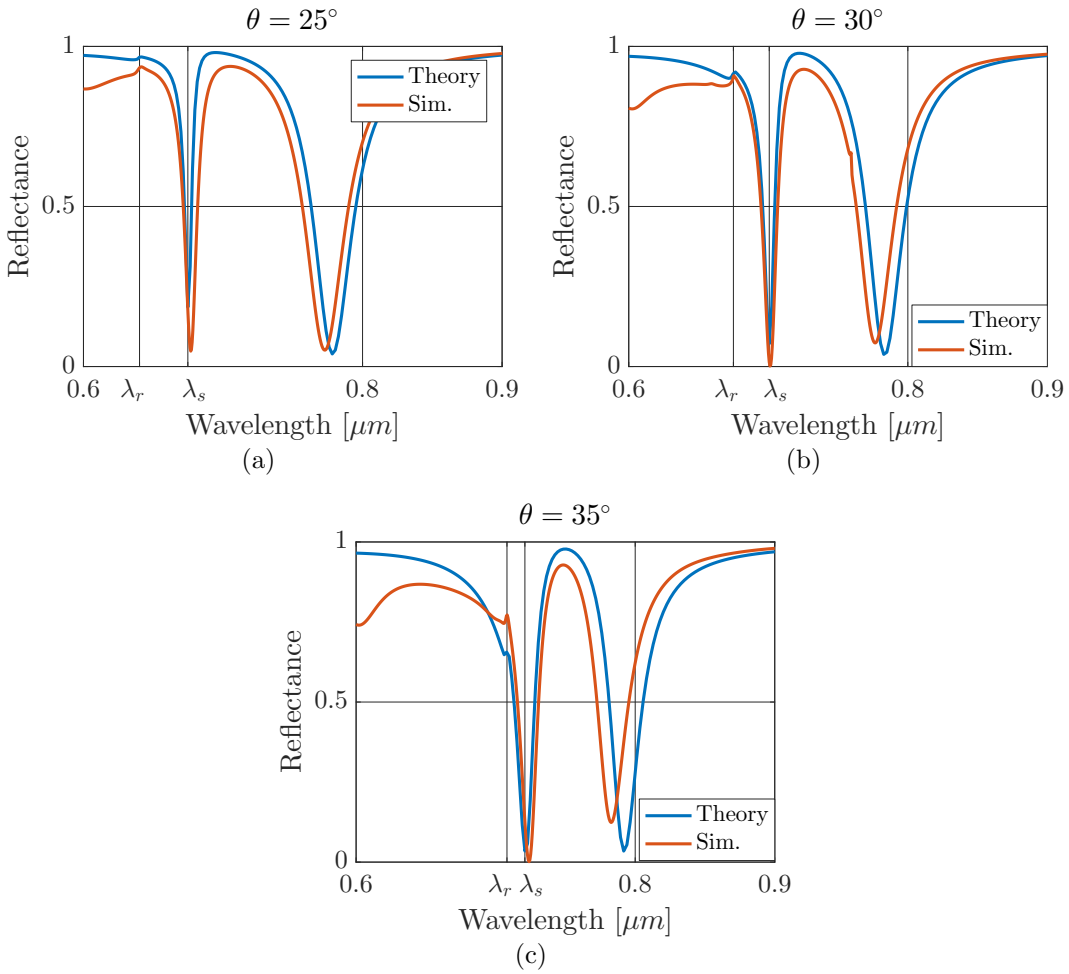

FIGURE 6.5: Calculated reflectance spectra of a gold film-coupled nanopatch array with $a = 450nm, W = 100nm, h = 13nm$, and $\epsilon_g = 2.37$ using the analytic theory and compared with full wave simulations for different incidence angles.

6.4 Experiment

6.4.1 Sample Fabrication and Characterization

For experimental verification, a sample of film-coupled periodic nano patch arrays (PNPA) was fabricated. First, on the top of a commercial template-stripped gold film with a thickness of $50nm$, a $13nm$ thick Al_2O_3 ALD layer was deposited on a Plasma-Enhanced Atomic Layer Deposition (PE-ALD) System. On the top of the ALD layer, a photo resist PMMA A2 950k was spin-coated to reach a thickness

of $120nm$ and baked at 180 °C for 2 minutes. Then arrays of nano patches were patterned using electron-beam lithography (EBL) at $50kV$ on an Elionix ELS-7500 EX E-Beam Lithography System. After the EBL exposure, the exposed photo resist was developed in a mixture of MIBK and IPA with a volume ratio of $1:3$ for $70s$ and thoroughly rinsed with IPA, thus forming a resist mask with nano patch patterns. Subsequently, a $50nm$ thick gold layer was deposited on the resist mask using a CHA Solution electron beam (E-Beam) evaporator at the rate of $2\mathring{A}/s$. Eventually, the remaining photo resist was lifted off with acetone for 30 minutes and thoroughly rinsed with IPA.

Fig.2 shows the scanning electron microscopic (SEM) top-view image and atomic force microscopy (AFM) image of the fabricated patterns. The side length of the patches is $100nm$ as estimated from SEM and the thickness is about $50nm$ with a surface roughness of $2nm$ as measured in AFM.

6.4.2 Optical Measurement

The light source used in the system is a tungsten-halogen lamp with an effective blackbody temperature of 2796 K providing a spectral range of 360 to 2,600 nm. The light source is directly coupled into a fiber optic cable with a core diameter of $400\mu m$ and a numerical aperture (NA) of 0.39. The light is focused onto a $500\mu m$ pinhole using an achromatic doublet lens to create a spatial filter and provide a cleaner beam profile. The light passes through a second achromatic doublet lens and a polarizer before coming to focus 21 mm after passing through the lens onto the metsurface sample. The sample rotation stage was coaxially aligned with a second rotation stage with the axis of rotation is aligned such that it is located on the surface of the sample. The second rotation stage controls the position of the fiber optic cable (core diameter $400\mu m$ and NA 0.39) used to gather the light from the sample and send it to a connected Czerny-Turner style spectrometer. The spectrometer covers

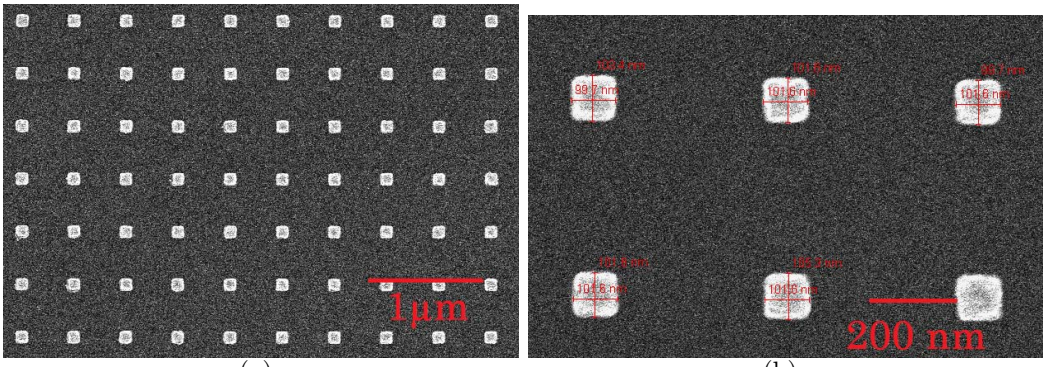

(a) (b)

FIGURE 6.6: Characterizations of the PNPA sample. (a) Top view of SEM image; (b) AFM image

a wavelength range from 500 to 1,000 nm and has a full width half max (FWHM) accuracy of 0.6 nm at 633 nm. Ray tracing of the optical system was performed to maximize the light throughput while minimizing the deviation from the intended angle of the light incident on the metasurface. The change in beam diameter between sample and fiber detector as well as the distance between them was measured in the ray tracing model and the calculated value for the deviation from the intended angle was a range of +/- 0.5986 degrees.

6.5 Results and Discussion

The measured reflectance spectra are plotted together with the theoretical reflectance and reflectance from full-wave simulations in fig. 6.7. There is good agreement between all three, although the main resonance is clearly shallower and slightly broader at small angles of incidence. We attribute this to inhomogeneous broadening since not all of the nanopatches will have the same size or radius of curvature on the corners, which slightly shifts their resonance frequencies. The diffuse anomaly is clearly seen at all angles of incidence, and the location of the diffuse anomaly agrees for all angles, although the analytic prediction of the depth of the diffuse anomaly becomes much worse at high angles. The sharp anomaly on the other hand is difficult

to observe experimentally, but a good example of it is in the reflectance plot at 35 degrees.

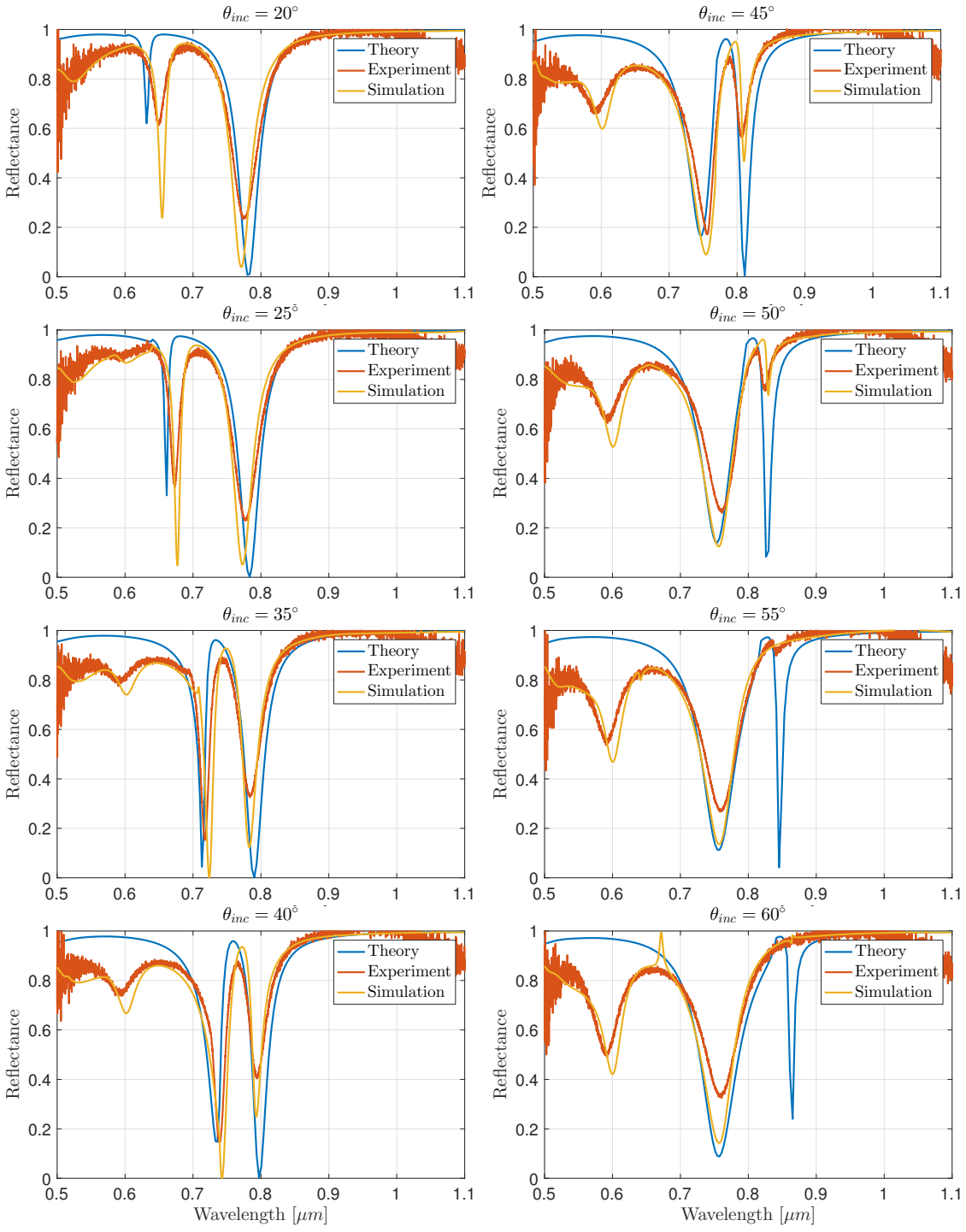

FIGURE 6.7: Comparison of theoretical and experimental results for various incident angles.

7

Optical Bistability in Film-Coupled Metasurfaces

Optical bistable systems are able to present two different output powers depending on the intensity of the incident beam and the hysterisis of the excitation, and is a commonly proposed mechanism for realizing all-optical logic elements such as switches, modulators or memories for all-optical computing and communication.[100] Optical bistability is normaly present in a system consisting of an electromagnetic resonator cavity filled with a nonlinear optical material with a large third order susceptibilty, such that the index of refraction is intensity-dependent. However, in most accessible materials, these nonlinear optical effects are either too weak or slow in order to observe significant responses. However, these nonlinear optical effects can be enhanced by long interaction lengths or electric field enhancements in strong cavity resonances.[101][102]

One of the most interesting optical logic elements is the optical switch. As is widely recognized, there are several critical requirements for on-chip all-optical switches, such as small device footprints, a low energy consumption and a high operating speed with a big switching contrast. Avoiding the systematic conversion into and out of electrical signals, the performance of optical switches on footprints and en-

ergy consumption can be vastly superior than their electrical counterparts.[103][104] Moreover, optical switches can operate at a relatively high speed relative to electronic switches.

The current available all-optical switching technologies for practical chip-integrated applications are silicon photonics, high-index contrast waveguides, single photons, photonic crystals, and plasmonics.[105][106] It was pointed that the energy consumption for various photonic devices is linearly proportional to the ratio of $\omega V/Q$, where ω means the frequency of light and Q is the quality factor of the cavity, while V is the effective mode volume.[107] Of particular interest, for photonic crystals, the extremely high Q, which is on the order of several millions, makes as low as the femto-Joule level of power consumption.[104] On the other hand, the ultrahigh Q of photonic crystals leads to a relatively low switching speed, except for the intrinsic wavelength-size footprints. A recent study using GaAs-based photonic crystals by passivating with Al_2O_3 can realize optical switching at 100 fj energy consumption with 10 ps time resolution and a switching contrast of 7 dB.[108]

Another alternative way to reduce the switching energy is to reduce the mode volume. Plamonic structures are well-knwon to be able to confine light into resonators with very mode volumes, and therefore much effort has been devoted to develop plasmonic optical switches. One particular example is a plasmonic nanocomposite switch, which was able to reach a sub-femtoJoule energy consumption[109]. It would be advantageous to introduce the film-coupled nanocube metasurface, whose significantly enhanced field have been utilized to investigate various optical phenomena such as perfect absorption, photoluminescence, Purcell effect as well as optical bistability.[29][110][39][111] Compared to the well-developed theories such as coupled-mode theory(CMT), perturbation theories for photonic crystals and discrete dipole approximation(DDA) for some other platforms [104][112][113], the theoretical study especially the nonlinear part on the film-coupled nanocube system is still in its pre-

liminary stage.[28][3][92].

This chapter presents an analytical treatment of optical bistability in periodic arrays of plasmonic patch antennas by expanding the field in the gap as a sum of eigenmodes as was done in [28], and taking into account the surface plasmon coupling between them using the interaction constants as was done in [92]. All the the theory was done by myself, and the full-wave simulations were performed by Zhiqin Huang.

The electric field in the gap is expanded into a set of modes in the form

$$\mathbf{E}(\omega, \mathbf{r}) = \sum_{\mu} e_{\mu}(\omega)\mathbf{E}_{\mu}(\mathbf{r}) \tag{7.1}$$

where the (dimensionless) amplitudes of the modes follow

$$e_{\mu}(\omega) = \frac{-i\omega \int \mathbf{J} \cdot \mathbf{E}_{\mu}^{*} dV / U_{\mu}}{\tilde{\omega}_{\mu}^{2} - \omega^{2}} \tag{7.2}$$

In this expression, $U_{\mu} = \int \epsilon |\mathbf{E}_{\mu}|^{2} dV$ is the mode volume, and $\tilde{\omega}_{\mu} = \omega_{\mu}(1 - i/2Q)$ is the complex resonance frequency of the μ^{th} mode of the film-coupled nanopatch system. In ref. [28], it was shown that the resonance frequency ω_{μ}, and the two wavenumbers describing the transverse profile of the cavity mode $k_{x\mu}$ and κ_{μ} are given by simultaneously solving the set of three nonlinear equations,

$$\tan\left(\frac{k_{x\mu}h}{2}\right) + \frac{j\kappa_{\mu}}{k_{x\mu}\mathrm{Re}\{\epsilon(\omega_{\mu})\}} = 0 \tag{7.3a}$$

$$\left(\frac{\mu\pi}{W}\right)^{2} + k_{x\mu}^{2} = \frac{\omega_{\mu}^{2}}{c^{2}} \tag{7.3b}$$

$$\left(\frac{\mu\pi}{W}\right)^{2} - \kappa_{\mu}^{2} = \mathrm{Re}\{\epsilon(\omega_{\mu})\}\frac{\omega_{\mu}^{2}}{c^{2}}. \tag{7.3c}$$

We have modified equations (7.3) from those given in ref. [28] in order to limit the set of modes to only those that are excited under normal incidence. The Q-factor is given by an Ohmic loss contribution Q^{Ω} and a radiative loss contribution Q^{r}, such

that $1/Q_\mu = 1/Q_\mu^r + 1/Q_\mu^\Omega$. The Ohmic Q-factor is calculated using a perturbation theory, provided in ref. [28], and is given by

$$1/Q_\mu^\Omega = P_\mu^\Omega/\omega_\mu = \frac{W^2 \mathrm{Re}\{-ik_{x\mu}\sin(k_{x\mu}h/2)\}}{\pi^2\mu^2 h} \tag{7.4}$$

The radiative Q for a periodic lattice of film-coupled nanopatches was computed in [3], and is in general dependent on the angle of the incident radiation. However, at normal incidence, it is simply given by

$$Q_\mu^r = \begin{cases} \frac{ka^2\cos(\theta)}{2h|1-r_m|^2} & \mu \text{ odd} \\ \\ \infty & \mu \text{ even.} \end{cases} \tag{7.5}$$

where r_m is the reflection coefficient of the metal film at normal incidence, as according to the Fresnel formulae. Further corrections to the resonance frequency and Q-factor due to the mutual coupling of the nanopatch antennas through the surface plasmon interaction can be found in [92], which are important corrections in order to obtain an accurate bistability model. Later in this work we will return to these corrections and examine their on the bistability properties of the film-coupled nanopatch system.

When the gap size is small, the electric field of the mode in the gap is given approximately by[28]

$$\mathbf{E}_\mu = \tilde{E}\hat{z}\cos(\mu\pi x/W) \tag{7.6}$$

where $\tilde{E}$ is an arbitrary normalization constant with units of V/m. The mode volume is then $U_\mu = \epsilon_0\tilde{E}^2 hW^2/2$.

When the nanopatch is driven by an arbitrary incident magnetic field $\mathbf{H}_{inc}$, an electric surface current arises in the slots equal to $\mathbf{K}_e = \mathbf{H}_{inc} \times \mathbf{n}$, where $\mathbf{n}$ is the normal vector to the surface of the cavity created by the gap between the nanopatch and the metal film. The current $\mathbf{J}$ that normally represents any current in the cavity

that drives the mode can therefore be split up into the sum of two parts: the effective surface current $\mathbf{K}_e$ which provides the coupling to the incident magnetic field, plus any currents induced in the cavity by the nonlinear susceptibility, which we will label $\mathbf{J}_{nl}$. Therefore we can write

$$\mathbf{J} = i\omega\mathbf{P}_{nl} + (\mathbf{H}_{inc} \times \mathbf{n})\left(\delta(x) + \delta(x - W)\right) \tag{7.7}$$

Including this surface current term in the numerator of Eq. (7.2) yields

$$e_\mu(\omega)\left(\tilde{\omega}_\mu^2 - \omega^2\right) = \frac{\omega^2}{U_\mu}\int \mathbf{P}_{nl} \cdot \mathbf{E}_\mu^* dV - i4\omega^2 Z_0 H_{inc}/kW\tilde{E}. \tag{7.8}$$

where $k = \omega/c$ is the wavenumber in free space, and we have made the assumption that the incident magnetic field is oriented in the y-direction: $\mathbf{H}_{inc} = \hat{\mathbf{y}}H_{inc}$.

Optical bistability is due to nonlinear currents that are driven by the mode fields, which are related to the electric field in the gap by

$$\mathbf{P}_{nl}(\mathbf{r},\omega) = \frac{3\epsilon_0\chi^{(3)}}{4}\mathbf{E}(\mathbf{r},\omega)|\mathbf{E}(\mathbf{r},\omega)|^2 \tag{7.9a}$$

$$\approx \frac{3\epsilon_0\chi^{(3)}}{4}e_\mu(\omega)|e_\mu(\omega)|^2\mathbf{E}_\mu(\mathbf{r})|\mathbf{E}_\mu(\mathbf{r})|^2 \tag{7.9b}$$

where the approximation in eq. (7.9b) is made by assuming that the field in the gap is dominated by a single mode, and here in this work we choose to focus on the fundamental mode, where $\mu = 1$. If the nonlinear material is restricted to just the dielectric in the gap, then

$$e_\mu(\omega)\left[\tilde{\omega}_\mu^2 - \omega^2\left(1 + \frac{3\epsilon_0\chi^{(3)}}{4U_\mu}|e_\mu(\omega)|^2\int|\mathbf{E}_\mu(\mathbf{r})|^4 \mathrm{d}V\right)\right] = -i4\omega^2 Z_0 H_{inc}/kW\tilde{E}. \tag{7.10}$$

Using $\int|\mathbf{E}_\mu(\mathbf{r})|^4\mathrm{d}V = \tilde{E}^4 hW^2 3/8$, we have

$$e_\mu(\omega)\left[\tilde{\omega}_\mu^2 - \omega^2\left(1 + \frac{9\chi^{(3)}}{16}|e_\mu(\omega)|^2\tilde{E}^2\right)\right] = -i4\omega^2 Z_0 H_{inc}/kW\tilde{E} \tag{7.11}$$

The gap mode of the plasmonic patch antenna is known to scatter as a pair of magnetic dipoles, one for each side of the patch. When the width W of the patch is deeply subwavelength and the mode number μ is odd, these two magnetic dipoles will constructively interfere and may be treated as a single magnetic dipole that is related to the amplitude of the gap-mode by,

$$\mathbf{m} = \frac{i2hW\tilde{E}}{Z_0 k} e_\mu(\omega)\hat{\mathbf{y}}. \tag{7.12}$$

Hence, we can assume to be operating near the resonance frequency of the fundamental ($\mu = 1$) mode, and transform eq. (7.11)to solve for the magntidue of the magnetic dipole moment $\mathbf{m} = m\hat{\mathbf{y}}$ rather than the mode amplitude $e_\mu(\omega)$,

$$m\left[\tilde{\omega}_\mu^2 - \omega^2\left(1 + \phi_{nl}|m|^2\right)\right] = \omega^2 \frac{8h}{k^2} H_{inc} \tag{7.13}$$

with

$$\phi_{nl} = \frac{9\chi^{(3)}}{16}\left(\frac{Z_0 k}{2hW}\right)^2. \tag{7.14}$$

Now, the total magnetic field incident upon any individual nanopatch antenna is the sum of the field of the incident plane wave that excites the array, and the magnetic field due to all of the other nanopatch antennas in the array. The total magnetic field of the incident plane wave on the surface of the metal film is simply given by $(1 - r_m)H_0\hat{\mathbf{y}}$, where H_0 is the magnetic field of the incident beam. On the other hand, the magnetic field due to all the other nanopatches can be written in terms of the Green's function of a magnetic dipole over a metal film. Let the Green's function of a geometry where half of the space is a metal film and the other half of the space is empty be designated by $\mathbf{G}(\mathbf{r}, \mathbf{r}')$. If all of the dipoles on the surface are in phase such that $\mathbf{m}_i = \mathbf{m}$ for all dipoles j, the field due to all of the dipoles on any one particular dipole is $\sum_j \mathbf{G}(\mathbf{r}_i, \mathbf{r}_j)\mathbf{m}$. The sum over all $\mathbf{r}_j$ of the Green's function

is referred to in effective medium theory as the *interaction constant*, and is defined by $\mathbf{C} = \sum_j \mathbf{G}(\mathbf{r}_i, \mathbf{r}_j)$. This interaction constant $\mathbf{C}$, which is generally a function of both frequency and the lattice spacings, has been calculated explicitly in [92] for a rectangular lattice of magnetic dipoles that are placed near enough to a metal film such that the surface plamon interaction dominates the Green's function.

The total magnetic field incident upon any particular nanopatch antenna can therefore be written

$$H_{inc} = (1 - r_m)H_0 + Cm \tag{7.15}$$

since the interaction constant $\mathbf{C} = C\mathbf{I}$ may be taken to be a scalar quantity C for any square lattice.

Thus taking into account the mutual coupling of the nanopatches, the equation of motion for the magnetic dipole moments of the metasurface is

$$m(\omega)\left[\tilde{\omega}_\mu^2 - \omega^2\left(1 + \phi_0 + \phi_{nl}|m(\omega)|^2\right)\right] = 8hc^2(1 - r)H_0 \tag{7.16}$$

where $\phi_0 = 8hC/k^2$.

The actual dipole moment in the time domain must be purely real, and therefore at steady state it must follow

$$m(t) = \frac{m(\omega)e^{i\omega t} + m(-\omega)e^{-i\omega t}}{2} \tag{7.17}$$

where $m(-\omega) = m(\omega)^*$. Hence, we also have that

$$m^*(\omega)\left[\tilde{\omega}_\mu^{*2} - \omega^2\left(1 + \phi_0^* + \phi_{nl}^*|m(\omega)|^2\right)\right] = 8hc^2(1 - r)H_0^* \tag{7.18}$$

and therefore,

$$|m|^2\left|\tilde{\omega}_\mu^2 - \omega^2\left(1 + \phi_0 + \phi_{nl}|m|^2\right)\right|^2 = 128|1 - r|^2c^4I/Z_0 \tag{7.19}$$

where $I = E_0^2/Z0$ is the intensity of the incident plane wave. This is a third order polynomial in $|x_\mu(\omega)|^2$, which is a real quantity, and therefore it has three real roots

under certain conditions. Once the roots of eq. (7.19) are found, the complex mode amplitude $x_\mu(\omega)$ can be found using eq. (7.11).

Hence, when a periodic array of plasmonic patch antennas are excited to a mode amplitude of x_μ, the array radiates a plane wave with a magnetic field of

$$\mathbf{H}_d = \frac{-ik}{2a^2}(1-r)\mathbf{m}. \tag{7.20}$$

The factor of $(1-r)$ is included to account for the secondary wave from the lattice of dipoles that is reflected off of the metal film.

The far-field scattering properties of a periodic array of optical patch antennas is finally given by the reflected field off of the film plus the field radiated by the array of patch antennas. Then the total reflection coefficient is

$$r_{tot} = -r + \frac{-i4(1-r)^2 khc^2/a^2}{\tilde{\omega}_\mu^2 - \omega^2(1+\phi_0+\phi_{nl}|m|^2)}. \tag{7.21}$$

To verify the developed theory, we design a film-coupled nanocube metasurface to realize perfect absorption at a certain wavelength. Fig. 7.1 is one designed structure, which is composed by periodically distributed silver nanocubes coupled to a metallic film. The edge-size of the nanocubes is 80 nm, while the round corner for nanocubes is set to be 8 nm, which is consistent with previous fabrication results. The thickness of silver metal film is designed as 100 nm and the periodicity of nanocubes is 550 nm. In this special study, vacuum is used as the spacer layer and the thickness is set to be 5 nm. According to the linear simulation results obtained from a commercial finite element software Multiphysics COMSOL, the resonance wavelength of the structure is around 618.1 nm, meaning perfect absorption at this wavelength. The other dip around 560 nm shown in the figure as well is caused by the Wood's anomaly.

In order to verify the prediction of the developed theory on optical bistability for film-coupled metasurfaces, we check the nonlinear numerical simulation in COMSOL.

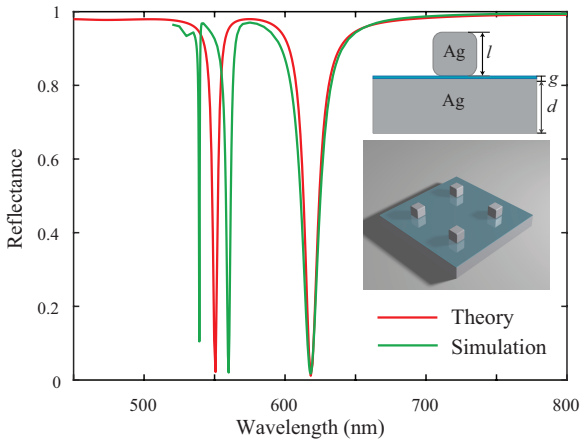

FIGURE 7.1: (Color online) Linear study of reflectance spectrum of designed meta-surface. The perfect absorption occurs at 623.5 nm. Insert with a 3D schematic of a film-coupled periodic nanocubes

We choose a longer wavelength of 650 nm which satisfies the optical bistability condition of $|(\lambda_{\text{res}} - \lambda_{\text{nl}})/(w/2)| > \sqrt{3}$, where w is the full-width at half-maximum (FWHM). [113] We keep the linear permittivity of the spacer as 1, that of vacuum, while we continue to use an optical Kerr material with a relative permittivity $\epsilon_r = \epsilon_L + 3/4\chi^{(3)}|E_{loc}|^2$, with a third order susceptibility of $\chi^{(3)} = 4.4 \times 10^{-18}\ m^2/V^2$.[114] To effectively obtain two stable outputs with one input, we use the same technique introduced in Ref. [111]. For the upper branch of the hysteresis loop in the reflectance as a function of input intensity, we start the nonlinear simulation with a relatively low input intensity and then continuously increase the intensity. It is critical to specify that the solution of previous simulation is used as the initial value as the next step. Similarly, for the lower branch, the nonlinear studies are executed starting with a relatively high input intensity. In the unstable region, the step size of input intensity has been adjusted when necessary. According to the nonlinear simulation result shown in Fig. 7.2, the threshold intensity for bistability is around 0.6 MW/cm^2, converted into power requirement of an optical switch, it is at atto-joule level.

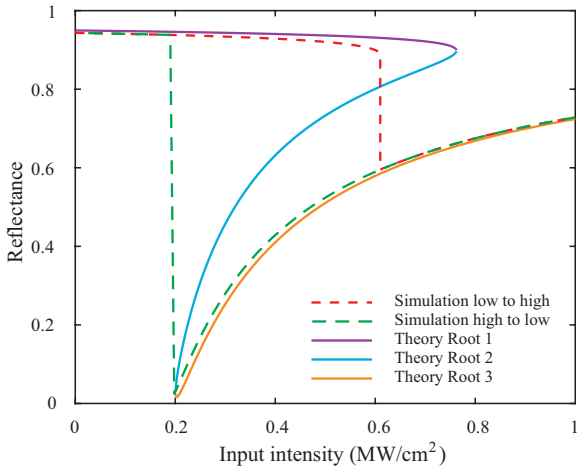

FIGURE 7.2: (Color online) Comparison between theory and simulation result at 650 nm. The dashed curves come from simulation while the solid curves come from theory prediction.

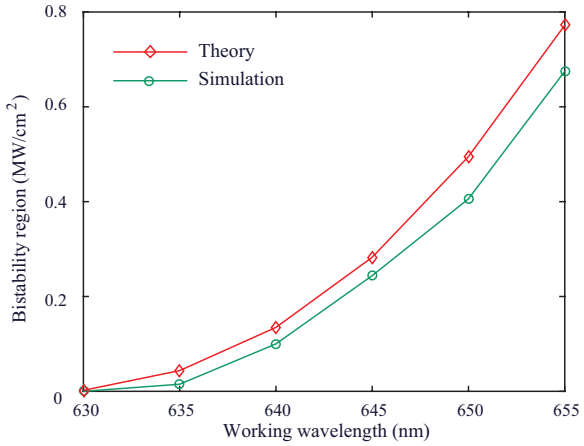

FIGURE 7.3: (Color online) Sensitivity analysis on the working wavelength. The theory results agree excellently with those of simulation results.

A comparison has been made between the theoretical prediction and numerical simulation. As shown in Fig. 7.2 , the results from these two methods are in excellent agreement. The dashed curves come from the result of numerical studies while the solid curves are from theory prediction. The difference between these two might be caused by the round corner of nanocubes.

8

Lasing in a Single Film-Coupled Optical Nanopatch Antenna

Plasmonic metamaterials have been the focus of several recent efforts to develop nanoscale coherent sources by taking advantage of the enhancement of localized density of states in order to modify radiative processes. Here we present acombined analytic and simulated investigation of single nanocube lasing by plasmonic enhancement of laser-dye gain medium emission, including an analytic prediction for threshold intensity. We apply our model to a basic Fabry-Pérot cavity, a 2D plasmonic nanostripe, and a 3D plasmonic nanocube; the nanostructures are separated from a gold film by a dye-doped dielectric spacer layer, which forms the plasmonic structure for field enhancement. We report excellent agreement between analytic predictions of lasing threshold and finite-element simulation measurements for each of the three structures examined, and we provide a series of graphics that demonstrate the extensibility of this model to other geometries and parameters of the nanocube structure.

In recent years, plasmonic and metamaterial nanostructures have attracted strong attention as coherent radiation sources. These structures provide nanometer-scale

cavity volumes in which laser gain media can be placed to leverage the high field enhancement through the Purcell effect [52, 39] to improve radiation. Several efforts have recently demonstrated a variety of material and structural configurations to produce nanolasing. Many of these incorporate semiconductor materials as gain media and structures [115, 116, 117, 118, 119, 120, 121], some make use of quantum dot emitters [122, 123], and a few use fluorescent dye-doped dielectrics [124, 125, 126, 127, 128]. Some are structured in arrays [129, 125, 127, 126, 128] while others explore single nanorod structures [115, 117, 120, 121] or core-shell spheres [124]. These efforts to demonstrate experimental low-threshold, nanoscale lasers drive us to further explore nanoscale visible-wavelength laser cavities doped with laser-dye gain molecules (readily applicable to multiple dyes) while also developing and implementing fully analytical expressions—for predicting lasing behavior—that are easily extensible to arrays of the single nanoparticle systems we analyze.

In order to exploit radiative properties of the analytically well-known system of lasing for the development of novel sources, we combine existing analytical models for nanocube modes with lasing population equations, applicable to dye media, to find predictive equations for threshold intensity and other parameters. First, we apply our models to a basic Fabry-Pérot cavity to demonstrate agreement between derived expressions and known threshold metrics. Then, we propose a single plasmonic nanocube structure with a dye-doped dielectric spacer as a novel, low-threshold, nanoscale laser source but with the addition of a comprehensive analytical description which supports easily adjustable calculations for different dimensions and dye materials. Previous efforts to develop thorough quasi-analytical models for these plasmonic nanocube structures have driven our application of that theory to radiative devices. We draw on the recent work of coupled-mode theory applied to plasmonic nanocubes [28, 3], leveraging these analytic descriptions of the field distribution beneath a film-coupled nanocube to arrive at analytic descriptions of plasmonic lasing

for single nanocube-spacer-film structures.

The field enhancement associated with these structures, explored in [52], allows for an ideal structure for exploiting the radiative capabilities when incorporating a gain media in the enhancement region. We apply a four-level laser system of rate equations and the parameters corresponding to Rhodamine-800 dye, as in [130], to extend the previous coupled mode theory model to a plasmonic nanocube lasing model. The small mode volume, V_{eff}, associated with a single nanocube cavity offsets the small Q-factor, resulting in low threshold intensity required to excite the gain medium to lasing conditions; this low threshold is the result of field enhancement, proportional to the ratio of Q to V_{eff}, through the Purcell effect[131].

We derive the required incident threshold intensity for lasing by applying the mode amplitude equations at threshold to derive the corresponding critical photon count, maximum field enhancement, and Q-factors for a normally-incident external plane wave. Ultimately, we seek to provide clarification for nanolasing with a fully analytical model supported by simulation and to confirm the quasi-analytical model for a single nanocube laser, which can later be extended to arrays of nanoparticles, as in [132], or experimentally demonstrated. To this end, careful effort is taken to maintain the applicability of this analytic development of theory and predictive modeling thorough experimentally feasible parameters. The theory was all developed by myself, while the full-wave simulations were performed by Roberto Zecca and Xander Deputy.

8.1 Rate equations

We begin with a model for a four-level gain material, as depicted in Fig. 8.1. Let the absorption band gap and emission band gap be represented by $\hbar\omega_a$ and $\hbar\omega_e$, respectively. The lifetime of the non-radiative, fast transition from level three to level two is τ, and assumed to be equal to the lifetime of the non-radiative transition

from level two to level one, while the spontaneous decay rate is given by $1/\tau_{21}$. Dipole moments $\mathbf{P}_a$ and $\mathbf{P}_e$ can be associated with the optical interaction of both the absorption and emission lines. In the following, the tilde indicates fields that vary harmonically in time, whereas symbols for frequency-domain quantities will not have a tilde. The rate equations are [133, 130]

$$\frac{d\tilde{N}_3}{dt} = \frac{1}{\hbar\omega_a}\left(\frac{\partial\tilde{\mathbf{P}}_a}{\partial t}\cdot\tilde{\mathbf{E}}\right) - \frac{\tilde{N}_3}{\tau} \tag{8.1a}$$

$$\frac{d\tilde{N}_2}{dt} = \frac{1}{\hbar\omega_e}\left(\frac{\partial\tilde{\mathbf{P}}_e}{\partial t}\cdot\tilde{\mathbf{E}}\right) + \frac{\tilde{N}_3}{\tau} - \frac{\tilde{N}_2}{\tau_{21}} \tag{8.1b}$$

$$\frac{d\tilde{N}_1}{dt} = -\frac{1}{\hbar\omega_e}\left(\frac{\partial\tilde{\mathbf{P}}_e}{\partial t}\cdot\tilde{\mathbf{E}}\right) - \frac{\tilde{N}_1}{\tau} + \frac{\tilde{N}_2}{\tau_{21}} \tag{8.1c}$$

$$\frac{d\tilde{N}_0}{dt} = -\frac{1}{\hbar\omega_a}\left(\frac{\partial\tilde{\mathbf{P}}_a}{\partial t}\cdot\tilde{\mathbf{E}}\right) + \frac{\tilde{N}_1}{\tau}, \tag{8.1d}$$

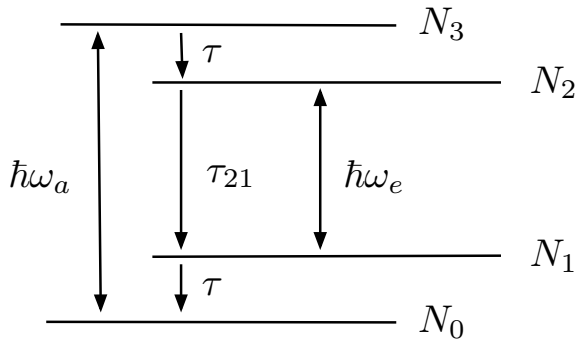

FIGURE 8.1: Four-level system

and we assume that all quantities are both spatially and temporally dependent. The equations of motion of the dipole moments are in turn given by

$$\left(\frac{\partial^2}{\partial t^2} + 2\Gamma_c \frac{\partial}{\partial t} + \omega_a^2\right) \tilde{\mathbf{P}}_a = \sigma_a \Delta\tilde{N}_a \tilde{\mathbf{E}} \tag{8.2a}$$

$$\left(\frac{\partial^2}{\partial t^2} + 2\Gamma_c \frac{\partial}{\partial t} + \omega_e^2\right) \tilde{\mathbf{P}}_e = \sigma_e \Delta\tilde{N}_e \tilde{\mathbf{E}}, \tag{8.2b}$$

where Γ_c is the coherence decay rate of the gain material, $\Delta\tilde{N}_a = \tilde{N}_0 - \tilde{N}_3$, $\Delta\tilde{N}_e = \tilde{N}_1 - \tilde{N}_2$, and σ_a and σ_e are phenomenological interaction constants [130]. We seek the steady-state behavior of population levels, given by the solution of

$$0 = \frac{1}{\hbar\omega_a} \left\langle \frac{\partial\tilde{\mathbf{P}}_a}{\partial t} \cdot \tilde{\mathbf{E}} \right\rangle - \frac{\tilde{N}_3}{\tau} \tag{8.3a}$$

$$0 = \frac{1}{\hbar\omega_e} \left\langle \frac{\partial\tilde{\mathbf{P}}_e}{\partial t} \cdot \tilde{\mathbf{E}} \right\rangle + \frac{\tilde{N}_3}{\tau} - \frac{\tilde{N}_2}{\tau_{21}} \tag{8.3b}$$

$$0 = -\frac{1}{\hbar\omega_e} \left\langle \frac{\partial\tilde{\mathbf{P}}_e}{\partial t} \cdot \tilde{\mathbf{E}} \right\rangle - \frac{\tilde{N}_1}{\tau} + \frac{\tilde{N}_2}{\tau_{21}} \tag{8.3c}$$

$$0 = -\frac{1}{\hbar\omega_a} \left\langle \frac{\partial\tilde{\mathbf{P}}_a}{\partial t} \cdot \tilde{\mathbf{E}} \right\rangle + \frac{\tilde{N}_1}{\tau}, \tag{8.3d}$$

where $\langle\cdot\rangle$ denotes time-averaging. The spasing emission is assumed to be very narrow in linewidth, and so we assume a slowly varying envelope approximation (SVEA) for the form of $\tilde{\mathbf{P}}_e$. If the system is driven optically with a monochromatic laser at the absorption frequency, then the SVEA is also justified for the absorption dipole moment. To simplify the calculations, we first drop the absorption and emission subscripts, and just consider terms of the form $\frac{\partial\tilde{\mathbf{P}}}{\partial t} \cdot \tilde{\mathbf{E}}/\hbar\omega_i$, with the SVEA applied to both the dipole moment and the electric field:

$$\tilde{\mathbf{P}}(\mathbf{r}, t) = \mathbb{R}\mathrm{e}\left[\mathbf{P}(\mathbf{r})\, e^{i\omega t}\right] \tag{8.4a}$$

$$\tilde{\mathbf{E}}(\mathbf{r}, t) = \mathbb{R}\mathrm{e}\left[\mathbf{E}(\mathbf{r})\, e^{i\omega t}\right] \tag{8.4b}$$

$$\mathbf{P}(\mathbf{r}) = \alpha(\omega)\, \Delta N \mathbf{E}(\mathbf{r}). \tag{8.4c}$$

Combining this with Eq. (8.2), we obtain

$$\alpha_i(\omega) = \frac{\sigma_i}{\omega_i^2 - \omega^2 + i2\Gamma_c\omega}, \tag{8.5}$$

where the i-subscript differentiates between the emission and the absorption lines. We shall drop the explicit spatial dependence of fields henceforth. The optical interaction term becomes

$$\frac{\partial\tilde{\mathbf{P}}}{\partial t}\cdot\tilde{\mathbf{E}} = -\frac{\omega}{2}\mathbb{Im}\left(\mathbf{P}\cdot\mathbf{E}\,e^{i2\omega t} + \mathbf{P}\cdot\mathbf{E}^*\right) \tag{8.6}$$

The absorption rate, which in the rate equations appears as a term of the form $R_i(\omega,\mathbf{r}) = \frac{1}{\hbar\omega_i}\left\langle\frac{\partial\tilde{\mathbf{P}}}{\partial t}\cdot\tilde{\mathbf{E}}\right\rangle$, is given by the time average of eq. (8.6):

$$\begin{aligned} R_i(\omega,\mathbf{r}) &= \frac{1}{\hbar\omega_i}\left\langle\frac{\partial\tilde{\mathbf{P}}}{\partial t}\cdot\tilde{\mathbf{E}}\right\rangle = -\frac{\omega}{2\hbar\omega_i}\mathbb{Im}\left(\mathbf{P}\cdot\mathbf{E}^*\right) \\ &= \Delta N_i(\mathbf{r})\,\beta_i(\omega)\,|\mathbf{E}(\omega,\mathbf{r})|^2, \end{aligned} \tag{8.7}$$

where $\beta_i(\omega) = -\mathbb{Im}\left[\alpha_i(\omega)\right]/2\hbar$ represent the frequency response of the absorption and emission lines. Now this form for the optical interaction term can be used in the rate equations Eq. (8.3) to derive the spasing frequency and threshold. At steady state, we have that

$$N_3 = \tau R_a \tag{8.8a}$$

$$N_2 = \tau_{21}(R_e + R_a) \tag{8.8b}$$

$$N_1 = N_3 \tag{8.8c}$$

$$N_0 = N - 2N_1 - N_2. \tag{8.8d}$$

Moreover, in the limit that $\tau \ll \tau_{21}$,

$$\Delta N_e = N_1 - N_2 \approx -N_2 = -\tau_{21}(R_e + R_a) \tag{8.9a}$$

$$\Delta N_a = N_0 - N_3 \approx N - N_2 = N - \tau_{21}(R_e + R_a). \tag{8.9b}$$

8.2 Analytical Solution of the Interaction between an Optical Cavity and a Homogeneous Gap Material

The field in the cavity may be expanded in a sum of resonant eigenmodes,

$$\mathbf{E}(\omega, \mathbf{r}) = \sum_{\mu} e_{\mu}(\omega)\mathbf{E}_{\mu}(\mathbf{r}) \tag{8.10}$$

where the mode amplitudes follow

$$e_{\mu}(\omega) = \frac{\omega^2 \int \mathbf{P} \cdot \mathbf{E}_{\mu}^{*} \mathrm{d}V / U_{\mu}}{\omega_{\mu}^2 - \omega^2 + i\omega_{\mu}\Gamma_{\mu}(\omega)} \tag{8.11}$$

where $\Gamma_{\mu} = \omega_{\mu}/Q$, Q being the quality factor of the cavity (as referred to the FWHM of the power or intensity resonance curve), and $U_{\mu} = \int \epsilon_0 |\mathbf{E}_{\mu}|^2 \mathrm{d}V$ is the mode volume. Considering the emission physics at signal frequency ω_s, the numerator may be rewritten using the gain medium polarizability as

$$\begin{aligned} &\frac{\omega_s^2}{U_{\mu}} \int \mathbf{P}_e(\omega_s) \cdot \mathbf{E}_{\mu}^{*} \mathrm{d}V \\ &= -\frac{\omega_s^2 \alpha_e(\omega_s) e_{\mu}(\omega_s)}{U_{\mu}} \int N_2(\mathbf{r}) |\mathbf{E}_{\mu}(\mathbf{r})|^2 \mathrm{d}V, \end{aligned} \tag{8.12}$$

and we define an effective population inversion as

$$\mathcal{N}' = \frac{V_c \epsilon_0}{U_{\mu}} \int N_2(\mathbf{r}) |\mathbf{E}_{\mu}(\mathbf{r})|^2 \mathrm{d}V, \tag{8.13}$$

where $V_c = hW^2$ is the volume of the cavity. We then obtain

$$e_{\mu}(\omega_s) \left(\omega_{\mu}^2 - \omega_s^2 + i\omega_s \Gamma_{\mu}(\omega_s) + \frac{\omega_s^2 \alpha_e(\omega_s) \mathcal{N}'}{V_c \epsilon_0} \right) = 0. \tag{8.14}$$

When the emission frequency corresponds to the resonance frequency of the cavity, the lasing frequency must also correspond to that frequency, and therefore $\omega_s = \omega_{\mu} = \omega_e$. The critical population inversion then becomes

$$\mathcal{N}_c' = \frac{2\Gamma_{\mu}(\omega_e)\Gamma_c(\omega_e) V_c \epsilon_0}{\sigma_e}. \tag{8.15}$$

In order to find the pumping threshold, we also define the total population inversion

$$\mathcal{N} = \int N_2(\mathbf{r}) \mathrm{d}V, \tag{8.16}$$

which is given by the steady-state rate equations as

$$\mathcal{N} = \tau_{21} \int (R_e + R_a)\, \mathrm{d}V. \tag{8.17}$$

Like $\mathcal{N}'$, $\mathcal{N}$ is a unit-less quantity. When the cavity is at threshold, $R_e = 0$, since there are no photons in the cavity (neglecting any photons from spontaneous emission), and therefore the critical total population inversion is given by

$$\mathcal{N}_c = \tau_{21} \int R_a \mathrm{d}V. \tag{8.18}$$

The required mode amplitude at the excitation frequency is therefore

$$|e_\mu(\omega_p)|_c^2 = \frac{\epsilon_0 \mathcal{N}_c}{\tau_{21} \beta_a(\omega_p)\, U_\mu\, (N - \mathcal{N}_c'/V_c)}, \tag{8.19}$$

where ω_p is the pump frequency (which in general need not be exactly the same as ω_a). Since the number of photons at the pumping frequency is $\phi_p = |e_\mu(\omega_p)|^2 U_\mu / \hbar\omega_p$, the critical number of photons at the pumping frequency is

$$\phi_{p,c} = \frac{\epsilon_0 \mathcal{N}_c}{\tau_{21} \hbar\omega_p \beta_a(\omega_p)\, (N - \mathcal{N}_c'/V_c)}. \tag{8.20}$$

By inspection of the denominator in the two previous equations, it becomes evident that the combination of $\mathcal{N}'$, V_c, and N determines whether lasing is at all possible.

8.3 Finite-element implementation

When implementing the model into a finite-element solver, such as COMSOL Multiphysics, the population density fields ΔN can be calculated using a dedicated

algebraic solver, coupled to two optical physics, for the pump and signal. When operating in the frequency domain, it is generally necessary to "seed" a signal, as its arising from spontaneous emission is more problematic to model. In the following, let us assume that the pump and signal seed are exactly centered at the absorption and emission lines, respectively (ω_a, ω_e), which will simplify the argument without altering its conclusions. Manipulating Eq. (8.9) with the aid of Eq. (8.7), we obtain

$$\Delta N_e \left(\beta_e |\mathbf{E}_e|^2 + \beta_a |\mathbf{E}_a|^2 + \frac{1}{\tau_{21}} \right) + N \beta_a |\mathbf{E}_a|^2 = 0 \tag{8.21a}$$

$$N + \Delta N_e - \Delta N_a = 0. \tag{8.21b}$$

which can be solved in parallel with the electric fields. The electromagnetic physics will, in general, have each a driving term representing their interaction. If making the undepleted pump approximation, the pump driving term can be neglected, or it is even possible to simply postulate a form of the pump field without actually simulating it. The nonlinear driving term for the emission physics will be, in weak formalism,

$$\mu_0 \omega_e^2 \mathbf{P}_e \cdot \text{test}\left(\mathbf{E}_e\right) = \mu_0 \omega_e^2 \alpha_e \Delta N_e \mathbf{E}_e \cdot \text{test}\left(\mathbf{E}_e\right). \tag{8.22}$$

As an alternative approach, the stimulated emission dynamics can be included as an complex imaginary addition to the gain material's relative permittivity, provided $\mu_r = 1$. On resonance α_e is purely imaginary and has a negative sign, so the contribution to permittivity takes the form:

$$\Delta \epsilon_{r,\text{nonlinear}} = \frac{\alpha_e \Delta N_e}{\epsilon_0} = i \frac{\mathbb{I}\text{m}\left(\alpha_e\right) \Delta N_e}{\epsilon_0}. \tag{8.23}$$

We remind the reader here that, in the presence of population inversion, ΔN_e has a negative sign according to the convention we choose. This makes the the nonlinear permittivity contribution positive (which corresponds to gain).

8.4 Application to a Fabry-Pérot Resonator

Assuming a cavity created out of a Fabry-Pérot resonator, the mode of the cavity will follow

$$\mathbf{E}_\mu = E_0 \cos\left(\frac{\pi x}{L}\right)\hat{\mathbf{z}}. \tag{8.24}$$

The mode volume is then $U_\mu = E_0^2 \epsilon_0 L/2$, and $V_c = L$. At threshold, the effective population inversion is both given by

$$\mathcal{N}' = 2E_0^2 \int N_2(x) \cos^2\left(\frac{\pi x}{L}\right) \mathrm{d}x \tag{8.25}$$

and

$$\mathcal{N}_c' = \frac{2\Gamma_\mu \Gamma_c L \epsilon_0}{\sigma_e}. \tag{8.26}$$

The primary difficulty in making use of Eq. (8.20) to find the critical number of pumping photons in the cavity is that it is difficult to know *a priori* what the spatial dependence of N_2 is in order to explicitly calculate $\mathcal{N}_c$. If we make the *ansatz* that the population inversion corresponds to the absorption rate, which is proportional to the field in the cavity, then we may assume that N_2 varies as the cavity mode. Hence, we assume a functional form of $N_2(x)$ such that $N_2(x) = N_2 E_0^2 \cos^2(\pi x/L)$, so that $\mathcal{N}_c = (2/3)\mathcal{N}_c'$. The critical number of photons in the cavity is then immediately given by

$$\phi_{p,c} = \frac{2\epsilon_0}{3\hbar\omega_p} \frac{\mathcal{N}_c'}{\tau_{21}\beta_a(\omega_p)(N - \mathcal{N}_c'/V_c)}. \tag{8.27}$$

The Fabry-Pérot simulation setup, displayed in Fig. 8.2 consists, from left to right, of: vacuum; a dielectric wall with refractive index $n_1 = 10$; the cavity of length $\lambda_e/2/n_0$, where $n_0 = 1$ and λ_e is the signal vacuum wavelength, chosen to be equal to the emission line; a second dielectric wall with $n_1 = 10$ to enclose the cavity;and a second vacuum domain. The dielectric walls have thickness $\lambda_e/4/n_1$,

FIGURE 8.2: Fabry-Pérot cavity: (left) vacuum domain; (middle left) dielectric wall; (center) cavity domain; (middle right) second dielectric wall; (right) second vacuum domain. The pump beam enters from the left and travels to the right.

and the vacuum domains have length λ_e. We excite the cavity from the leftmost boundary with an incident plane wave with its electric field polarized in the out-of-plane direction. Perfect magnetic conductor (PMC) boundary conditions applied to the top and bottom boundaries of all domains simulate periodicity in the upward (y) direction, along which the fields do not vary, making this essentially a 1D simulation. Implementation of the pump, emission, and population density physics nodes is as described in Sec. 8.3.

The simulation results are presented in Fig. 8.3, where it is evident that the threshold occurs quite precisely at the point where $\phi_p = \phi_{p,c}$ and $\mathcal{N}' = \mathcal{N}'_c$ and the signal photon count starts diverging in an exponential-like way. The agreement between the curves for the first two metrics is not perfect, but that is to be expected given the inherent limitations of numerical approaches and the approximation for N_2 previously introduced in this section.

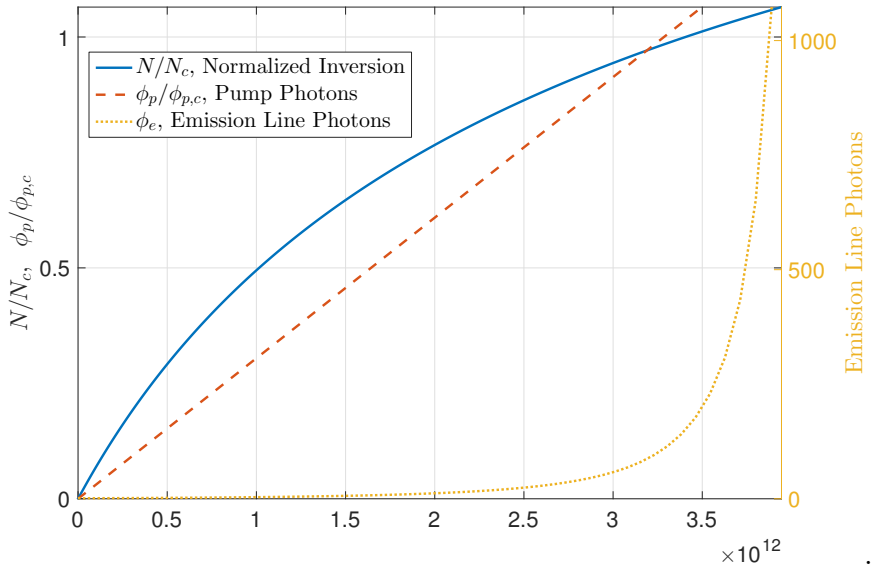

FIGURE 8.3: Fabry-Pérot cavity metrics as a function of incident pump intensity: total population inversion (fraction of critical number, blue continuous line), number of pump photons in cavity (fraction of critical number, red dashed line), number of signal photons in cavity (absolute number, yellow dotted line, right y-axis).

8.5 Application to Single Plasmonic Nanoparticles

We now apply the model to a single film-coupled plasmonic nanoparticle. In particular, in this section we study the 2D(3D) problem of a gold nanostripe(patch) of square cross-section (with fillets) separated from a thick gold substrate by a nanometric dielectric layer. An illustration of the 2D nanostripe geometry is given in section 8.5, which is essentially a 2D slice of the 3D nanopatch geometry.

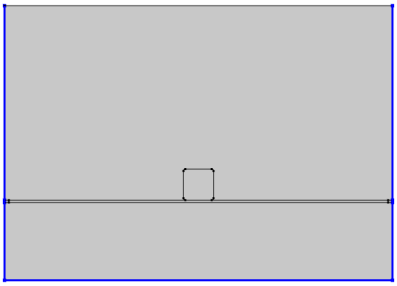

FIGURE 8.4: Example setup with scattering boundary conditions and single nanoparticle simulation

In order to derive the threshold for both the nanostripe and nanopatch geometries, we apply the same temporal coupled mode theory that was developed in chapter 3. Approximating the slots under the cube as perfect magnetic conductors (PMCs), the μ-th mode in the gap ($\{x, y\} \in \{[0, W] \times [-h/2, h/2]\}$) takes the form [28]

$$E_\mu^x = E_0 \frac{k_{y\mu} W}{\pi\mu} \sin(k_{y\mu} y) \sin\left(\frac{\mu\pi x}{W}\right) \tag{8.28a}$$

$$E_\mu^y = E_0 \cos(k_{y\mu} y) \cos\left(\frac{\mu\pi x}{W}\right) \tag{8.28b}$$

$$H_\mu^y = -i \frac{E_0}{\eta_0} \frac{\omega_\mu}{c\pi\mu} \cos(k_{y\mu} y) \sin\left(\frac{\mu\pi x}{W}\right) \tag{8.28c}$$

$$E_\mu^z = H_\mu^x = H_\mu^y = 0, \tag{8.28d}$$

where W is the side length of the square cross-section, η_0 is the impedance of vacuum, c is the speed of light in vacuum, ω_μ is the resonance frequency, and $k_{y\mu}$ is a transverse wavenumber found by solving the dispersion relation for a metal-insulator-metal plasmonic waveguide [28]. For small values of h, it is straightforward to apply the same arguments as in Sec. 8.4 to obtain

$$U_\mu = \frac{E_0^2 \epsilon_0 V_c}{2} \tag{8.29a}$$

$$\mathcal{N}_c' = \frac{2\Gamma_\mu(\omega_e)\,\Gamma_c(\omega_e)\,V_c\epsilon_0}{\sigma_e} \tag{8.29b}$$

$$\mathcal{N}_c = \frac{2}{3}\mathcal{N}_c', \tag{8.29c}$$

with $V_c = hW$ and where it is still understood that the emission line and cavity resonance are aligned by design (cf. Sec. 8.2). For 3D nanocubes, modes can be labeled by two integer indices m, n [28], corresponding to the nodes along the x– and z–directions. If we consider the $n = 0$ family of modes, Eqs. (8.28) and (8.29) are still valid by letting $m = \mu$. In this case, however, $V_c = hW^2$.

At threshold, therefore, the mode amplitude due to the pumping frequency ω_p

must be

$$|e_\mu(\omega_p)|_c^2 = \frac{4}{3E_0^2\tau_{21}\beta_a(\omega_p)}\frac{\mathcal{N}_c'}{NV_c - \mathcal{N}_c'}, \tag{8.30}$$

corresponding to a pump photon count of

$$\phi_{p,c} = \frac{2\epsilon_0 V_c}{3\hbar\omega_p\tau_{21}\beta_a(\omega_p)}\frac{\mathcal{N}_c'}{NV_c - \mathcal{N}_c'}. \tag{8.31}$$

When using an external wave to couple to the cavity modes, the fraction of incident energy that enters the cavity depends on the specifics of the system at hand. The maximum field enhancement in the cavity, defined as the ratio between maximum field amplitude norm in the cavity to field amplitude norm of a normally incident plane wave at frequency ω, is given by

$$\frac{\max|\mathbf{E}_{\text{cavity}}|}{E_{\text{inc}}} = \frac{4c\omega}{W}\frac{|1 - r_{\text{TM}}|}{\left(\omega_\mu^2 - \omega^2\right)^2 + \frac{\omega_\mu^4}{Q_\mu^2(\omega)}}, \tag{8.32}$$

where r_{TM} is the reflection coefficient for a TM wave. With the previously stated assumptions, it is fairly straightforward [3] to show that the intensity of plane wave incident at a near-normal angle required to reach threshold is

$$\begin{aligned} I_{\text{inc},\mu,c} =& \frac{\eta_0\epsilon_0^2 W^2}{24\tau_{21}\beta_a(\omega_p)}\frac{1}{|1 - r_{\text{TM}}|^2}\frac{\left(\omega_\mu^2 - \omega_p^2\right)^2 + \frac{\omega_\mu^4}{Q_\mu^2(\omega_p)}}{\omega_p^2} \\ &\times \frac{\mathcal{N}_c'}{NV_c - \mathcal{N}_c'}, \end{aligned} \tag{8.33}$$

and that only coupling to μ-odd modes is possible in this configuration. The Q-factor of the mode, Q_μ, is due to two mechanisms, namely Ohmic and radiation losses: $Q_\mu^{-1} = \left(Q_\mu^\Omega\right)^{-1} + \left(Q_\mu^{\text{rad}}\right)^{-1}$, the latter of which are frequency-dependent. Explicit

expressions for the partial Q-factors are given by [28, 3]

$$Q_{\mu}^{\Omega} = \frac{\pi^2 h \mu^2}{2W^2 \mathbb{R}\mathrm{e}\left[-ik_{y\mu}\sin\left(\frac{k_{y\mu}h}{2}\right)\right]} \tag{8.34a}$$

$$Q_{\mu,\mathrm{2D}}^{\mathrm{rad}} = \frac{W}{4h}\left(\frac{\omega_\mu}{\omega_p}\right)^2 \tag{8.34b}$$

$$Q_{\mu,\mathrm{3D}}^{\mathrm{rad}} = \frac{3\pi c \omega_\mu^2}{8h\omega_p^3}. \tag{8.34c}$$

These analytical results are summarized in Fig. 8.5.

The 2D single plasmonic nanostripe used in the simulation and analytics has a height and width of 98.5nm, with a dielectric gap of 6nm, placed on top of a 200nm thick gold film. The dielectric spacer has index of refraction of one for simplicity and contains the gain medium physics. The relative electric permittivity of gold is taken from Johnson and Christy[63]. The nanostripe is excited by an incident Gaussian beam from above (normal incidence), as described in section 8.3. The remaining external boundaries are assigned scattering boundary conditions (SBCs) to simulate open boundaries, providing a good approximation to the Sommerfeld radiation condition without extending the simulation domain infinitely (distinct lack of periodicity) [134]. The pump, emission, and population density physics are implemented as described in section 8.3.

We have chosen to pump both the nanostripe and the nanopatch at normal incidence with a Gaussian beam of width greater than the particle size. The choice of a Gaussian beam is at the same time realistic and convenient from the computational point of view. In fact, the decreasing energy profile of the Gaussian beam allows us to use scattering boundary conditions on the lateral boundaries without excessive concerns with regards to their performance at near-grazing angles.

The simulation results for the 2D nanostripe, presented in Fig. 8.6, indicate that the threshold occurs at $14 \times 10^6 W/m^2$, where $\phi_p = \phi_{p,c}$ and $\mathcal{N}' = \mathcal{N}'_c$, which are in

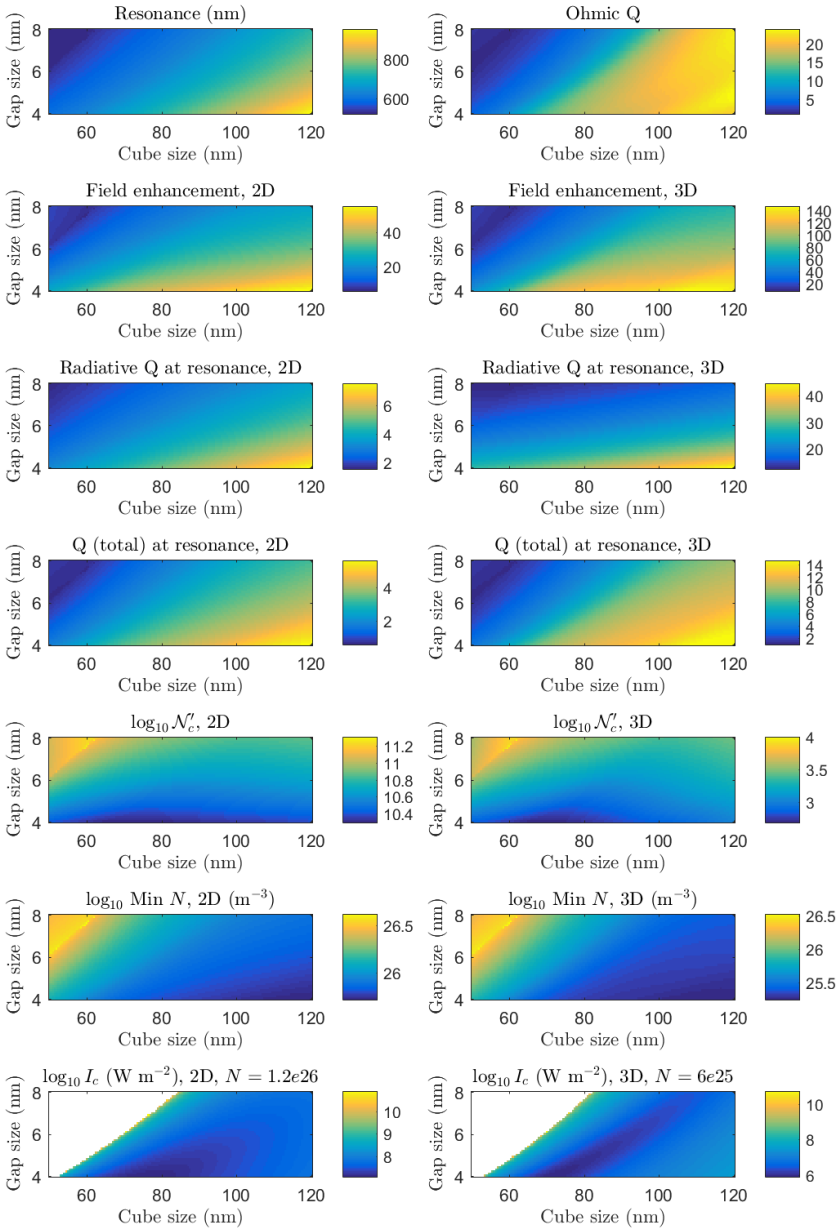

FIGURE 8.5: (Color online) Behavior of film-coupled plasmonic nanoparticle (nanostripe and nanocube) as a function of particle size (horizontal axis) and gap size (vertical axis). First row: resonance of fundamental mode, in units of vacuum wavelength (left); Ohmic quality factor (right). For subsequent rows, quantities in the left column refer to the 2D case, and those in the right column to the 3D. Second row: field enhancement at resonance. Third row: radiative quality factor at resonance. Fourth row: total quality factor at resonance. Fifth row: critical effective population (threshold condition). Sixth row: minimum density of carriers to ensure lasing is possible. Seventh row: threshold incident intensity (normally incident plane wave) for a given value of N. The white regions indicate conditions that make lasing unfeasible.

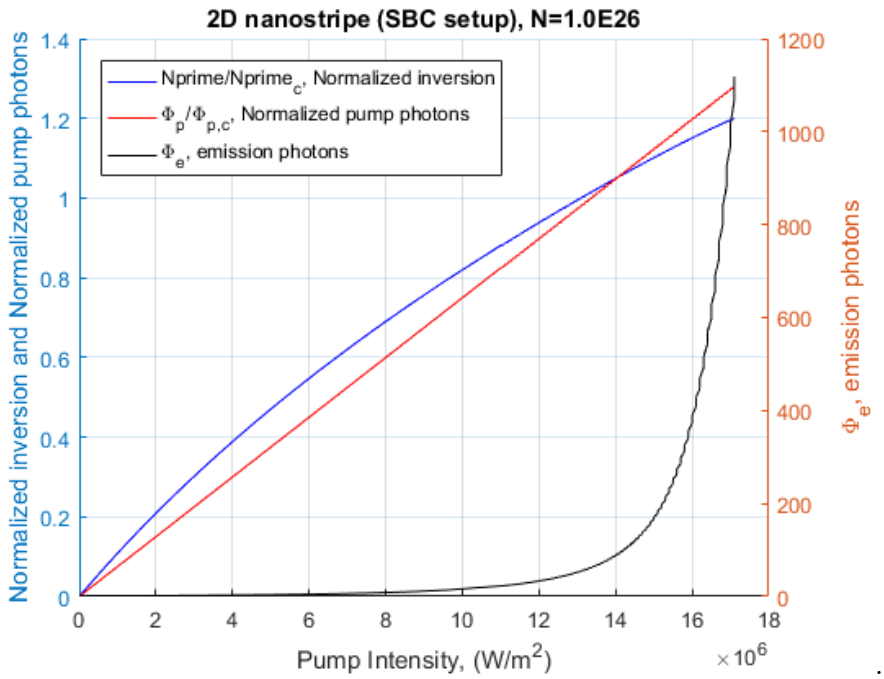

FIGURE 8.6: Prediction of lasing threshold for the 2D nanostripe according to both coupled mode theory and simulation.

strong agreement with the analytically predicted threshold intensity. Additionally, the emission photon count begins to diverge exponentially at the threshold pump intensity within a reasonable margin, as expected for the limitations of numerical approximations.

The 3D single plasmonic nanopatch simulation is an extension of the 2D nanostripe simulation. We ascribe the same material parameters as those of the corresponding domains of the 2D simulation (vacuum, gold nanocube, thin dielectric spacer layer, gold film) and the same boundary conditions to simulate open boundaries with an incident Gaussian beam, whose electric field is polarized in the y-direction, applied at normal incidence from above the nanopatch. The side length of the cube is chosen to match that of the 2D stripe, $W = 98.35nm$, and the fillet radius is adjusted to 11.6nm to maintain a resonant frequency close to the corresponding emission wavelength of the dye, 710nm.

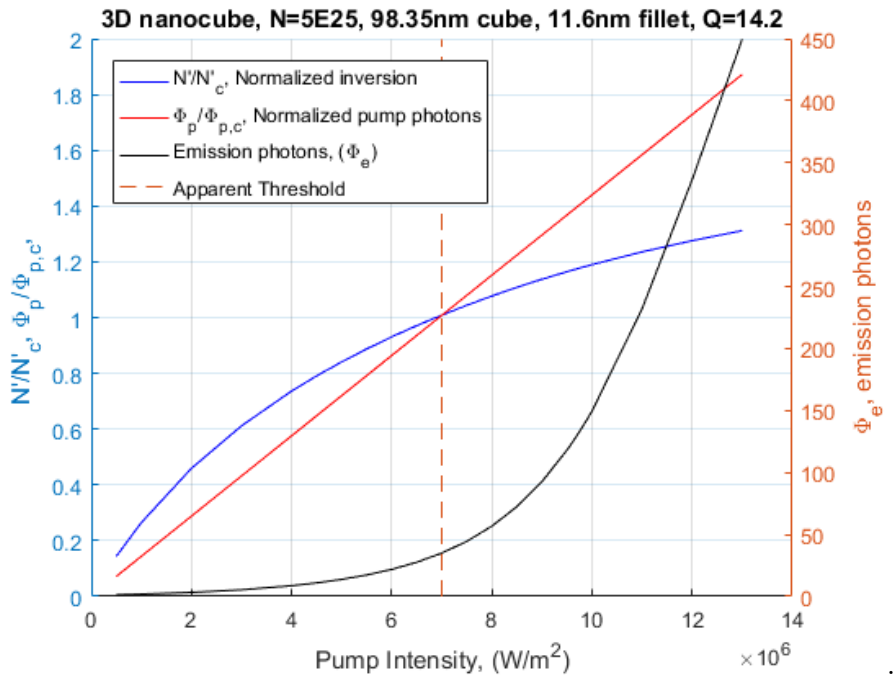

FIGURE 8.7: Prediction of lasing threshold for the 3D nanopatch according to both coupled mode theory and simulation.

The analytic results for the 3D nanopatch, presented in Fig. 8.7, indicate that the threshold occurs around $8 \times 10^6 W/m^2$ where $\phi_p = \phi_{p,c}$ and $\mathcal{N}' = \mathcal{N}'_c$, which are in strong agreement with the threshold in the simulation curve. As in the 2D nanostripe case, the emission photon count begins to diverge exponentially at the threshold pump intensity within a reasonable margin determined by the limitations of the numerical approximations made previously.

9

Surface Modes of Film-Coupled Metasurfaces

In chapter 8, the threshold and critical population intensities for single film-coupled nanopatch antennas were analytically predicted using a coupled-mode theory approach. Here we turn our attention to arrays of film-coupled nanopatch antennas that form a film-coupled metasurface. Experimental works demonstrating lasing in metasurfaces have very recently attracted significant interest[135, 136, 137, 138, 139] because the surface can demonstrate spatial coherence over very large areas of the metasurface, showing that all the metamaterial elements are oscillating collectively due to their strong mutual coupling. Here we present the first steps towards a fully analytical treatment of lasing in metasurface modes by proving the existence of surface modes and solving for the complex eigenfrequencies of the modes. Moreover, we demonstrate that these modes radiate in collimated beams from the surface that then can be immediately useful as a source or coupled to an optical fiber. The theory and simulations from this section was developed solely by myself, and has yet to be published in a journal.

Formally, computing the threshold for single nanopatch antennas was done in the previous chapters by expanding the Green's function in the gap region into a sum

of modes with different resonance frequencies, with Ohmic and radiative loss rates that were included perturbatively. The interaction between the gain material and the eigenmodes of the optical cavity formed by the gap region was then taken into account by considering the coupling between the each cavity mode and the driving polarization formed by electronic transitions in the gain material. Treating the same problem for a periodic array of nanopatch antennas is significantly more complex due to the interaction between the nanopatches. In this case the Green's function must again be expanded as a set of modes, but the modes now are the modes of the entire film-coupled metasurface as opposed to simply the modes in the gap region under the nanoparticle. Moreover, the inclusion of radiative and Ohmic losses into this calculation cannot be done perturbatively in this case as it was for the individual nanopatch because there is no longer a well-defined optical cavity. Instead, we resort to the theory of *quasi-normal modes* to expand the Green's function and calculate complex resonance frequencies. Quasi-normal modes was originally developed in [140], which is a way to solve for the time domain Green's function as a sum of eigenmodes $f_\nu(\mathbf{r})$ that spatially satisfy the radiation condition at infinity, and decay in time as a complex exponential with eigenfrequency ω_ν. Explicity, it is an expansion of the form,

$$G(t,t',\mathbf{r},\mathbf{r}') = \sum_\nu \frac{f_\nu(\mathbf{r})f_\nu(\mathbf{r}')}{\langle f_\nu(\mathbf{r})|f_\nu(\mathbf{r})\rangle} e^{i\omega_\nu(t-t')}. \tag{9.1}$$

Expansions of this form that are complete are not always possible, and they depend on the form of the cavity involved. A good review of quasinormal mode theory is available in [141]. Solving for the lasing modes of a structure using quasinormal modes has several advantages over the mode structure typically used in quantum electrodynamics, where it is assumed that the universe takes on a finite size Λ and the limit is taken as $\Lambda \to \infty$[142, 143]. For quasinormal modes no limit need be taken, and radiation losses are naturally accounted for[140].

Because the theory of quasi-normal modes is most fundamentally a time-domain approach, we derive the eigenmode equations for the structure using a Lagrangian formalism. We do not prove completeness of the set, but simply prove that a set of these modes exist and follow the Sommerfeld radiation condition at infinity. A calculation similar to this one was done by Fano[144], although his formulation was quasistatic and therefore could not account for any radiative losses. Freedhoff and Kranendok also published a derivation of complex eigenfrequencies of one dimensional arrays of dipoles in free space and solved for their normal modes[35], but they approximated the Green's function and interaction constant as only dependent on the real part of the eigenfrequency and thus avoided the difficulties of singularities that form when the eigenfrequency is complex.

9.1 Analytical Treatment

In order to solve for the collective modes of a film-coupled metasurface, we begin in the usual fashion of approximating each nanopatch as a magnetic dipole. Let the system be a set of magnetic charges q_m with effective mass $\tilde{\mu}$ be attached to a lattice at positions $\mathbf{u}_\nu$ by springs with spring constant k, damping rate γ_Ω, and resonance frequency $\omega_0 = \sqrt{k/\tilde{\mu}}$. The Lagrangian for this system is,

$$\begin{aligned} L =& (1/2)\tilde{\mu}\sum_\nu |\dot{\mathbf{x}}_\nu|^2 - (1/2)k\sum_\nu \dot{\mathbf{x}}_\nu \\ &+ q_m \sum_\nu (\dot{\mathbf{x}}_\nu \cdot \mathbf{A}(\mathbf{r}_\nu) - \phi(\mathbf{r}_\nu)) \end{aligned} \tag{9.2}$$

where $\mathbf{x}_\nu(t) = \mathbf{r}_\nu(t) - \mathbf{u}_\nu$ are the displacements of the magnetic charges from their fixed lattice positions. We can rescale the Lagrangian to change it to a function of the magnetic dipole moments $\mathbf{m}_\nu = q_m \mathbf{x}_\nu$ without changing the equations of motion

by defining

$$L' = \frac{q_m^2}{\tilde{\mu}} L = (1/2) \sum_\nu |\dot{\mathbf{m}}_\nu|^2 - (1/2)\omega_0^2 \sum_\nu \dot{\mathbf{m}}_\nu + \frac{q_m^2}{\tilde{\mu}} \sum_\nu (\dot{\mathbf{m}}_\nu \cdot \mathbf{A}(\mathbf{r}_\nu) - q_m \phi(\mathbf{r}_\nu)) \tag{9.3}$$

Lagrange's equations in the context of frictional dissipative forces take the form

$$\frac{d}{dt}\frac{\partial L'}{\partial \dot{\mathbf{m}}_\rho} - \frac{\partial L'}{\partial \mathbf{m}_\rho} = \mathbf{Q}'_\rho \tag{9.4}$$

where $\mathbf{Q}'_\rho = -\gamma_\Omega \dot{\mathbf{m}}_\rho$. The first two terms on the left-hand side are each given by,

$$\frac{d}{dt}\frac{\partial L'}{\partial \dot{\mathbf{m}}_\rho} = \ddot{\mathbf{m}}_\rho + \frac{q_m}{\tilde{\mu}} \left(q_m \dot{\mathbf{A}} + \dot{\mathbf{m}}_\rho (\nabla \otimes \mathbf{A}) \right) \tag{9.5a}$$

$$\frac{\partial L'}{\partial \mathbf{m}_\rho} = -\omega_0^2 \mathbf{m}_\rho + \frac{q_m}{\tilde{\mu}} \left(\nabla (\dot{\mathbf{m}}_\rho \cdot \mathbf{A}) - q_m \nabla \phi \right) \tag{9.5b}$$

Putting these terms together, the equations of motion are,

$$\ddot{\mathbf{m}}_\rho + \gamma_\Omega \dot{\mathbf{m}}_\rho + \omega_0^2 \mathbf{m}_\rho$$

$$= \frac{q_m}{\tilde{\mu}} \left(q_m (-\nabla \phi - \dot{\mathbf{A}}) + \nabla (\dot{\mathbf{m}}_\rho \cdot \mathbf{A}) - \dot{\mathbf{m}}_\rho (\nabla \otimes \mathbf{A}) \right) \tag{9.6a}$$

$$= \frac{q_m}{\tilde{\mu}} \left(q_m (-\nabla \phi - \dot{\mathbf{A}}) + \dot{\mathbf{m}}_\rho \times (\nabla \times \mathbf{A}) \right) \tag{9.6b}$$

$$= \frac{q_m}{\tilde{\mu}} \left(q_m \mathbf{H} + \dot{\mathbf{m}}_\rho \times \mathbf{E} \right) \tag{9.6c}$$

where in the last equation $\mathbf{H} = -\nabla\phi - \dot{\mathbf{A}}$ and $\mathbf{E} = \nabla \times \mathbf{A}$ were used. For transverse modes $\dot{\mathbf{m}}_\rho \times \mathbf{E} = 0$ and so we are left simply with

$$\ddot{\mathbf{m}}_\rho + \gamma_\Omega \dot{\mathbf{m}}_\rho + \omega_0^2 \mathbf{m}_\rho = \frac{q_m^2}{\tilde{\mu}} \sum_{\nu \neq \rho} \int \mathbf{G}(\mathbf{r}_\rho - \mathbf{r}_\nu, t - t') \mathbf{m}_\nu(t') dt' \tag{9.7}$$

Now we look for solutions of the form

$$\mathbf{m}_\nu(t) = \mathbf{m} u(t) e^{i\tilde{\omega} t - \mathbf{k} \cdot \mathbf{r}_\nu} \tag{9.8}$$

where $u(t)$ is a unit step function. Substituting eq. (9.8) into eq. (9.7), we obtain

$$\sum_{\nu\neq\rho} \frac{(q_m^2/\tilde{\mu})e^{-i\mathbf{k}\cdot(\mathbf{r}_\nu-\mathbf{r}_\rho)}}{\omega_0^2-\tilde{\omega}^2+i\gamma\tilde{\omega}} \int_{-\infty}^{\infty} G_m(\mathbf{r}_\rho-\mathbf{r}_\nu,t'-t)u(t')e^{i\tilde{\omega}t'}dt' = 1 \tag{9.9}$$

where $G_m(\mathbf{r},t) = \mathbf{m}\mathbf{G}(\mathbf{r},t)\mathbf{m}/|\mathbf{m}|^2$ is the relevant component of Green's tensor. The quantity

$$\alpha(\tilde{\omega}) = \frac{q_m^2/\tilde{\mu}}{\omega_0^2-\tilde{\omega}^2+i\gamma\tilde{\omega}} \tag{9.10}$$

can be recognized as the polarizability of the magnetic dipoles, while

$$\begin{aligned}&\int_{-\infty}^{\infty} G_m(\mathbf{r}_\rho-\mathbf{r}_\nu,t'-t)u(t')e^{i\tilde{\omega}t'}dt' \\ &= \frac{1}{2\pi i}\int_{-\infty}^{\infty} \frac{G_m(\mathbf{r}_\rho-\mathbf{r}_\nu,\omega)}{\omega-\tilde{\omega}}e^{i\omega t}d\omega\end{aligned} \tag{9.11}$$

is the inverse Fourier transform of the product of the frequency domain Green's function and the spectral decomposition of the dipole oscillation. Evaluating this for the particular case of $\rho = 0$ for which we assume that $\mathbf{r}_0 = 0$, the final eigenmode equation for a mode of complex $\tilde{\omega}$ as a function of any wave-vector $\mathbf{k}$ is

$$\sum_{\nu\neq 0} e^{-i\mathbf{k}\cdot\mathbf{r}_\nu}\frac{\alpha(\tilde{\omega})}{2\pi i}\int_{-\infty}^{\infty}\frac{G_m(\mathbf{r}_\nu,\omega)}{\omega-\tilde{\omega}}e^{i(\omega-\tilde{\omega})t}d\omega = 1. \tag{9.12}$$

If $\mathbf{G}(\mathbf{r},\omega)$ has no poles, then this expression can be simply evaluated using the residue theorem,

$$\alpha(\tilde{\omega})\sum_{\nu\neq 0} e^{-i\mathbf{k}\cdot\mathbf{r}_\nu}G_m(\mathbf{r}_\nu,\tilde{\omega}) = \alpha(\tilde{\omega})C(\tilde{\omega},\mathbf{k}) = 1. \tag{9.13}$$

The quantity $C(\tilde{\omega})$ is the classical interaction constant from effective medium theory. This equation agrees with the quasistatic solution found by Fano. However, if $G_m(\mathbf{r},\omega)$ has poles or branch cuts in the upper half of the complex plane, then this expression is not exactly correct.

In appendix D, the exact Green's function of a magnetic dipole over a metal film is calculated via Sommerfeld integration. However, a particular path in the integral is chosen that splits the field up into the sum of three terms:

$$\mathbf{G}(\omega, \mathbf{r}, \mathbf{r}') = \mathbf{G}^{rad}(\omega, \mathbf{r}, \mathbf{r}') + \mathbf{G}^{ref}(\omega, \mathbf{r}, \mathbf{r}') + \mathbf{G}^{spp}(\omega, \mathbf{r}, \mathbf{r}'). \tag{9.14}$$

where the directly radiated field $\mathbf{G}_{rad}(\omega, \mathbf{r}, \mathbf{r}')$ is given by the free-space Green's function,

$$G_{yy}^{rad}(\omega, \mathbf{r}, \mathbf{r}') = \left(k^2 + \frac{\partial^2}{\partial y^2}\right) \frac{e^{-ik|\mathbf{r}-\mathbf{r}'|}}{4\pi|\mathbf{r}-\mathbf{r}'|}, \tag{9.15}$$

and the surface plasmon bound field is given by

$$G_{yy}^{spp}(\omega, \mathbf{r}, \mathbf{r}') = \frac{-i\sqrt{-\epsilon}\beta_{sp}^3}{4(1-\epsilon)} \left[H_0^{(2)}(\beta_{sp}\rho) - \cos(2\theta) H_2^{(2)}(\beta_{sp}\rho)\right] e^{-ik_z^+|z+d|}. \tag{9.16}$$

where $\beta_s p = k\sqrt{\epsilon/(\epsilon+1)}$ is the surface plasmon propagation constant. The reflected field is given by the Sommerfeld integral over γ,

$$G_{yy}^{ref}(\omega, \mathbf{r}, \mathbf{r}') = \frac{i}{8\pi} \int_\gamma \left[\frac{k^2 r_{TM}(\beta)}{\beta k_z} \frac{\partial^2}{\partial x^2} H_0^{(2)}(\beta\rho) + \frac{k_z r_{TE}(\beta)}{\beta} \frac{\partial^2}{\partial y^2} H_0^{(2)}(\beta\rho)\right] e^{-ik_z|z+2d|} d\beta. \tag{9.17}$$

where we have used $k_z = \sqrt{k^2 - \beta^2}$, and r_{TM} and r_{TE} are the Fresnel reflection coefficients of the metal film.

Returning now to the eigenvalue problem, we are seeking solutions to

$$\sum_{\nu \neq 0} e^{-i\mathbf{k}\cdot\mathbf{r}_\nu} \frac{\alpha(\tilde{\omega})}{2\pi i} \int_{-\infty}^{\infty} \frac{G_m(\mathbf{r}_\nu, \omega)}{\omega - \tilde{\omega}} e^{i(\omega-\tilde{\omega})t} d\omega = 1. \tag{9.18}$$

where the sum is over all the dipoles in the lattice excluding the dipole at the origin, and we are seeking a complex $\tilde{\omega}$ such that the condition in eq. (9.19) will be satisfied. Exchanging the order of summation and integration, we can recognize that this just

amounts to taking the Fourier transform of the frequency domain interaction constant

$$\frac{\alpha(\tilde{\omega})}{2\pi i}\int_{-\infty}^{\infty}\frac{C(\omega,\mathbf{k})}{\omega-\tilde{\omega}}e^{i(\omega-\tilde{\omega})t}d\omega=1. \tag{9.19}$$

Just as the Green's function was split in the last section into radiative, reflected, and surface plasmon contributions, we split the interaction constant here into the sum of three parts,

$$C(\omega,\mathbf{k})=C^{rad}(\omega,\mathbf{k})+C^{ref}(\omega,\mathbf{k})+C^{spp}(\omega,\mathbf{k}) \tag{9.20}$$

where each part is the sum of it's corresponding Green's function over all the dipoles,

$$C^{rad}(\omega,\mathbf{k})=\sum_{\nu\neq 0}G^{rad}_{yy}(\omega,\mathbf{r}_\nu) \tag{9.21}$$

$$C^{ref}(\omega,\mathbf{k})=\sum_{\nu\neq 0}G^{ref}_{yy}(\omega,\mathbf{r}_\nu) \tag{9.22}$$

$$C^{spp}(\omega,\mathbf{k})=\sum_{\nu\neq 0}G^{spp}_{yy}(\omega,\mathbf{r}_\nu). \tag{9.23}$$

Taking the Fourier transform of these interaction constants for complex eigenfrequencies is not at all straight forward because, when the imaginary part of the eigenfrequency is non-zero, the Green's function diverges for dipoles at infinity. This is a physical response, for a system that has no beginning time, dipoles at infinity began oscillating infinitely long ago, and therefore the mode amplitude that is observed by the dipole at the origin is the amplitude that was emitted by the dipole at infinity infinitely long ago. If the complex eigenfrequency is chosen such that the dipoles decay in time, then the amplitude of all the dipoles diverges at negative infinity in time, and therefore the frequency domain Green's function diverges for dipoles at infinity.

One could take the Fourier transform of the Green's function before taking the infinite sum, which solves the problem with the diverging Green's function because

the system then has a well-defined time at which it was "turned on" (i.e. $t = 0$), since this introduces a front or "optical precursor" for the field radiated by each dipole. Dipoles a distance greater than ct away will not contribute to the interaction constant, and therefore the field experienced by the dipole at the origin is finite. For any time t, one could therefore sum the fields due to all the dipoles within a radius $r = ct$ away from the dipole at the origin, and thereby find the time-domain interaction constant. However this approach isn't practical from a numerical standpoint due to the slow convergence of the interaction constant.

In light of the difficulty of actually computing the complete interaction constant for this problem, we focus on the surface plasmon contribution and take the exact Fourier transform only of $C^{spp}(\omega, \mathbf{k})$ and approximate the other interaction constants by their frequency domain values. Although all three components are important even at these wavelengths, the dominant impact and contribution even to the Fourier transform of the interaction constant will be due to $C^{spp}(\omega, \mathbf{k})$. In this case our eigenfrequency problem becomes, approximately,

$$\alpha(\tilde{\omega}) \left[\frac{1}{2\pi i} \int_{-\infty}^{\infty} \frac{C^{spp}(\omega, \mathbf{k})}{\omega - \tilde{\omega}} e^{i(\omega - \tilde{\omega})t} d\omega + C^{rad}(\mathrm{Re}\{\tilde{\omega}\}, \mathbf{k}) + C^{ref}(\mathrm{Re}\{\tilde{\omega}\}, \mathbf{k}) \right] = 1. \tag{9.24}$$

For the surface plasmon contribution, one can use a geometric series argument to show that the field in the frequency domain due to dipoles at infinity cancels at the origin, even though their fields diverge in the frequency domain. To show this, we return to the $C^{spp}(\omega, \mathbf{k})$ interaction constant that was computed in chapter 5. Recall that $C^{spp}(\omega, \mathbf{k})$ was computed as the sum of three terms such that $C^{spp}(\omega, \mathbf{k}) = C^{0D}(\omega) + C^{1D}(\omega, k_y) + C^{2D}(\omega, \mathbf{k})$. The first term, C^{0D} includes only the dipole at the origin and therefore does not cause any difficulties when taking the Fourier transform. $C^{1D}(\omega, k_y)$ is also rapidly converging and therefore does not introduce any difficulties either. The main contribution to the surface modes and Wood's

anomalies comes from the singularities in $C^{2D}(\omega, \mathbf{k})$, which was shown in chapter 5 to be,

$$C^{2D}(\omega, \mathbf{k}) = \frac{-i2\beta_{sp}\sqrt{-\epsilon}}{a_y(1-\epsilon)} e^{-2k_z^+ d} \sum_{\mu=-\infty}^{\infty} \Gamma_\mu \sum_{\nu=1}^{\infty} e^{-i\Gamma_\mu \nu a_x} \cos(k_x \nu a_x) \tag{9.25}$$

with $\Gamma_\mu = \sqrt{\beta_{sp}^2 - (2\pi\mu/a_y - k_y)^2}$. Recall that this C^{2D} interaction constant is the sum of the surface plasmons emitted by all the dipoles of all the columns of the lattice, excluding the column along the $x = 0$ axis. Splitting up the cosine function into a sum of complex exponentials, we obtain

$$C^{2D}(\omega, \mathbf{k}) = \frac{-i\beta_{sp}\sqrt{-\epsilon}}{a_y(1-\epsilon)} e^{-2k_z^+ d} \sum_{\mu=-\infty}^{\infty} \Gamma_\mu \sum_{\nu=1}^{\infty} e^{-i\nu(\Gamma_\mu + k_x)a_x} + e^{-i\nu(\Gamma_\mu - k_x)a_x}. \tag{9.26}$$

Applying the geometric series theorem which states that $\sum_{n=1}^{\infty} r^n = r/(1-r)$ when $|r| < 1$, we obtain

$$C^{2D}(\omega, \mathbf{k}) = \frac{-i\beta_{sp}\sqrt{-\epsilon}}{a_y(1-\epsilon)} e^{-2k_z^+ d} \sum_{\mu=-\infty}^{\infty} \frac{\Gamma_\mu e^{-i(\Gamma_\mu + k_x)a_x}}{1 - e^{-i(\Gamma_\mu + k_x)a_x}} + \frac{\Gamma_\mu e^{-i(\Gamma_\mu - k_x)a_x}}{1 - e^{-i(\Gamma_\mu - k_x)a_x}}. \tag{9.27}$$

This finally presents an explicit form for the sum if the surface plasmon fields from all of the dipoles, including the dipoles at infinity, and it will be finite when evaluated at complex resonance frequencies. We now consider the Fourier transform

$$\frac{1}{2\pi i} \int_{-\infty}^{\infty} \frac{C^{2D}(\omega, \mathbf{k})}{\omega - \tilde{\omega}} e^{i(\omega - \tilde{\omega})t} d\omega \tag{9.28}$$

Taking the Fourier transform of this equation is not easily done exactly analytically, because of the branch cuts due to Γ_μ. However, the contribution to the integral due to these branches will introduce terms that oscillate at their branch point frequencies, which are the frequencies that satisfy $\beta(\omega) = (2\pi\mu/a_y - k_y)$. The pole in the dielectric constant at $\omega_{sp}/\sqrt{2}$ for a Drude metal will also introduce terms that oscillate at

$\omega_{sp}/\sqrt{2}$. Ignoring these terms because they are not coherent with the dipoles that are assumed to oscillate at $\tilde{\omega}$, we can approximate

$$\frac{1}{2\pi i}\int_{-\infty}^{\infty}\frac{C^{2D}(\omega,\mathbf{k})}{\omega-\tilde{\omega}}e^{i(\omega-\tilde{\omega})t}d\omega \approx C^{2D}(\tilde{\omega},\mathbf{k})e^{-i\tilde{\omega}t} \tag{9.29}$$

and finally end up with the approximate eigenfrequency equation,

$$\alpha(\tilde{\omega})\left[C^{spp}(\tilde{\omega},\mathbf{k})+C^{rad}(\mathrm{Re}\{\tilde{\omega}\},\mathbf{k})+C^{ref}(\mathrm{Re}\{\tilde{\omega}\},\mathbf{k})\right]=1. \tag{9.30}$$

Returning to eq. (9.27), the branches of the Γ_ν need to be specified before the Fourier transform is taken. Here is the point where the boundary conditions of quasi-normal modes must be applied, which are that the waves must be outgoing for $r \to \infty$ away from the source. Recognizing the sum over ν as a sum over rows of dipoles, each value of Γ_μ represents a different diffracted order from each row. When $r \to \infty$, only the modes that are propagating make it to infinity, which are the modes where $\mathrm{Im}\{\Gamma_\mu\} \geqslant 0$. If $\mathrm{Im}\{\sqrt{\beta(\tilde{\omega})^2-(2\pi\mu/a_y-k_y)^2}\} \geqslant 0$ and $\mathrm{Re}\{\sqrt{\beta(\tilde{\omega})^2-(2\pi\mu/a_y-k_y)^2}\} \geqslant 0$ then the positive branch of the square root is chosen, which corresponds to a mode that is propagating outwards and therefore exponentially increasing in space. On the other hand, if $\mathrm{Im}\{\sqrt{\beta(\tilde{\omega})^2-(2\pi\mu/a_y-k_y)^2}\} \leqslant 0$ then the positive sign on the square root must again be chosen regardless of the value of the real part. Under most circumstances, the real part of Γ_μ will be negative for evanescent modes, which means that evanescent modes typically have their pointing vector oriented inwards towards the column of dipoles. Finally, if $\mathrm{Im}\{\sqrt{\beta(\tilde{\omega})^2-(2\pi\mu/a_y-k_y)^2}\} \geqslant 0$ and $\mathrm{Re}\{\sqrt{\beta(\tilde{\omega})^2-(2\pi\mu/a_y-k_y)^2}\} \leqslant 0$ then the mode is propagating at infinity, but propagating inwards which violates the radiation condition. In this case the minus sign must be chosen on the square root operation in order to satisfy the radiation condition at infinity. The choice of minus sign here indicates that the exponential decay of the column of dipoles has happened so quickly that a mode that would otherwise have been propagating has become evanescent.

9.2 Comparison with Numerical Simulations

To test the theory, we simulate a periodic film-coupled nanopatch antenna structure in comsol. The nanopatches in this geometry were silver and separated from a silver film by a gap of 5nm, which was assumed to be vacuum. The period between the nanopatches was $a = 550nm$, and the width of the nanopatches was taken to be $W = 80nm$. In this geometry, the wavenumber k_x was swept in the x-direction with periodic boundary conditions, while PMC boundary conditions were used in the y-direction to ensure that the magnetic dipole moment of the nanopatch antenna was oriented in the y-direction so that transverse modes were found. The boundary condition in the z-dimension was placed $3\mu m$ away from the metal film to enforce a radiation condition at infinity. Under these boundary conditions, the complex eigenfrequency was found in comsol that was nearest in wavenumber to $2\pi/a$. An example of the fields of the surface mode found in comsol for $k_x = 0$ is shown in fig. 9.1. In fig. 9.1(a), the z-component of the electric field shows a combination of gap mode field enhancement with a surface plasmon wave propagating between the nanopatches and coupling them together. In In fig. 9.1(b) the real part of the y-component of the magnetic field shows a plane wave propagating away from the structure, which forms the radiation losses of the surface mode.

The analytic eigenfrequency was found by numerically finding the roots of eq. (9.30) using matlab's fzero function. As was pointed out in chapter 6, an approximation for the surface mode eigenfrequency when the polarizability is small the point where the interaction diverges, i.e. $|C(\mathbf{k}, \omega)| \to \infty$. Looking at eq. (9.27), it's clear that this point is when $\beta_{sp}(\omega) = 2\pi\nu/a_x - k_x$ for any integer value of ν. This approximation is plotted alongside the analytic solution and the full-wave simulation results in fig. 9.2 for values of $k_x a_x$ from 0 to $\pi/4$, and for the full range of $k_x a_x$ in fig. 9.3.

Looking closely at figs. 9.2 and 9.3, it's clear that the analytic solution provides

an excellent prediction of both the real and imaginary parts of the surface mode eigenfrequency for smaller values of k_x, but for $k_x a_x > 0.5$ the prediction starts to break down, particularly for the imaginary part of the eigenfrequency. This is likely because, as was shown in chapter 4, the radiation loss rate of the lattice goes as $1/\cos(\theta)$, with θ being the angle of the radiated beam. Hence, as $k_x \to k$, the radiative and Sommerfeld integral components of the interaction constant will become more important, and here we have approximated them as independent of the imaginary part of the eigenfrequency.

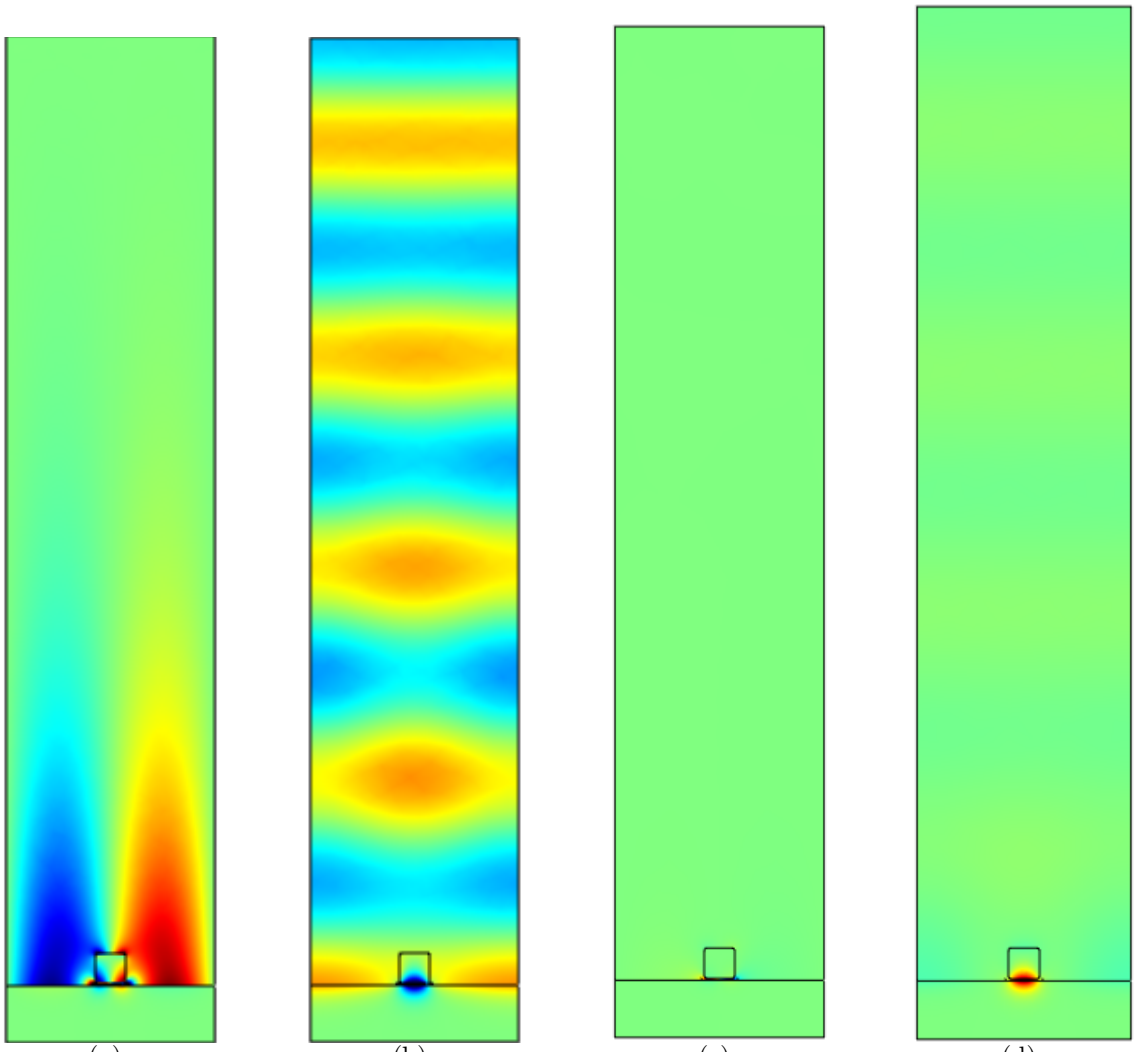

(a) (b) (c) (d)

FIGURE 9.1: Full-wave simulation results of the real parts of (a) E_z and (b) H_y for the surface mode at $k_x = 0$. These can be compared with the full-wave simulation results showing the (a) E_z and (b) H_y components of the cavity eigenmode of a single nanopatch antenna, where the total field is much more concentrated in the gap and the surface plasmon contribution is significantly lessened.

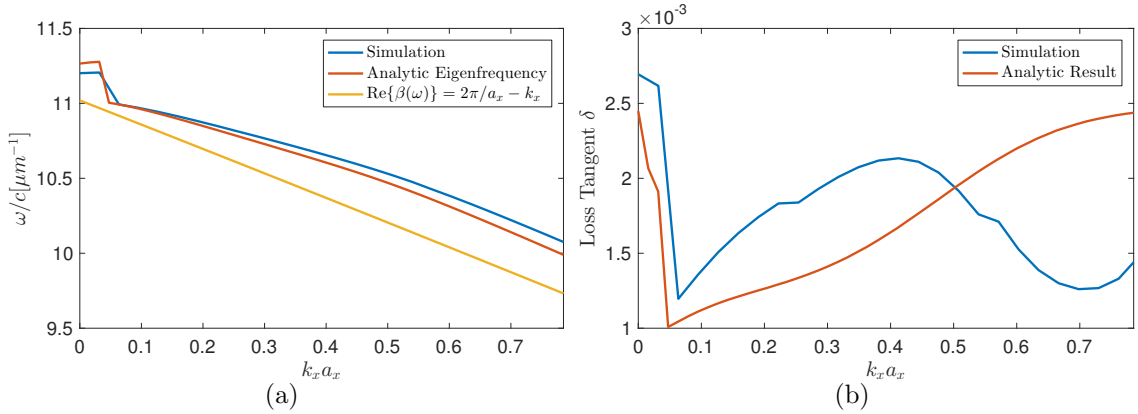

FIGURE 9.2: Simulation results for the surface mode eigenfrequency as a function of transverse wavenumber k_x for a silver film-coupled metasurface of nanopatch antennas. The analytic eigenfrequency as predicted by numerically solving eq. (9.30), and this is compared with the approximate solution given by the surface plasmon wavelength.

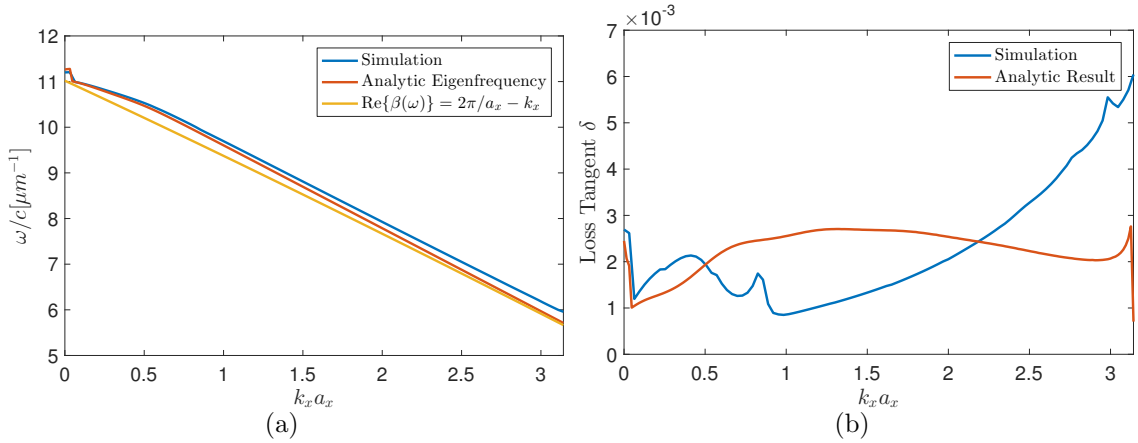

FIGURE 9.3: Comparison of simulation and analytic eigenfrequency results for a larger range of $k_x a_x$.

10

Conclusions

The film-coupled metasurface platform has been thoroughly explored as a means to achieve a vast range of useful optical phenomena, from absorbing applications in the linear regime to nonlinear applications including optical bistability and lasing. The versatility of the structure and remarkable properties come from the finely controllable gap thickness between the nanopatches and metal film, which gives a field enhancement in the gap an allows the structure to be treated as an array of plasmonic cavities that are mutually coupled by surface plasmons. The small mode volume, enhancement factor, and artifical optical magnetism of the elements ultimately give rise to the array of useful applications that have been explored in this thesis.

Not only does the structure give useful applications, but starting from the coupled mode theory treatment of the gap resonances of the film-coupled patch antennas in chapter 3, explicit and accurate analytic expressions have been derived for all of these applications in both linear and nonlinear optics. Chapter 3 focuses on deriving the equations of motion for the modes of the cavity, their eigenfrequencies and radiation and Ohmic loss rates. For some phenomena, like perfect absorption and Wood's anomalies, analytic treatment of the structure gives a satisfactory explanation for

why the phenomenon occurs. For applications to devices in engineering, the analytic formulae give a quick means to optimize the structure and predict what parameters are necessary for good device performance, as was done extensively in the chapter on lasing from single nanopatch antennas.

The analytical treatment of film-coupled metasurfaces in this work is largely based on the discrete dipole approximation of metamaterial elements, which ultimately forms the foundation of classical effective medium theory. A review of the mathematical methods of effective medium theory are presented in chapter 2, and these concepts are heavily used again in chapters 5 and 6 in order to explain the mechanisms of conservation of energy in the lattice and Wood's anomalies.

Chapter 3 focuses on deriving the equations of motion for the modes of the cavity, their eigenfrequencies and radiation and Ohmic loss rates. This eventually leads to an explanation for why the nanopatch antenna scatters as a magnetic dipole in chapter 4, which in turn provides an explanation for why the surface can behave as a perfect absorber. Perfect absorption is ultimately explained for TM polarization is ultimately explained as a complex interplay between the radiation pattern of the nanopatches and the radiation loss rate of the surface as a function of incident angle. Analytic expressions given in chapter 4 for the reflection coefficient of a film coupled metasurface moreover yield design equations that help specify the exact geometry needed for a film-coupled nanopatch antenna metasurace to achieve perfect absorption.

Chapter 5 extends the analysis of linear optics in film-coupled metasurfaces by developing an effective medium theory that is appropriate for film-coupled metasurfaces, where the coupling between the elements is dominated by the surface plasmon interaction. Appendices appendices A and B were developed to make this portion of the work possible by reworking traditional coupled mode theory in a cylindrical Hankel basis. This is a very nontrivial extension of traditional unconjugated cou-

pled mode theory because Hankel functions are not, strictly speaking, a source free solution of Maxwell's equations, and the source that is implied in the basis must be taken into account when formulating the coupling of a dipole to the modes from unconjugated Lorentz reciprocity.

The developments of chapter 5 lead to, for the first time, and explanation of the sharp and diffuse Wood's anomalies in chapter 6 from an effective medium standpoint. The theory is not only explanatory for the underlying mechanisms, but when combined with the analytic form of the polarizability derived in **??** and chapter 4, it is also predictive to a very high degree of accuracy of the measured reflectance spectra and Wood's anomalies of a lithographically fabricated film-coupled metasurface sample.

Chapter chapter 7 reaches into the first application in this dissertation of film-coupled metasurfaces to nonlinear optics, where a nonlinear material is placed in the gap region between the optical patch antenna and the metal film. The coupled mode theory and equations of motion for the mode amplitudes derived in chapter 3 and the surface plasmon coupling developed in **??** are used together to predict optical bistability of the metasurface, and these formula successfully predict the reflectance from numerical simulations.

Chapter 8 provides an analytical treatment of lasing of single film-coupled patch antennas by introducing a semiclassical four-level gain material into the gap region. Once again the cavity eigenmode expansion from chapter 3 is used to analytically predict lasing thresholds, and these are found to accurately agree with numerical simulations for both two-dimentional nanostripes and three-dimensional nanopatches.

Although lasing in single optical patch antennas is of interest, an even more useful application is lasing of an entire film-coupled metasurface, where all of the elements would couple together and radiate coherently. When an atom emits a photon in it's environment, the radiated field depends on the exact Green's function of the

atom, which will depend in turn on the lattice properties that the dipole is placed in. Chapter chapter 9 develops an expansion of the Green's function as a sum of lattice eigenmodes with complex eigenfrequencies. The complex eigenfrequency predicts both the quality factor and resonance frequency of the lasing modes of the film-coupled metasurface. This final chapter provides an exciting conclusion where lasing of a film-coupled metasurface is predicted that will radiate a plane-wave like beam from the surface that then can be coupled to an optical fiber or otherwise used in free space. This idea has recently gathered much experimental interest, but chapter 9 provides the first rigorous analytical explanation of the collective lasing modes of such a structure. In future work, the analytical formula developed here can guide experiments and designs for lasing film coupled metasurfaces.

Appendix A

Solutions to Maxwell's Equations in Cylindrical Coordinates

A.1 Separation of Variables

This appendix is a presentation of the solutions solutions to Maxwell's equations in cylindrical coordinates. This kind of expansion has been done before, and the results in reference [89] are summarized here for the sake of the self-containment and consistency of notation in this dissertation. We start with the z-component of the electric and magnetic fields, which must follow the Helmholtz equation,

$$(\nabla^2 + \epsilon k^2) \begin{Bmatrix} E_z \\ H_z \end{Bmatrix} = 0 \tag{A.1}$$

where $k = \omega/c$ is defined as the free space wavenumber. By splitting the Laplacian operator into normal and planar components, expressing it in cylindrical coordinates, and then using the curl equations, one can express all of the components of the electric

and magnetic fields solely in terms of derivatives of the z-components[88, 89]:

$$\begin{aligned}
E_r =& \frac{1}{\beta^2}\left[\frac{\partial^2 E_z}{\partial z \partial r} - \frac{ikZ_0}{r}\frac{\partial H_z}{\partial \theta}\right] \\
E_\theta =& \frac{1}{\beta^2}\left[\frac{1}{r}\frac{\partial^2 E_z}{\partial \theta \partial z} + ikZ_0\frac{\partial H_z}{\partial r}\right] \\
H_r =& \frac{1}{\beta^2}\left[\frac{ik\epsilon}{Z_0 r}\frac{\partial E_z}{\partial \theta} + \frac{\partial^2 H_z}{\partial r \partial z}\right] \\
H_\theta =& \frac{1}{\beta^2}\left[\frac{-ik\epsilon}{Z_0}\frac{\partial E_z}{\partial r} + \frac{1}{r}\frac{\partial^2 H_z}{\partial \theta \partial z}\right]
\end{aligned} \tag{A.2}$$

We define TE waves as those where $E_z = 0$, and TM waves as those where $H_z = 0$. Using these definitions, we perform separation of variables on the z-component of the field:

$$E_z(r, \theta, z) = R_{\mu\nu}(r)\Theta_\nu(\theta)Z_\mu(z). \tag{A.3}$$

This provides the solution for TM modes. TM modes are found by assuming

$$H_z(r, \theta, z) = R_{\mu\nu}(r)\Theta_\nu(\theta)Z_\mu(z). \tag{A.4}$$

Plugging these expressions into (A.1) one at a time, with the laplacian expressed in cylindrical coordinates, we can separate the variables as,

$$\frac{d^2 Z_\mu}{dz^2} + k^2\epsilon(z)Z_\mu = \beta_\mu^2 Z_\mu \tag{A.5a}$$

$$\frac{d^2\Theta_\nu}{d\theta^2} = -\nu^2\Theta_\nu \tag{A.5b}$$

$$r\frac{d}{dr}\left(r\frac{dR_\nu}{dr}\right) + [(\beta_\mu r)^2 - \nu^2]R_\nu = 0 \tag{A.5c}$$

where the variables β_μ and ν are constants of separation. The $\Theta_\nu(\theta)$ and $Z_\mu(z)$ functions must be indexed by mode numbers ν and μ respectively, since we assume here that the boundary conditions are applied in the z and θ coordinates, which turns

eqs. (A.5a) and (A.5b) into an eigenvalue problem with β_μ^2 and ν^2 as eigenvalues. The r-coordinate is assumed to have no boundary conditions, so $R_{\mu\nu}(r)$ inherits it's mode numbers from the $\Theta_\nu(\theta)$ and $Z_\mu(z)$ functions through the separation of variables process.

The solutions to eq. (A.5b) are given immediately as,

$$\Theta_\nu(\theta) = e^{i\nu\theta}, \tag{A.6}$$

and since the expression for $\Theta_\nu(\theta)$ must be 2π periodic, ν must be an integer.

The boundary conditions corresponding to the z-coordinate will yield an eigenvalue problem for $Z_\mu(z)$, with β_μ^2 as the eigenvalue. The boundary conditions themselves will come from substituting $Z_\mu(z)$ into (A.2), and requiring that the fields either decay to zero at infinity (which yields the surface plasmon guided solution), or satisfy the radiation condition at infinity (which yields the radiation modes).

The $Z_\mu(z)$ functions that correspond to bound modes can be normalized so that

$$\int_{-\infty}^{\infty} \epsilon(z)[Z_\mu^{TM}(z)]^2 \mathrm{d}z = L \tag{A.7a}$$

$$\int_{-\infty}^{\infty} [Z_\mu^{TE}(z)]^2 \mathrm{d}z = L \tag{A.7b}$$

for bound (SPP) modes, where L is an arbitrary normalization constant with units of length. This particular normalization needs to be used in order for the orthogonality relationship given in eq. (B.11) to have the same normalization for TM and TE modes, and ensures that the $Z_\mu(z)$ functions will be dimensionless.

In the particular example of the interface between a dielectric and a metal film, there is only one TM bound mode, which is the SPP. In this case, the z-dependence is given by

$$Z^{TM}(z) = \begin{cases} \frac{k_z^-}{k}\sqrt{\frac{2k_z^+ L}{1-\epsilon}} e^{-k_z^+ z} & z \geqslant 0 \\ \\ \frac{-k_z^+}{k}\sqrt{\frac{2k_z^+ L}{1-\epsilon}} e^{k_z^- z} & z \leqslant 0 \end{cases} \tag{A.8}$$

where $k_z^+ = ik/\sqrt{\epsilon+1}$, and $k_z^- = -i\epsilon k/\sqrt{\epsilon+1}$, and the eigenvalue that corresponds to this solution is $\beta = k\sqrt{\epsilon/(\epsilon+1)}$.

In the particular case of a parallel plate waveguide, the boundary conditions are that the electric field tangent to the walls of the guide be zero. This yields separate boundary conditions depending on whether the mode is TE or TM, and the result is that, for a waveguide filled with a single dielectric,

$$Z_\mu^{TM}(z) = \sqrt{\frac{2}{\epsilon(1+\delta_{\nu 0})}}\cos\left(\frac{\mu\pi}{h}z\right) \qquad \mu = 0, 1, 2, 3.... \tag{A.9}$$

$$Z_\mu^{TE}(z) = \sqrt{\frac{2}{(1+\delta_{\nu 0})}}\sin\left(\frac{\mu\pi}{h}z\right) \qquad \mu = 1, 2, 3.... \tag{A.10}$$

Algorithms are provided in appendix A.2.1 and **??** to solve for the $Z_\mu^{TM}(z)$ and $Z_\mu^{TE}(z)$ functions for a parallel plate waveguide with an arbitrary dielectric stack.

The solutions for the $R_\nu(r)$ equation are the Hankel functions $H_\nu^{(2)}(\beta_\mu r)$ for outgoing waves and $H_\nu^{(1)}(\beta_\mu r)$ for incoming waves (assuming an $e^{i\omega t}$ time dependence). Putting all of this together and substituting into (A.2), we have an expansion for the TM modes in terms of the *cylindrical Bessel functions*,

$$E_{\mu\nu z}^{TM} = n_\mu H_\nu^{(2)}(\beta_\mu r)e^{i\nu\theta}Z_\mu^{TM}(z) \tag{A.11a}$$

$$E_{\mu\nu r}^{TM} = \frac{1}{k}\frac{\partial}{\partial(\beta_\mu r)}H_\nu^{(2)}(\beta_\mu r)e^{i\nu\theta}\frac{dZ_\mu^{TM}(z)}{dz} \tag{A.11b}$$

$$E_{\mu\nu\theta}^{TM} = \frac{i\nu}{k}\frac{H_\nu^{(2)}(\beta_\mu r)}{\beta_\mu r}e^{i\nu\theta}\frac{dZ_\mu^{TM}(z)}{dz} \tag{A.11c}$$

$$H_{\mu\nu z}^{TM} = 0 \tag{A.11d}$$

$$H_{\mu\nu r}^{TM} = \frac{-\nu\epsilon}{Z_0}\frac{H_\nu^{(2)}(\beta_\mu r)}{\beta_\mu r}e^{i\nu\theta}Z_\mu^{TM}(z) \tag{A.11e}$$

$$H_{\mu\nu\theta}^{TM} = \frac{-i\epsilon}{Z_0}\frac{\partial}{\partial(\beta_\mu r)}H_\nu^{(2)}(\beta_\mu r)e^{i\nu\theta}Z_\mu^{TM}(z) \tag{A.11f}$$

and the TE modes,

$$E^{TE}_{\mu\nu z} = 0 \tag{A.12a}$$

$$E^{TE}_{\mu\nu r} = \nu \frac{H^{(2)}_\nu(\beta_\mu r)}{\beta_\mu r} e^{i\nu\theta} Z^{TE}_\mu(z) \tag{A.12b}$$

$$E^{TE}_{\mu\nu\theta} = i \frac{\partial}{\partial(\beta_\mu r)} H^{(2)}_\nu(\beta_\mu r) e^{i\nu\theta} Z^{TE}_\mu(z) \tag{A.12c}$$

$$H^{TE}_{\mu\nu z} = \frac{n_\mu}{Z_0} H^{(2)}_\nu(\beta_\mu r) e^{i\nu\theta} Z^{TE}_\mu(z) \tag{A.12d}$$

$$H^{TE}_{\mu\nu r} = \frac{1}{Z_0 k} \frac{\partial}{\partial(\beta_\mu r)} H^{(2)}_\nu(\beta_\mu r) e^{i\nu\theta} \frac{dZ^{TE}_\mu(z)}{dz} \tag{A.12e}$$

$$H^{TE}_{\mu\nu\theta} = \frac{i\nu}{Z_0 k} \frac{H^{(2)}_\nu(\beta_\mu r)}{\beta_\mu r} e^{i\nu\theta} \frac{dZ^{TE}_\mu(z)}{dz} \tag{A.12f}$$

Note that the electric field of the eigenmodes has been normalized here to be dimensionless, and the magnetic field has units of inverse impedance. The modes have also been normalized by a factor of $n_\mu = \beta_\mu/k$ in order for both the TE and TM modes to obey the same orthogonality relationship in eq. (B.11).

It is useful to express the modes in a $\{\sin(\nu\theta), \cos(\nu\theta)\}$ basis instead of the complex exponential basis. In that basis, the TM modes are given by

$$E^{TMc}_{\mu\nu z} = n_\mu H^{(2)}_\nu(\beta_\mu r) \cos(\nu\theta) Z^{TM}_\mu(z) \tag{A.13a}$$

$$E^{TMc}_{\mu\nu r} = \frac{1}{k} \frac{\partial}{\partial(\beta_\mu r)} H^{(2)}_\nu(\beta_\mu r) \cos(\nu\theta) \frac{dZ^{TM}_\mu(z)}{dz} \tag{A.13b}$$

$$E^{TMc}_{\mu\nu\theta} = \frac{-\nu}{k} \frac{H^{(2)}_\nu(\beta_\mu r)}{\beta_\mu r} \sin(\nu\theta) \frac{dZ^{TM}_\mu(z)}{dz} \tag{A.13c}$$

$$H^{TMc}_{\mu\nu z} = 0 \tag{A.13d}$$

$$H^{TMc}_{\mu\nu r} = \frac{-i\nu\epsilon}{Z_0} \frac{H^{(2)}_\nu(\beta_\mu r)}{\beta_\mu r} \sin(\nu\theta) Z^{TM}_\mu(z) \tag{A.13e}$$

$$H^{TMc}_{\mu\nu\theta} = \frac{-i\epsilon}{Z_0} \frac{\partial}{\partial(\beta_\mu r)} H^{(2)}_\nu(\beta_\mu r) \cos(\nu\theta) Z^{TM}_\mu(z) \tag{A.13f}$$

$$E^{TMs}_{\mu\nu z} = n_\mu H^{(2)}_\nu(\beta_\mu r)\sin(\nu\theta)Z^{TM}_\mu(z) \tag{A.14a}$$

$$E^{TMs}_{\mu\nu r} = \frac{1}{k}\frac{\partial}{\partial(\beta_\mu r)}H^{(2)}_\nu(\beta_\mu r)\sin(\nu\theta)\frac{dZ^{TM}_\mu(z)}{dz} \tag{A.14b}$$

$$E^{TMs}_{\mu\nu\theta} = \frac{-i\nu}{k}\frac{H^{(2)}_\nu(\beta_\mu r)}{\beta_\mu r}\cos(\nu\theta)\frac{dZ^{TM}_\mu(z)}{dz} \tag{A.14c}$$

$$H^{TMs}_{\mu\nu z} = 0 \tag{A.14d}$$

$$H^{TMs}_{\mu\nu r} = \frac{i\nu\epsilon}{Z_0}\frac{H^{(2)}_\nu(\beta_\mu r)}{\beta_\mu r}\cos(\nu\theta)Z^{TM}_\mu(z) \tag{A.14e}$$

$$H^{TMs}_{\mu\nu\theta} = \frac{-i\epsilon}{Z_0}\frac{\partial}{\partial(\beta_\mu r)}H^{(2)}_\nu(\beta_\mu r)\sin(\nu\theta)Z^{TM}_\mu(z) \tag{A.14f}$$

The TE modes in the $\{\sin(\nu\theta), \cos(\nu\theta)\}$ basis are,

$$E^{TEc}_{\mu\nu z} = 0 \tag{A.15a}$$

$$E^{TEc}_{\mu\nu r} = -\nu\frac{H^{(2)}_\nu(\beta_\mu r)}{\beta_\mu r}\sin(\theta)Z^{TE}_\mu(z) \tag{A.15b}$$

$$E^{TEc}_{\mu\nu\theta} = -\frac{\partial}{\partial(\beta_\mu r)}H^{(2)}_\nu(\beta_\mu r)\cos(\theta)Z^{TE}_\mu(z) \tag{A.15c}$$

$$H^{TEc}_{\mu\nu z} = \frac{in_\mu}{Z_0}H^{(2)}_\nu(\beta_\mu r)\cos(\theta)Z^{TE}_\mu(z) \tag{A.15d}$$

$$H^{TEc}_{\mu\nu r} = \frac{i}{Z_0 k}\frac{\partial}{\partial(\beta_\mu r)}H^{(2)}_\nu(\beta_\mu r)\cos(\theta)\frac{dZ^{TE}_\mu(z)}{dz} \tag{A.15e}$$

$$H^{TEc}_{\mu\nu\theta} = \frac{-i\nu}{Z_0 k}\frac{H^{(2)}_\nu(\beta_\mu r)}{\beta_\mu r}\sin(\theta)\frac{dZ^{TE}_\mu(z)}{dz} \tag{A.15f}$$

$$E^{TEs}_{\mu\nu z} = 0 \tag{A.16a}$$

$$E^{TEs}_{\mu\nu r} = \nu \frac{H^{(2)}_{\nu}(\beta_\mu r)}{\beta_\mu r} \cos(\theta) Z^{TE}_{\mu}(z) \tag{A.16b}$$

$$E^{TEs}_{\mu\nu\theta} = -\frac{\partial}{\partial(\beta_\mu r)} H^{(2)}_{\nu}(\beta_\mu r) \sin(\theta) Z^{TE}_{\mu}(z) \tag{A.16c}$$

$$H^{TEs}_{\mu\nu z} = \frac{i n_\mu}{Z_0} H^{(2)}_{\nu}(\beta_\mu r) \sin(\theta) Z^{TE}_{\mu}(z) \tag{A.16d}$$

$$H^{TEs}_{\mu\nu r} = \frac{i}{Z_0 k} \frac{\partial}{\partial(\beta_\mu r)} H^{(2)}_{\nu}(\beta_\mu r) \sin(\theta) \frac{dZ^{TE}_{\mu}(z)}{dz} \tag{A.16e}$$

$$H^{TEs}_{\mu\nu\theta} = \frac{i\nu}{Z_0 k} \frac{H^{(2)}_{\nu}(\beta_\mu r)}{\beta_\mu r} \cos(\theta) \frac{dZ^{TE}_{\mu}(z)}{dz}. \tag{A.16f}$$

A.2 Transfer Matrix Method for Multilayer Planar Waveguide Modes

Consider a planar waveguide that contains multiple layers of dielectric material inside it. The expansion into cylindrical bessel functions will be valid in each layer individually, but the relative amplitudes of these bessel functions in each layer must be set correctly in order for the electric and magnetic fields to satisfy the boundary conditions between the various layers. We will use a transfer matrix formalism to construct a quasi-analytic approach to finding the propagation constants β_μ and z-dependence of the fields $Z_\mu(z)$ in a multilayer planar waveguide structure. Each layer i may have a different z-dependence on the fields, which will be given by the function $Z_i(z)$. Since the waveguide modes are valid in each layer independently, each function $Z_i(z)$ can be expressed as some sum of sine and cosine functions with some wavenumber $\xi_i = k\sqrt{\epsilon_i - n_\mu^2}$, where $n_\mu = \beta_\mu/k$ is the index of the m^{th} waveguide mode.

$$Z_i(z) = A_{ci} \cos(\xi_i z) + A_{si} \sin(\xi_i z) \tag{A.17}$$

The boundary conditions between the various dielectric layers are that the normal components of $D = \epsilon E$ are continuous, and the tangential components of E are continuous across the boundaries. These boundary conditions, however, yield different conditions on the functions $Z_\mu^{TE}(z)$ and $Z_\mu^{TM}(z)$. Each of these cases are treated separately below.

A.2.1 TM Modes

For TM modes, continuity of the displacement field and tangential electric field yield the boundary conditions,

$$\epsilon_i Z_i^{TM}(h_i) = \epsilon_{i+1} Z_{i+1}^{TM}(h_i) \tag{A.18}$$

$$\frac{d}{dz} Z_i^{TM}|_{h_i} = \frac{d}{dz} Z_{i+1}^{TM}|_{h_i}. \tag{A.19}$$

These boundary conditions can be written as a 2×2 matrix equation relating the coefficients between the layers,

$$\mathbf{M}_i(\xi_i, h_i)\mathbf{A}_i = \mathbf{M}_{i+1}(\xi_{i+1}, h_i)\mathbf{A}_{i+1} \tag{A.20}$$

where $\mathbf{A}_i = (A_{ci}, A_{si})^t$. The matrices are given by

$$\mathbf{M}_i(\xi_i, h_i) = \begin{bmatrix} \epsilon_i \cos(\xi_i h_i) & \epsilon_i \sin(\xi_i h_i) \\ -\xi_i \sin(\xi_i h_i) & \xi_i \cos(\xi_i h_i) \end{bmatrix} \tag{A.21}$$

If a planar waveguide has N layers of dielectric material, then these matrices can be used to establish a linear relationship between the coefficients in the first layer $\mathbf{A}_1$ and the coefficients in the final layer $\mathbf{A}_N$.

$$\mathbf{A}_1 = \mathbf{M}_1^{-1}(\xi_1, h_1)\mathbf{M}_2(\xi_2, h_1)\mathbf{M}_2^{-1}(\xi_2, h_2)... \ \mathbf{M}_N(\xi_N, h_{N-1})\mathbf{A}_N \tag{A.22}$$

$$\mathbf{A}_1 = \mathbf{T}\mathbf{A}_N \tag{A.23}$$

where $\mathbf{T}$ is a 2×2 matrix formed by the multiplication of all of the $\mathbf{M}_i$ matrices as shown above. One approach to solving this problem is to get all of the unknowns,

$\mathbf{A}_1$ and $\mathbf{A}_N$, into a single vector. Doing that will turn this equation into a 2×4 rectangular matrix equation.

$$(\mathbf{A}_1 - \mathbf{T}\mathbf{A}_N) = 0 \tag{A.24}$$

$$\begin{bmatrix} \mathbf{I} & \mathbf{T} \end{bmatrix} \begin{bmatrix} \mathbf{A}_1 \\ \mathbf{A}_N \end{bmatrix} = \begin{bmatrix} 0 \\ 0 \end{bmatrix} \tag{A.25}$$

The boundary conditions of the metal surface of the waveguide are that the tangential components of the electric field must be zero.

$$\frac{d}{dz} Z_0^{TM}|_0 = 0 \tag{A.26}$$

$$\frac{d}{dz} Z_N^{TM}|_{h_N} = 0 \tag{A.27}$$

This condition can also be written as a 2×4 rectangular matrix equation.

$$\begin{bmatrix} 0 & 1 & 0 & 0 \\ 0 & 0 & -\xi_N \sin(\xi_N h_N) & \xi_N \cos(\xi_N h_N) \end{bmatrix} \begin{bmatrix} \mathbf{A}_1 \\ \mathbf{A}_N \end{bmatrix} = \begin{bmatrix} 0 \\ 0 \end{bmatrix} \tag{A.28}$$

The linear relationship between the coefficients given in eq. (A.42) and the boundary conditions in eq. (A.28) can be combined to yield a 4×4 matrix equation.

$$\begin{bmatrix} 1 & 0 & T_{11} & T_{12} \\ 0 & 1 & T_{21} & T_{22} \\ 0 & 1 & 0 & 0 \\ 0 & 0 & -\xi_N \sin(\xi_N h_N) & \xi_N \cos(\xi_N h_N) \end{bmatrix} \begin{bmatrix} \mathbf{A}_1 \\ \mathbf{A}_N \end{bmatrix} = \begin{bmatrix} 0 \\ 0 \end{bmatrix} \tag{A.29}$$

A solution only exists if the determinant of the matrix is zero.

$$\mathbf{M}_{sys}(\xi_1, \xi_2, ...\xi_N) \begin{bmatrix} \mathbf{A}_1 \\ \mathbf{A}_N \end{bmatrix} = \begin{bmatrix} 0 \\ 0 \end{bmatrix} \tag{A.30}$$

$$\det\left(\mathbf{M}_{sys}(\xi_1, \xi_2, ...\xi_N)\right) = 0 \tag{A.31}$$

This matrix is a function of the z-wavenumbers $(\xi_1, \xi_2, ...\xi_N)$, which are all unknown, so it would appear that we have a single equation and N unknowns for N layers.

However, recall that each of the ξ_i is actually a function of the radial propagation constant β.

$$\xi_i = \sqrt{\epsilon_i k^2 - \beta^2} \tag{A.32}$$

Then there is one equation to solve with only one unknown, β, which can be solved numerically.

$$\det\left(\mathbf{M}_{sys}(\beta)\right) = 0 \tag{A.33}$$

The propagation constant β and the determinant of the matrix $\det\left(\mathbf{M}_{sys}\right)$ each have both real and imaginary parts, and both the real and imaginary parts of the determinant must be zero. Therefore when this equation is numerically solved we effectively end up with two equations and two unknowns. Finding β associated with different m values just involves choosing a different starting point with the numerical solver. The numerical solver will find the solution that is "closest" to your initial starting point.

Once β is determined, all of the ξ_i are immediately determined by eq. (A.49). We can also choose to set $\mathbf{A}_1 = (1, 0)$, since this will satisfy the boundary conditions of the waveguide, and normalize the entire $Z_\mu(z)$ function so that $Z_\mu(0) = 1$. Then each of the following amplitude coefficients $\mathbf{A}_i$ can be determined using eq. (A.38).

A.2.2 TE Modes

For TE modes, continuity of the displacement field and tangential electric field yield the boundary conditions,

$$Z_i^{TM}(h_i) = Z_{i+1}^{TM}(h_i) \tag{A.34}$$

$$\frac{d}{dz} Z_i^{TM}|_{h_i} = \frac{d}{dz} Z_{i+1}^{TM}|_{h_i}. \tag{A.35}$$

$$\tag{A.36}$$

These boundary conditions can be written as a 2×2 matrix equation relating the coefficients between the layers,

$$\mathbf{M}_i(\xi_i, h_i)\mathbf{A}_i = \mathbf{M}_{i+1}(\xi_{i+1}, h_i)\mathbf{A}_{i+1} \tag{A.37}$$

where $\mathbf{A}_i = (A_{ci}, A_{si})^t$. The matrices are given by

$$\mathbf{M}_i(\xi_i, h_i) = \begin{bmatrix} \cos(\xi_i h_i) & \sin(\xi_i h_i) \\ -\xi_i \sin(\xi_i h_i) & \xi_i \cos(\xi_i h_i) \end{bmatrix} \tag{A.38}$$

If a planar waveguide has N layers of dielectric material, then these matrices can be used to establish a linear relationship between the coefficients in the first layer $\mathbf{A}_1$ and the coefficients in the final layer $\mathbf{A}_N$.

$$\mathbf{A}_1 = \mathbf{M}_1^{-1}(\xi_1, h_1)\mathbf{M}_2(\xi_2, h_1)\mathbf{M}_2^{-1}(\xi_2, h_2)... \ \mathbf{M}_N(\xi_N, h_{N-1})\mathbf{A}_N \tag{A.39}$$

$$\mathbf{A}_1 = \mathbf{T}\mathbf{A}_N \tag{A.40}$$

where $\mathbf{T}$ is a 2×2 matrix formed by the multiplication of all of the $\mathbf{M}_i$ matrices as shown above. One approach to solving this problem is to get all of the unknowns, $\mathbf{A}_1$ and $\mathbf{A}_N$, into a single vector. Doing that will turn this equation into a 2×4 rectangular matrix equation.

$$(\mathbf{A}_1 - \mathbf{T}\mathbf{A}_N) = 0 \tag{A.41}$$

$$\begin{bmatrix} \mathbf{I} & \mathbf{T} \end{bmatrix} \begin{bmatrix} \mathbf{A}_1 \\ \mathbf{A}_N \end{bmatrix} = \begin{bmatrix} 0 \\ 0 \end{bmatrix} \tag{A.42}$$

The boundary conditions of the metal surface of the waveguide are that the tangential components of the electric field must be zero.

$$Z_0^{TE}|_0 = 0 \tag{A.43}$$

$$Z_N^{TE}|_{h_N} = 0 \tag{A.44}$$

This condition can also be written as a 2×4 rectangular matrix equation.

$$\begin{bmatrix} 1 & 0 & 0 & 0 \\ 0 & 0 & \cos(\xi_N h_N) & \sin(\xi_N h_N) \end{bmatrix} \begin{bmatrix} \mathbf{A}_1 \\ \mathbf{A}_N \end{bmatrix} = \begin{bmatrix} 0 \\ 0 \end{bmatrix} \tag{A.45}$$

The linear relationship between the coefficients given in eq. (A.42) and the boundary conditions in eq. (A.45) can be combined to yield a 4×4 matrix equation.

$$\begin{bmatrix} 1 & 0 & T_{11} & T_{12} \\ 0 & 1 & T_{21} & T_{22} \\ 1 & 0 & 0 & 0 \\ 0 & 0 & \cos(\xi_N h_N) & \sin(\xi_N h_N) \end{bmatrix} \begin{bmatrix} \mathbf{A}_1 \\ \mathbf{A}_N \end{bmatrix} = \begin{bmatrix} 0 \\ 0 \end{bmatrix} \tag{A.46}$$

A solution only exists if the determinant of the matrix is zero.

$$\mathbf{M}_{sys}(\xi_1, \xi_2, ...\xi_N) \begin{bmatrix} \mathbf{A}_1 \\ \mathbf{A}_N \end{bmatrix} = \begin{bmatrix} 0 \\ 0 \end{bmatrix} \tag{A.47}$$

$$\det\left(\mathbf{M}_{sys}(\xi_1, \xi_2, ...\xi_N)\right) = 0 \tag{A.48}$$

This matrix is a function of the z-wavenumbers $(\xi_1, \xi_2, ...\xi_N)$, which are all unknown, so it would appear that we have a single equation and N unknowns for N layers. However, recall that each of the ξ_i is actually a function of the radial propagation constant β.

$$\xi_i = \sqrt{\epsilon_i k^2 - \beta^2} \tag{A.49}$$

Then there is one equation to solve with only one unknown, β, which can be solved numerically.

$$\det\left(\mathbf{M}_{sys}(\beta)\right) = 0 \tag{A.50}$$

The propagation constant β and the determinant of the matrix $\det\left(\mathbf{M}_{sys}\right)$ each have both real and imaginary parts, and both the real and imaginary parts of the determinant must be zero. Therefore when this equation is numerically solved we effectively end up with two equations and two unknowns. Finding β associated with different m values just involves choosing a different starting point with the numerical solver. The numerical solver will find the solution that is "closest" to your initial starting point.

Once β is determined, all of the ξ_i are immediately determined by eq. (A.49). We can also choose to set $\mathbf{A}_1 = (1, 0)$, since this will satisfy the boundary conditions of the waveguide, and normalize the entire $Z_\mu(z)$ function so that $Z_\mu(0) = 1$. Then each of the following amplitude coefficients $\mathbf{A}_i$ can be determined using eq. (A.38).

Appendix B

Coupled Mode Theory in a Cylindrical Hankel Basis

This appendix derives the generation of electromagnetic waves by an arbitrary distribution of polarization and magnetization fields, but with the waves expanded in a cylindrical Hankel basis. I developed the theory in order to solve for the surface plasmon cylindrical wave of a magnetic dipole placed close to a metal film, in order to develop an effective medium theory of film-coupled magnetic metasurfaces that can be applied to optical patch antennas[92]. I worked by myself, under the guidance of my advisor Dr. David R. Smith. In the initial attempts to solve this problem, we discovered that traditional coupled mode theory could not be applied, because most traditional formulations assume that the basis of eigenmodes that is used for the expansion of the field is source-free. This is not true for Hankel functions, and so accurately solving this problem required a new, careful development starting from unconjugated Lorentz reciprocity.

B.1 Derivation From Unconjugated Lorentz Reciprocity

Coupled mode theory is a method to find solutions to Maxwell's equations,

$$\nabla \times \mathbf{E} = -i\omega\mu_0\mathbf{H} - i\omega\mu_0\mathbf{M} \tag{B.1}$$

$$\nabla \times \mathbf{H} = i\omega\epsilon_0\mathbf{E} + i\omega\mathbf{P} \tag{B.2}$$

by expanding the field in a sum of modes

$$\mathbf{E} = \sum_{\mu\nu} A_{\mu\nu}\mathbf{E}_{\mu\nu} \tag{B.3a}$$

$$\mathbf{H} = \sum_{\mu\nu} A_{\mu\nu}\mathbf{H}_{\mu\nu} \tag{B.3b}$$

where the modes are themselves solutions of Maxwell's equations:

$$\nabla \times \mathbf{E}_{\mu\nu} = -i\omega\mu_0\mathbf{H}_{\mu\nu} - i\omega\mu_0\mathbf{M}_{\mu\nu} \tag{B.4}$$

$$\nabla \times \mathbf{H}_{\mu\nu} = i\omega\epsilon_0\epsilon\mathbf{E}_{\mu\nu} + i\omega\mathbf{P}_{\mu\nu}. \tag{B.5}$$

Here, we are viewing the solution to Maxwell's equations as the actual fields distributed everywhere in the system, with $\mathbf{P}$ and $\mathbf{M}$ representing the actual electric and magnetic polarizations of each of the metamaterial elements. This will problem will be solved by expanding the fields in an eigenmode basis, which is given by the cylindrical waveguide modes. We will consider these modes in a Hankel function basis, where the modes are all propagating waves. The details of these modes and their derivation are given in the appendix. However, there are two important properties of these modes that must first be noted before deriving the coupled mode theory equations.

Firstly, it ought to be noted that the cylindrical Hankel functions are *not* source-free solutions to Maxwell's equations. Normally, coupled mode theory is developed using a basis of source-free solutions of Maxwell's equations (i.e $\mathbf{P}_\nu = \mathbf{M}_\nu = 0$), which are therefore eigenmodes of Maxwell's equations. This is the assumption that was

used in references [89, 90] when deriving the coupling of sources to Hankel cylindrical modes. However, the cylindrical Hankel basis that we are considering is not a set of source-free solutions to Maxwell's equations, since each of those modes imply the existence of of a point-source at the origin. For example, the source implied by the fundamental TM mode may be found by using the integral form of Maxwell's equations,

$$i\omega \int_S \mathbf{P}^{\pm}_{\mu\nu} \cdot \mathrm{d}\mathbf{a} = \int_{\partial S} \mathbf{H}^{\pm}_{\mu\nu} \cdot \mathrm{d}\mathbf{l} - i\omega\epsilon_0\epsilon \int_S \mathbf{E}^{\pm}_{\mu\nu} \cdot \mathrm{d}\mathbf{a} \tag{B.6}$$

where the + sign corresponds to solutions that are outgoing waves and the − sign corresponds to solutions that are incoming waves. The surface S may be chosen to be a small disk oriented in the $\hat{\mathbf{z}}$ direction with any arbitrary radius. If the TE and TM modes with $\nu = 0$ (see appendix A) are used in eq. (B.6), then the right hand side evaluates to

$$i\omega \int_S \mathbf{P}^{\pm}_{\mu 0} \cdot \mathrm{d}\mathbf{a} = \frac{\mp 4\epsilon(z) Z_\mu(z)}{\beta_\mu Z_0}, \tag{B.7}$$

which is independent of the radius of the disk. Clearly, $\mathbf{P}^{\pm}_{\mu\nu}$ cannot be zero everywhere. Moreover, since the right-hand side is entirely independent of the radius of the disk of integration, the integral on the left must also be independent of the disk of integration. The argument $\mathbf{P}^{\pm}_{\mu\nu}$ must either go as $1/r$, or else have a delta function form in the radial coordinate. Since the Hankel functions are known to be source-free solutions when $r \neq 0$, $\mathbf{P}^{\pm}_{\mu\nu}$ must have a delta-function form. Hence, we have that

$$\mathbf{P}^{TM\pm}_{\mu 0} = \hat{\mathbf{z}} \frac{\pm i 4\epsilon_0 \epsilon(z) Z_\mu(z)}{\beta_\mu k} \frac{\delta(r)}{2\pi r} \tag{B.8a}$$

$$\mathbf{M}^{TM\pm}_{\mu 0} = 0 \tag{B.8b}$$

$$\mathbf{P}^{TE\pm}_{\mu 0} = 0 \tag{B.8c}$$

$$\mathbf{M}^{TE\pm}_{\mu 0} = \hat{\mathbf{z}} \frac{\pm i 4 Z_\mu(z)}{\beta_\mu k} \frac{\delta(r)}{2\pi r}. \tag{B.8d}$$

However, as shall be seen, there will be no need to exactly evaluate all of the electric and magnetic polarizations for each of the modes. This task will be particularly difficult when evaluating the sources corresponding to modes with $\nu \geqslant 1$, since there is no obvious way to define a surface such that the integral converges.

However, making some simple observations about the properties that these sources must have will provide a way forward. The absorbed power for each solution is given by Poynting's theorem as

$$P_{abs}^{\pm} = \mathrm{Re}\left\{\int \mathbf{J}\cdot\mathbf{E}\mathrm{d}V\right\} = -\omega\mathrm{Im}\left\{\int \mathbf{P}_{\mu\nu}^{\pm}\cdot\mathbf{E}_{\mu\nu}^{\pm}\mathrm{d}V\right\} \tag{B.9}$$

The outgoing and incoming wave solutions to Maxwell's equations must be related to each other such that $P_{abs}^{-} = -P_{abs}^{+}$. This absorbed power must also be finite, and so the phase of $\mathbf{P}_{\mu\nu}^{\pm}$ must be such that $\mathrm{Im}\{\mathbf{P}_{\mu\nu}^{\pm}\cdot\mathbf{E}_{\mu\nu}^{\pm}\}$ only involves the $J_\nu(\beta_\mu r)$ portion of the Bessel function, which implies that

$$\mathrm{Im}\{\mathbf{P}_{\mu\nu}^{+}\cdot\mathbf{E}_{\mu\nu}^{-}\} = \mathrm{Im}\{\mathbf{P}_{\mu\nu}^{+}\cdot\mathbf{E}_{\mu\nu}^{+}\} = -\mathrm{Im}\{\mathbf{P}_{\mu\nu}^{-}\cdot\mathbf{E}_{\mu\nu}^{-}\}. \tag{B.10}$$

Therefore it follows that $\mathbf{P}_{\mu\nu}^{-} = -\mathbf{P}_{\mu\nu}^{+}$. An extension of the argument to include magnetic currents will also show that $\mathbf{M}_{\mu\nu}^{-} = -\mathbf{M}_{\mu\nu}^{+}$, and these conclusions are consistent with eqs. (B.8a) to (B.8d).

The second important point to make note of regarding the cylindrical Hankel basis used here is the orthogonality property,

$$\int \left(\mathbf{E}_{\mu\nu}^{+}\times\mathbf{H}_{\rho\sigma}^{-} - \mathbf{E}_{\rho\sigma}^{-}\times\mathbf{H}_{\mu\nu}^{+}\right)\cdot\mathrm{d}\mathbf{a} = \frac{4L(1+\delta_{\nu 0})}{Z_0 k}\delta_{\rho\mu}\delta_{\sigma\nu} \tag{B.11}$$

where the integration is carried out over the surface of a cylinder of any radius aligned along the z-axis. This orthogonality relationship can be derived directly using the expressions for the modes given in appendix A, which was also shown in [89], although with a different normalization. The choice of normalization that yields eq. (B.11) is

given in appendix A, where the constant L is defined in eqs. (A.7a) and (A.7b) and has units of length. This particular choice of normalization leaves the electric field of the modes as dimensionless, the magnetic field with units of inverse impedance, and therefore the inner product of the modes has units of area times inverse impedance.

Coupled mode theory is derived using Lorentz reciprocity, and the unconjugated form of Lorentz reciprocity states that, for two solutions to Maxwell's equations $\{\mathbf{E}_1, \mathbf{H}_1, \mathbf{P}_1, \mathbf{M}_1\}$ and $\{\mathbf{E}_2, \mathbf{H}_2, \mathbf{P}_2, \mathbf{M}_2\}$,

$$\begin{aligned} &\nabla \cdot (\mathbf{E}_1 \times \mathbf{H}_2 - \mathbf{E}_2 \times \mathbf{H}_1) = \\ &i\omega \left(\mathbf{P}_1 \cdot \mathbf{E}_2 - \mu_0 \mathbf{M}_1 \cdot \mathbf{H}_2 - \mathbf{P}_2 \cdot \mathbf{E}_1 + \mu_0 \mathbf{M}_2 \cdot \mathbf{H}_1\right). \end{aligned} \tag{B.12}$$

First, we will derive the Rayleigh-Carson reciprocity theorem from eq. (B.12) by requiring $\{\mathbf{E}, \mathbf{H}, \mathbf{P}, \mathbf{M}\}$ to be the particular solution to Maxwell's equations that we are seeking, and $\{\mathbf{E}_2, \mathbf{H}_2, \mathbf{P}_2, \mathbf{M}_2\} = \{\mathbf{E}^+_{\mu\nu}, \mathbf{H}^+_{\mu\nu}, \mathbf{P}^+_{\mu\nu}, \mathbf{M}^+_{\mu\nu}\}$, and taking the volume integral of eq. (B.12) over all space. This yields,

$$\begin{aligned} &\int \left(\mathbf{E} \times \mathbf{H}^+_{\mu\nu} - \mathbf{E}^+_{\mu\nu} \times \mathbf{H}\right) \cdot \mathrm{d}\mathbf{a} = \\ &i\omega \int \left(\mathbf{P} \cdot \mathbf{E}^+_{\mu\nu} - \mu_0 \mathbf{M} \cdot \mathbf{H}^+_{\mu\nu} - \mathbf{P}^+_{\mu\nu} \cdot \mathbf{E} + \mu_0 \mathbf{M}^+_{\mu\nu} \cdot \mathbf{H}\right) \mathrm{d}V. \end{aligned} \tag{B.13}$$

If the sources $\mathbf{P}$ and $\mathbf{M}$ do not extend to infinity so that all of the modes that compose $\mathbf{E}$ and $\mathbf{H}$ at infinity are outgoing waves, then the orthogonality relationship in eq. (B.11) will guarantee that the surface integral will vanish. The result is the Rayleigh-Carson reciprocity theorem,

$$\int \left(\mathbf{P} \cdot \mathbf{E}^+_{\mu\nu} - \mu_0 \mathbf{M} \cdot \mathbf{H}^+_{\mu\nu}\right) \mathrm{d}V = \int \left(\mathbf{P}^+_{\mu\nu} \cdot \mathbf{E} - \mu_0 \mathbf{M}^+_{\mu\nu} \cdot \mathbf{H}\right) \mathrm{d}V. \tag{B.14}$$

Now, let $\{\mathbf{E}, \mathbf{H}, \mathbf{P}, \mathbf{M}\}$ remain as the solution to Maxwell's equations that we are seeking, but set $\{\mathbf{E}_2, \mathbf{H}_2, \mathbf{P}_2, \mathbf{M}_2\} = \{\mathbf{E}^-_{\mu\nu}, \mathbf{H}^-_{\mu\nu}, \mathbf{P}^-_{\mu\nu}, \mathbf{M}^-_{\mu\nu}\}$. The electric and magnetic fields $\mathbf{E}$ and $\mathbf{H}$ may moreover be expanded using eqs. (B.3a) and (B.3b).

Using eqs. (B.3a) and (B.3b) in eq. (B.12) and taking the volume integral of both sides, and applying the orthogonality condition in eq. (B.11) yields

$$A_{\mu\nu} = \frac{ik^2}{4L\epsilon_0(1+\delta_{\nu 0})} \times$$
$$\int \left(\mathbf{P} \cdot \mathbf{E}^-_{\mu\nu} - \mu_0 \mathbf{M} \cdot \mathbf{H}^-_{\mu\nu} - \mathbf{P}^-_{\mu\nu} \cdot \mathbf{E} + \mu_0 \mathbf{M}^-_{\mu\nu} \cdot \mathbf{H} \right) \mathrm{d}V. \tag{B.15}$$

Using the particular property of the cylindrical Hankel sources that $\mathbf{P}^-_{\mu\nu} = -\mathbf{P}^+_{\mu\nu}$ and $\mathbf{M}^-_{\mu\nu} = -\mathbf{M}^+_{\mu\nu}$, and applying eq. (B.14), we obtain

$$A_{\mu\nu} = \frac{ik^2}{4L\epsilon_0(1+\delta_{\nu 0})} \int \mathbf{P} \cdot (\mathbf{E}^+_{\mu\nu} + \mathbf{E}^-_{\mu\nu}) - \mu_0 \mathbf{M} \cdot (\mathbf{H}^+_{\mu\nu} + \mathbf{H}^-_{\mu\nu}) \mathrm{d}V. \tag{B.16}$$

The result in eq. (B.16) allows the calculation of the coupling of a dipole to cylindrical Hankel functions, because the singularity at the origin is canceled in the sum of incoming and outgoing waves.

B.2 Example: Electric Dipole Above a Metal Film

As an example of the new coupled mode theory equation eq. (B.16), consider an electric dipole placed at position $(x, y, z) = (0, 0, d)$, with dipole moment $\mathbf{p} = p_z \hat{\mathbf{z}}$, and that a metal film with relative dielectric constant ϵ occupying the space $z < 0$. The coupling to the surface plasmon is calculated using the quantity,

$$E^{TM+}_{\nu z} + E^{TM-}_{\nu z} = 2 n_{sp} Z(z) \cos(\nu\theta) J_\nu(\beta r) \tag{B.17a}$$
$$E^{TE+}_{\nu z} + E^{TE-}_{\nu z} = 0. \tag{B.17b}$$

where $n_{sp} = \beta/k$, and the index μ has been removed since there is only one bound mode ($\mu = 0$), which corresponds to the surface plasmon. The mode amplitudes

excited by this source are then,

$$A_\nu^{TMc} = \frac{p_z \beta^2 Z_0}{4L} Z^{TM}(d)\delta_{\nu 0} \tag{B.18a}$$

$$A_\nu^{TMs} = 0 \tag{B.18b}$$

$$A_\nu^{TEc} = 0 \tag{B.18c}$$

$$A_\nu^{TEs} = 0. \tag{B.18d}$$

The z-component of the electric field emitted by this source is therefore

$$E_z = \frac{p_z}{\epsilon_0} \frac{i\beta^5\sqrt{-\epsilon}}{2k^2(1-\epsilon)} e^{-k_z^+(z+d)} H_0^{(2)}(\beta r). \tag{B.19}$$

The power dissipated into the surface plasmon by this dipole is given by $P_{sp} = (\omega/2)\mathrm{Im}\{\mathbf{p}^* \cdot \mathbf{E}\}$, which is

$$P_{sp} = \omega \frac{|p_z|^2}{\epsilon_0} \frac{\beta^5\sqrt{-\epsilon}}{4k^2(1-\epsilon)} e^{-2k_z^+ d} \tag{B.20}$$

The result in eq. (B.20) agrees with equation 3.21 in [145] for the power emitted into the surface plasmon. Alternatively, we can consider an electric dipole placed parallel to the surface. A similar calculation using these same methods will also yield the same result as equation 3.21 in [145] for the horizontal electric dipole.

B.3 Example: Electric Dipole at the Origin

Consider a single point electric dipole that is oriented along the z-axis that is placed at some height z_0 and at the origin in a planar waveguide. The polarization density of that geometry would be $\mathbf{P} = p_z \hat{\mathbf{z}} \delta^{(3)}(\mathbf{r} - z_0 \hat{\mathbf{z}})$. Using eq. (B.16), the mode amplitudes

excited by the electric dipole are

$$A_{\mu\nu}^{TMc} = \frac{-ip_z k^2 n_\mu}{4h\epsilon_0} Z_\mu^{TM}(z_0)\delta_{\nu 0} \tag{B.21a}$$

$$A_{\mu\nu}^{TMs} = 0 \tag{B.21b}$$

$$A_{\mu\nu}^{TEc} = 0 \tag{B.21c}$$

$$A_{\mu\nu}^{TEs} = 0 \tag{B.21d}$$

and therefore, according to eq. (B.3a), the total electric field emitted by the dipole is

$$E_z = \sum_{\mu=0}^{\infty} \frac{-ip_z\beta_\mu^2}{4h\epsilon_0} Z_\mu^{TM}(z_0) H_0^{(2)}(\beta_\mu r) Z_\mu^{TM}(z). \tag{B.22}$$

If the waveguide is very short (i.e., $h < \lambda/2$, with λ being the free-space wavelength) then only the fundamental mode propagates, and so the electric field is well approximated far from the dipole using only the fundamental mode. Moreover, if the waveguide is empty, then $Z_\mu(z) = 1$, and the field from the dipole becomes simply

$$\mathbf{E} \approx \hat{\mathbf{z}} \frac{-ip_z\beta_\mu^2}{4h\epsilon\epsilon_0} H_0^{(2)}(\beta_\mu r). \tag{B.23}$$

This electric dipole is approximately equivalent to a current line source at the origin with current $I = i\omega p_z/h$. In terms of this current, the scattered field is

$$\mathbf{E} \approx \hat{\mathbf{z}} \frac{-I\beta_\mu^2}{4\omega\epsilon\epsilon_0} H_0^{(2)}(\beta_\mu r) \tag{B.24}$$

which is the correct expression for the electric field emitted by an infinite current-carrying wire[51]. It is important to note that the fundamental equation we are considering, eq. (B.16), disagrees with the published expressions in literature for coupled mode theory in a cylindrical Hankel basis. Other authors have neglected the fact that this basis is not source free, which ultimately leads to the same expression

as eq. (B.16) but without taking the real part of the electric field and imaginary part of the magnetic field. If the real and imaginary parts were not taken, as in [89], then the coupled mode theory equations would predict an infinite mode amplitude scattered by the dipole due to the singularity in the imaginary part of the Hankel function at the origin.

B.4 Example: Electric Dipole at an Arbitrary Position

Consider an electric dipole oriented in the $\hat{\mathbf{z}}$ direction, but placed at some arbitrary position $\mathbf{r}_0 = (r_0, \theta_0, z_0$. The polarization density that describes this situation is $\mathbf{P} = p_z \hat{\mathbf{z}} \delta^{(3)}(\mathbf{r} - \mathbf{r}_0)$. If the height of the waveguide is short relative to the wavelength, then only the $\mu = 0$ TM mode propagates. However, there is no cutoff for the ν mode number, so all mode numbers in ν must be included. We will also assume that the waveguide is only filled with a single dielectric, so $Z_\mu(z) = 1$. Using eq. (B.16), the mode amplitudes are

$$A_{0\nu}^{TMc} = \frac{-ik\beta p_z}{2h\epsilon\epsilon_0(1+\delta_{\nu 0})} J_\nu(\beta r_0)\cos(\nu\theta_0) \tag{B.25a}$$

$$A_{0\nu}^{TMs} = \frac{-ik\beta p_z}{2h\epsilon\epsilon_0(1+\delta_{\nu 0})} J_\nu(\beta r_0)\sin(\nu\theta_0). \tag{B.25b}$$

The total z-component of the electric field is the given by the sum over all modes,

$$E_z = \sum_{\nu=0}^{\infty} \frac{-i\beta^2 p_z}{2h\epsilon\epsilon_0(1+\delta_{\nu 0})} \Big[J_\nu(\beta r_0)\cos(\nu\theta_0) H_\nu^{(2)}(\beta r)\cos(\nu\theta) + J_\nu(\beta r_0)\sin(\nu\theta_0) H_\nu^{(2)}(\beta r)\sin(\nu\theta) \Big]. \tag{B.26a}$$

$$E_z = \frac{-i\beta^2 p_z}{4h\epsilon\epsilon_0} \sum_{\nu=-\infty}^{\infty} \Big[J_\nu(\beta r_0)\cos(\nu\theta_0) H_\nu^{(2)}(\beta r)\cos(\nu\theta) + J_\nu(\beta r_0)\sin(\nu\theta_0) H_\nu^{(2)}(\beta r)\sin(\nu\theta) \Big]. \tag{B.26b}$$

Using Bessel's addition theorem, which states that

$$H_0^{(2)}(\beta|\mathbf{r}-\mathbf{r}_0|) = \sum_{\nu=-\infty}^{\infty} \big[J_\nu(\beta r_0)\cos(\nu\theta_0)H_\nu^{(2)}(\beta r)\cos(\nu\theta) + J_\nu(\beta r_0)\sin(\nu\theta_0)H_\nu^{(2)}(\beta r)\sin(\nu\theta)\big], \tag{B.27}$$

the electric field becomes exactly what eq. (B.23) predicts, but centered around $\mathbf{r}_0$ instead of at the origin:

$$\mathbf{E} = \hat{\mathbf{z}}\frac{-ip_z\beta_\mu^2}{4h\epsilon\epsilon_0}H_0^{(2)}(\beta_\mu|\mathbf{r}-\mathbf{r}_0|). \tag{B.28}$$

Therefore, eq. (B.16) predicts that the fields radiated by a dipole are invariant to a translation of the origin about which the modes are expanded.

B.5 Example: Magnetic Dipole at the Origin

Consider a magnetic dipole sitting at the origin, so that $\mathbf{M} = m_y\hat{\mathbf{y}}\delta(z-z_0)\delta(r)/2\pi r$. A careful calculation shows that

$$H_{\mu\nu y}^{TM+}(d\hat{\mathbf{z}}) + H_{\mu\nu y}^{TM-}(d\hat{\mathbf{z}}) = \frac{-i}{Z_0}Z_\mu^{TM}(z_0)\delta_{\nu 1} \tag{B.29a}$$

$$H_{\mu\nu y}^{TE+}(d\hat{\mathbf{z}}) + H_{\mu\nu y}^{TE-}(d\hat{\mathbf{z}}) = \frac{i}{Z_0 k}\frac{d}{dz}Z_\mu^{TE}(z_0)\delta_{\nu 1}. \tag{B.29b}$$

So the mode amplitudes excited by this source are

$$A_{\mu\nu}^{TMc} = \frac{-m_y\epsilon k^2 Z_0}{4h}Z_\mu^{TM}(z_0)\delta_{\nu 1} \tag{B.30a}$$

$$A_{\mu\nu}^{TMs} = 0 \tag{B.30b}$$

$$A_{\mu\nu}^{TEc} = 0 \tag{B.30c}$$

$$A_{\mu\nu}^{TEs} = \frac{m_y k Z_0}{4h}\frac{d}{dz}Z_\mu^{TE}(z_0)\delta_{\nu 1}. \tag{B.30d}$$

If the waveguide is filled with a single dielectric with a relative dielectric constant of ϵ, then

$$Z_\mu^{TM}(z) = \sqrt{\frac{2}{\epsilon(1+\delta_{\mu 0})}}\cos\left(\frac{\mu\pi}{h}z\right) \qquad \mu = 0, 1, 2, 3.... \tag{B.31a}$$

$$Z_\mu^{TE}(z) = \sqrt{\frac{2}{(1+\delta_{\mu 0})}}\sin\left(\frac{\mu\pi}{h}z\right) \qquad \mu = 1, 2, 3.... \tag{B.31b}$$

The excited magnetic field is therefore

$$H_\theta = \sum_\mu \frac{-im_y\epsilon k^2\cos(\mu\pi z_0/h)}{2h(1+\delta_{\mu 0})}\frac{\partial H_1^{(2)}(\beta_\mu r)}{\partial(\beta_\mu r)}\cos(\theta)\cos\left(\frac{\mu\pi}{h}z\right)$$

$$+\sum_\mu \frac{-im_y k^2\cos(\mu\pi z_0/h)}{2h(1+\delta_{\mu 0})}\left(\frac{\mu\pi}{kh}\right)^2\frac{H_1^{(2)}(\beta_\mu r)}{\beta_\mu r}\cos(\theta)\cos\left(\frac{\mu\pi}{h}z\right) \tag{B.32}$$

$$H_\theta = \sum_{\mu=0}^{\infty}\frac{-im_y k^2\cos(\mu\pi z_0/h)}{2h(1+\delta_{\mu 0})}\cos(\theta)\cos\left(\frac{\mu\pi}{h}z\right)\times$$

$$\left(\epsilon\frac{\partial H_1^{(2)}(\beta_\mu r)}{\partial(\beta_\mu r)} + (\epsilon - n_\mu^2)\frac{H_1^{(2)}(\beta_\mu r)}{\beta_\mu r}\right) \tag{B.33}$$

If the dipole is a complementary metamaterial unit cell so that $z_0 = 0$ or $z_0 = h$, and the waveguide is empty so that $\epsilon = 1$, then the final expression for the total polar component of the magnetic field is

$$H_\theta =$$

$$\sum_{\mu=0}^{\infty}\frac{-im_y k^2\cos(\theta)}{2h(1+\delta_{\mu 0})}\left(\epsilon H_0^{(2)}(\beta_\mu r) - n_\mu^2\frac{H_1^{(2)}(\beta_\mu r)}{\beta_\mu r}\right)\cos\left(\frac{\mu\pi}{h}z\right). \tag{B.34}$$

$$H_\theta =$$

$$\frac{-im_y k^2}{4h}\cos(\theta)\sum_{\mu=-\infty}^{\infty}\left(\epsilon H_0^{(2)}(\beta_\mu r) - n_\mu^2\frac{H_1^{(2)}(\beta_\mu r)}{\beta_\mu r}\right)e^{i\mu\pi z/h}. \tag{B.35}$$

In order to check whether or not this solution is correct, we can check this answer against the field radiated by an infinite, one-dimensional stack of magnetic dipoles that are stacked along the z-axis with a spacing of $2h$, and oriented in the y-direction. If the complementary metamaterial unit cell is placed in the upper surface of the planar waveguide at position $z = h$, then the lower surface will cast an image of this dipole at a position $z = -h$. The upper plane of the waveguide will again cast an image of the image dipole at $z = 3h$, and so on, and so the problem is equivalent to the field radiated by an infinite stack of dipoles. This problem has been worked out by summing the fields of the infinite stack of dipoles exactly using Poisson's summation technique, which gives exactly the same answer as eq. (B.35). In fact, it turns out that there is a one-to-one correspondence between the waveguide modes excited by the dipole and the Poisson summation terms.

Appendix C

Derivation of Radiated Power by a Film-Coupled Magnetic Metasurface

Here I derive the total time averaged Poynting vector in a plane above a metasurface of magnetic dipoles that are placed infinitesimally close to a metal film, which is used in chapter 6 to explain sharp Wood's anomalies. Let the dipoles be oriented in the $\hat{\mathbf{y}}$ direction, and the normal vector to the film be $\hat{\mathbf{z}}$, and the magnetic dipoles have a phase vector relative to each other $\mathbf{k} = k_x\hat{\mathbf{x}} + k_y\hat{\mathbf{y}} + k_z\hat{\mathbf{z}}$ such that the dipole moment of the ν^{th} dipole is related to the μ^{th} dipole by $m_\nu = m_\mu e^{-i\mathbf{k}\cdot(\mathbf{r}_\nu - \mathbf{r}_\mu)} = me^{-i\mathbf{k}\cdot\mathbf{r}_\nu}$, where $\mathbf{r}_\rho = x_\rho\hat{\mathbf{x}} + y_\rho\hat{\mathbf{y}}$ is the location of the ρ^{th} dipole.

In the absence of the metal film, the Hertzian potential of the periodic array of dipoles can be written as the infinite sum

$$\Pi_y(\mathbf{r}) = \frac{m}{4\pi}\sum_{\mu=-\infty}^{\infty}\sum_{\nu=-\infty}^{\infty}\frac{e^{-ik\sqrt{z^2+(x-a_x\nu)^2+(y-a_y\mu)^2}}}{\sqrt{z^2+(x-a_x\nu)^2+(y-a_y\mu)^2}}e^{-i(k_xa_x\nu+k_ya_y\mu)} \tag{C.1}$$

where we have assumed a regular lattice spacing a_x in the x-direction and a_y in the

y-direction. This can be shown via Poisson's summation technique to be[3]

$$\Pi_y(\mathbf{r}) = \frac{-im}{2a_x a_y} \sum_{\mu=-\infty}^{\infty} \sum_{\nu=-\infty}^{\infty} \frac{e^{-i\mathbf{G}_{\mu\nu}\cdot\mathbf{r}}}{G^z_{\mu\nu}} \tag{C.2}$$

where $\mathbf{G}_{\mu\nu} = G^x_{\mu\nu}\hat{\mathbf{x}} + G^y_{\mu\nu}\hat{\mathbf{y}} + G^z_{\mu\nu}\hat{\mathbf{z}}$ is given by

$$G^x_{\mu\nu} = 2\pi\nu/a_x - k_x \tag{C.3a}$$

$$G^y_{\mu\nu} = 2\pi\mu/a_y - k_y \tag{C.3b}$$

$$G^z_{\mu\nu} = \sqrt{k^2 - (G^x_{\mu\nu})^2 - (G^y_{\mu\nu})^2}. \tag{C.3c}$$

The total magnetic field can be found from the Hertzian vector potential as

$$\mathbf{H} = \left(k^2\mathbf{I} + \nabla\otimes\nabla\right)\Pi. \tag{C.4}$$

The total field is hence decomposed into a sum of plane waves. These plane waves will need to be further decomposed into transverse-electric (TE) and transverse-magnetic (TM) components in order to find the field reflected from the metal film. The TE component of the field can be found by first finding the z-component of the magnetic field using eqs. (C.2) and (C.4). The full magnetic field is,

$$H_x = \frac{\partial}{\partial x}\frac{\partial}{\partial y}\Pi_y = \frac{im}{2a_x a_y}\sum_{\mu,\nu}\frac{G^x_{\mu\nu}G^y_{\mu\nu}}{G^z_{\mu\nu}}e^{-i\mathbf{G}_{\mu\nu}\cdot\mathbf{r}} \tag{C.5a}$$

$$H_y = \left(k^2 + \frac{\partial^2}{\partial y^2}\right)\Pi_y = \frac{im}{22a_x a_y}\sum_{\mu,\nu}\frac{k^2 - (G^y_{\mu\nu})^2}{G^z_{\mu\nu}}e^{-i\mathbf{G}_{\mu\nu}\cdot\mathbf{r}} \tag{C.5b}$$

$$H_z = \frac{\partial}{\partial z}\frac{\partial}{\partial y}\Pi_y = \frac{im}{2a_x a_y}\sum_{\mu,\nu}G^y_{\mu\nu}e^{-i\mathbf{G}_{\mu\nu}\cdot\mathbf{r}}. \tag{C.5c}$$

The full electric field may then be found by applying Ampère's law to eqs. (C.5a)

to (C.5c). The result is,

$$E_x = \frac{-iZ_0mk}{2a_xa_y}\sum_{\mu,\nu} e^{-i\mathbf{G}_{\mu\nu}\cdot\mathbf{r}} \tag{C.6a}$$

$$E_y = 0 \tag{C.6b}$$

$$E_z = \frac{iZ_0mk}{2a_xa_y}\sum_{\mu,\nu} \frac{G^x_{\mu\nu}}{G^z_{\mu\nu}} e^{-i\mathbf{G}_{\mu\nu}\cdot\mathbf{r}}. \tag{C.6c}$$

The fields given in eqs. (C.5a) to (C.5c) and (C.6a) to (C.6c) are the total fields of the magnetic dipole array in the absence of the metal film. The time averaged Poynting vector radiating away from the metasurface in this case will be $\langle \mathbf{S}\cdot\hat{\mathbf{z}}\rangle_t = (1/2)E_xH_y^*$.

In the presence of the metal film, the total fields will be those given eqs. (C.5a) to (C.5c) and (C.6a) to (C.6c) plus the reflected fields from the metal film. However, the fields in eqs. (C.5a) to (C.5c) and (C.6a) to (C.6c) contain both TE and TM components, and these need to be separated before the reflected fields can be added. The only component of the fields in eqs. (C.5a) to (C.5c) and (C.6a) to (C.6c) that is purely TE is the H_z component, while the only component of the fields that is purely TM is the E_z component. Hence, in order to decompose the total field into a sum of TE and TM fields, the x- and y-components of the TE part of the field must be constructed from the H_z field in eq. (C.5c), while the x- and y- components of the TM part of the field must be constructed from the E_z field in eq. (C.6c). This cannot be done in a straightforward manner in terms of derivatives of the total field, but it can be directly computed from the individual μ,ν components of the total field that vary in the z-direction as $e^{-iG_{\mu\nu}z}$. Hence we first decompose the E_z field into a sum of terms $E_z = \frac{iZ_0mk}{2a_xa_y}\sum_{\mu,\nu} E_{z\mu\nu}$ where $E_{z\mu\nu} = \frac{G^x_{\mu\nu}}{G^z_{\mu\nu}} e^{-i\mathbf{G}_{\mu\nu}\cdot\mathbf{r}}$. Likewise, the H_z field may be composed according to $H_z = \frac{im}{2a_xa_y}\sum_{\mu,\nu} H_{z\mu\nu}$, where $H_{z\mu\nu} = G^y_{\mu\nu} e^{-i\mathbf{G}_{\mu\nu}\cdot\mathbf{r}}$. The

transverse fields of each μ, ν term can be found using[88],

$$E^{TM}_{x\mu\nu} = \frac{-iG^z_{\mu\nu}}{k^2 - (G^z_{\mu\nu})^2}\frac{\partial}{\partial x}E_{z\mu\nu} \tag{C.7a}$$

$$E^{TE}_{x\mu\nu} = \frac{-iZ_0 k}{k^2 - (G^z_{\mu\nu})^2}\frac{\partial}{\partial y}H_{z\mu\nu} \tag{C.7b}$$

$$H^{TM}_{y\mu\nu} = \frac{-iZ_0 k}{k^2 - (G^z_{\mu\nu})^2}\frac{\partial}{\partial x}E_{z\mu\nu} \tag{C.7c}$$

$$H^{TE}_{y\mu\nu} = \frac{-iG^z_{\mu\nu}}{k^2 - (G^z_{\mu\nu})^2}\frac{\partial}{\partial y}H_{z\mu\nu}. \tag{C.7d}$$

Finally, we sum the various components over the μ, ν indices to obtain the total decomposition of the field into TE and TM components:

$$E^{TE}_x = \frac{-iZ_0 mk}{2a^2}\sum_{\mu,\nu}\frac{(G^y_{\mu\nu})^2}{k^2 - (G^z_{\mu\nu})^2}e^{-i\mathbf{G}_{\mu\nu}\cdot\mathbf{r}} \tag{C.8a}$$

$$E^{TM}_x = \frac{-iZ_0 mk}{2a^2}\sum_{\mu,\nu}\frac{(G^x_{\mu\nu})^2}{k^2 - (G^z_{\mu\nu})^2}e^{-i\mathbf{G}_{\mu\nu}\cdot\mathbf{r}} \tag{C.8b}$$

$$H^{TE}_y = \frac{-im}{2a^2}\sum_{\mu,\nu}\frac{(G^z_{\mu\nu})^2}{k^2 - (G^z_{\mu\nu})^2}\frac{(G^x_{\mu\nu})^2}{G^z_{\mu\nu}}e^{-i\mathbf{G}_{\mu\nu}\cdot\mathbf{r}} \tag{C.8c}$$

$$H^{TM}_y = \frac{-im}{2a^2}\sum_{\mu,\nu}\frac{k^2}{k^2 - (G^z_{\mu\nu})^2}\frac{(G^x_{\mu\nu})^2}{G^z_{\mu\nu}}e^{-i\mathbf{G}_{\mu\nu}\cdot\mathbf{r}}. \tag{C.8d}$$

It can be checked that adding eqs. (C.8a) and (C.8b) yields eq. (C.6a), and adding eqs. (C.8c) and (C.8d) yields eq. (C.5b). The total electric field can now be constructed as the direct wave from the metasurface of magnetic dipoles, plus the reflected TE and TM waves, which are given by the reflection coefficients $r_{TE}(G^z_{\mu\nu})$

and $r_{TM}(G^z_{\mu\nu})$:

$$E_x = \frac{-iZ_0mk}{2a^2}\sum_{\mu,\nu}\left[(G^y_{\mu\nu})^2(1-r_{TE}(G^z_{\mu\nu}))+(G^x_{\mu\nu})^2(1-r_{TM}(G^z_{\mu\nu}))\right]\frac{e^{-i\mathbf{G}_{\mu\nu}\cdot\mathbf{r}}}{k^2-(G^z_{\mu\nu})^2} \tag{C.9a}$$

$$H_y = \frac{-iZ_0mk}{2a^2}\sum_{\mu,\nu}\left[G^z_{\mu\nu}(G^y_{\mu\nu})^2(1-r_{TE}(G^z_{\mu\nu}))+\frac{k^2}{G^z_{\mu\nu}}(G^x_{\mu\nu})^2(1-r_{TM}(G^z_{\mu\nu}))\right]\frac{e^{-i\mathbf{G}_{\mu\nu}\cdot\mathbf{r}}}{k^2-(G^z_{\mu\nu})^2}. \tag{C.9b}$$

The time-averaged Poynting vector in the normal direction with respect to the film-coupled metasurface is finally,

$$\begin{aligned}\langle\mathbf{S}\cdot\hat{\mathbf{z}}\rangle_t &= (1/2)E_xH_y^* \\ &= \frac{Z_0k|m|^2}{8a^4}\sum_{\mu,\nu}\left(k^2-(G^z_{\mu\nu})^2\right)^{-1}\Bigg[G^z_{\mu\nu}(G^y_{\mu\nu})^4|1-r_{TE}(G^z_{\mu\nu})|^2+\frac{k^2}{G^{z*}_{\mu\nu}}(G^x_{\mu\nu})^4|1-r_{TM}(G^z_{\mu\nu})|^2 \\ &\quad+\frac{k^2}{G^{z*}_{\mu\nu}}(G^x_{\mu\nu})^2(G^y_{\mu\nu})^2\left(1-r_{TE}(G^z_{\mu\nu})\right)\left(1-r_{TM}(G^z_{\mu\nu})\right)^* \\ &\quad+G^z_{\mu\nu}(G^x_{\mu\nu})^2(G^y_{\mu\nu})^2\left(1-r_{TE}(G^z_{\mu\nu})\right)^*\left(1-r_{TM}(G^z_{\mu\nu})\right)\Bigg].\end{aligned} \tag{C.10}$$

We note that the last two terms of eq. (C.10) are interference terms between TE and TM components of the field that are radiating as two beams at the same angle.

Appendix D

Exact Green's Functions of Film-Coupled Magnetic Dipoles from Sommerfeld Integration

In this chapter I calculate the total field radiated by planar arrays of electric and magnetic dipoles. This can be found using the vector potential $\mathbf{A}$ for electric dipoles, while for magnetic dipoles this is done using the magnetic vector potential $\mathbf{F}$. In the Lorentz guage, these satisfy the vector differential equations

$$\nabla^2\mathbf{A} + k^2\mathbf{A} = -iZ_0k\mathbf{P} \tag{D.1a}$$

$$\nabla^2\mathbf{F} + k^2\mathbf{F} = \frac{-ik}{c}\mathbf{M} \tag{D.1b}$$

These can be solved component-wise when separated into a Cartesian basis. In terms of components, each component forms a scalar wave equation that can be solved by the scalar Green's function, such that

$$\mathbf{A} = iZ_0k\int g(\mathbf{r},\mathbf{r}')\mathbf{P}(\mathbf{r}')d^3\mathbf{r}' \tag{D.2a}$$

$$\mathbf{F} = \frac{ik}{c}\int g(\mathbf{r},\mathbf{r}')\mathbf{M}(\mathbf{r}')d^3\mathbf{r}' \tag{D.2b}$$

where

$$
\begin{aligned}
g(\mathbf{r},\mathbf{r}') &= \frac{e^{-ik|\mathbf{r}-\mathbf{r}'|}}{4\pi|\mathbf{r}-\mathbf{r}'|} \\
&= \frac{-i}{8\pi}\int_{-\infty}^{\infty}\frac{\beta}{k_z}H_0^{(2)}(\beta\rho)e^{-ik_z|z|}d\beta \\
&= \frac{-i}{8\pi}\int_{-\infty}^{\infty}H_0^{(2)}(\beta\rho)e^{-ik_z|z|}dk_z
\end{aligned}
\tag{D.3}
$$

and $\beta^2 + k_z^2 = k^2$. Once the potentials are known, the fields are given by

$$
\mathbf{E} = \frac{-ic}{k}\left(k^2\mathbf{I} + \nabla\otimes\nabla\right)\mathbf{A} - \frac{1}{\epsilon_0}\nabla\times\mathbf{F} \tag{D.4a}
$$

$$
\mathbf{H} = \frac{1}{\mu_0}\nabla\times\mathbf{A} + \frac{-ic}{k}\left(k^2\mathbf{I} + \nabla\otimes\nabla\right)\mathbf{F}. \tag{D.4b}
$$

This way of solving the problem is particularly convenient because the first term in each equation is the field due to the electric dipoles, while the second term is the field due to the magnetic dipoles, where each potential that is used is calculated using the scalar Green's function rather than the dyadic Green's function.

The fields calculated in this manner contain both TE and TM components, and these need to be separated before the reflected fields can taken into account. The only component of the fields that is purely TE is the H_z component, while the only component of the fields that is purely TM is the E_z component. Hence, in order to decompose the total field into a sum of TE and TM fields, the x- and y-components of the TE part of the field must be constructed from the H_z field, while the x- and y- components of the TM part of the field must be constructed from the E_z field. This cannot be done in a straightforward manner in terms of derivatives of the total field, but it can be directly computed from the individual k_z components of the total field that vary in the z-direction as $e^{-ik_z z}$. The transverse fields of each k_z spectral

component can be found using,

$$E_x^{TM}(\beta) = \frac{1}{\beta^2}\frac{\partial^2}{\partial x \partial z}E_z(\beta) \tag{D.5a}$$

$$E_x^{TE}(\beta) = \frac{-iZ_0 k}{\beta^2}\frac{\partial}{\partial y}H_z(\beta) \tag{D.5b}$$

$$H_y^{TM}(\beta) = \frac{-ik/Z_0}{\beta^2}\frac{\partial}{\partial x}E_z(\beta) \tag{D.5c}$$

$$H_y^{TE}(\beta) = \frac{1}{\beta^2}\frac{\partial^2}{\partial y \partial z}H_z(\beta). \tag{D.5d}$$

The total fields will then be finally given by

$$\mathbf{E}(\mathbf{r}) = \int_{-\infty}^{\infty} \left[\mathbf{E}^{TM}(\beta, \mathbf{r}) + \mathbf{E}^{TE}(\beta, \mathbf{r})\right] d\beta \tag{D.6a}$$

$$\mathbf{H}(\mathbf{r}) = \int_{-\infty}^{\infty} \left[\mathbf{H}^{TM}(\beta, \mathbf{r}) + \mathbf{H}^{TE}(\beta, \mathbf{r})\right] d\beta \tag{D.6b}$$

The relevant component of Green's tensor for this problem is the y-component of the field due to a magnetic dipole oriented in the y-direction, which is

$$H_y(\beta) = \frac{-i}{8\pi}\frac{\beta}{k_z}\left(k^2 + \frac{\partial^2}{\partial y^2}\right)H_0^{(2)}(\beta\rho)e^{-ik_z|z|}. \tag{D.7}$$

However, this has both TE and TM components. To do this we start with the z-components of the field, which are

$$H_z(\beta) = \frac{-i}{8\pi}\frac{\beta}{k_z}\frac{\partial^2}{\partial y \partial z}H_0^{(2)}(\beta\rho)e^{-ik_z|z|} \tag{D.8}$$

$$E_z(\beta) = \frac{-Z_0}{8\pi}\frac{\beta}{k_z}\frac{\partial}{\partial x}H_0^{(2)}(\beta\rho)e^{-ik_z|z|} \tag{D.9}$$

The TE and TM decomposition of the H_y field is then

$$H_y^{TE}(\beta) = \frac{i}{8\pi}\frac{k_z}{\beta}\frac{\partial^2}{\partial y^2}H_0^{(2)}(\beta\rho)e^{-ik_z|z|} \tag{D.10}$$

$$H_y^{TM}(\beta) = \frac{i}{8\pi}\frac{k^2}{\beta k_z}\frac{\partial^2}{\partial x^2}H_0^{(2)}(\beta\rho)e^{-ik_z|z|} \tag{D.11}$$

It can be shown that the sum of these TE and TM components are equivalent to the total field in eq. (D.7).

When a dipole is placed over a metal film with reflection coefficients r_{TM} and r_{TE} by a distance d, the final fields are therefore

$$H_y^{TM} = \frac{i}{8\pi}\frac{\partial^2}{\partial x^2}\int_{-\infty}^{\infty}\frac{k^2}{\beta k_z}H_0^{(2)}(\beta\rho)\left(e^{-ik_z|z-d|} + r_{TM}e^{-ik_z|z+2d|}\right)d\beta \tag{D.12a}$$

$$H_y^{TE} = \frac{i}{8\pi}\frac{\partial^2}{\partial y^2}\int_{-\infty}^{\infty}\frac{k_z}{\beta}H_0^{(2)}(\beta\rho)\left(e^{-ik_z|z-d|} + r_{TE}e^{-ik_z|z+2d|}\right)d\beta \tag{D.12b}$$

Summing the TE and TM components, the total field can be written in terms of the free space field plus a reflected field as

$$H_y = \left(k^2 + \frac{\partial^2}{\partial y^2}\right)\frac{e^{-ikr_d}}{4\pi r_d} + H_y^{TMr} + H_y^{TEr} \tag{D.13}$$

$$H_y^{TMr} = \frac{i}{8\pi}\frac{\partial^2}{\partial x^2}\int_{-\infty}^{\infty}\frac{k^2 r_{TM}(\beta)}{\beta k_z}H_0^{(2)}(\beta\rho)e^{-ik_z|z+2d|}d\beta \tag{D.14a}$$

$$H_y^{TEr} = \frac{i}{8\pi}\frac{\partial^2}{\partial y^2}\int_{-\infty}^{\infty}\frac{k_z r_{TE}(\beta)}{\beta}H_0^{(2)}(\beta\rho)e^{-ik_z|z+2d|}d\beta \tag{D.14b}$$

with $r_d = |\mathbf{r} - \hat{\mathbf{z}}d|$, and

$$r_{TM} = \frac{\epsilon k_z - k_{mz}}{\epsilon k_z + k_{mz}} \tag{D.15a}$$

$$r_{TE} = \frac{k_z - k_{mz}}{k_z + k_{mz}} \tag{D.15b}$$

$$k_z = \sqrt{k^2 - \beta^2} \tag{D.15c}$$

$$k_{mz} = \sqrt{\epsilon k^2 - \beta^2}. \tag{D.15d}$$

If $\epsilon < -1$ then there exists a pole in r_{TM} when $\beta = k\sqrt{\epsilon/(\epsilon+1)}$, which we will define as β_{sp} since this pole represents the surface plasmon that is created by the dipole. The Sommerfeld integrals in eq. (D.14a) will be much quicker to evaluate

numerically if the integration path is lifted off the real axis and deviated around the surface plasmon pole. Let us call this deformed path γ, and add back the contribution due to the pole separately. The residue in r_{TM} at β_{sp} is $\frac{2k_z^2\epsilon^2}{\beta(\epsilon^2-1)}$, and applying Cauchy's residue theorem yields

$$H_y^{TMr} = \frac{i\sqrt{-\epsilon}\beta_{sp}}{2(1-\epsilon)}\frac{\partial^2}{\partial x^2}H_0^{(2)}(\beta_{sp}\rho)e^{-ik_z^+|z+d|} + \frac{i}{8\pi}\frac{\partial^2}{\partial x^2}\int_\gamma \frac{k^2 r_{TM}(\beta)}{\beta k_z}H_0^{(2)}(\beta\rho)e^{-ik_z|z+d|}d\beta \tag{D.16}$$

Carrying through the second derivative in x shows that the first term is exactly the same contribution to the surface plasmon field that was derived in eq. (5.6) in chapter 5 using coupled mode theory:

$$\begin{aligned} H_y^{TMr} = {} & \frac{-i\sqrt{-\epsilon}\beta_{sp}^3}{4(1-\epsilon)}\left[H_0^{(2)}(\beta_{sp}\rho) - \cos(2\theta)H_2^{(2)}(\beta_{sp}\rho)\right]e^{-ik_z^+|z+d|} \\ & + \frac{i}{8\pi}\frac{\partial^2}{\partial x^2}\int_\gamma \frac{k^2 r_{TM}(\beta)}{\beta k_z}H_0^{(2)}(\beta\rho)e^{-ik_z|z+d|}d\beta. \end{aligned} \tag{D.17}$$

Hence, when the Sommerfeld integral is deviated along the path γ that passes around the surface plasmon pole, the complete frequency domain Green's function for a single film-coupled magnetic dipole can be split into three contributions:

$$\mathbf{G}(\omega,\mathbf{r},\mathbf{r}') = \mathbf{G}^{rad}(\omega,\mathbf{r},\mathbf{r}') + \mathbf{G}^{ref}(\omega,\mathbf{r},\mathbf{r}') + \mathbf{G}^{spp}(\omega,\mathbf{r},\mathbf{r}'). \tag{D.18}$$

where the directly radiated field $\mathbf{G}_{rad}(\omega,\mathbf{r},\mathbf{r}')$ is given by the free-space Green's function,

$$G_{yy}^{rad}(\omega,\mathbf{r},\mathbf{r}_0) = \left(k^2 + \frac{\partial^2}{\partial y^2}\right)\frac{e^{-ik|\mathbf{r}-\mathbf{r}_0|}}{4\pi|\mathbf{r}-\mathbf{r}_0|}, \tag{D.19}$$

the reflected field is given by the Sommerfeld integral over γ,

$$G_{yy}^{ref}(\omega,\mathbf{r},\mathbf{r}_0) = \frac{i}{8\pi}\int_\gamma \left[\frac{k^2 r_{TM}(\beta)}{\beta k_z}\frac{\partial^2}{\partial x^2}H_0^{(2)}(\beta\rho) + \frac{k_z r_{TE}(\beta)}{\beta}\frac{\partial^2}{\partial y^2}H_0^{(2)}(\beta\rho)\right]e^{-ik_z|z+2d|}d\beta. \tag{D.20}$$

and finally the surface plasmon bound field is given by

$$G_{yy}^{spp}(\omega, \mathbf{r}, \mathbf{r}_0) = \frac{-i\sqrt{-\epsilon}\beta_{sp}^3}{4(1-\epsilon)} \left[H_0^{(2)}(\beta_{sp}\rho) - \cos(2\theta) H_2^{(2)}(\beta_{sp}\rho) \right] e^{-ik_z^+|z+d|}. \qquad \text{(D.21)}$$

Appendix E

Modeling Two-Dimensional Metamaterial Devices using the Discrete Dipole Approximation

E.1 Developing the 2D Green's Function

The discrete dipole approximation (DDA) is a way to compute the exact scattered field of an arbitrary arrangement of electric and magnetic dipoles $\{\mathbf{p}_i, \mathbf{m}_i\}$ at positions $\mathbf{r}_i$, that are illuminated by an arbitrary source field $\{\mathbf{E}_0, \mathbf{H}_0\}$, within the context of an environment that is described by a particular electric and magnetic Green's function $\{\mathbf{G}, \mathbf{F}\}$. This section describes two-dimensional DDA in free space, which refers to an arrangement of dipoles that are placed in free space and scatter according to a free space Green's function, but where the dipoles are stacked in finite columns in the z-direction with some lattice constant a. In addition, this appendix only considers the situation where the electric dipoles are oriented in the z-direction and the magnetic dipoles are oriented in the xy-plane. This particular development of the DDA is novel, and was developed solely by myself. It is a more sophisticated and well-developed version of a work that I published in [30].

The free-space tensorial Green's function $\mathbf{G}$, which is the Green's function de-

scribing the vector wave equation, can be computed using the scalar Green's function G,

$$G = \frac{e^{-ikr}}{4\pi r} \tag{E.1}$$

which is the Green's function for the scalar wave equation in spherical coordinates. The tensorial Green's function is then given by

$$\mathbf{G} = \left(k^2\mathbf{I} + \nabla \otimes \nabla\right) G. \tag{E.2}$$

The electric and magnetic fields from an individual dipole are the product of the Green's tensor with the dipole moment:

$$\mathbf{E}(\mathbf{r}) = \epsilon_0^{-1}\mathbf{G}(\mathbf{r}, \mathbf{r}_0)\mathbf{p} \tag{E.3a}$$

$$\mathbf{H}(\mathbf{r}) = c\mathbf{F}(\mathbf{r}, \mathbf{r}_0)\mathbf{p} \tag{E.3b}$$

$$\mathbf{H}(\mathbf{r}) = \mathbf{G}(\mathbf{r}, \mathbf{r}_0)\mathbf{m} \tag{E.3c}$$

$$\mathbf{E}(\mathbf{r}) = -Z_0\mathbf{F}(\mathbf{r}, \mathbf{r}_0)\mathbf{m} \tag{E.3d}$$

where $\mathbf{F} = \frac{1}{ik}\nabla \times \mathbf{G}$.

The basic statement of the discrete dipole approximation is that the total field incident on an individual dipole is equal to some external driving field $\{\mathbf{E}_0, \mathbf{H}_0\}$, plus the fields from all of the dipoles in the lattice:

$$\bar{\bar{\alpha}}_m^{-1}\mathbf{m}_i = \mathbf{H}_0(\mathbf{r}_i) + \sum_j \left(\mathbf{G}(\mathbf{r}_i - \mathbf{r}_j)\mathbf{m}_j + c\mathbf{F}(\mathbf{r}_j - \mathbf{r}_i)\mathbf{p}_j\right) \tag{E.4a}$$

$$\epsilon_0\bar{\bar{\alpha}}_e^{-1}\mathbf{p}_i = \epsilon_0\mathbf{E}_0(\mathbf{r}_i) + \sum_j \left(\mathbf{G}(\mathbf{r}_i - \mathbf{r}_j)\mathbf{p}_j - c^{-1}\mathbf{F}(\mathbf{r}_i - \mathbf{r}_j)\mathbf{m}_j\right). \tag{E.4b}$$

The sum over all dipoles could be rearranged into a double sum by first grouping all of the dipoles into columns in the z-direction, and then summing the columns. Let the k^{th} column be deonoted Λ_k, which we define to be the set the indices j of all dipoles $\mathbf{p}_j$ that have the same coordinates in the xy-plane, i.e. $\Lambda_k = \{j | x_j = x_k, y_j = y_k\}$,

where x_k and y_k are the location of the column in the xy-plane. Then the total field incident on dipole i can be rewritten

$$\bar{\bar{\alpha}}_m^{-1}\mathbf{m}_i = \mathbf{H}_0(\mathbf{r}_i) + \sum_k \sum_{j\in\Lambda_k} \left(\mathbf{G}(\mathbf{r}_i - \mathbf{r}_j)\mathbf{m}_j + c\mathbf{F}(\mathbf{r}_j - \mathbf{r}_i)\mathbf{p}_j\right) \tag{E.5a}$$

$$\epsilon_0\bar{\bar{\alpha}}_e^{-1}\mathbf{p}_i = \epsilon_0\mathbf{E}_0(\mathbf{r}_i) + \sum_k \sum_{j\in\Lambda_k} \left(\mathbf{G}(\mathbf{r}_i - \mathbf{r}_j)\mathbf{p}_j - c^{-1}\mathbf{F}(\mathbf{r}_i - \mathbf{r}_j)\mathbf{m}_j\right). \tag{E.5b}$$

It may be claimed, by the symmetry of the system, that all dipoles $j \in \Lambda_k$ have their dipole moments equal such that $\mathbf{p}_j = \mathbf{p}_k$ and $\mathbf{m}_j = \mathbf{m}_k$ for all $j \in \Lambda_k$. Then the sum can again be rewritten

$$\bar{\bar{\alpha}}_m^{-1}\mathbf{m}_i = \mathbf{H}_0(\mathbf{r}_i) + \sum_k \left(\mathbf{G}^{1D}(\mathbf{r}_i - \mathbf{r}_k)\mathbf{m}_k + c\mathbf{F}^{1D}(\mathbf{r}_j - \mathbf{r}_i)\mathbf{p}_k\right) \tag{E.6a}$$

$$\epsilon_0\bar{\bar{\alpha}}_e^{-1}\mathbf{p}_i = \mathbf{E}_0(\mathbf{r}_i) + \sum_k \left(\mathbf{G}^{1D}(\mathbf{r}_i - \mathbf{r}_k)\mathbf{p}_j - c^{-1}\mathbf{F}^{1D}(\mathbf{r}_i - \mathbf{r}_k)\mathbf{m}_j\right). \tag{E.6b}$$

where

$$\mathbf{G}^{1D}(\mathbf{r}_i - \mathbf{r}_k) = \sum_{j\in\Lambda_k} \mathbf{G}(\mathbf{r}_i - \mathbf{r}_j) \tag{E.7a}$$

$$\mathbf{F}^{1D}(\mathbf{r}_i - \mathbf{r}_k) = \sum_{j\in\Lambda_k} \mathbf{F}(\mathbf{r}_i - \mathbf{r}_j) \tag{E.7b}$$

and $\mathbf{r}_k = (x_k, y_k, 0)$. These Green's functions represent the field that is radiated by a column of dipoles, which is essentially a line source.

The $k = i$ term corresponds to the dipoles that lie in the same column as dipole i, and this term may be moved to the left-hand-side of each equation, giving

$$\left[\bar{\bar{\alpha}}_m^{-1} - \mathbf{G}^{1D}(\mathbf{0})\right]\mathbf{m}_i = \mathbf{H}_0(\mathbf{r}_i) + \sum_{k\neq i} \left(\mathbf{G}^{1D}(\mathbf{r}_i - \mathbf{r}_k)\mathbf{m}_k + c\mathbf{F}^{1D}(\mathbf{r}_j - \mathbf{r}_i)\mathbf{p}_k\right) \tag{E.8a}$$

$$\left[\epsilon_0\bar{\bar{\alpha}}_e^{-1} - \mathbf{G}^{1D}(\mathbf{0})\right]\mathbf{p}_i = \epsilon_0\mathbf{E}_0(\mathbf{r}_i) + \sum_k \left(\mathbf{G}^{1D}(\mathbf{r}_i - \mathbf{r}_k)\mathbf{p}_j - c^{-1}\mathbf{F}^{1D}(\mathbf{r}_i - \mathbf{r}_k)\mathbf{m}_j\right). \tag{E.8b}$$

where we have used $\mathbf{F}(\mathbf{0}) = 0$, and

$$\mathbf{G}^{1D}(0) = \sum_{j\in\Lambda_i} \mathbf{G}(\mathbf{r}_j) = \mathbf{C}^{1D} = \begin{bmatrix} C_{xx}^{1D} & 0 & 0 \\ 0 & C_{yy}^{1D} & 0 \\ 0 & 0 & C_{zz}^{1D} \end{bmatrix}. \tag{E.9}$$

Expressions for C_{xx}^{1D}, C_{yy}^{1D}, and C_{zz}^{1D} are given in eqs. (2.19a) and (2.19b). This way of writing the equations allows the problem to be re-cast using the effective electric and magnetic polarizability of each column of dipoles $\{\alpha_e^{1D}, \alpha_m^{1D}\}$, which are defined as

$$\bar{\bar{\alpha}}_e^{1D} = \left(\bar{\bar{\alpha}}_e^{-1} - \epsilon_0^{-1}\mathbf{C}^{1D}\right)^{-1} \tag{E.10a}$$

$$\bar{\bar{\alpha}}_m^{1D} = \left(\bar{\bar{\alpha}}_m^{-1} - \mathbf{C}^{1D}\right)^{-1}. \tag{E.10b}$$

Hence, the final equations for the DDA in two-dimensions are,

$$\begin{bmatrix} (\bar{\bar{\alpha}}_{m,i}^{1D})^{-1}\delta_{ij} - \mathbf{G}_{ij}^{1D} & c\mathbf{F}_{ij}^{1D} \\ -c^{-1}\mathbf{F}_{ij}^{1D} & \epsilon_0(\alpha_{e,i}^{1D})^{-1}\delta_{ij} - \mathbf{G}_{ij}^{1D} \end{bmatrix} \begin{bmatrix} \mathbf{m}_j \\ \mathbf{p}_j \end{bmatrix} = \begin{bmatrix} \mathbf{H}_0(\mathbf{r}_i) \\ \epsilon_0\mathbf{E}_0(\mathbf{r}_i) \end{bmatrix} \tag{E.11}$$

The left-hand side is now a $3N \times 3N$ matrix that can be inverted to solve for all the electric and magnetic dipole moments.

All that remains is to derive an explicit equation for the Green's functions of the columns, $\mathbf{G}^{1D}$ and $\mathbf{F}^{1D}$. The effective Green's tensor for the one-dimensional stack of dipoles will be given by

$$G_{rx}^{1D} = \left(k^2\cos(\theta) + \partial_r\partial_x\right) G^{1D} \tag{E.12a}$$

$$G_{\theta x}^{1D} = \left(-k^2\sin(\theta) + \frac{1}{r}\partial_\theta\partial_x\right) G^{1D} \tag{E.12b}$$

$$G_{zx}^{1D} = \partial_z\partial_x G^{1D} \tag{E.12c}$$

$$G_{ry}^{1D} = \left(k^2\sin(\theta) + \partial_r\partial_y\right) G^{1D} \tag{E.12d}$$

$$G_{\theta y}^{1D} = \left(k^2\cos(\theta) + \frac{1}{r}\partial_\theta\partial_y\right) G^{1D} \tag{E.12e}$$

$$G_{zy}^{1D} = \partial_z\partial_y G^{1D} \tag{E.12f}$$

$$G_{rz}^{1D} = \partial_r\partial_z G^{1D} \tag{E.12g}$$

$$G_{\theta z}^{1D} = \frac{1}{r}\partial_\theta\partial_z G^{1D} \tag{E.12h}$$

$$G_{zz}^{1D} = \left(k^2 + \partial_z\partial_z\right) G^{1D} \tag{E.12i}$$

where

$$G^{1D} = \frac{1}{4\pi} \sum_{\mu=-\infty}^{\infty} \frac{e^{-ik\sqrt{r^2+(z-\mu a)^2}}}{\sqrt{r^2+(z-\mu a)^2}} \tag{E.13}$$

is the scalar Green's function. Applying Poisson's summation technique to eq. (E.13) shows that the effective scalar Green's function will be

$$G^{1D} = \frac{-i}{4a} \sum_{\mu=-\infty}^{\infty} H_0^{(2)}(\beta_\mu r) e^{i2\pi\mu z/a} \tag{E.14}$$

where $\beta_\mu = n_\mu k = \sqrt{k^2 - (2\pi\mu/a)^2}$. Therefore,

$$G_{ry}^{1D} = \frac{-ik^2\sin(\theta)}{4a} \sum_{\mu=-\infty}^{\infty} \left(H_0^{(2)}(\beta_\mu r) - n_\mu^2 \frac{\partial H_1^{(2)}(\beta_\mu r)}{\partial(\beta_\mu r)} \right) e^{i2\pi\mu z/a} \tag{E.15a}$$

$$G_{\theta y}^{1D} = \frac{-ik^2\cos(\theta)}{4a} \sum_{\mu=-\infty}^{\infty} \left(H_0^{(2)}(\beta_\mu r) - n_\mu^2 \frac{H_1^{(2)}(\beta_\mu r)}{\beta_\mu r} \right) e^{i2\pi\mu z/a} \tag{E.15b}$$

$$G_{zy}^{1D} = \frac{-ik^2\sin(\theta)}{4a} \sum_{\mu=-\infty}^{\infty} n_\mu \left(\frac{2\pi\mu}{ka} \right) H_1^{(2)}(\beta_\mu r) e^{i2\pi\mu z/a}. \tag{E.15c}$$

The number of summations required can be reduced by half by converting the sum to a $\cos(2\pi\mu z/a), \sin(2\pi\mu z/a)$ basis. The remainder of the relevant components of Green's tensor are given below:

$$G_{rx}^{1D} = \frac{-ik^2\cos(\theta)}{2a} \sum_{\mu=0}^{\infty} \left(H_0^{(2)}(\beta_\mu r) - n_\mu^2 \frac{\partial H_1^{(2)}(\beta_\mu r)}{\partial(\beta_\mu r)} \right) \frac{\cos(\frac{2\pi\mu z}{a})}{(1+\delta_{\mu 0})} \tag{E.16a}$$

$$G_{\theta x}^{1D} = \frac{ik^2\sin(\theta)}{2a} \sum_{\mu=0}^{\infty} \left(H_0^{(2)}(\beta_\mu r) - n_\mu^2 \frac{H_1^{(2)}(\beta_\mu r)}{\beta_\mu r} \right) \frac{\cos(\frac{2\pi\mu z}{a})}{(1+\delta_{\mu 0})} \tag{E.16b}$$

$$G_{zx}^{1D} = \frac{-ik^2\cos(\theta)}{2a} \sum_{\mu=1}^{\infty} n_\mu \left(\frac{2\pi\mu}{ka} \right) H_1^{(2)}(\beta_\mu r) \sin(2\pi\mu z/a) \tag{E.16c}$$

$$G_{ry}^{1D} = \frac{-ik^2\sin(\theta)}{2a}\sum_{\mu=0}^{\infty}\left(H_0^{(2)}(\beta_\mu r) - n_\mu^2\frac{\partial H_1^{(2)}(\beta_\mu r)}{\partial(\beta_\mu r)}\right)\frac{\cos(\frac{2\pi\mu z}{a})}{(1+\delta_{\mu 0})} \tag{E.17a}$$

$$G_{\theta y}^{1D} = \frac{-ik^2\cos(\theta)}{2a}\sum_{\mu=0}^{\infty}\left(H_0^{(2)}(\beta_\mu r) - n_\mu^2\frac{H_1^{(2)}(\beta_\mu r)}{\beta_\mu r}\right)\frac{\cos(\frac{2\pi\mu z}{a})}{(1+\delta_{\mu 0})} \tag{E.17b}$$

$$G_{zy}^{1D} = \frac{-ik^2\sin(\theta)}{2a}\sum_{\mu=1}^{\infty} n_\mu\left(\frac{2\pi\mu}{ka}\right)H_1^{(2)}(\beta_\mu r)\sin(2\pi\mu z/a) \tag{E.17c}$$

$$G_{rz}^{1D} = \frac{-ik^2}{2a}\sum_{\mu=1}^{\infty} n_\mu\left(\frac{2\pi\mu}{ka}\right)H_1^{(2)}(\beta_\mu r)\sin(2\pi\mu z/a) \tag{E.18a}$$

$$G_{\theta z}^{1D} = 0 \tag{E.18b}$$

$$G_{zz}^{1D} = \frac{-ik^2}{2a}\sum_{\mu=0}^{\infty} n_\mu^2 H_0^{(2)}(\beta_\mu r)\frac{\cos(\frac{2\pi\mu z}{a})}{(1+\delta_{\mu 0})} \tag{E.18c}$$

$$F_{rx}^{1D} = \frac{-k^2\sin(\theta)}{2a}\sum_{\mu=1}^{\infty}\left(\frac{2\pi\mu}{ka}\right)H_0^{(2)}(\beta_\mu r)\sin(2\pi\mu z/a) \tag{E.19a}$$

$$F_{\theta x}^{1D} = \frac{-k^2\cos(\theta)}{2a}\sum_{\mu=1}^{\infty}\left(\frac{2\pi\mu}{ka}\right)H_0^{(2)}(\beta_\mu r)\sin(2\pi\mu z/a) \tag{E.19b}$$

$$F_{zx}^{1D} = \frac{k^2\sin(\theta)}{2a}\sum_{\mu=0}^{\infty} n_\mu H_1^{(2)}(\beta_\mu r)\frac{\cos(\frac{2\pi\mu z}{a})}{(1+\delta_{\mu 0})} \tag{E.19c}$$

$$F_{ry}^{1D} = \frac{k^2\cos(\theta)}{2a}\sum_{\mu=1}^{\infty}\left(\frac{2\pi\mu}{ka}\right)H_0^{(2)}(\beta_\mu r)\sin(2\pi\mu z/a) \tag{E.20a}$$

$$F_{\theta y}^{1D} = \frac{-k^2\sin(\theta)}{2a}\sum_{\mu=1}^{\infty}\left(\frac{2\pi\mu}{ka}\right)H_0^{(2)}(\beta_\mu r)\sin(2\pi\mu z/a) \tag{E.20b}$$

$$F_{zy}^{1D} = \frac{-k^2\cos(\theta)}{2a}\sum_{\mu=0}^{\infty} n_\mu H_1^{(2)}(\beta_\mu r)\frac{\cos(\frac{2\pi\mu z}{a})}{(1+\delta_{\mu 0})} \tag{E.20c}$$

$$F_{rz}^{1D} = 0 \tag{E.21a}$$

$$F_{\theta z}^{1D} = \frac{k^2}{2a} \sum_{\mu=0}^{\infty} n_\mu H_1^{(2)}(\beta_\mu r) \frac{\cos(\frac{2\pi\mu z}{a})}{(1+\delta_{\mu 0})} \tag{E.21b}$$

$$F_{zz}^{1D} = 0. \tag{E.21c}$$

E.2 DDA Cross-sections in Two and Three Dimensions

When a three dimensional body scatters, the total field in the limit that $r \to \infty$ must follow

$$\mathbf{E} = \mathbf{E}_{inc} + \mathbf{F}(\mathbf{k}, \mathbf{k}_0) \frac{e^{-ikr}}{r}. \tag{E.22}$$

where $\mathbf{k} = (\omega/c)\hat{\mathbf{r}}(\theta, \phi) : \mathbb{R}^2 \to NS^2$ indicates a direction of the scattered field, and hence $\mathbf{F}(\mathbf{k}, \mathbf{k}_0)$ is the scattered far field pattern scattered in direction $\mathbf{k}$ when the incident field is a plane wave with wave vector $\mathbf{k}_0$. If the scattered field is due to a set of point electric dipoles with dipole moments $\mathbf{p}_i$, then the far field pattern is given by

$$\mathbf{F}(\theta, \phi) = \frac{k^2}{4\pi\epsilon_0} \sum_i \left[\mathbf{p}_i - \hat{\mathbf{k}}(\hat{\mathbf{k}} \cdot \mathbf{p}_i) \right] e^{i\mathbf{k}\cdot\mathbf{r}_i}. \tag{E.23}$$

The $e^{i\mathbf{k}\cdot\mathbf{r}_i}$ term in the equation above is known as the array factor of the dipoles. According to the optical theorem, if the incident field is of the form $\mathbf{E}_{inc} = \mathbf{E}_0 e^{-i\mathbf{k}_0\cdot\mathbf{r}}$, then the total scattering cross section is

$$\sigma_t = \frac{4\pi}{k|\mathbf{E}_0|^2} \mathrm{Im}\{\mathbf{F}|_{\mathbf{k}=\mathbf{k}_0} \cdot \mathbf{E}_0^*\}. \tag{E.24}$$

Since the array factor has the same functional form in the expression for the far-field scattering amplitude, the inner product of the far-field scattering amplitude with the

polarization vector can be re-written as

$$\mathbf{F}|_{\mathbf{k}=\mathbf{k}_0} \cdot \mathbf{E}_0^* = \frac{k^2}{4\pi\epsilon_0} \sum_i \mathbf{p}_i \cdot \mathbf{E}_0^* e^{i\mathbf{k}_0 \cdot \mathbf{r}_i} = \frac{k^2}{4\pi\epsilon_0} \sum_i \mathbf{p}_i \cdot \mathbf{E}_{inc}^*, \tag{E.25}$$

$$\sigma_t = \frac{k}{\epsilon_0 |\mathbf{E}_0|^2} \sum_i \mathrm{Im}\left\{\mathbf{p}_i \cdot \mathbf{E}_{inc}^*\right\} = \frac{\omega}{2I_0} \sum_i \mathrm{Im}\left\{\mathbf{p}_i \cdot \mathbf{E}_{inc}^*\right\}. \tag{E.26}$$

where $I_0 = |\mathbf{E}_0|^2/2Z_0$ is the intensity of the incident light wave.

The physical interpretation of this formula can be illuminated with the use of Poynting's theorem. Before applying Poynting's theorem, we recognize that there are two systems that are solutions to Maxwell's equations that might be considered. The first system is one where the material is considered as passive, and so all dipoles are not source terms but are defined by some polarizability tensor. In this system, the fields are solutions to Maxwell's equations where $\mathbf{P} = \bar{\bar{\alpha}}\mathbf{E} = \bar{\bar{\alpha}}\left(\mathbf{E}_{inc} + \mathbf{E}_{scatt}\right)$, and Poynting's theorem for this states that

$$\frac{\omega}{2} \int \mathrm{Im}\{\mathbf{P} \cdot \mathbf{E}^*\} \mathrm{d}V = -\int \mathbf{E} \times \mathbf{H}^* \cdot \mathrm{d}\mathbf{a} = P_{abs} = I_0 \sigma_{abs}. \tag{E.27}$$

The second system that might be considered is one where the dipole moments $\mathbf{p}_j$ are considered as source terms in Maxwell's equations rather than as passive dipoles, and the fields that are the solution to Maxwell's equation with this source are $\mathbf{E}_{scatt}$. Poynting's theorem applied to this second system states that

$$\begin{aligned} \frac{\omega}{2} \int \mathrm{Im}\{\mathbf{P} \cdot \mathbf{E}_{scatt}^*\} \mathrm{d}V &= -\int \mathbf{E}_{scatt} \times \mathbf{H}_{scatt}^* \cdot \mathrm{d}\mathbf{a} \\ &= -P_{scatt} = -I_0 \sigma_{scatt}. \end{aligned} \tag{E.28}$$

Returning now to eq. (E.27), the total field may be split up into incident and scattered fields, which gives

$$\frac{\omega}{2} \int \mathrm{Im}\{\mathbf{P} \cdot \mathbf{E}_{inc}^*\} \mathrm{d}V = P_{abs} + P_{scatt} = I_0 \sigma_t \tag{E.29}$$

and hence, $\sigma_t = \frac{\omega}{2I_0} \sum_i \mathrm{Im}\left\{\mathbf{p}_i \cdot \mathbf{E}^*_{inc}\right\}$. The physical understanding of this formula is that total work done on the incident field is the real part of the time derivative of $-\sum_i \mathbf{p}_i \cdot \mathbf{E}^*_{inc}$, and the total cross section is the work done divided by the intensity of the incident light.

In two-dimensions, the total cross section per unit length would become

$$\sigma_t = \frac{\omega}{2aI_0} \sum_i \mathrm{Im}\left\{\mathbf{p}_i \cdot \mathbf{E}^*_{inc}\right\} \tag{E.30}$$

where a is the spacing between dipoles in the z-direction. This formula can be easily generalized to use magnetic dipoles by applying a generalized form of Poynting's theorem to include the magnetic current. The result is,

$$\sigma_t = \frac{\omega}{2aI_0} \sum_i \mathrm{Im}\left\{\mathbf{p}_i \cdot \mathbf{E}^*_{inc} + \mathbf{m}_i \cdot \mathbf{H}^*_{inc}\right\}. \tag{E.31}$$

E.3 2D DDA Validation Against Mie Theory

In this section, the 2D-DDA is validated against Mie theory using two cases: a purely electric cylinder with dielectric constant ϵ, and a purely magnetic cylinder with permeability μ. In both cases, the incident field is assumed to be a plane wave with the electric field polarized along the axis of the cylinder. The extinction and scattering cross sections for an infinite cylinder in Mie theory are given by

$$\sigma_{ext} = \frac{4}{k} \sum_{\nu=-\infty}^{\infty} |a_\nu|^2 \tag{E.32a}$$

$$\sigma_{ext} = \frac{4}{k} \sum_{\nu=-\infty}^{\infty} \mathrm{Re}\{a_\nu\} \tag{E.32b}$$

In the first case of the electric cylinder, $n = \sqrt{\epsilon}$, and the Mie coefficients are given by,

$$a_\nu = \frac{J_\nu(nka)J'_\nu(ka) - nJ_\nu(ka)J'_\nu(nka)}{J_\nu(nka)H^{(2)'}_\nu(ka) - nH^{(2)}_\nu(ka)J'_\nu(nka)}. \tag{E.33}$$

In the second case, $\epsilon = 0$ and $n = \sqrt{\mu}$, and the Mie coefficients are given by

$$a_\nu = \frac{nJ_\nu(nka)J'_\nu(ka) - J_\nu(ka)J'_\nu(nka)}{nJ_\nu(nka)H^{(2)'}_\nu(ka) - H^{(2)}_\nu(ka)J'_\nu(nka)}. \tag{E.34}$$

To test both of these cases, a DDA model of a cylinder of radius R was discretized into a rectangular lattice of dipoles with lattice spacing $a = R/12$. The extinction and scattering cross sections were computed using the equations of the previous section. The cross sections of the cylinder with the electric response are shown in fig. E.1(a), and the results of the cylinder with the magnetic response are shown in fig. E.1(b).

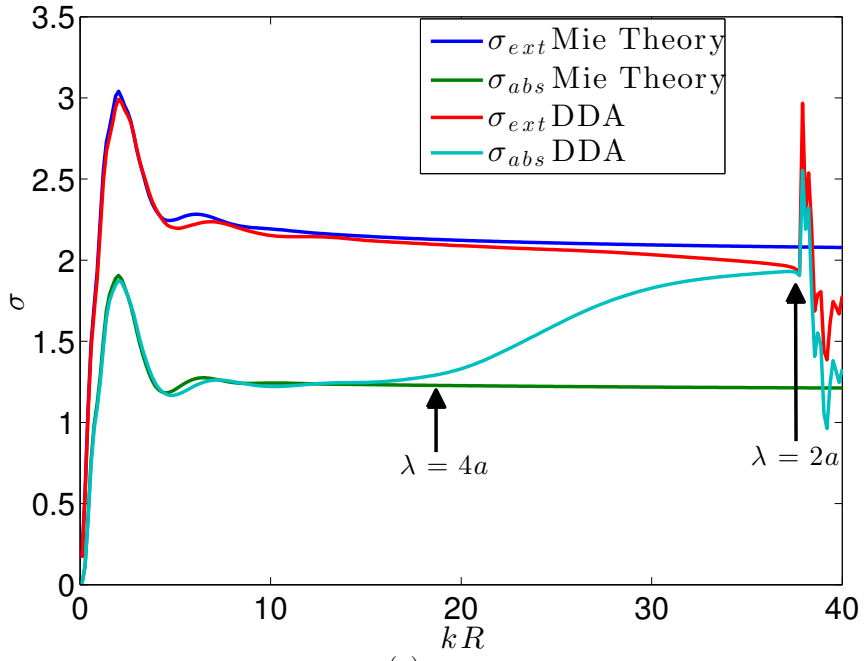

(a)

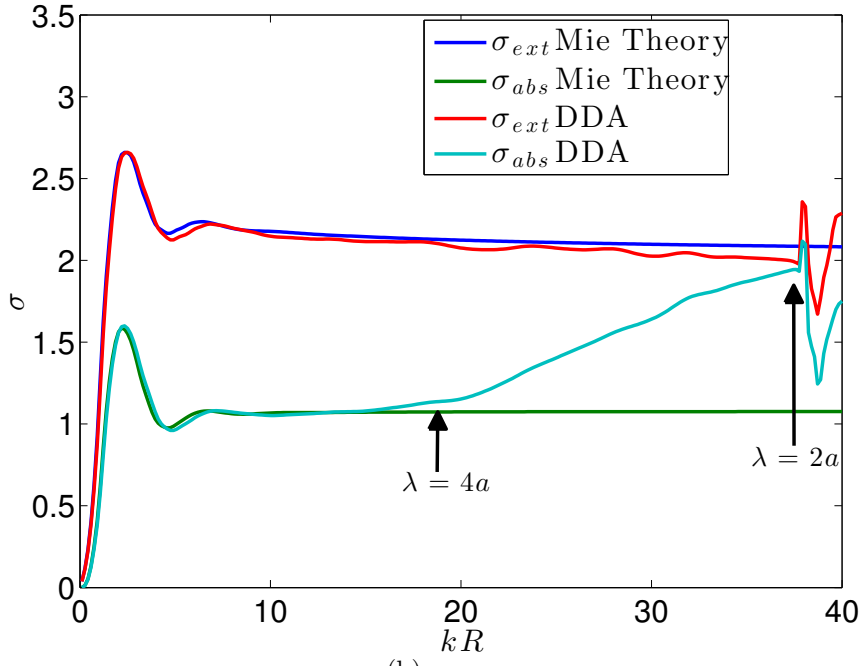

(b)

FIGURE E.1: Comparison of the extinction and scattering cross section of infinite cylinders under illumination by a plane wave at normal incidence, with the electric field polarized along the axis of the cylinder. (a) A cylinder with $\epsilon = 3 - i$ and $\mu = 1$. (b) A cylinder with $\epsilon = 1$ and $\mu = 3 - i$.

Appendix F

Modeling Metamaterial Antennas using the Discrete Dipole Approximation (DDA)

This appendix is a summary of theory that I have developed towards two independent semi-analytical approaches to modeling holographic metamaterial antennas. Laura Pulido assisted with running many of the full-wave simulations that are used to compare with the theory. It is set aside as an appendix because it is quite disjoint from the theme of the remainder of the dissertation.

F.1 Planar Waveguide DDA

One common geometry for metamaterials is in the form of complementary metamaterials that are cut into one side of a planar waveguide. These metamaterial structures are of particular interest in designing holographic metamaterial antennas[146], and in this case the Green's function of the dipoles representing the complementary metamaterial lattice must be modified using a waveguide mode basis inside the waveguide, and using the Green's function of a dipole over a ground plane in the half-space above the waveguide. An example of a metamaterial antenna designed using complemen-

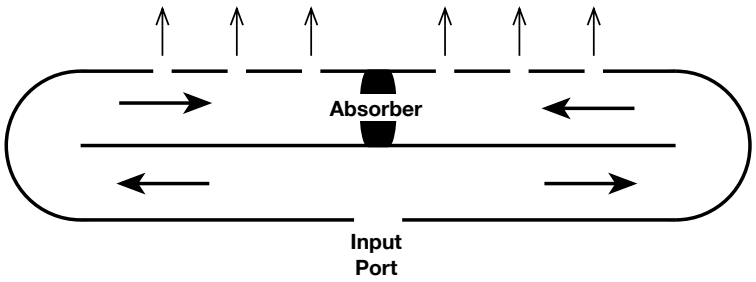

FIGURE F.1: Example feed structure for a holographic metamaterial antenna using a complementary metasurface.

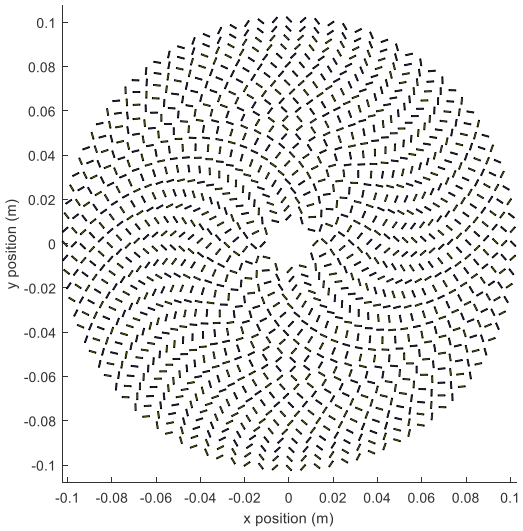

FIGURE F.2: Example of how the metamaterial elements might be arranged the upper surface of the antenna.

tary elements is given in fig. F.1. The antenna is fed through a central port at the bottom of the antenna, and then travels around the lower chamber and into the upper chamber, where it excites the complementary metamaterial elements, which in turn radiate a beam into the far-field. An example for how the unit cells might be arranged in the upper surface is shown in fig. F.2.

In this section the standard DDA method is adapted to model geometries like the one shown in fig. F.1, where complementary metamaterial elements are placed on

the surface of a parallel plate (i.e. planar) waveguide. The unit cells in this geometry scatter both into the waveguide and into free space. The unit cells therefore couple to each other both through the interior of the waveguide and over the top of the waveguide. The mutual interaction through both paths can be modeled by using the appropriate Green's function: the interaction through the waveguide is described by a planar waveguide Green's function and the interaction over the top of the waveguide is described by the free space Green's function. This section of the report provides a novel derivation of the planar waveguide Green's function in a cylindrical Hankel basis using the unconjugated form of Lorentz reciprocity, and then use this result to model a holographic metamaterial antenna and predict far field patterns using a discrete dipole approach. The planar waveguide Green's function is then used to model the entire antenna using the DDA approach. The interaction between the elements over the top of the waveguide is also included, but it is shown that this interaction is much less significant than the interaction through the waveguide.

Formulating the discrete dipole approximation for a system of dipoles is done by writing down the total fields incident on each of the dipoles, which are equal to the incident field plus the fields due to all of the other dipoles. The field emitted by a dipole is described using Green's functions, which are unique to a particular geometry, and defined so that $\mathbf{H} = \bar{\mathbf{G}}^{mm}\mathbf{m} + \frac{1}{Z_0}\bar{\mathbf{G}}^{me}\mathbf{p}$, and $\mathbf{E} = \bar{\mathbf{G}}^{ee}\mathbf{p} + Z_0\bar{\mathbf{G}}^{em}\mathbf{m}$, where $\bar{\mathbf{G}}^{ee}$ and $\bar{\mathbf{G}}^{mm}$ are the tensorial electric and magnetic Green's functions, $\bar{\mathbf{G}}^{em} = -\bar{\mathbf{G}}^{me}$ is the magneto-electric Green's tensor, and Z_0 is the impedance of free space. Using this notation, the total field incident on the i^{th} dipole is

$$(\alpha_m^i)^{-1}\mathbf{m}_i = \mathbf{H}_0(\mathbf{r}_i) + \sum_{j\neq i}\left(\mathbf{G}^{mm}(\mathbf{r}_i - \mathbf{r}_j)\mathbf{m}_j + \frac{1}{Z_0}\mathbf{G}^{me}(\mathbf{r}_i - \mathbf{r}_j)\mathbf{p}_j\right) \tag{F.1a}$$

$$(\alpha_e^i)^{-1}\mathbf{p}_i = \mathbf{E}_0(\mathbf{r}_i) + \sum_{j\neq i}\left(\mathbf{G}^{ee}(\mathbf{r}_i - \mathbf{r}_j)\mathbf{p}_j + Z_0\mathbf{G}^{em}(\mathbf{r}_i - \mathbf{r}_j)\mathbf{m}_j\right). \tag{F.1b}$$

This can all be rewritten as a matrix equation that solves for the electric and magnetic

dipole moments:

$$\begin{bmatrix} (\alpha_m^i)^{-1}\delta_{ij} - \mathbf{G}_{ij}^{mm} & \frac{1}{Z_0}\mathbf{G}_{ij}^{me} \\ -Z_0\mathbf{G}_{ij}^{em} & (\alpha_e^i)^{-1}\delta_{ij} - \mathbf{G}_{ij}^{ee} \end{bmatrix} \begin{bmatrix} \mathbf{m}_j \\ \mathbf{p}_j \end{bmatrix} = \begin{bmatrix} \mathbf{H}_0(\mathbf{r}_i) \\ \mathbf{E}_0(\mathbf{r}_i) \end{bmatrix} \tag{F.2}$$

where $\mathbf{G}_{ij} = \mathbf{G}(\mathbf{r}_i - \mathbf{r}_j)$ if $i \neq j$ and $\mathbf{G}_{ij} = 0$ if $i = j$. The matrix on the left-hand-side may be defined using the Green's functions of the waveguide, and inverted to solve for the dipole moments.

In previous works, the Green's function here was the free space Green's function[30], but in the context of complementary metamaterial device, the Green's function needs to be replaced with that of a planar waveguide. To this end, the Green's function of a planar waveguide is derived in appendix F.2 by expanding the Green's function in cylindrical waveguide modes.

The system matrix in the DDA will need to be expressed in terms of vector components, and the only neat way to reconcile the basis of vector fields is to use a coordinate system where the basis is invariant to a linear translation so that all the dipoles share the basis. Hence, the cleanest coordinate system to use is cartesian. The components of Green's tensor can be converted into a cartesian basis using the transformation,

$$G_{xx}^{mm} = \cos(\theta)G_{rx}^{mm} - \sin(\theta)G_{\theta x}^{mm} \tag{F.3a}$$

$$G_{xy}^{mm} = \cos(\theta)G_{ry}^{mm} - \sin(\theta)G_{\theta y}^{mm} \tag{F.3b}$$

$$G_{yy}^{mm} = \sin(\theta)G_{ry}^{mm} + \cos(\theta)G_{\theta y}^{mm} \tag{F.3c}$$

$$G_{yx}^{mm} = \sin(\theta)G_{rx}^{mm} + \cos(\theta)G_{\theta x}^{mm}. \tag{F.3d}$$

From a computational standpoint, the number of elements of Green's tensor that need to be computed can be reduced by exploiting the symmetries of Green's tensor, which are valid whenever both the vector and covector basis that are used to express the tensor are expressed using the same coordinate system. In cartesian coordinates,

the $\mathbf{G}^{ee}$ and $\mathbf{G}^{mm}$ tensors are symmetric,

$$G^{mm}_{xy} = G^{mm}_{yx} \tag{F.4}$$

Note that we do not have the typical property that $\mathbf{G}^{mm} = \mathbf{G}^{ee}$, since the boundary conditions of the waveguide break this symmetry. However, $\mathbf{G}^{me} = -\mathbf{G}^{em}$ still holds, and the $\mathbf{G}^{em}$ and $\mathbf{G}^{me}$ tensors themselves are antisymmetric, so

$$G^{me}_{xz} = G^{em}_{zx} \tag{F.5a}$$

$$G^{me}_{yz} = G^{em}_{zy}. \tag{F.5b}$$

The results of modeling a 70cm aperture at 12.1GHz using the DDA and a full-wave solver are shown in figs. F.3(a) and F.3(b). The far-field pattern from the full-wave solver is labeled "HFSS" in the figure. The "Array Factor" computation ignores the interaction between the elements. The "DDA PPWG" is the DDA model that only includes the interaction between the elements through the waveguide, while the "DDA PPWG+FS" curve is the DDA model that includes the interaction over the top of the waveguide through the free space Green's function. "Previous Computation" is an industry-standard model that assumes a surface impedance description of the metamaterial elements.

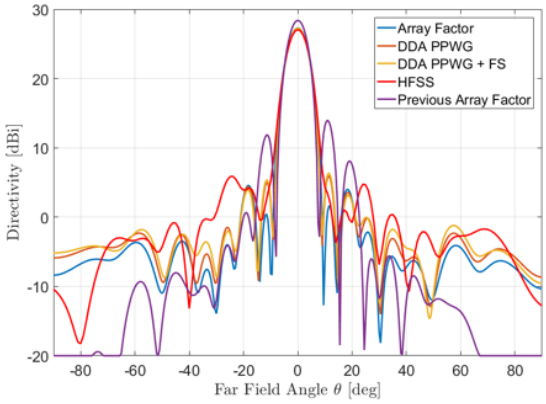

(a)

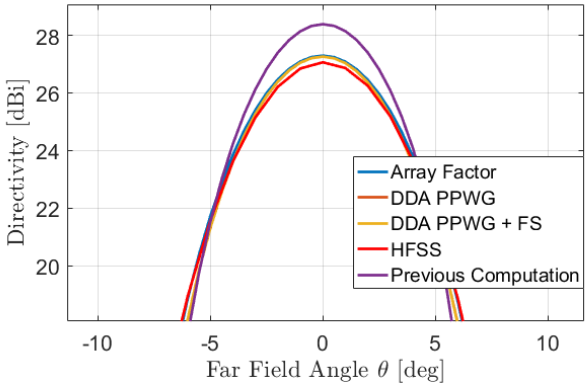

(b)

FIGURE F.3: (a) Comparison of various antenna models with a full-wave simulation of the antenna. A description of the various curves is in the main text.

.

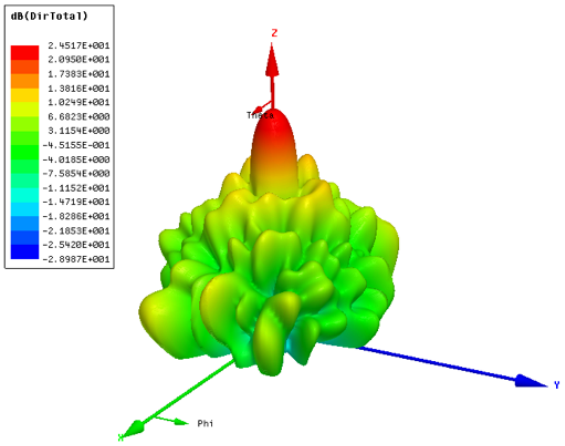

(a)

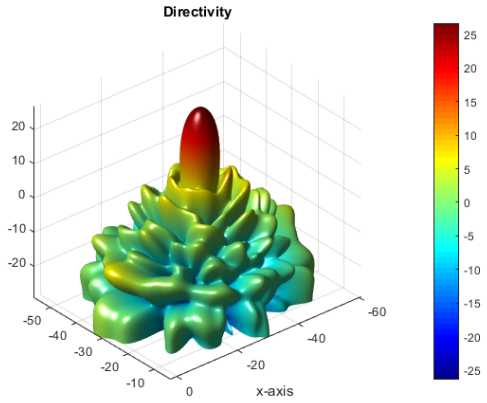

(b)

FIGURE F.4: Comparison of 3D far-field plots generated by both (a) a full-wave solver and (b) the planar-waveguide DDA approach.

.

F.2 Green's Functions In Planar Waveguides

The field emitted by dipoles is described using Green's functions, which are defined so that

$$\mathbf{H} = \bar{\mathbf{G}}^{mm}\mathbf{m} + \frac{1}{Z_0}\bar{\mathbf{G}}^{me}\mathbf{p} \tag{F.6a}$$

$$\mathbf{E} = \bar{\mathbf{G}}^{ee}\mathbf{p} + Z_0\bar{\mathbf{G}}^{em}\mathbf{m} \tag{F.6b}$$

where $\bar{\mathbf{G}}^{ee}$ and $\bar{\mathbf{G}}^{mm}$ are the tensorial electric and magnetic Green's functions, $\bar{\mathbf{G}}^{em} = -\bar{\mathbf{G}}^{me}$ is the magneto-electric Green's tensor, and Z_0 is the impedance of free space. The various components of these tensors can be constructed using the methods of coupled mode theory as outlined above. First, we choose to expand the tensors in a basis of tensor products in cylindrical coordinates,

$$\begin{aligned}\bar{\mathbf{G}} = {} & G_{rx}\hat{\mathbf{r}}\otimes\hat{\mathbf{x}} + G_{\theta x}\hat{\theta}\otimes\hat{\mathbf{x}} + G_{zx}\hat{\mathbf{z}}\otimes\hat{\mathbf{x}} \\ & + G_{ry}\hat{\mathbf{r}}\otimes\hat{\mathbf{y}} + G_{\theta y}\hat{\theta}\otimes\hat{\mathbf{y}} + G_{zy}\hat{\mathbf{y}}\otimes\hat{\mathbf{x}} \\ & + G_{rz}\hat{\mathbf{r}}\otimes\hat{\mathbf{z}} + G_{\theta z}\hat{\theta}\otimes\hat{\mathbf{z}} + G_{zz}\hat{\mathbf{z}}\otimes\hat{\mathbf{z}}.\end{aligned} \tag{F.7a}$$

Note that, whenever performing an expansion in cylindrical coordinates, a particular origin is implied. Here we assume that the origin will be the location of the dipole. Once this expansion is done, the various tensor components can be evaluated by considering what the resulting fields would be for dipoles oriented in different directions. Here we will first compute the tensor components in the mixture of cylindrical and cartesian coordinates as shown in eq. (F.7a), and then convert the tensor to pure cartesian coordinates, so it will be of the form

$$\begin{aligned}\bar{\mathbf{G}} = {} & G_{xx}\hat{\mathbf{x}}\otimes\hat{\mathbf{x}} + G_{yx}\hat{\mathbf{y}}\otimes\hat{\mathbf{x}} + G_{zx}\hat{\mathbf{z}}\otimes\hat{\mathbf{x}} \\ & + G_{xy}\hat{\mathbf{y}}\otimes\hat{\mathbf{y}} + G_{yy}\hat{\mathbf{y}}\otimes\hat{\mathbf{y}} + G_{zy}\hat{\mathbf{y}}\otimes\hat{\mathbf{x}} \\ & + G_{yz}\hat{\mathbf{y}}\otimes\hat{\mathbf{z}} + G_{xz}\hat{\mathbf{y}}\otimes\hat{\mathbf{z}} + G_{zz}\hat{\mathbf{z}}\otimes\hat{\mathbf{z}}.\end{aligned} \tag{F.8a}$$

Based on eq. (F.7a), the magnetic field emitted by a magnetic dipole oriented in the y-direction reduces to $H_\theta = G^{mm}_{\theta y}m_y$, the magnetic field emitted by an electric

dipole oriented in the z-direction reduces to $H_\theta = G^{me}_{\theta z} p_z$, and so on. Following the methods of coupled mode theory outlined in the previous sections, these components of Green's tensor must be given by

$$\begin{aligned} G^{mm}_{rx} =& \frac{-ik^2\cos(\theta)}{4h}\sum_{\mu=0}^{\infty}\epsilon(z_0)Z^{TM}_\mu(z_0)\epsilon(z)Z^{TM}_\mu(z)\frac{H^{(2)}_1(\beta_\mu r)}{\beta_\mu r} \\ &+ \frac{\partial_z Z^{TE}_\mu(z_0)\partial_z Z^{TE}_\mu(z)}{k^2}\frac{\partial H^{(2)}_1(\beta_\mu r)}{\partial(\beta_\mu r)} \end{aligned} \tag{F.9a}$$

$$\begin{aligned} G^{mm}_{\theta x} =& \frac{ik^2\sin(\theta)}{4h}\sum_{\mu=0}^{\infty}\epsilon(z_0)Z^{TM}_\mu(z_0)\epsilon(z)Z^{TM}_\mu(z)\frac{\partial H^{(2)}_1(\beta_\mu r)}{\partial(\beta_\mu r)} \\ &- \frac{\partial_z Z^{TE}_\mu(z_0)\partial_z Z^{TE}_\mu(z)}{k^2}\frac{H^{(2)}_1(\beta_\mu r)}{\beta_\mu r} \end{aligned} \tag{F.9b}$$

$$G^{mm}_{zx} = 0 \tag{F.9c}$$

$$\begin{aligned} G^{mm}_{ry} =& \frac{-ik^2\sin(\theta)}{4h}\sum_{\mu=0}^{\infty}\epsilon(z_0)Z^{TM}_\mu(z_0)\epsilon(z)Z^{TM}_\mu(z)\frac{H^{(2)}_1(\beta_\mu r)}{\beta_\mu r} \\ &+ \frac{\partial_z Z^{TE}_\mu(z_0)\partial_z Z^{TE}_\mu(z)}{k^2}\frac{\partial H^{(2)}_1(\beta_\mu r)}{\partial(\beta_\mu r)} \end{aligned} \tag{F.9d}$$

$$\begin{aligned} G^{mm}_{\theta y} =& \frac{-ik^2\cos(\theta)}{4h}\sum_{\mu=0}^{\infty}\epsilon(z_0)Z^{TM}_\mu(z_0)\epsilon(z)Z^{TM}_\mu(z)\frac{\partial H^{(2)}_1(\beta_\mu r)}{\partial(\beta_\mu r)} \\ &- \frac{\partial_z Z^{TE}_\mu(z_0)\partial_z Z^{TE}_\mu(z)}{k^2}\frac{H^{(2)}_1(\beta_\mu r)}{\beta_\mu r} \end{aligned} \tag{F.9e}$$

$$G^{mm}_{zy} = 0 \tag{F.9f}$$

$$G^{ee}_{zz} = \sum_{\mu=0}^{\infty} \frac{-i\beta_\mu^2}{4h} Z_\mu^{TM}(z_0) H_0^{(2)}(\beta_\mu r) Z_\mu^{TM}(z) \tag{F.10a}$$

$$G^{ee}_{rz} = \frac{ik^2}{4h} \sum_{\mu=0}^{\infty} \frac{n_\mu Z_\mu^{TM}(z_0) \partial_z Z_\mu^{TM}(z)}{k} H_1^{(2)}(\beta_\mu r) \tag{F.10b}$$

$$G^{ee}_{\theta z} = 0 \tag{F.10c}$$

$$G^{me}_{rz} = 0 \tag{F.11a}$$

$$G^{me}_{\theta z} = \frac{k^2}{4h} \sum_{\mu=0}^{\infty} n_\mu Z_\mu^{TM}(z_0) \epsilon(z) Z_\mu^{TM}(z) H_1^{(2)}(\beta_\mu r) \tag{F.11b}$$

$$G^{me}_{zz} = 0 \tag{F.11c}$$

$$\begin{aligned} G^{em}_{rx} = & \frac{-k^2 \sin(\theta)}{4h} \sum_{\mu=0}^{\infty} \frac{\epsilon(z_0) Z_\mu^{TM}(z_0) \partial_z Z_\mu^{TM}(z)}{k} \frac{\partial H_1^{(2)}(\beta_\mu r)}{\partial(\beta_\mu r)} \\ & - \frac{\partial_z Z_\mu^{TE}(z_0) Z_\mu^{TE}(z)}{k} \frac{H_1^{(2)}(\beta_\mu r)}{\beta_\mu r} \end{aligned} \tag{F.12a}$$

$$\begin{aligned} G^{em}_{\theta x} = & \frac{-k^2 \cos(\theta)}{4h} \sum_{\mu=0}^{\infty} \frac{\epsilon(z_0) Z_\mu^{TM}(z_0) \partial_z Z_\mu^{TM}(z)}{k} \frac{H_1^{(2)}(\beta_\mu r)}{\beta_\mu r} \\ & - \frac{\partial_z Z_\mu^{TE}(z_0) Z_\mu^{TE}(z)}{k} \frac{\partial H_1^{(2)}(\beta_\mu r)}{\partial(\beta_\mu r)} \end{aligned} \tag{F.12b}$$

$$G^{em}_{zx} = \frac{-k^2 \sin(\theta)}{4h} \sum_{\mu=0}^{\infty} n_\mu Z_\mu^{TM}(z_0) \epsilon(z_0) Z_\mu^{TM}(z) H_1^{(2)}(\beta_\mu r) \tag{F.12c}$$

$$G_{ry}^{em} = \frac{k^2\cos(\theta)}{4h}\sum_{\mu=0}^{\infty}\frac{\epsilon(z_0)Z_\mu^{TM}(z_0)\partial_z Z_\mu^{TM}(z)}{k}\frac{\partial H_1^{(2)}(\beta_\mu r)}{\partial(\beta_\mu r)} - \frac{\partial_z Z_\mu^{TE}(z_0)Z_\mu^{TE}(z)}{k}\frac{H_1^{(2)}(\beta_\mu r)}{\beta_\mu r} \tag{F.13a}$$

$$G_{\theta y}^{em} = \frac{-k^2\sin(\theta)}{4h}\sum_{\mu=0}^{\infty}\frac{\epsilon(z_0)Z_\mu^{TM}(z_0)\partial_z Z_\mu^{TM}(z)}{k}\frac{H_1^{(2)}(\beta_\mu r)}{\beta_\mu r} - \frac{\partial_z Z_\mu^{TE}(z_0)Z_\mu^{TE}(z)}{k}\frac{\partial H_1^{(2)}(\beta_\mu r)}{\partial(\beta_\mu r)} \tag{F.13b}$$

$$G_{zy}^{em} = \frac{k^2\cos(\theta)}{4h}\sum_{\mu=0}^{\infty} n_\mu Z_\mu^{TM}(z_0)\epsilon(z_0)Z_\mu^{TM}(z)H_1^{(2)}(\beta_\mu r) \tag{F.13c}$$

where r and θ are defined in the local coordinates of the dipole, and z_0 is the position on the z-axis of the dipole.

The complexity of these Green's functions can be greatly reduced using two simplifications. Firstly, In the context of planar waveguides, only electric dipoles in the z-direction and magnetic dipoles lying in the xy-plane are relevant to the problem. Assuming that the dipoles have these orientations reduces the set of matrix elements that are relevant to the problem to $\{G_{rx}^{mm}, G_{\theta x}^{mm}, G_{ry}^{mm}, G_{\theta y}^{mm}, G_{zz}^{ee}, G_{\theta z}^{me}, G_{rz}^{me}, G_{zx}^{em}, G_{zy}^{em}\}$.

The second simplification that may be applied is to neglect all of the modes that are in cutoff, so that only the $\mu = 0$ mode is taken into account in the interaction of the dipoles. The relevant components of the Green's tensors with these simplifica-

tions are

$$G_{rx}^{mm} = \frac{-ik^2\cos(\theta)}{4h}\epsilon(z_0)Z_0^{TM}(z_0)\epsilon(z)Z_0^{TM}(z)\frac{H_1^{(2)}(\beta_0 r)}{\beta_0 r} \tag{F.14a}$$

$$G_{\theta x}^{mm} = \frac{ik^2\sin(\theta)}{4h}\epsilon(z_0)Z_0^{TM}(z_0)\epsilon(z)Z_0^{TM}(z)\frac{\partial H_1^{(2)}(\beta_0 r)}{\partial(\beta_0 r)} \tag{F.14b}$$

$$G_{ry}^{mm} = \frac{-ik^2\sin(\theta)}{4h}\epsilon(z_0)Z_0^{TM}(z_0)\epsilon(z)Z_0^{TM}(z)\frac{H_1^{(2)}(\beta_0 r)}{\beta_0 r} \tag{F.14c}$$

$$G_{\theta y}^{mm} = \frac{-ik^2\cos(\theta)}{4h}\epsilon(z_0)Z_0^{TM}(z_0)\epsilon(z)Z_0^{TM}(z)\frac{\partial H_1^{(2)}(\beta_0 r)}{\partial(\beta_0 r)} \tag{F.14d}$$

$$G_{zz}^{ee} = \frac{-i\beta_0^2}{4h}Z_0^{TM}(z_0)Z_0^{TM}(z)H_0^{(2)}(\beta_0 r) \tag{F.15}$$

$$G_{rz}^{me} = 0 \tag{F.16a}$$

$$G_{\theta z}^{me} = \frac{k^2}{4h}n_0 Z_0^{TM}(z_0)\epsilon(z_0)Z_0^{TM}(z)H_1^{(2)}(\beta_\mu r) \tag{F.16b}$$

$$G_{zx}^{em} = \frac{-k^2\sin(\theta)}{4h}n_0 Z_0^{TM}(z_0)\epsilon(z_0)Z_0^{TM}(z)H_1^{(2)}(\beta_\mu r) \tag{F.17a}$$

$$G_{zy}^{em} = \frac{k^2\cos(\theta)}{4h}n_0 Z_0^{TM}(z_0)\epsilon(z_0)Z_0^{TM}(z)H_1^{(2)}(\beta_\mu r) \tag{F.17b}$$

F.3 Cavity DDA

There are two drawbacks to the planar waveguide geometry, and to address these drawbacks this section proposes an entirely different approach to solving the problem of modeling holographic metamaterial antennas with the kind of feed structure shown in fig. F.1. The first drawback involves how the DDA matrix equations scale with increasing aperture size. When the DDA equations are formed for any arrangement of metamaterials elements, the size of the matrix that must be inverted is $N \times N$, where

N is the number of dipoles. However, when the dipoles are placed in a geometry that is like a cavity, it is possible to expand the fields in the cavity as a sum of cavity modes. In this case, an alternative matrix problem can be formulated, where the size of the matrix is $M \times M$, where M is the number of modes, rather than $N \times N$. In general, the number of modes that need to be included is approximately kR, where k is the wavenumber in free space and R is the radius of the aperture. On the other hand, the number of metamaterial elements in the aperture scales as $(R/a)^2$ where a is the distance between the elements. This means that for larger apertures it may be beneficial from a computational standpoint to try to set up the problem in terms of cavity eigenmodes.

The second drawback of the planar-waveguide DDA is that it entirely ignores the dynamics of the bottom chamber of the feed-structure, and it is possible that the scattered fields from the unit cells could propagate through the lower chamber and thereby interact with elements on the other side of the antenna. However, if the eigenmodes of the cavity are found, and the full problem is solved in terms of these eigenmodes, then all interactions through all possible paths of the cavity will automatically be taken into account.

The cavity modes of the feed structure shown in fig. F.1 are solved for in appendix F.4 in the absence of the ports or metamaterial elements. This section of the document explains how to formulate the solution of the entire problem including the ports and metamaterial elements using an expansion into a cavity eigenmode basis.

The general idea behind using a discrete dipole approximation is to model a system as a set of point scatterers. In the context of metamaterials, each metamaterial element may be thought of as an individual point scatterer. The discrete dipole approximation is implemented by creating a matrix equation that describes the coupling between all the metamaterial elements, and inverting that matrix to solve for the total fields everywhere. When implementing the discrete dipole approximation

in different geometries, the only change in the formalism that needs to be made is to alter the expression for the coupling between the dipoles. This coupling is given by the scattered fields of the dipoles, which is described by the Green's function for that particular geometry.

$$\mathbf{E}(\mathbf{r}) = \int \mathbf{G}(\mathbf{r}, \mathbf{r}')\mathbf{P}(\mathbf{r})\mathrm{d}V \tag{F.18}$$

In a waveguide, the Green's function is a sum over waveguide modes, and that formalism has been used to implement the discrete dipole approximation in both linear and planar waveguides. In the case of the linear waveguide, the waveguide modes are solutions to an eigenvalue problem in two dimensions, with the propagation constant being the eigenvalue. In other words, they are standing waves in two dimensions, and propagating waves in the third dimension, with the propagation constant being uniquely defined for each mode. In that case, time (or frequency) is a continuous parameter that may be freely chosen. However, a cavity defines a three dimensional eigenvalue problem, which yields standing waves in all three dimensions. In this case, the eigenvalue is the frequency, and it is no longer a free parameter but is restricted to specific values that are unique to each eigenmode. The cavity eigenmodes along with their eigenfrequencies define how dipoles interact within a cavity, in the same way that the waveguide modes along with their corresponding propagation constants define the interaction between dipoles in a linear waveguide. It is well known that the Green's function for electric dipoles in a cavity can be written as,[14]

$$\mathbf{G}_e(\mathbf{r}, \mathbf{r}') = -\omega^2\mu_0 \sum_\nu \frac{\mathbf{E}_\nu(\mathbf{r}) \otimes \mathbf{E}_\nu(\mathbf{r}')}{k^2 - k_\nu^2} \tag{F.19}$$

where the functions $\mathbf{E}_\nu(\mathbf{r})$ are the cavity eigenmodes, which are defined by the source-free solutions of Maxwell's equations in the cavity:

$$\nabla^2\mathbf{E}_\nu = -k_\nu^2\mathbf{E}_\nu. \tag{F.20}$$

These modes are chosen to be normalized so that $\int |\mathbf{E}_\nu|^2 \mathrm{d}V = 1$. The scattering due to magnetic dipoles can be defined in a similar manner using the tensor product of the magnetic fields of the cavity modes.

F.3.1 Modeling the Feed Structure Using an Eigenmode Expansion

The total field in the cavity can be expanded in terms of a sum of cavity modes such that $\mathbf{E} = \sum_\mu e_\mu(\omega)\mathbf{E}_\mu(\mathbf{r})$. When there is a distribution of polarization density in the cavity, $\mathbf{P}(\mathbf{r})$, the expansion coefficients $e_\nu(\omega)$ can be easily found using the Green's function, and are given by[30]

$$e_\mu(\omega) = \frac{\omega^2 \int \mathbf{E}_\mu \cdot \mathbf{P} \mathrm{d}V / U_\mu}{\omega_\mu^2 - \omega^2} \tag{F.21}$$

where $U_\mu = \epsilon_0 \int |\mathbf{E}_\mu|^2 \mathrm{d}V \equiv 1$ is the energy contained in a particular mode. Note that the driving term, $\int (\mathbf{E}_\mu \cdot \mathbf{P})\, \mathrm{d}V$, is equivalent to the time average of the potential energy of the polarization density when exposed to the eigenmode field $\mathbf{E}_\mu$ with unit amplitude.

Therefore, the problem to finding the exact field distribution in the cavity reduces to the problem of finding the polarization density function, $\mathbf{P}(\mathbf{r})$, inside the cavity. When the cavity is empty, this polarization is only composed of the two ports used in the feed structure, both of which can be modeled as point electric dipoles. One of the ports is an active drive port that is located at the center of the lower chamber of the cavity, and the other is a passive receiver located at the center of the upper chamber. The passive receiver can be modeled as an anisotropic electric dipole $\mathbf{p}_r = \bar{\alpha}\mathbf{E}(\mathbf{r}_r)$ with a polarizability tensor given by $\bar{\alpha} = \alpha \hat{z} \otimes \hat{z}$, where α is a purely imaginary constant for a perfectly absorbing receiver and $\mathbf{r}_r$ is the position of the receiver. The drive port can be modeled as an electric dipole with a fixed dipole moment, $\mathbf{p}_s$, oriented in the $\hat{z}$ direction. However, the drive port can also absorb impinging waves, which is the physical mechanism that ultimately gives rise to the

return loss of the antenna. So the total dipole moment of the source port must be written $\mathbf{p}_s = \mathbf{p}_d + \bar{\alpha}\mathbf{E}(\mathbf{r}_s)$, where $\mathbf{r}_s$ is the position of the drive port.

The total dipole moment density of the system is therefore a sum of three dipoles

$$\mathbf{P}(\mathbf{r}) = \left(\mathbf{p}_d\delta^{(3)} + \bar{\alpha}\mathbf{E}(\mathbf{r})\right)\delta^{(3)}(\mathbf{r}-\mathbf{r}_s) + \bar{\alpha}\mathbf{E}(\mathbf{r})\delta^{(3)}(\mathbf{r}-\mathbf{r}_r), \tag{F.22}$$

one of which is fixed and two of which are passive. This polarization density depends on the electric field profile, but it can be plugged back into eq. (F.21) to self-consistently solve for the mode amplitudes $e_\mu(\omega)$.

$$e_\mu \frac{\omega_\mu^2 - \omega^2}{\omega^2} = \left(\mathbf{p}_d \cdot \mathbf{E}_\mu(\mathbf{r}_s)\right)/U_\mu + \mathbf{E}(\mathbf{r}_s)\frac{\bar{\alpha}}{U_\mu}\mathbf{E}_\mu(\mathbf{r}_s) + \mathbf{E}(\mathbf{r}_r)\frac{\bar{\alpha}}{U_\mu}\mathbf{E}_\mu(\mathbf{r}_r) \tag{F.23}$$

The total field in the cavity can be expanded in terms of eigenmodes, $\mathbf{E} = \sum_\mu e_\mu(\omega)\mathbf{E}_\mu(\mathbf{r})$, yielding

$$\sum_\nu \left[U_\nu \frac{\omega_\nu^2 - \omega^2}{\omega^2}\delta_{\mu\nu} - \mathbf{E}_\nu(\mathbf{r}_s)\bar{\alpha}\mathbf{E}_\mu(\mathbf{r}_s) - \mathbf{E}_\nu(\mathbf{r}_r)\bar{\alpha}\mathbf{E}_\mu(\mathbf{r}_r)\right] e_\nu = \left(\mathbf{p}_d \cdot \mathbf{E}_\mu(\mathbf{r}_s)\right). \tag{F.24}$$

Note that the entire equation has units of energy. The left-hand side forms a matrix equation that can be inverted to solve for the mode amplitudes in the cavity, $e_\mu(\omega)$, which form the solution of the system. This method can be generalized to include an arbitrary number of electric dipoles at positions $\mathbf{r}_i$ and with polarizabilities $\bar{\alpha}_i$ by introducing a sum in the matrix equation

$$\sum_\nu \left[U_\nu \frac{\omega_\nu^2 - \omega^2}{\omega^2}\delta_{\mu\nu} - \sum_i \mathbf{E}_\nu(\mathbf{r}_i)\bar{\alpha}_i\mathbf{E}_\mu(\mathbf{r}_i)\right] e_\nu = \left(\mathbf{p}_d \cdot \mathbf{E}_\mu(\mathbf{r}_s)\right). \tag{F.25}$$

Figure F.5 illustrates the result of compiling these equations to compute the z-component of the electric field in the feed structure for a cavity with dimensions given in table F.1.

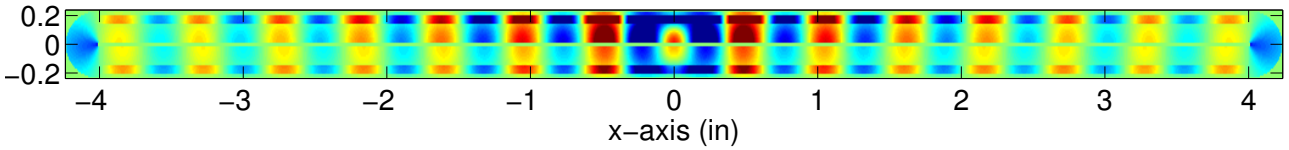

FIGURE F.5: The z-component of the electric field in the cavity feed structure according to the discrete dipole model.

.

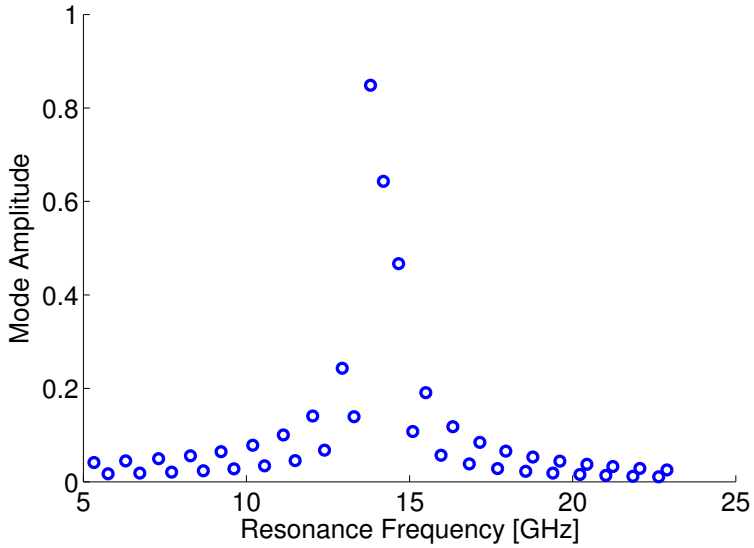

FIGURE F.6: Eigemode amplitudes $|e_\mu|$ of the feed structure plotted versus their resonance frequencies, $\omega_\mu/2\pi$.

.

Parameter	Value
R	5 in
a	0.008 in
h	0.225 in
$(\delta h_1, \delta h_2, \delta h_3)$	$(0.14, 0.06, 0.025)$ in
$(\epsilon_1, \epsilon_2, \epsilon_3)$	$(3, 1, 4.5)$
frequency	14.1 GHz

Table F.1: Table of dimensions used in feed-structure geometry.

F.3.2 Modeling Cavities with Electric and Magnetic Dipoles

Let us expand both the electric and magnetic fields in the cavity into a sum of modes.

$$\mathbf{E} = \sum_{\mu} e_{\mu}(\omega)\mathbf{E}_{\mu}(\mathbf{r}) \tag{F.26}$$

$$\mathbf{H} = \sum_{\mu} h_{\mu}(\omega)\mathbf{H}_{\mu}(\mathbf{r}) \tag{F.27}$$

The mode amplitudes are given by,

$$e_{\mu}(\omega) = \frac{\omega^2}{\omega_{\mu}^2 - \omega^2}\left(\int \mathbf{P}\cdot\mathbf{E}_{\mu}\mathrm{d}^3\mathbf{r} - (\omega_{\mu}/\omega)\int \mathbf{M}\cdot\mathbf{H}_{\mu}\mathrm{d}^3\mathbf{r}\right)/U_{\mu} \tag{F.28}$$

$$h_{\mu}(\omega) = \frac{\omega^2}{\omega_{\mu}^2 - \omega^2}\left((\omega_{\mu}/\omega)\int \mathbf{P}\cdot\mathbf{E}_{\mu}\mathrm{d}^3\mathbf{r} - \int \mathbf{M}\cdot\mathbf{H}_{\mu}\mathrm{d}^3\mathbf{r}\right)/U_{\mu}. \tag{F.29}$$

Since the electric field mode amplitude $e_{\mu}(\omega)$ will closely follow the magnetic field mode amplitude, we can take an average of the two fields defined by $a_{\mu} \equiv (e_{\mu}(\omega) + h_{\mu}(\omega))/2$. The average of the two mode amplitudes then follows

$$a_{\mu}(\omega) = \frac{\omega}{\omega_{\mu} - \omega}\left(\int \mathbf{P}\cdot\mathbf{E}_{\mu}\mathrm{d}^3\mathbf{r} - \int \mathbf{M}\cdot\mathbf{H}_{\mu}\mathrm{d}^3\mathbf{r}\right)/2U_{\mu}, \tag{F.30}$$

and we make the approximation that the electric and magnetic fields are given by this averaged amplitude coefficient:

$$\mathbf{E} = \sum_{\mu} a_{\mu}(\omega)\mathbf{E}_{\mu}(\mathbf{r}) \tag{F.31}$$

$$\mathbf{H} = \sum_{\mu} a_{\mu}(\omega)\mathbf{H}_{\mu}(\mathbf{r}). \tag{F.32}$$

Averaging the amplitude coefficient cuts the order of the system in half, which will decrease the computational time by a factor of four. Following the steps of the previous section to create a matrix equation for the mode amplitudes yields,

$$\sum_{\nu}\left[2U_{\nu}\frac{\omega_{\nu} - \omega}{\omega}\delta_{\mu\nu} - \sum_{i}\mathbf{E}_{\nu}(\mathbf{r}_i)\bar{\alpha}_{ei}\mathbf{E}_{\mu}(\mathbf{r}_i) + \sum_{i}\mathbf{H}_{\nu}(\mathbf{r}_i)\bar{\alpha}_{mi}\mathbf{H}_{\mu}(\mathbf{r}_i)\right]a_{\nu} = \left(\mathbf{p}_d\cdot\mathbf{E}_{\mu}(\mathbf{r}_s)\right). \tag{F.33}$$

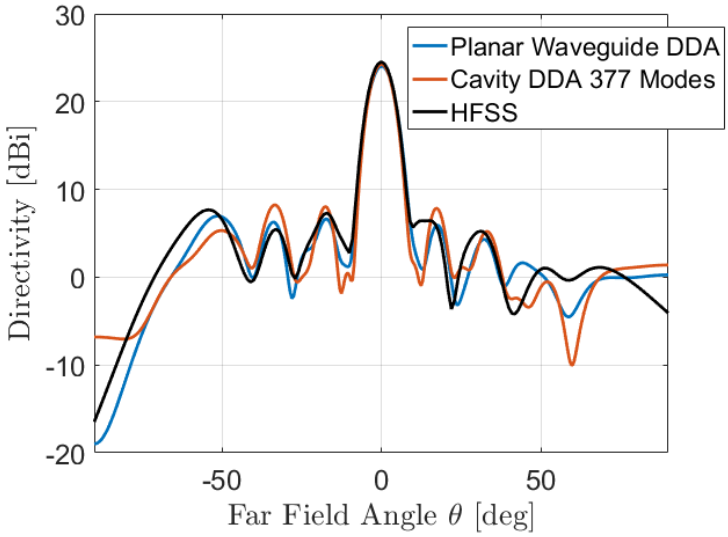

FIGURE F.7: Comparison between the cavity DDA, the planar waveguide DDA, and a full-wave model of the same 70cm aperture antenna at 12.1GHz.

.

Once the amplitude coefficients a_μ are known, the total electric and magnetic fields can be reconstructed using eqs. (F.31) and (F.32). Once the total fields are known, the final dipole moments can be found using the standard polarizability equations $\mathbf{p}_i = \bar{\alpha}_{ei}\mathbf{E}(\mathbf{r}_i)$ and $\mathbf{m}_i = \bar{\alpha}_{mi}\mathbf{H}(\mathbf{r}_i)$. Once the dipole moments are known, the far-fields may be calculated using the standard array factor calculation. The far-fields generated by the cavity DDA from this section, the planar waveguide DDA from appendix F.1, and a full-wave numerical solver are presented in fig. F.7. The cavity DDA model was clearly converged after $M = 377$ modes, even though the antenna involved $N = 1287$ dipoles.

F.4 Cavity Modes in the Edge-fed Antenna Structure

The edge-fed antenna structure naturally forms a cavity as shown in fig. F.9. It is typically fed by a central coaxial cable from the bottom of the cavity, and there is usually also a second port introduced in the bottom of the upper cavity chamber that

absorbs the power that is injected by the feed port. If the system is thought of as a cavity, then the feed port can be thought of as an active electric dipole source, and the absorber port can likewise be thought of as a perfectly absorbing passive dipole with a purely imaginary polarizability. The feed port will drive standing waves in the structure, and the absorbing dipole will reflect standing waves with a $\pi/2$ phase difference relative to the feed dipole. The sum of those two standing waves will in turn create a traveling wave that creates the phenomena of absorption.

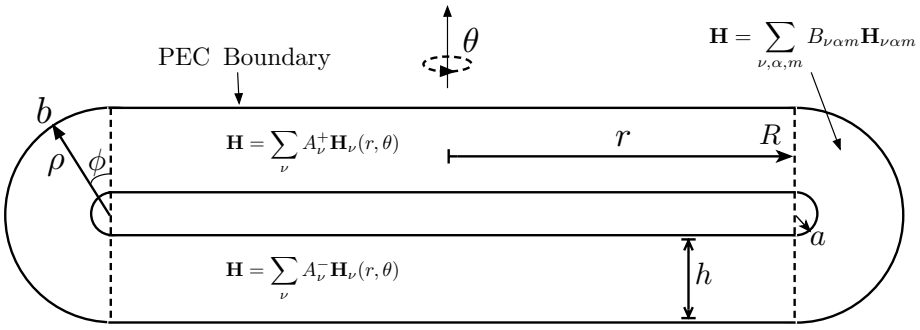

FIGURE F.8: Illustration of edge-fed cavity design. The cavity is split into three virtual cavities. The upper and lower cavities are cylinders which are described by a cylindrical coordinate system $\{r, \theta, z\}$. These two cavities are joined together by a third cavity that is a split, coaxial cavity which is bent into a torus, and is described by coordinate system $\{\rho, \phi, \xi\}$.

.

In order to solve for the resonances of a complex cavity, the various parts need to be split into regions that are more easily solvable, and then rejoined to form a complete cavity. We choose to sever the cavity into three chambers by cutting it by the cylindrical surface illustrated by the dotted line in fig. F.9. Cutting it along that surface will split the cavity into three regions. The upper and lower regions are two cylindrically shaped cavities, and the solutions to Maxwell's equations in these regions are a sum of cylindrical planar waveguide modes, as were used in the planar waveguide DDA.

The region that connects the upper and lower cylindrical cavities is shaped like a torus that is cut in half, but with a coaxial wire. Unfortunately, Maxwell's equations in a toriodal coordinate system are only separable in the quasistatic limit, and the solutions in the quasistatic limit are given by complex hypergeometric functions. Since this would be rather difficult to handle both in code and in theory, a simpler solution might be found by approximating it as a bent coaxial cable. If this region were straightened out into a normal coaxial wire, then the solutions would be given by the modes of a coaxial cable, which are easily separable in the full form of Maxwell's equations and yield simple analytic solutions.

The question is, how good is the approximation when choosing to treat a torus as a bent cylinder? The answer can be given by transformation optics, which would say that the problem of a torus is equivalent to the problem of a straight cylinder with a linear gradient in the the permeability and permittivity across the face of the cylinder. The gradient in the material parameters in the straight cylinder would be smaller if the major radius of curvature of the torus is longer, and vice versa. If the radius of the cylinder (which is equivalent to the minor radius of the torus) is small relative to the major radius in the torus, then the actual variation in the material parameters across the face of the cylinder will be very small, and can either be neglected or treated perturbatively using the a technique like the Rayleigh-Ritz method. Using the dimensions in fig. F.9, the approximation made is that R/b is small. In that limit, the fields in the torus can be expanded using coaxial waveguide modes, which are described by a cylindrical coordinate system $\{\rho, \phi, \xi\}$. We can further identify the propagation axis of the coaxial cable ξ with the polar angle of the cylinders, so that $\xi = R\theta$.

The general strategy used to solve the problem is to expand the solutions in each of the three cavity domains in terms of their fundamental solutions as given by the boundary conditions of their individual domains. These modes, or fundamental so-

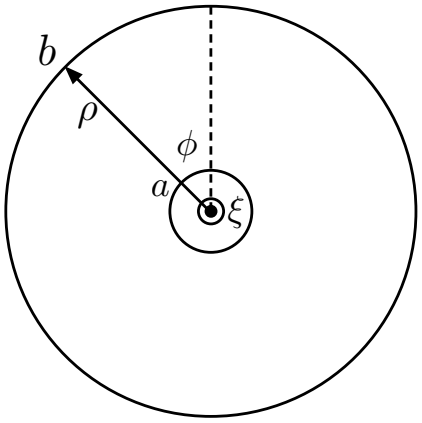

FIGURE F.9: Coaxial cable coordinates, where ρ is the radial vector, ϕ is the polar angle, and ξ is the propagation axis. When this geometry is curved around the two cylindrical cavities with cylindrical coordinates $\{r, \theta, z\}$, we can identify the coordinate systems using $\xi = R\theta$

.

lutions, will be functions of frequency. The coefficients for each fundamental solution can be found by requiring that the electric and magnetic fields be continuous across the boundary. Normally, this would yield

In the upper and lower cylindrical chambers, we expand the fields as a sum of modes

$$\mathbf{H} = \sum_{\mu,\nu} A^{+}_{\mu\nu} \mathbf{H}_{\mu\nu}(\mathbf{r}) \tag{F.34}$$

where the TM cylindrical waveguide modes are given by

$$
\begin{aligned}
E^c_{\mu\nu z} &= \tilde{E} n_\mu J_\nu(\beta_\mu r)\cos(\nu\theta) Z_\mu(z) \\
E^c_{\mu\nu r} &= \frac{\tilde{E}}{k}\frac{\partial}{\partial(\beta_\mu r)} J_\nu(\beta_\mu r)\cos(\nu\theta)\frac{dZ_\mu(z)}{dz} \\
E^c_{\mu\nu\theta} &= \frac{-\nu\tilde{E}}{k}\frac{J_\nu(\beta_\mu r)}{\beta_\mu r}\sin(\nu\theta)\frac{dZ_\mu(z)}{dz} \\
H^c_{\mu\nu z} &= 0 \\
H^c_{\mu\nu r} &= \frac{-i\tilde{E}\nu\epsilon}{Z_0\beta_\mu}\frac{1}{r} J_\nu(\beta_\mu r)\sin(\nu\theta) Z_\mu(z) \\
H^c_{\mu\nu\theta} &= \frac{-i\tilde{E}\epsilon}{Z_0\beta_\mu}\frac{\partial}{\partial r} J_\nu(\beta_\mu r)\cos(\nu\theta) Z_\mu(z).
\end{aligned}
\tag{F.35a}
$$

In the coaxial cable geometry, the modes are also given by eq. (F.35a), but with the substitutions $r \to \rho$, $z \to R\theta$, $\theta \to \psi$. The radial dependence will also need to be altered from the bessel function of the first kind, $J_\nu(\beta_\mu\rho)$, to a more general $R_\nu(\gamma_\mu\rho) = J_\nu(\gamma_\mu\rho) + a_\mu Y_\nu(\gamma_\mu\rho)$, where a_μ is an arbitrary constant which must be fixed by the boundary condition that the $\hat{\phi}$ component of the electric field must go to zero on the inner radius of the coaxial cable. The way in which all of the various propagation constants are fixed must be altered for the modes in the torus, because the periodic boundary condition in the ϕ direction has to be removed, and its propagation constant, which we will call α, needs to be allowed to be the free variable.

The relationships between the propagation constants, which are fixed by separation of variables, need to be set as follows. The first independent mode number is ν, which is the same as the ν used in the cylindrical cavity, which is fixed by the periodic boundary conditions applied to the $\xi = R\theta$ coordinate. The mode number ν then fixes the propagation constant $\gamma_\nu = \sqrt{k^2 - (2\pi\nu/R)^2}$ in the ρ di-

rection. This in turn fixes what α must be, since the derivative of $R_\alpha(\gamma_\nu\rho) = J_\alpha(\gamma_\nu\rho) + a_\nu Y_\alpha(\gamma_\nu\rho)$ must be zero when $\rho = b$. Thus, the function $\alpha_{\mu\nu}(k)$ is defined as $\{\alpha \in \mathbb{C} : (\partial_\rho R_\alpha(\gamma_\nu(k)\rho))|_{\rho=b} = 0\}$, which is a transcendental equation that must be numerically solved. This is a countable, discrete set for any value of k, which is why the second index μ is used. Elements on this set where $\alpha_{\mu\nu}$ is purely imaginary are modes which are in cutoff, and elements where $\alpha_{\mu\nu}$ are purely real are propagating modes that can travel circumferentially around the coaxial cable.

The coefficient a_ν is the only free parameter left, which is used to define $R_\alpha(\gamma_\nu\rho) = J_\alpha(\gamma_\nu\rho) + a_\nu Y_\alpha(\gamma_\nu\rho)$. This parameter is defined such that the electric field on the inner surface must be zero, so $(\partial_\rho R_\alpha(\gamma_\nu(k)\rho))|_{\rho=a} = 0$. This is a second transcendental equation that is coupled to the equation for α, and so those two transcendental equations must be numerically solved as simultaneous coupled transcendental equations.

If the primary mode in the cylindrical cavities is TM, then the mode in the torus with the largest coupling to the TM cylindrical mode will be the TE mode. We denote these mode fields using $\mathscr{E}_\lambda, \mathscr{H}_\lambda$ to distinguish them from the cylindrical

cavity modes, and they are given by

$$\begin{aligned}
\mathscr{E}^{c}_{\mu\nu\xi} &= 0 \\
\mathscr{E}^{c}_{\mu\nu\rho} &= \tilde{E}\alpha \frac{R_\alpha(\gamma_\nu \rho)}{\gamma_\nu \rho} \cos(\nu\theta) e^{i\alpha\phi} \\
\mathscr{E}^{c}_{\mu\nu\phi} &= \frac{i\tilde{E}}{\gamma_\nu} \partial_\rho R_\alpha(\gamma_\nu \rho) \cos(\nu\theta) e^{i\alpha\phi} \\
\mathscr{H}^{c}_{\mu\nu\xi} &= \frac{\tilde{E} n_\nu}{Z_0} R_\alpha(\gamma_\nu \rho) \cos(\nu\theta) e^{i\alpha\phi} \\
\mathscr{H}^{c}_{\mu\nu\rho} &= \frac{-\tilde{E}\nu n_\nu}{Z_0 \gamma_\nu^2 R} \partial_\rho R_\alpha(\gamma_\nu \rho) \sin(\nu\theta) e^{i\alpha\phi} \\
\mathscr{H}^{c}_{\mu\nu\phi} &= \frac{-i\tilde{E} n_\nu \nu\alpha}{Z_0 \gamma_\nu R} \frac{R_\alpha(\gamma_\nu \rho)}{\gamma_\nu \rho} \sin(\nu\theta) e^{i\alpha\phi}.
\end{aligned} \tag{F.36a}$$

where we have suppressed the indices μ, ν on $\alpha_{\mu\nu}$ for the sake of clarity in the notation. Note that these are propagating modes that do not have a node at any point.

F.4.1 Solving the two-compartment cavity eigenvalue problem

The problem at hand has two primary symmetries: the symmetry of rotation about the z-axis and the reflection about the xy plane. The rotational symmetry can be used to simplify the problem by recognizing that the polar mode number, ν, must be the same in both the torus and both the upper and lower cylinders, and so we will neglect that mode number in this section for the sake of clarity in the notation.

The symmetry of reflection defines an imaginary boundary between the upper and lower halves of the system, and the resonances of the cavity must be either symmetric or antisymmetric about the xy plane. This means we can consider only the upper or lower half of the cavity at a time by closing off the other half using either a PEC or PMC boundary inside the torus that lies on the xy plane, where the PEC boundary will yield modes that are asymmetric in the electric field, and the PMC

boundary will yield modes that are symmetric in the electric field. Applying that boundary restricts the basis of TM modes in the torus to those that go as $\sin(\alpha\phi)$, and restricts the basis of TE modes to those that go as $\cos(\alpha\phi)$. The modes with a PEC boundary condition at $z = 0$ are

$$\begin{aligned}
\mathscr{E}^c_{\mu\nu\xi} &= 0 \\
\mathscr{E}^c_{\mu\nu\rho} &= i\tilde{E}\alpha\frac{R_\alpha(\gamma_\nu\rho)}{\gamma_\nu\rho}\cos(\nu\theta)\sin(\alpha\phi) \\
\mathscr{E}^c_{\mu\nu\phi} &= \frac{i\tilde{E}}{\gamma_\nu}\partial_\rho R_\alpha(\gamma_\nu\rho)\cos(\nu\theta)\cos(\alpha\phi) \\
\mathscr{H}^c_{\mu\nu\xi} &= \frac{\tilde{E}n_\nu}{Z_0}R_\alpha(\gamma_\nu\rho)\cos(\nu\theta)\cos(\alpha\phi) \\
\mathscr{H}^c_{\mu\nu\rho} &= \frac{-\tilde{E}\nu n_\nu}{Z_0\gamma_\nu^2 R}\partial_\rho R_\alpha(\gamma_\nu\rho)\sin(\nu\theta)\cos(\alpha\phi) \\
\mathscr{H}^c_{\mu\nu\phi} &= \frac{\tilde{E}n_\nu\nu\alpha}{Z_0\gamma_\nu R}\frac{R_\alpha(\gamma_\nu\rho)}{\gamma_\nu\rho}\sin(\nu\theta)\sin(\alpha\phi).
\end{aligned} \tag{F.37a}$$

while the modes with a PMC boundary at $z = 0$ are

$$\begin{aligned}
\mathscr{E}^s_{\mu\nu\xi} &= 0 \\
\mathscr{E}^s_{\mu\nu\rho} &= -i\tilde{E}\alpha \frac{R_\alpha(\gamma_\nu \rho)}{\gamma_\nu \rho} \cos(\nu\theta)\cos(\alpha\phi) \\
\mathscr{E}^s_{\mu\nu\phi} &= \frac{i\tilde{E}}{\gamma_\nu} \partial_\rho R_\alpha(\gamma_\nu \rho)\cos(\nu\theta)\sin(\alpha\phi) \\
\mathscr{H}^s_{\mu\nu\xi} &= \frac{\tilde{E} n_\nu}{Z_0} R_\alpha(\gamma_\nu \rho)\cos(\nu\theta)\sin(\alpha\phi) \\
\mathscr{H}^s_{\mu\nu\rho} &= \frac{-\tilde{E}\nu n_\nu}{Z_0 \gamma_\nu^2 R} \partial_\rho R_\alpha(\gamma_\nu \rho)\sin(\nu\theta)\sin(\alpha\phi) \\
\mathscr{H}^s_{\mu\nu\phi} &= \frac{-\tilde{E} n_\nu \nu\alpha}{Z_0 \gamma_\nu R} \frac{R_\alpha(\gamma_\nu \rho)}{\gamma_\nu \rho} \sin(\nu\theta)\cos(\alpha\phi).
\end{aligned} \tag{F.38a}$$

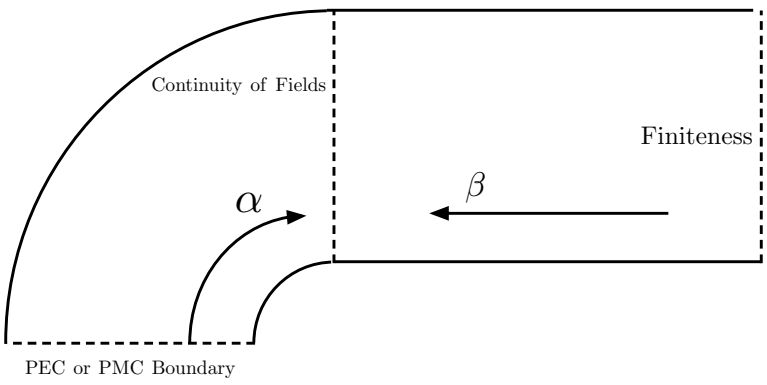

FIGURE F.10: Illustration of simplified eigenvalue problem, with imaginary PEC or PMC boundaries placed at the line $z = 0$.

.

We will use the scripted notation $\mathscr{E}_\lambda, \mathscr{H}_\lambda$ to denote the electric and magnetic fields waveguide modes in the torus, and E_μ, H_μ to denote the fields in the cylinders.

We will also use a superscripted E to denote TE modes, and a superscripted M to denote TM modes. In the upper cylinder, we expand the field into a set of TE and TM cylindrical, planar waveguide modes

$$\mathbf{H} = \sum_{\lambda} a_{\lambda}^{E} H_{\lambda}^{E} + a_{\lambda}^{M} H_{\lambda}^{M}, \tag{F.39}$$

while the torus, we expand the field into a set of TE and TM coaxial cable modes

$$\mathbf{H} = \sum_{\lambda} b_{\lambda}^{E} \mathscr{H}_{\lambda}^{E} + b_{\lambda}^{M} \mathscr{H}_{\lambda}^{M} \tag{F.40}$$

The boundary condition between the cylinder and the torus is that the electric and magnetic fields must be continuous. Taking the cross product with $E_{\mu'}^{M}$, integrating over the boundary between the torus and the cylinder, and applying mode orthogonality yields a matrix equation relating the amplitude coefficients in the cylinder to a linear combination of amplitude coefficients in the torus,

$$a_{\mu'}^{M} = b_{\mu}^{E} X_{\mu'}^{\mu,EM} + b_{\mu}^{M} X_{\mu'}^{\mu,MM} \tag{F.41}$$

where

$$X_{\mu'}^{\mu,EM} = \frac{\int E_{\mu'}^{M} \times \mathscr{H}_{\mu}^{E*} \cdot \mathbf{n} \mathrm{d}S}{\int E_{\mu'}^{M} \times H_{\mu'}^{M*} \cdot \mathbf{n} \mathrm{d}S} \tag{F.42a}$$

$$X_{\mu'}^{\mu,MM} = \frac{\int E_{\mu'}^{M} \times \mathscr{H}_{\mu}^{M*} \cdot \mathbf{n} \mathrm{d}S}{\int E_{\mu'}^{M} \times H_{\mu'}^{M*} \cdot \mathbf{n} \mathrm{d}S} \tag{F.42b}$$

Repeating the same procedure with $E_{\mu'}^{M}, \mathscr{E}_{\mu'}^{E}, \mathscr{E}_{\mu'}^{M}$, will yield three more equations relating the coefficients.

$$a_{\mu'}^{E} = b_{\mu}^{E} X_{\mu'}^{\mu,EE} + b_{\mu}^{M} X_{\mu'}^{\mu,ME} \tag{F.43}$$

$$b_{\mu'}^{M} = a_{\mu}^{E} \chi_{\mu'}^{\mu,EM} + a_{\mu}^{M} \chi_{\mu'}^{\mu,MM} \tag{F.44}$$

$$b_{\mu'}^{E} = a_{\mu}^{E} \chi_{\mu'}^{\mu,EE} + a_{\mu}^{M} \chi_{\mu'}^{\mu,ME}. \tag{F.45}$$

where

$$\chi_{\mu'}^{\mu,EM} = \frac{\int \mathscr{E}_{\mu'}^{oM} \times H_{\mu}^{E*} \cdot \mathbf{n} \mathrm{d}S}{\int \mathscr{E}_{\mu'}^{oM} \times \mathscr{H}_{\mu'}^{M*} \cdot \mathbf{n} \mathrm{d}S} \tag{F.46a}$$

$$\chi_{\mu'}^{\mu,MM} = \frac{\int \mathscr{E}_{\mu'}^{oM} \times H_{\mu}^{M*} \cdot \mathbf{n} \mathrm{d}S}{\int \mathscr{E}_{\mu'}^{oM} \times \mathscr{H}_{\mu'}^{M*} \cdot \mathbf{n} \mathrm{d}S} \tag{F.46b}$$

These equations can be assembled into a block-matrix eigenvalue equation for the coefficients in the cylinder.

$$\begin{bmatrix} \chi_{\mu}^{\lambda,EE} X_{\mu'}^{\mu,EE} + \chi_{\mu}^{\lambda,EM} X_{\mu'}^{\mu,ME} & \chi_{\mu}^{\lambda,ME} X_{\mu'}^{\mu,EE} + \chi_{\mu}^{\lambda,MM} X_{\mu'}^{\mu,ME} \\ \chi_{\mu}^{\lambda,EE} X_{\mu'}^{\mu,EM} + \chi_{\mu}^{\lambda,EM} X_{\mu'}^{\mu,MM} & \chi_{\mu}^{\lambda,ME} X_{\mu'}^{\mu,EM} + \chi_{\mu}^{\lambda,MM} X_{\mu'}^{\mu,MM} \end{bmatrix} \begin{bmatrix} a_{\lambda}^{E} \\ a_{\lambda}^{M} \end{bmatrix} = \begin{bmatrix} a_{\mu'}^{E} \\ a_{\mu'}^{M} \end{bmatrix} \tag{F.47}$$

This method would involve analytically computing many matrix elements and computationally solving for the eigenvalues, which would be long and involved. However, if the transition between the cylinder and the torus is approximately reflectionless, a simpler method can be used. Instead of requiring that all of the components of the field be continuous, we can focus on the two main components of the field for TM waves in the cylindrical guide:

$$b_{\mu\nu} \mathscr{H}_{\xi}^{\mu\nu} = -a_{\mu\nu} H_{\theta}^{\mu\nu} \tag{F.48}$$

$$b_{\mu\nu} \mathscr{E}_{\rho}^{\mu\nu} = a_{\mu\nu} E_{z}^{\mu\nu} \tag{F.49}$$

. Taking overlap integrals can reduce the equations to a two-by-two matrix equation, which only has a solution if the determinant is zero. This results in the condition

$$\left(\frac{\int \mathscr{H}_{\xi}^{\mu\nu} H_{\theta}^{\mu\nu *} \mathrm{d}S}{\int \mathscr{E}_{\rho}^{\mu\nu} E_{z}^{\mu\nu *} \mathrm{d}S} \right) \left(\frac{\int |E_{z}^{\mu\nu}|^2 \mathrm{d}S}{\int |H_{\theta}^{\mu\nu}|^2 \mathrm{d}S} \right) = -1 \tag{F.50}$$

Plugging in eqs. (F.35a) and (F.37a), this reduces to the condition that

$$\Gamma n_{\nu} n_{\mu} \cos(\alpha\pi/2) J_{\nu}(\beta_{\mu} R) + \alpha \sin(\alpha\pi/2) J_{\nu}'(\beta_{\mu} R) = 0 \tag{F.51}$$

must be satisfied for resonances of asymmetric modes, where

$$\Gamma = \left(\frac{\int \epsilon(z) R_\alpha(\gamma_\nu z) Z_\mu^*(z) \mathrm{d}z}{\int (R_\alpha(\gamma_\nu z)/\gamma_\nu z) Z_\mu^*(z) \mathrm{d}z} \right) \left(\frac{\int |Z_\mu(z)|^2 \mathrm{d}z}{\int |\epsilon(z) Z_\mu(z)|^2 \mathrm{d}z} \right). \tag{F.52}$$

These asymmetric modes satisfy the PEC boundary condition at $z = 0$. Using eqs. (F.35a) and (F.37a), the resonance condition for the symmetric modes can also be derived

$$\Gamma n_\nu n_\mu \sin(\alpha\pi/2) J_\nu(\beta_\mu R) - \alpha \cos(\alpha\pi/2) J'_\nu(\beta_\mu R) = 0 \tag{F.53}$$

which satisfy a PMC boundary condition at $z = 0$. These are again transcendental equations that must be solved numerically, as shown in fig. F.11, where the magnitude of the left-hand sides of eq. (F.52) and eq. (F.53) are plotted. The resonance frequencies of the entire cavity structure can then be identified as the frequencies where these functions are zero.

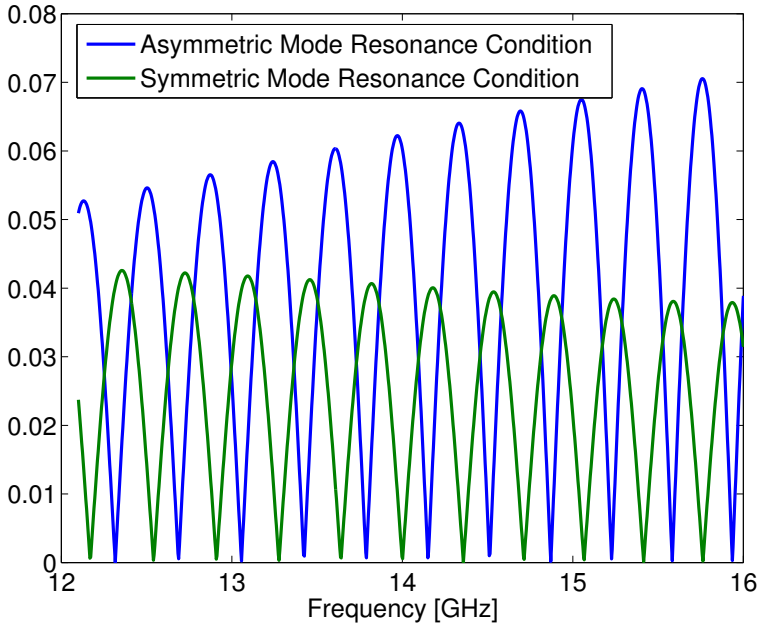

FIGURE F.11: Illustration of method to finding the resonance frequencies of the cavity. The resonance frequencies for the symmetric and asymmetric modes are the points where these functions are zero.

.

F.4.2 Mode Volume Calculation

The mode volume is defined as

$$U_{\mu\nu} = \int \epsilon(\mathbf{r}) E_{\mu\nu}^2(\mathbf{r}) \mathrm{d}^3\mathbf{r} = -\int \mu(\mathbf{r}) H_{\mu\nu}^2(\mathbf{r}) \mathrm{d}^3\mathbf{r} = (1/2) \int \epsilon(\mathbf{r}) E_{\mu\nu}^2(\mathbf{r}) - \mu(\mathbf{r}) H_{\mu\nu}^2(\mathbf{r}) \mathrm{d}^3\mathbf{r} \tag{F.54}$$

We will perform the calculation first with the assumption that $\frac{d}{dz} Z_\mu(z) = 0$, which is a good assumption if the waveguide only supports one propagating mode, and is only filled with a single dielectric slab. This implies that the electric field is given by

$$\begin{aligned} E_{\mu\nu z}^c &= \tilde{E} n_\mu J_\nu(\beta_\mu r) \cos(\nu\theta) Z_\mu(z) \\ E_{\mu\nu r}^c &= 0 \\ E_{\mu\nu\theta}^c &= 0 \end{aligned} \tag{F.55}$$

and so the integral can be computing using only the z-component of the electric field. The next simplification that may be made is to split the cavity into upper and lower chambers, with the claim that the mode volume in the upper chamber is equal to the mode volume in the lower chamber. Then,

$$U_{\mu\nu} = 2 \int_{V^+} \epsilon(\mathbf{r}) E_{\mu\nu}^2(\mathbf{r}) \mathrm{d}^3\mathbf{r} \tag{F.56}$$

where V^+ is the volume of the upper chamber. Then the volume of the toroidal portion of the upper chamber can be approximately taken into account by extending the radius of the upper chamber to some artificial radius R', where $R' = R + (\alpha_{\mu\nu}/\beta_\mu)\pi/2$. This phase assumes that the phase of the reflection coefficient between the cylindrical portion of the upper chamber and the toroidal portion of the upper chamber is zero. If that phase is zero, then this extension just extends the upper cylindrical portion of the chamber by the same amount of phase that would have propagated in the toroidal portion. Using this extension of the upper chamber, the mode volume can

be written

$$U_{\mu\nu} = 2n_\mu^2 \int_0^h \epsilon(z)|Z_\mu(z)|^2 \mathrm{d}z \int_0^{2\pi} \cos^2(\nu\theta)\mathrm{d}\theta \int_0^{R'} r J_\nu^2(\beta r)\mathrm{d}r. \tag{F.57}$$

Using the identity

$$\int_0^d x J_\nu(x)\mathrm{d}x = \frac{d^2}{4}\left(J_\nu^2(d) + J_{\nu-1}^2(d) - J_{\nu-1}(d)J_{\nu+1}^2(d) - J_{\nu-2}^2(d)J_\nu^2(d) - (2/d)J_{\nu-1}(d)J_\nu(d)\right) \tag{F.58}$$

and assuming the normalization $\int_0^h \epsilon(z)|Z_\mu(z)|^2\mathrm{d}z = h$, the mode volume is given by

$$U_{\mu\nu} = \frac{2h\pi}{k^2}(1+\delta_{0\nu})\left(\frac{d^2}{4}\right)\left(J_\nu^2(d) + J_{\nu-1}^2(d) - J_{\nu-1}(d)J_{\nu+1}^2(d) - J_{\nu-2}^2(d)J_\nu^2(d) - (2/d)J_{\nu-1}(d)J_\nu(d)\right) \tag{F.59}$$

where $d = \beta_\mu R + \alpha_{\mu\nu}\pi/2$.

Bibliography

[1] D. Schurig, J. Mock, B. Justice, S. A. Cummer, J. B. Pendry, A. Starr, and D. Smith, "Metamaterial electromagnetic cloak at microwave frequencies," *Science*, vol. 314, no. 5801, pp. 977–980, 2006.

[2] H. Lorentz, "Ueber die beziehung zwischen der fortpflanzungsgeschwindigkeit des lichtes und der körperdichte," *Annalen der Physik*, vol. 245, no. 4, pp. 641–665, 1880.

[3] P. T. Bowen, A. Baron, and D. R. Smith, "Theory of patch-antenna metamaterial perfect absorbers," *Physical Review A*, vol. 93, no. 6, p. 063849, 2016.

[4] R. W. Wood, "On a remarkable case of uneven distribution of light in a diffraction grating spectrum," *Proceedings of the Physical Society of London*, vol. 18, p. 269, 1902.

[5] L. Rayleigh, "On the dynamical theory of gratings," *Proceedings of the Royal Society of London*, vol. 79, pp. 399–416, 1907.

[6] L. Rayleigh, "Iii. note on the remarkable case of diffraction spectra described by prof. wood," *The London, Edinburgh, and Dublin Philosophical Magazine and Journal of Science*, vol. 14, no. 79, pp. 60–65, 1907.

[7] H. Lorentz, "Collected papers, vol. 1," *Martinus Nijhoff, The Hague*, p. 1, 1936.

[8] G. de Haas-Lorentz, H. Lorentz, and J. Auer, *H.A. LORENTZ: Impressions of His Life and Work*. NHPC, 1957.

[9] J. V. Kranendonk and J. Sipe, "V foundations of the macroscopic electromagnetic theory of dielectric media," in *Progress in Optics, Vol. 15* (E. Wolf, ed.), vol. 15 of *Progress in Optics*, pp. 245 – 350, Elsevier, 1977.

[10] P. P. Ewald, "Zur begründung der kristalloptik," *Annalen der Physik*, vol. 354, no. 1, pp. 1–38, 1916.

[11] v. E. Madelung, "Das elektrische feld in systemen von regelmäßig angeordneten punktladungen," *Phys. Z*, vol. 19, pp. 524–532, 1918.

[12] H. Hoek, *Algemeene theorie der optische activiteit van isotrope media*. Dissertation, Rijksuniversiteit te Leiden., 1939.

[13] S. R. De Groot, "The maxwell equations," *Studies in statistical mechanics*, vol. 4, 1969.

[14] R. E. Collin, Antennas, and P. Society, *Field theory of guided waves*. IEEE/OUP series on electromagnetic wave theory, New York: IEEE Press, 1991. Published under the sponsorship of the IEEE Antennas and Propagation Society.

[15] R. Clausius, *Abhandlungen über die mechanische Wärmetheorie*. Friedrich Vieweg und Sohn, Braunschweig, 1867.

[16] O. F. Mossotti, "Discussione analitica sullinfluenza che lazione di un mezzo dielettrico ha sulla distribuzione dellelettricit alla superficie di pi corpi elettrici disseminati in esso," *Memorie di Mathematica e di Fisica della Societ Italiana della Scienza Residente in Modena*, vol. 24, pp. 49–74, 1850.

[17] L. Lorenz, "Ueber die refractionsconstante," *Annalen der Physik*, vol. 247, no. 9, pp. 70–103, 1880.

[18] J. Sipe and J. Van Kranendonk, "Macroscopic electromagnetic theory of resonant dielectrics," *Physical Review A*, vol. 9, no. 5, p. 1806, 1974.

[19] B. T. Draine, "The discrete-dipole approximation and its application to interstellar graphite grains," *The Astrophysical Journal*, vol. 333, pp. 848–872, 1988.

[20] S. A. Tretyakov, A. J. Viitanen, S. I. Maslovski, and I. E. Saarela, "Impedance boundary conditions for regular dense arrays of dipole scatterers," *Antennas and Propagation, IEEE Transactions on*, vol. 51, no. 8, pp. 2073–2078, 2003.

[21] S. Tretyakov, *Analytical Modeling in Applied Electromagnetics*. Artech House, 2003.

[22] H. A. Lorentz, *The theory of electrons and its applications to the phenomena of light and radiant heat*, vol. 29. BG Teubner, 1916.

[23] J. D. Jackson, *Classical Electrodynamics*. Wiley, 3 ed., 1999.

[24] L. Rosenfeld, *Theory of electrons*, vol. 1. North-Holland, 1951.

[25] P. A. Belov and C. R. Simovski, "Homogenization of electromagnetic crystals formed by uniaxial resonant scatterers," *Physical Review E*, vol. 72, no. 2, p. 026615, 2005.

[26] M. Marino, A. Carati, and L. Galgani, "Classical light dispersion theory in a regular lattice," *Annals of Physics*, vol. 322, no. 4, pp. 799–823, 2007.

[27] N. Landy and D. R. Smith, "Two-dimensional metamaterial device design in the discrete dipole approximation," *Journal of Applied Physics*, vol. 116, no. 4, p. 044906, 2014.

[28] P. T. Bowen and D. R. Smith, "Coupled-mode theory for film-coupled plasmonic nanocubes," *Physical Review B*, vol. 90, no. 19, p. 195402, 2014.

[29] G. M. Akselrod, J. Huang, T. B. Hoang, P. T. Bowen, L. Su, D. R. Smith, and M. H. Mikkelsen, "Large-area metasurface perfect absorbers from visible to near-infrared," *Advanced Materials*, vol. 27, no. 48, pp. 8028–8034, 2015.

[30] P. T. Bowen, T. Driscoll, N. B. Kundtz, and D. R. Smith, "Using a discrete dipole approximation to predict complete scattering of complicated metamaterials," *New Journal of Physics*, vol. 14, no. 3, p. 033038, 2012.

[31] A. I. Dimitriadis, D. L. Sounas, N. V. Kantartzis, C. Caloz, and T. D. Tsiboukis, "Surface susceptibility bianisotropic matrix model for periodic metasurfaces of uniaxially mono-anisotropic scatterers under oblique te-wave incidence," *Antennas and Propagation, IEEE Transactions on*, vol. 60, no. 12, pp. 5753–5767, 2012.

[32] T. D. Karamanos, A. I. Dimitriadis, *et al.*, "Polarizability matrix extraction of a bianisotropic metamaterial from the scattering parameters of normally incident plane waves," *Advanced Electromagnetics*, vol. 1, no. 3, pp. 64–70, 2012.

[33] D. J. Griffiths, "Hyperfine splitting in the ground state of hydrogen," *Am. J. Phys*, vol. 50, no. 8, p. 8, 1982.

[34] L. Novotny and B. Hecht, *Principles of nano-optics*. Cambridge university press, 2012.

[35] H. Freedhoff and J. V. Kranendonk, "Theory of coherent resonant absorption and emission at infrared and optical frequencies," *Canadian Journal of Physics*, vol. 45, no. 5, pp. 1833–1859, 1967.

[36] A. D. Scher and E. F. Kuester, "Extracting the bulk effective parameters of a metamaterial via the scattering from a single planar array of particles," *Metamaterials*, vol. 3, no. 1, pp. 44–55, 2009.

[37] E. F. Kuester, M. A. Mohamed, M. Piket-May, and C. L. Holloway, "Averaged transition conditions for electromagnetic fields at a metafilm," *Antennas and Propagation, IEEE Transactions on*, vol. 51, no. 10, pp. 2641–2651, 2003.

[38] M. A. Yurkin and A. G. Hoekstra, "The discrete dipole approximation: an overview and recent developments," *Journal of Quantitative Spectroscopy and Radiative Transfer*, vol. 106, no. 1, pp. 558–589, 2007.

[39] G. M. Akselrod, C. Argyropoulos, T. B. Hoang, C. Ciracì, C. Fang, J. Huang, D. R. Smith, and M. H. Mikkelsen, "Probing the mechanisms of large purcell enhancement in plasmonic nanoantennas," *Nature Photonics*, vol. 8, no. 11, pp. 835–840, 2014.

[40] T. B. Hoang, G. M. Akselrod, and M. H. Mikkelsen, "Ultrafast room-temperature single photon emission from quantum dots coupled to plasmonic nanocavities," *Nano letters*, 2016.

[41] W. R. Holland and D. G. Hall, "Frequency shifts of an electric-dipole resonance near a conducting surface," *Phys. Rev. Lett.*, vol. 52, pp. 1041–1044, Mar 1984.

[42] A. Aubry, D. Y. Lei, S. A. Maier, and J. B. Pendry, "Plasmonic hybridization between nanowires and a metallic surface: A transformation optics approach," *ACS Nano*, vol. 5, no. 4, pp. 3293–3308, 2011.

[43] M. H. Mikkelsen, A. Rose, T. B. Hoang, F. McGuire, J. J. Mock, C. Ciraci, and D. R. Smith, "Tunable plasmonic platform for giant fluorescence enhancement," in *CLEO: 2014*, p. FW1C.3, Optical Society of America, 2014.

[44] S. Mukherjee, F. Libisch, N. Large, O. Neumann, L. V. Brown, J. Cheng, J. B. Lassiter, E. A. Carter, P. Nordlander, and N. J. Halas, "Hot electrons do the impossible: Plasmon-induced dissociation of h2 on au," *Nano Letters*, vol. 13, no. 1, pp. 240–247, 2013.

[45] C. Argyropoulos, C. Ciraci, and D. R. Smith, "Enhanced optical bistability with film-coupled plasmonic nanocubes," *Applied Physics Letters*, vol. 104, no. 6, pp. –, 2014.

[46] D. J. Bergman and M. I. Stockman, "Surface plasmon amplification by stimulated emission of radiation: Quantum generation of coherent surface plasmons in nanosystems," *Phys. Rev. Lett.*, vol. 90, p. 027402, Jan 2003.

[47] W. Wenseleers, F. Stellacci, T. Meyer-Friedrichsen, T. Mangel, C. A. Bauer, S. J. K. Pond, S. R. Marder, and J. W. Perry, "Five orders-of-magnitude enhancement of two-photon absorption for dyes on silver nanoparticle fractal clusters," *The Journal of Physical Chemistry B*, vol. 106, no. 27, pp. 6853–6863, 2002.

[48] E. Poutrina, C. Ciracì, D. J. Gauthier, and D. R. Smith, "Enhancing four-wave-mixing processes by nanowire arrays coupled to a gold film," *Opt. Express*, vol. 20, pp. 11005–11013, May 2012.

[49] J. J. Mock, R. T. Hill, A. Degiron, S. Zauscher, A. Chilkoti, and D. R. Smith, "Distance-dependent plasmon resonant coupling between a gold nanoparticle and gold film," *Nano Letters*, vol. 8, no. 8, pp. 2245–2252, 2008.

[50] A. Moreau, C. Cirac, J. J. Mock, R. T. Hill, Q. Wang, B. J. Wiley, A. Chilkoti, and D. R. Smith, "Controlled-reflectance surfaces with film-coupled colloidal nanoantennas," *Nature*, vol. 492, p. 8689, 2012.

[51] C. A. Balanis, *Antenna Theory: Analysis and Design*. Wiley-Interscience, New York, 2005.

[52] C. Ciraci, J. Britt Lassiter, A. Moreau, and D. R. Smith, "Quasi-analytic study of scattering from optical plasmonic patch antennas," *Journal of Applied Physics*, vol. 114, no. 16, pp. –, 2013.

[53] J. B. Lassiter, F. McGuire, J. J. Mock, C. Cirac, R. T. Hill, B. J. Wiley, A. Chilkoti, and D. R. Smith, "Plasmonic waveguide modes of film-coupled metallic nanocubes," *Nano Letters*, vol. 13, no. 12, pp. 5866–5872, 2013. PMID: 24199752.

[54] S. Fan, W. Suh, and J. D. Joannopoulos, "Temporal coupled-mode theory for the fano resonance in optical resonators," *J. Opt. Soc. Am. A*, vol. 20, pp. 569–572, Mar 2003.

[55] L. Verslegers, Z. Yu, P. B. Catrysse, and S. Fan, "Temporal coupled-mode theory for resonant apertures," *J. Opt. Soc. Am. B*, vol. 27, pp. 1947–1956, Oct 2010.

[56] H. Haus, *Waves and fields in optoelectronics*. Prentice-Hall Series in Solid State Physical Electronics, Prentice Hall, Incorporated, 1984.

[57] Q. Bai, M. Perrin, C. Sauvan, J.-P. Hugonin, and P. Lalanne, "Efficient and intuitive method for the analysis of light scattering by a resonant nanostructure," *Opt. Express*, vol. 21, pp. 27371–27382, Nov 2013.

[58] Y. Zeng, D. A. R. Dalvit, J. O'Hara, and S. A. Trugman, "Modal analysis method to describe weak nonlinear effects in metamaterials," *Phys. Rev. B*, vol. 85, p. 125107, Mar 2012.

[59] A. Raman and S. Fan, "Photonic band structure of dispersive metamaterials formulated as a hermitian eigenvalue problem," *Phys. Rev. Lett.*, vol. 104, p. 087401, Feb 2010.

[60] J. Yang, C. Sauvan, A. Jouanin, S. Collin, J.-L. Pelouard, and P. Lalanne, "Ultrasmall metal-insulator-metal nanoresonators: impact of slow-wave effects on the quality factor," *Opt. Express*, vol. 20, pp. 16880–16891, Jul 2012.

[61] F. Wang and Y. R. Shen, "General properties of local plasmons in metal nanostructures," *Phys. Rev. Lett.*, vol. 97, p. 206806, Nov 2006.

[62] S. Schelkunoff, "Some equivalence theorems of electromagnetics and their application to radiation problems," *Bell System Technical Journal, The*, vol. 15, pp. 92–112, Jan 1936.

[63] P. B. Johnson and R. W. Christy, "Optical constants of the noble metals," *Phys. Rev. B*, vol. 6, pp. 4370–4379, Dec 1972.

[64] L. Novotny, "Effective wavelength scaling for optical antennas," *Phys. Rev. Lett.*, vol. 98, p. 266802, Jun 2007.

[65] H. A. Atwater and A. Polman, "Plasmonics for improved photovoltaic devices," *Nat Mater*, vol. 9, pp. 205–213, Mar. 2010.

[66] J.-J. Greffet, R. Carminati, K. Joulain, J.-P. Mulet, S. Mainguy, and Y. Chen, "Coherent emission of light by thermal sources," *Nature*, vol. 416, pp. 61–64, 2002.

[67] P. L. Richards, "Bolometers for infrared and millimeter waves," *Journal of Applied Physics*, vol. 76, no. 1, pp. 1–24, 1994.

[68] K. Aydin, V. E. Ferry, R. M. Briggs, and H. A. Atwater, "Broadband polarization-independent resonant light absorption using ultrathin plasmonic super absorbers," *Nature communications*, vol. 2, p. 517, 2011.

[69] J. Hao, J. Wang, X. Liu, W. J. Padilla, L. Zhou, and M. Qiu, "High performance optical absorber based on a plasmonic metamaterial," *Applied Physics Letters*, vol. 96, no. 25, pp. –, 2010.

[70] J. Hao, L. Zhou, and M. Qiu, "Nearly total absorption of light and heat generation by plasmonic metamaterials," *Phys. Rev. B*, vol. 83, p. 165107, Apr 2011.

[71] N. Liu, M. Mesch, T. Weiss, M. Hentschel, and H. Giessen, "Infrared perfect absorber and its application as plasmonic sensor," *Nano Letters*, vol. 10, no. 7, pp. 2342–2348, 2010. PMID: 20560590.

[72] B. Zhang, Y. Zhao, Q. Hao, B. Kiraly, I.-C. Khoo, S. Chen, and T. J. Huang, "Polarization-independent dual-band infrared perfect absorber based on a metal-dielectric-metal elliptical nanodisk array," *Opt. Express*, vol. 19, pp. 15221–15228, Aug 2011.

[73] P. Bouchon, C. Koechlin, F. Pardo, R. Haïdar, and J.-L. Pelouard, "Wideband omnidirectional infrared absorber with a patchwork of plasmonic nanoantennas," *Opt. Lett.*, vol. 37, pp. 1038–1040, Mar 2012.

[74] C. Wu and G. Shvets, "Design of metamaterial surfaces with broadband absorbance," *Opt. Lett.*, vol. 37, pp. 308–310, Feb 2012.

[75] J. Hendrickson, J. Guo, B. Zhang, W. Buchwald, and R. Soref, "Wideband perfect light absorber at midwave infrared using multiplexed metal structures," *Opt. Lett.*, vol. 37, pp. 371–373, Feb 2012.

[76] M. Diem, T. Koschny, and C. M. Soukoulis, "Wide-angle perfect absorber/thermal emitter in the terahertz regime," *Phys. Rev. B*, vol. 79, p. 033101, Jan 2009.

[77] C. Wu, B. Neuner, G. Shvets, J. John, A. Milder, B. Zollars, and S. Savoy, "Large-area wide-angle spectrally selective plasmonic absorber," *Phys. Rev. B*, vol. 84, p. 075102, Aug 2011.

[78] N. I. Landy, S. Sajuyigbe, J. J. Mock, D. R. Smith, and W. J. Padilla, "Perfect metamaterial absorber," *Phys. Rev. Lett.*, vol. 100, p. 207402, May 2008.

[79] Y. Avitzour, Y. A. Urzhumov, and G. Shvets, "Wide-angle infrared absorber based on a negative-index plasmonic metamaterial," *Phys. Rev. B*, vol. 79, p. 045131, Jan 2009.

[80] C. M. Watts, X. Liu, and W. J. Padilla, "Metamaterial electromagnetic wave absorbers," *Advanced Materials*, vol. 24, no. 23, pp. OP98–OP120, 2012.

[81] N. I. Landy, C. M. Bingham, T. Tyler, N. Jokerst, D. R. Smith, and W. J. Padilla, "Design, theory, and measurement of a polarization-insensitive absorber for terahertz imaging," *Phys. Rev. B*, vol. 79, p. 125104, Mar 2009.

[82] H. Tao, N. I. Landy, C. M. Bingham, X. Zhang, R. D. Averitt, and W. J. Padilla, "A metamaterial absorber for the terahertz regime: design, fabrication and characterization," *Opt. Express*, vol. 16, pp. 7181–7188, May 2008.

[83] H. Tao, C. M. Bingham, A. C. Strikwerda, D. Pilon, D. Shrekenhamer, N. I. Landy, K. Fan, X. Zhang, W. J. Padilla, and R. D. Averitt, "Highly flexible wide angle of incidence terahertz metamaterial absorber: Design, fabrication, and characterization," *Phys. Rev. B*, vol. 78, p. 241103, Dec 2008.

[84] X. Liu, T. Tyler, T. Starr, A. F. Starr, N. M. Jokerst, and W. J. Padilla, "Taming the blackbody with infrared metamaterials as selective thermal emitters," *Phys. Rev. Lett.*, vol. 107, p. 045901, Jul 2011.

[85] H.-T. Chen, "Interference theory of metamaterial perfect absorbers," *Opt. Express*, vol. 20, pp. 7165–7172, Mar 2012.

[86] Y. Ra'di, C. R. Simovski, and S. A. Tretyakov, "Thin perfect absorbers for electromagnetic waves: Theory, design, and realizations," *Phys. Rev. Applied*, vol. 3, p. 037001, Mar 2015.

[87] S. Collin, F. Pardo, R. Teissier, and J.-L. Pelouard, "Efficient light absorption in metalsemiconductormetal nanostructures," *Applied Physics Letters*, vol. 85, no. 2, pp. 194–196, 2004.

[88] A. W. Snyder and J. Love, *Optical waveguide theory*. Springer Science & Business Media, 2012.

[89] C. Wu, T. Makino, J. Glinski, R. Maciejko, and S. I. Najafi, "Self-consistent coupled-wave theory for circular gratings on planar dielectric waveguides," *Lightwave Technology, Journal of*, vol. 9, no. 10, pp. 1264–1277, 1991.

[90] J. Yang, J.-P. Hugonin, and P. Lalanne, "Near-to-far field transformations for radiative and guided waves," *arXiv preprint arXiv:1510.06344*, 2015.

[91] F. Oberhettinger, *Fourier transforms of distributions and their inverses: a collection of tables*, vol. 16. Academic press, 2014.

[92] P. Bowen, A. Baron, and D. Smith, "Effective-medium description of a metasurface composed of a periodic array of nanoantennas coupled to a metallic film," *Physical Review A*, vol. 95, no. 3, p. 033822, 2017.

[93] U. Fano, "The theory of anomalous diffraction gratings and of quasi-stationary waves on metallic surfaces (sommerfelds waves)," *JOSA*, vol. 31, no. 3, pp. 213–222, 1941.

[94] A. Hessel and A. Oliner, "A new theory of woods anomalies on optical gratings," *Applied Optics*, vol. 4, no. 10, pp. 1275–1297, 1965.

[95] D. Maystre, "Sur la diffraction d'une onde plane par un reseau metallique de conductivite finie," *Optics Communications*, vol. 6, no. 1, pp. 50–54, 1972.

[96] D. Maystre, "A new general integral theory for dielectric coated gratings," *JOSA*, vol. 68, no. 4, pp. 490–495, 1978.

[97] D. Maystre, "Theory of woods anomalies," in *Plasmonics*, pp. 39–83, Springer, 2012.

[98] R. McPhedran and D. Maystre, "A detailed theoretical study of the anomalies of a sinusoidal diffraction grating," *Journal of Modern Optics*, vol. 21, no. 5, pp. 413–421, 1974.

[99] A. Maradudin, I. Simonsen, J. Polanco, and R. Fitzgerald, "Rayleigh and wood anomalies in the diffraction of light from a perfectly conducting reflection grating," *Journal of Optics*, vol. 18, no. 2, p. 024004, 2016.

[100] H. Gibbs, *Optical bistability: controlling light with light*. Elsevier, 1985.

[101] N. Doran and D. Wood, "Nonlinear-optical loop mirror," *Optics letters*, vol. 13, no. 1, pp. 56–58, 1988.

[102] V. R. Almeida, C. A. Barrios, R. R. Panepucci, and M. Lipson, "All-optical control of light on a silicon chip," *Nature*, vol. 431, no. 7012, pp. 1081–1084, 2004.

[103] M. Liu, X. Yin, E. Ulin-Avila, B. Geng, T. Zentgraf, L. Ju, F. Wang, and X. Zhang, "A graphene-based broadband optical modulator," *Nature*, vol. 474, no. 7349, pp. 64–67, 2011.

[104] K. Nozaki, T. Tanabe, A. Shinya, S. Matsuo, T. Sato, H. Taniyama, and M. Notomi, "Sub-femtojoule all-optical switching using a photonic-crystal nanocavity," *Nature Photonics*, vol. 4, no. 7, pp. 477–483, 2010.

[105] M. Notomi, A. Shinya, K. Nozaki, T. Tanabe, S. Matsuo, E. Kuramochi, T. Sato, H. Taniyama, and H. Sumikura, "Low-power nanophotonic devices based on photonic crystals towards dense photonic network on chip," *IET circuits, devices & systems*, vol. 5, no. 2, pp. 84–93, 2011.

[106] T. Volz, A. Reinhard, M. Winger, A. Badolato, K. J. Hennessy, E. L. Hu, and A. Imamoğlu, "Ultrafast all-optical switching by single photons," *Nature Photonics*, vol. 6, no. 9, pp. 605–609, 2012.

[107] M. Notomi, K. Nozaki, A. Shinya, S. Matsuo, and E. Kuramochi, "Toward fj/bit optical communication in a chip," *Optics Communications*, vol. 314, pp. 3–17, 2014.

[108] G. Moille, S. Combrié, L. Morgenroth, G. Lehoucq, F. Neuilly, B. Hu, D. Decoster, and A. de Rossi, "Integrated all-optical switch with 10 ps time resolution enabled by ald," *Laser & Photonics Reviews*, vol. 10, no. 3, pp. 409–419, 2016.

[109] Z. Chai, Y. Zhu, X. Hu, X. Yang, Z. Gong, F. Wang, H. Yang, and Q. Gong, "On-chip optical switch based on plasmon–photon hybrid nanostructure-coated multicomponent nanocomposite," *Advanced Optical Materials*, 2016.

[110] G. M. Akselrod, T. Ming, C. Argyropoulos, T. B. Hoang, Y. Lin, X. Ling, D. R. Smith, J. Kong, and M. H. Mikkelsen, "Leveraging nanocavity harmonics for control of optical processes in 2d semiconductors," *Nano letters*, vol. 15, no. 5, pp. 3578–3584, 2015.

[111] Z. Huang, A. Baron, S. Larouche, C. Argyropoulos, and D. R. Smith, "Optical bistability with film-coupled metasurfaces," *Optics letters*, vol. 40, no. 23, pp. 5638–5641, 2015.

[112] M. Soljačić, M. Ibanescu, S. G. Johnson, Y. Fink, and J. Joannopoulos, "Optimal bistable switching in nonlinear photonic crystals," *Physical Review E*, vol. 66, no. 5, p. 055601, 2002.

[113] F. Zhou, Y. Liu, Z.-Y. Li, and Y. Xia, "Analytical model for optical bistability in nonlinear metal nano-antennae involving kerr materials," *Optics express*, vol. 18, no. 13, pp. 13337–13344, 2010.

[114] C. Argyropoulos, C. Ciracì, and D. R. Smith, "Enhanced optical bistability with film-coupled plasmonic nanocubes," *Applied Physics Letters*, vol. 104, no. 6, p. 063108, 2014.

[115] R. F. Oulton, V. J. Sorger, T. Zentgraf, R.-M. Ma, C. Gladden, L. Dai, G. Bartal, and X. Zhang, "Plasmon lasers at deep subwavelength scale," *Nature*, vol. 461, no. 7264, pp. 629–632, 2009.

[116] M. Khajavikhan, A. Simic, M. Katz, J. Lee, B. Slutsky, A. Mizrahi, V. Lomakin, and Y. Fainman, "Thresholdless nanoscale coaxial lasers," *Nature*, vol. 482, no. 7384, pp. 204–207, 2012.

[117] Y.-J. Lu, J. Kim, H.-Y. Chen, C. Wu, N. Dabidian, C. E. Sanders, C.-Y. Wang, M.-Y. Lu, B.-H. Li, X. Qiu, *et al.*, "Plasmonic nanolaser using epitaxially grown silver film," *science*, vol. 337, no. 6093, pp. 450–453, 2012.

[118] N. Li, K. Liu, V. J. Sorger, and D. K. Sadana, "Monolithic iii–v on silicon plasmonic nanolaser structure for optical interconnects," *Nat. Sci. Rep.*, vol. 5, 2015.

[119] J. Liu, P. Garcia, S. Ek, N. Gregersen, T. Suhr, M. Schubert, J. Mørk, S. Stobbe, and P. Lodahl, "Random nanolasing in the anderson localized regime," *Nature Nanotechnology*, vol. 9, no. 4, pp. 285–289, 2014.

[120] Y.-J. Lu, C.-Y. Wang, J. Kim, H.-Y. Chen, M.-Y. Lu, Y.-C. Chen, W.-H. Chang, L.-J. Chen, M. I. Stockman, C.-K. Shih, *et al.*, "All-color plasmonic nanolasers with ultralow thresholds: autotuning mechanism for single-mode lasing," *Nano Lett.*, vol. 14, no. 8, pp. 4381–4388, 2014.

[121] Q. Zhang, G. Li, X. Liu, F. Qian, Y. Li, T. C. Sum, C. M. Lieber, and Q. Xiong, "A room temperature low-threshold ultraviolet plasmonic nanolaser," *Nat. Commun.*, vol. 5, p. 4953, 2014.

[122] K. Srinivasan, M. Borselli, O. Painter, A. Stintz, and S. Krishna, "Cavity q, mode volume, and lasing threshold in small diameter algaas microdisks with embedded quantum dots," *Opt. Express*, vol. 14, no. 3, pp. 1094–1105, 2006.

[123] J. Tatebayashi, S. Kako, J. Ho, Y. Ota, S. Iwamoto, and Y. Arakawa, "Room-temperature lasing in a single nanowire with quantum dots," *Nat. Photon.*, vol. 9, no. 8, pp. 501–505, 2015.

[124] M. Noginov, G. Zhu, A. Belgrave, R. Bakker, V. Shalaev, E. Narimanov, S. Stout, E. Herz, T. Suteewong, and U. Wiesner, "Demonstration of a spaser-based nanolaser," *Nature*, vol. 460, no. 7259, pp. 1110–1112, 2009.

[125] J. Y. Suh, C. H. Kim, W. Zhou, M. D. Huntington, D. T. Co, M. R. Wasielewski, and T. W. Odom, "Plasmonic bowtie nanolaser arrays," *Nano Lett.*, vol. 12, no. 11, pp. 5769–5774, 2012.

[126] C. Zhang, Y. Lu, Y. Ni, M. Li, L. Mao, C. Liu, D. Zhang, H. Ming, and P. Wang, "Plasmonic lasing of nanocavity embedding in metallic nanoantenna array," *Nano Letters*, vol. 15, no. 2, pp. 1382–1387, 2015.

[127] T. Hakala, H. Rekola, A. Väkeväinen, J.-P. Martikainen, M. Nečada, A. Moilanen, and P. Törmä, "Lasing in dark and bright modes of a finite-sized plasmonic lattice," *Nat. Commun.*, vol. 8, p. 13687, 2017.

[128] W. Zhou, M. Dridi, J. Y. Suh, C. H. Kim, M. R. Wasielewski, G. C. Schatz, T. W. Odom, *et al.*, "Lasing action in strongly coupled plasmonic nanocavity arrays," *Nat. Nanotechnol.*, vol. 8, no. 7, pp. 506–511, 2013.

[129] H. Zhu, X. Xu, X. Tian, J. Tang, H. Liang, L. Chen, Y. Xie, X. Zhang, C. Xiao, R. Li, *et al.*, "A thresholdless tunable raman nanolaser using a zno–graphene superlattice," *Adv. Mater.*, vol. 29, no. 2, 2017.

[130] S. Wuestner, A. Pusch, K. L. Tsakmakidis, J. M. Hamm, and O. Hess, "Gain and plasmon dynamics in active negative-index metamaterials," *Philosophical Transactions of the Royal Society of London A: Mathematical, Physical and Engineering Sciences*, vol. 369, no. 1950, pp. 3525–3550, 2011.

[131] E. M. Purcell, "Spontaneous transition probabilities in radio-frequency spectroscopy," *Phys. Rev*, vol. 69, p. 681, 1946.

[132] M. Dridi and G. C. Schatz, "Lasing action in periodic arrays of nanoparticles," *JOSA B*, vol. 32, no. 5, pp. 818–823, 2015.

[133] O. Svelto and D. Hanna, *Principles of lasers*, ch. 7, p. 249. New York, NY, Plenum, 4th ed., 1998.

[134] J.-M. Jin, *Theory and computation of electromagnetic fields*, ch. 9, p. 483. John Wiley & Sons, 2nd ed., 2015.

[135] M. Ramezani, A. Halpin, A. I. Fernández-Domínguez, J. Feist, S. R.-K. Rodriguez, F. J. Garcia-Vidal, and J. G. Rivas, "Plasmon-exciton-polariton lasing," *Optica*, vol. 4, no. 1, pp. 31–37, 2017.

[136] H.-Y. Wu, L. Liu, M. Lu, and B. T. Cunningham, "Lasing emission from plasmonic nanodome arrays," *Advanced Optical Materials*, vol. 4, no. 5, pp. 708–714, 2016.

[137] A. Yang, T. B. Hoang, M. Dridi, C. Deeb, M. H. Mikkelsen, G. C. Schatz, and T. W. Odom, "Real-time tunable lasing from plasmonic nanocavity arrays," *Nature communications*, vol. 6, 2015.

[138] T. Byrnes, N. Y. Kim, and Y. Yamamoto, "Exciton-polariton condensates," *Nature Physics*, vol. 10, no. 11, pp. 803–813, 2014.

[139] S. Rodriguez, J. Feist, M. Verschuuren, F. G. Vidal, and J. G. Rivas, "Thermalization and cooling of plasmon-exciton polaritons: towards quantum condensation," *Physical review letters*, vol. 111, no. 16, p. 166802, 2013.

[140] P. Leung, S. Liu, and K. Young, "Completeness and orthogonality of quasinormal modes in leaky optical cavities," *Physical Review A*, vol. 49, no. 4, p. 3057, 1994.

[141] E. Ching, P. Leung, A. M. van den Brink, W. Suen, S. Tong, and K. Young, "Quasinormal-mode expansion for waves in open systems," *Reviews of Modern Physics*, vol. 70, no. 4, p. 1545, 1998.

[142] R. Lang, M. O. Scully, and W. E. Lamb Jr, "Why is the laser line so narrow? a theory of single-quasimode laser operation," *Physical Review A*, vol. 7, no. 5, p. 1788, 1973.

[143] R. Loudon and T. von Foerster, "The quantum theory of light," *American Journal of Physics*, vol. 42, no. 11, pp. 1041–1042, 1974.

[144] U. Fano, "Atomic theory of electromagnetic interactions in dense materials," *Physical Review*, vol. 103, no. 5, p. 1202, 1956.

[145] G. W. Ford and W. H. Weber, "Electromagnetic interactions of molecules with metal surfaces," *Physics Reports*, vol. 113, no. 4, pp. 195–287, 1984.

[146] M. Johnson, P. Bowen, N. Kundtz, and A. Bily, "Discrete-dipole approximation model for control and optimization of a holographic metamaterial antenna," *Appl. Opt.*, vol. 53, pp. 5791–5799, Sep 2014.

Biography

Patrick Bowen was born in Columbia, SC on March 7, 1989. He grew up home-schooled by his parents Donald and Laura Bowen in Wake Forest, North Carolina, together with his siblings Amber, Brandon, and Grace Bowen. He obtained a double major Summa Cum Laude in Physics and Electrical Engineering in 2011 from North Carolina State University, during which time he spent a year at the University of Surrey in Guildford, UK on an exchange program. Patrick's studies at North Carolina State University were in part funded by the Goldwater Scholarship. Patrick then obtained his master's degree in 2013 from ETH Zürich in Zürich, Switzerland, funded by the Excellence Scholarship from that institution. Afterwards Patrick returned to North Carolina to obtain his PhD at Duke University, in part funded by the Pratt-Gardner fellowship.